12-15-2014

# Piezotransistive III-V Nitride Microcantilever Based Mems/Nems Sensor for Photoacoustic Spectroscopy of Chemicals

Abdul Hafiz Ibne Talukdar
*University of South Carolina - Columbia*

# PIEZOTRANSISTIVE III-V NITRIDE MICROCANTILEVER BASED MEMS/NEMS SENSOR FOR PHOTOACOUSTIC SPECTROSCOPY OF CHEMICALS

By

Abdul Hafiz Ibne Talukdar

Bachelor of Science
Bangladesh University of Engineering and Technology, 2008

Master of Science
King Abdullah University of Science and Technology, 2011

---

Submitted in Partial Fulfillment of the Requirements

For the Degree of Doctor of Philosophy in

Electrical Engineering

College of Engineering and Computing

University of South Carolina

2014

Accepted by:

Goutam Koley, Major Professor

Mohammod Ali, Committee Member

MVS Chandrashekhar, Committee Member

Sourav Banerjee, Committee Member

Lacy Ford, Vice Provost and Dean of Graduate Studies

## DEDICATION

*Dedicated to my Parents, my lovely wife Sonia, my great sisters and brother-in-laws for being always by my side and keeping me on track.*

## ACKNOWLEDGEMENTS

When I was a child, my father told me “Son, the title ‘Dr’ before your name would look good on the nameplate on the door”. That time I had no clue about Dr or PhD. Since then it has been a long journey for me with a lot of memories, surprises, failures and successes. My life was not an usual ones and the lifelong experiences do not set up a platform for PhD. It is always the Almighty, Allah, who has been sheltered me from all those storms. Without His mercy, the story could have written otherwise. I was, am and always will be thankful to Him. He gifted me with a great family, a family who never stop walking on the rough roads and never stop believing. My father and mother, the next persons who I want to thank from the bottom of my heart. Their constant support, motivation, guidance, love, and expectations, lead me to shape my career. My wife comes next, with whom I have passed six eventful years and still going on. I thank my wife, Sonia, without whom my life in abroad would have been nightmare. Words cannot describe her dedications towards me and her PhD. At time of sorrows, she filled me up with happiness, stood beside me against the odds, and she has been through a lot for me and my research works. Still she loves me and I cannot just thank you for that!

I have three lovely sisters and brother-in-laws, without whom I could not have thought about leaving my home country Bangladesh. They carry all the anxieties back home and let me do my work. It was literally impossible for me to finish the fabrication of

my devices and continue further, when my sister Anne was diagnosed with Oral cancer. Every morning when I talked to her over phone, being away from Columbia residing all alone in Atlanta, Georgia, her unclear voice on the phone and her strong motivation to fight the cancer, gave me immense strength and hopes to finish my PhD. I love you all and thank you for being the best siblings in the world. I want to thank my in laws who had given me a wonderful family to smile with.

At this point, I would like to thank my lab members for supporting me with their best efforts. James Tolson and Nick DeRoller, thanks a lot, without the circuit boards and current source (Nick), my research would not have progressed a bit. Thank you Ifat for being with me in the early days in Atlanta, figuring out how to get rid of the resist to progress further in fabrication. You had been a great friend and a colleague who comes forward to help without hesitation. I would like to thank Yihao with whom I have passed my PhD life in a closed lab in the basement, who sacrificed his times for my research. I would always appreciate the support from Alina, performing the vacuum test and taking initial SEM images. She had been a great friend to me. I am always grateful to Amol and Ahsan for being a wonderful colleague and friend. I am lucky to have a good friend like Arthur Illingworth whose excellence in machining had allowed me to set up the most complex experiements. Besides my colleagues, I would like to show appreciation to my friends around the world who supported me always and well wished for my future.

I would like to acknowledge Dr David Gottfried, Gary Spinner and Dr Mikkel Thomas in MiRC, Georgia Tech, without their support, the devices could not be fabricated. I would also like to Acknowledge Dr Thomas Thundat, Dr Dongkyu Lee, Dr Sam Kim, and Dr Faheem Khan who immensely helped me in Phtotacoustic spectroscopy and with

Laser Vibrometer in University of Alberta, AB, Canada. Those bitter cold nights in Alberta would not have turned into sweet memories without their selfless supports and scholarly discussions. I will be always thankful to Dr Soumitra Ghosroy for generously allowing me to use the SEM after hours, otherwise the beauty of the micro devices could not be documented. I am also thankful to Dr Ricardo for performing the gamma radiation exposure in Savannah River National Lab which enabled me to demonstrate the harsh environment testing.

Finally, the most important person in my PhD, Dr Goutam Koley, who is not only the supervisor and a great mentor, but also my friendly guardian. Without his guidance, support, and motivation, this long waited dream would not be a reality. He was always by my side when experiment was not working, considered my personal matters, and arranged for whatever I needed. I would always be grateful to him. My special thanks to Dr Mohammod Ali, Dr MVS Chandrashekhar, and Dr Sourav Banerjee for serving in my committee and managing time in their busy schedule.

# ABSTRACT

Microcantilevers are highly attractive as transducers for detecting chemicals, explosives, and biological molecules due to their high sensitivity, micro-scale dimensions, and low power consumption. Though optical transduction of the mechanical movement of the microcantilevers into an electrical signal is widely practiced, there is a continuous thrust to develop alternative transduction methods that are more conducive to the development of compact miniaturized sensors. Piezoelectric and piezoresistive transduction methods are two of the most popular ones that have been utilized to develop miniaturized sensor systems. Piezoelectric cantilevers, which are commonly made of PZT film, have demonstrated very high sensitivity; however, they suffer from incompatibility with Si based circuitry and challenges with dc and low frequency measurements due to the problem of charge leakage. On the other hand, piezoresistive microcantilever, which are mostly made of Si, can be easily integrated with existing Si based process technologies, but suffer from low sensitivity. In addition, none of the above material systems are suitable for high temperature (>300 °C) and harsh environment operation. III-V Nitride semiconductors are being extensively studied almost two decades for electronic and optoelectronic applications due to their exceptional physical and chemical properties, which include a wide bandgap, strong piezoelectric properties, high electron mobility, and chemical inertness. AlGaN/GaN heterostructures offer unique advantage over existing piezoresistive or piezoelectric materials, as it actually converts the piezoelectric response

of these materials to piezoresistive response, since the two dimensional electron gas (2DEG) formed at the AlGaN/GaN interface gets modulated by the stress induced change in piezoelectric polarization. The epitaxial growth of III-V Nitride layers on a Si substrate enables direct integration of nitride microelectromechanical systems (MEMS) with mature Si based integrated circuits to develop miniaturized sensor systems.

In spite of several technological advantages of III-V Nitride MEMS, of which a microcantilever is a simple example, only a handful of studies have been reported on their deflection characterization in static mode and none on dynamic bending mode. The effect of mechanical strain, on 2DEG density and output characteristics of AlGaN/GaN heterostructure field effect transistors (HFETs), have been reported earlier. High gauge factors (>100) have been reported for quasi-static and step bending response, however, the factors contributing to such high values, especially their deviation from much lower theoretical estimates, are poorly understood. Recently, very high gauge factor of -850 was reported for microcantilevers in transient condition, however, the corresponding dynamic response was not studied. Acoustic detection using microcantilevers have attracted interest in recent years, especially in photoacoustic spectroscopy, as they can offer up to two orders of higher sensitivity compared to existing acoustic sensors. III-V Nitride based ultrasonic microcantilevers sensors, offering high sensitivity, low noise, and harsh environment operation, are ideally suited for many demanding sensing applications that are not possible at present.

This dissertation aims the theory and application of III-V Nitride microcantilevers and a novel electronic transduction scheme named as ‘Piezotransistive Microcantilever’ to transduce femtoscale excitation. A complete fabrication process, measurement techniques

and several application aspects of this sensing technology specially acoustic wave detection generated in solid and air media with high sensitivity, have been demonstrated. This thesis reports on displacement measurement at the femtoscale level using a GaN microcantilever with an AlGaN/GaN Heterojuction Field Effect Transistor (HFET) integrated at the base that utilizes piezoelectric polarization induced changes in two dimensional electron gas (2DEG) to transduce displacement with very high sensitivity. With appropriate biasing of the HFET, an ultra-high Gauge Factor (GF) of 8700, the highest ever reported, was obtained, with an extremely low power consumption of <1 nW, which enabled direct electrical readout of the thermal noise spectra of the cantilever. The self-sensing piezotransistor was able to transduce external excitation with a superior noise limited resolution of 12.43 fm/$\sqrt{\text{Hz}}$ and an outstanding responsivity of 170 nV/fm, which is three orders higher that state-of-the-art technology, supported by both analytical calculations and laser vibrometry measurements. This extraordinary deflection sensitivity enabled unique detection of nanogram quantity of analytes using photoacoustic spectroscopy.

# TABLE OF CONTENTS

# LIST OF TABLES

## LIST OF FIGURES

# CHAPTER 1

## INTRODUCTION

"There's Plenty of Room at the Bottom," as Dr Richard P Feynman envisioned in his legendary speech at the annual meeting of the American Physical Society, Pasadena, CA, December 29, 1959 about electro mechanical systems. Though transistors were developed ahead of that time which were scaled down to nanoscale in this era, but the prime difference between transistor and electro-mechanical system is that the later needs more prolific attention application wise. Is it worth to have an electro-mechanical system scaled down to micro or nanoscale? Dr Feynman was not wrong about his envision, as we all now a days use something which has Micro-Electro-Mechanical System (MEMS) in it, for example our smartphones have accelerometers which is a MEMS. MEMS refer to devices that have a characteristic length of less than 1 mm but more than 1μm, that combine both electrical and mechanical components which are fabricated using integrated circuit batch-processing technologies. As the technology advances, MEMS devices are getting into nanoscale regime which are being called as Nano-Electro-Mechanical System (NEMS). Whether its MEMS or NEMS their applications have wide variety in the form of sensors, actuators, and transducers. Innovative designs have offered different MEMS structures, mostly suspended and surface mounted structures depending on the aim of applications.

Recently MEMS has evolved from a niche technology into an important mainstream technology[1-4]. Generally, MEMS refer to a collection of micromechanical structures, which can sense its ambient and have the ability to react to the corresponding changes in that environment with the use of micro/nano electronics. They make the system faster, more reliable, cheaper and capable of incorporating more complex functions. Applications of such systems include chemical, biological and trace gas sensors, microfluidic sensors and other fluid devices, microactuators, rf-MEMS up to GHz frequencies (filters, resonators, and switches), micro opto-electromechanical systems and many others[5-16]. This chapter will describe the choice of MEMS structure and material, and the possible applications along with the review of state of the art techniques.

## 1.1 Choice of Microstructure

Microfabricated cantilevers have been used in atomic force microscopy (AFM) for more than 20 years[13-16]. Cantilevers (like a tiny diving board or beams with one fixed and one free end) have been widely used in recent years as miniaturized, ultrasensitive, and fast-responding sensors for applications in chemistry, physics, biochemistry, and medicine[17-31]. Microcantilever sensors respond not only by bending (static mode) due to the absorption of molecules, change in pressure, temperature, and electrostatic field; as well as shift in resonance frequency, change in amplitude of oscillation also occurs in dynamic mode. Over a decade, microcantilever based sensing has witnessed an impressive progress due to multi-disciplinary scientific research, evident from the number of publications in the last 10 years (Fig. 1.1). In the last decade, microcantilever based sensors

have proved to become a versatile transduction platform for physical parameters, chemical, volatile organic molecules, explosives and biomolecule detection.

## 1.2 Choice of Material

Silicon (Si), the most abundant and matured technology, has been always considered as the prime material in semiconductor industries everywhere. However, application of Si has shown limitations in sensing applications in harsh environmental conditions, suffering from low

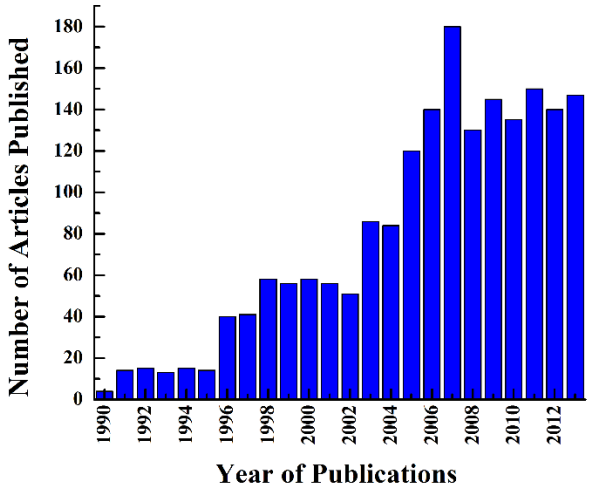


**Figure 1.1** The number of yearly peer reviewed publications as obtained from Google Scholar search with a key "cantilever sensor".

sensitivity and selectivity. Si cannot be used for high temperature applications as it loses the electrical and mechanical reliability at 500 ◦C[32]. One of the great advantages of the wide band gap semiconductors is their very high mechanical, thermal, chemical and biochemical stability, which offers exciting MEMS/NEMS sensing applications which require reliability, linearity, sensitivity, and selectivity[33]. Moreover, materials with a high Young's modulus can better maintain linearity between applied load and the induced

deformation. This particularly demands group-III nitrides, which has high Young's modulus. AlGaN/GaN heterostructures contain a highly conductive two-dimensional electron gas (2DEG) at the interface, which is sensitive to mechanical load, as well as to chemical modification of the surface, and can be used for novel sensing principles[34,35]. Presence of such a 2DEG is unique to AlGaN/GaN heterostructure, and is attributed to unintentional polarization doping, since it arises because of the strong polarization properties of the nitrides. Among the most common semiconductors (see Fig. 1.2) AlN (6.13 eV) and GaN (3.42 eV) have much higher bandgap compared to others[34]. Due to such wide bandgaps, their critical electric fields for breakdown are much higher than other III-V semiconductors. Though GaAs has much higher low field mobility, GaN is clearly superior in terms of saturation velocity (see Table 1.1)[34,35]. Together with high bandgap, high saturation velocity and high mobility makes nitrides ideal contenders for high power microwave application[36-42]. The presence of a direct and wide bandgap in AlGaN/GaN also make them very suitable for optoelectronic applications, especially in the green, blue, and UV regions of the spectrum, where there are virtually no other contenders.

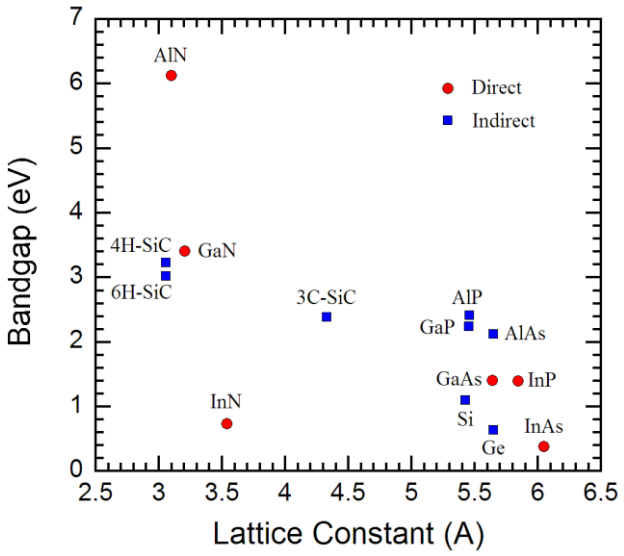


**Figure 1.2** Bandgap of common semiconductors versus their lattice constant[34,35].

**Table 1.1** Electronic properties of some common semiconductors[34,35]

| Properties | Si | GaAs (AlGaAs/ InGaAs) | InP (InAlAs/ InGaAs) | 4H- SiC (3C-SiC/ 6H-SiC) | GaN (AlGaN / GaN) |
|---|---|---|---|---|---|
| Bandgap (eV) | 1.11 | 1.42 | 1.35 | 3.26 | 3.42 |
| Electron Mobility ($cm^2/Vs$) | 1350 | 8500 (10000) | 5400 (10000) | 700 (2000) | 900 (2000) |
| Saturation velocity ($\times 10^7$ cm/s) | 1 | 1 (2.1) | 1 (2.3) | 2 | 1.5 (2.7) |
| 2DEG density ($cm^{-2}$) | NA | $< 4\times10^{12}$ | $< 4\times10^{12}$ | $< 3\times10^{12}$ | 1-2 $\times10^{13}$ |
| Critical Breakdown field ($\times 10^6$ V/cm) | 0.3 | 0.4 | 0.5 | 2 | 3.3 |
| Relative dielectric constant | 11.8 | 12.8 | 12.5 | 10 | 9 |

## 1.3 Motivation

Microcantilever based sensing not only gives the opportunity to develop micro sensor which can be implemented for the betterment of human health, national security, and ease of living, but it also offers a unique platform to integrate a complete sensor

package from scratch which involves designing and fabrication of micro/nano electronics embedding with mechanical structures, and finally packaging them for sensing application. These whole story requires an in depth knowledge and engineering of multidisciplinary research (i.e. pure science and different branches of engineering).

The choice of the material has its own reason. III-V Nitride are well known for high power electronics, radio frequency applications and optoelectronics. Recently there is a growing urge for developing sensor with these materials as they offer very unique material properties which would offer better sensors. There is always a challenge in every step to develop such sensors and that is what good enough to motivate a person to pursue a research on III-V Nitride MEMS/NEMS.

## 1.4 Outline of the dissertation

This dissertation is aimed to develop a novel sensing mechanism namely Photoacoustic Spectroscopy for detecting chemicals, with III-V nitride (mainly AlGaN/GaN) transistor embedded in microcantilever. Though the ultimate goal is to perform spectroscopy but the developed sensor offers wide range of applications including strain, displacement, and force sensors. This dissertation is organized in such a way to deliver the development of AlGaN/GaN Heterojunction Field Effect Transistor (HFET) embedded GaN microcantilever for photoacoustic spectroscopy, in a very convenient way to general audience and scientific community. The organizations of this dissertation is given below:

Chapter 2: Describes the basic theory of microcantilevers and AlGaN/GaN material; state-of-the-art research; theoretical analysis and useful formula.

Chapter 3: Covers exclusively the fabrication process of the devices and relevant issues and solutions. It also includes Scanning Electron Micrograph (SEM) of fabricated devices.

Chapter 4: Elucidates the piezoresistive transduction of both static and dynamic motion of the microcantilevers with AlGaN/GaN HFET. It includes the experiments performed, the observations, and the associated results.

Chapter 5: Describes the piezotransistive transduction of both static and dynamic motion of the microcantilevers with AlGaN/GaN HFET. It includes the analytical analysis, experiments performed, the observations, and the associated results. It also presents the operation, reliability, and consistency of the microcantilevers when exposed to harsh environment

Chapter 6: Demonstrate the performance of the microcantilever as a displacement sensor, pressure sensor, and performance of the device in harsh environment (gamma radiation). It also experimentally compares the novel technology with commercial optical method.

Chapter 7: Describes Photoacoustic spectroscopy in detail and demonstrates our proposed Piezotransistive transduction method of photoacoustic spectroscopy to detect several chemicals.

Chapter 8: Summarizes the contributions of this work and finally conclude the dissertation with future prospects and development of this research.

# CHAPTER 2

# III-V NITRIDE MICROCANTILEVER BASED MEMS SENSORS

Microcantilevers, one of the prominent MEMS structures, have been introduced as a novel sensing platform more than a decade ago. This technology has evolved as a great candidate as chemical, biological and physical sensors, due to their high sensitivity, low cost, array based sensing, fast response and low power requirement. In this chapter we discuss the history, status of microcantilever based sensors, theory, operation modes, different transduction schemes for microcantilever based MEMS sensors.

## 2.1 Microcantilever based sensors: history and status

### 2.1.1 History and current status

Measurement of adsorption-induced deflection or a shift in resonance frequency using Si beams was already described back in 1968, by Wilfinger *et al.*[43]. In 1971, Heng fabricated gold microcantilevers for mechanical filtering of the high-frequency signal [44]. Later in 1979, Petersen constructed Si cantilever-type MEMS switches to bridge the gap between Si transistors and mechanical relays [45]. Since the implementation of Atomic Force Microscope (AFM) in 1986 [46] microcantilevers have become more available commercially, initiating broad research interests with microcantilevers.

In 1994, Itoh *et al.* reported a zinc-oxide coated microcantilever with piezoresistive deflection readout [47]. Cleveland *et al.* detected nanogram changes in mass with AFM probe tips, by observing frequency change [48]. Gimzewski *et al.* showed the first chemical sensing applications [49] with cantilevers. During the early 90s, researchers in the Oak Ridge National Lab (ORNL) led by Dr. Thomas Thundat worked extensively on microcantilever base sensing, becoming the leaders in molecular sensing with microcantilevers [50] along with various sensing applications such as, mercury vapor sensor [51,52], infrared detector [53-55], trace gas sensors [56-58], and biomolecule sensing [59-61].

In recent years, the field of cantilever sensors has been very active, large number of articles has been published (see Fig. 1.1). Major sensing results include detection of vapors and volatile compounds [62] as well as the development of gas sensors based on the piezoresistive concept [63]. A field of growing interest is the detection of explosives [58], nerve agents [64], viruses [65], bacteria, [66]. Physical parameter sensing such as viscosity and density of liquid and monitoring pH level of solution are also reported in [67]. For biomedical applications, detection of DNA [65], proteins [68], prostate-specific antigen (PSA) [60] is possible. MEMS has promisingly advance in nanoscale regime with developing nanoelectromechanical system (NEMS) based sensors [69-71] offering higher sensitivity, lower power consumption and dense integration. But it comes with technical challenges to measuring deflection signals and fabrication process [49].

## 2.2 Theory of microcantilevers

Theoretically, a cantilever is a special case of classical Euler-Bernoulli beam where one end is free and other end is clamped [72]. There are several shapes of cantilever but the

basic shapes are namely (see Fig. 2.1), rectangular (red color), triangular (green), U shape (orange), and T shape (blue). The beam theory remains basically same but the definition of elastic constant and moment of inertia should be defined according to the shape.

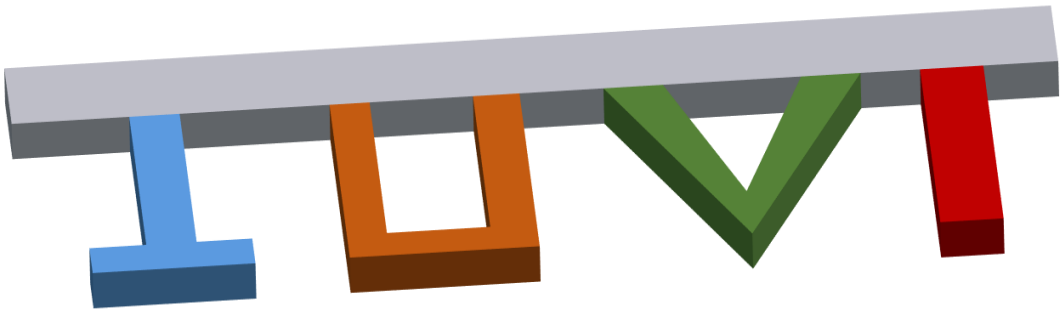

**Figure 2.1** Different shapes of cantilever.

### 2.2.1 Elastic properties

*2.2.1.1 Young's modulus:* Young's modulus or the modulus of elasticity is the tangent modulus of the strain versus strain curve of a particular material. It is the measure of how stiff a material is. The Young's modulus, $E$ is defined as,

$$E = \frac{\sigma}{\varepsilon} = \frac{F/A}{\Delta L/L} \tag{2.01}$$

where, $\sigma$ is the stress applied on the material measured by force ($F$) per unit area ($A$), and the $\varepsilon$ is the strain measured by the change in length ($\Delta L$) per unit length ($L$).

*2.2.1.2 2nd Moment of cross-sectional area*: Property of a cross section that can be used to predict the resistance of beams to bending and deflection, around an axis that lies

in the cross-sectional plane parallel to the width of the cantilever. The 2nd moment of cross-sectional area, *I* can be express as,

$$I = \int_A z^2 dA \tag{2.02}$$

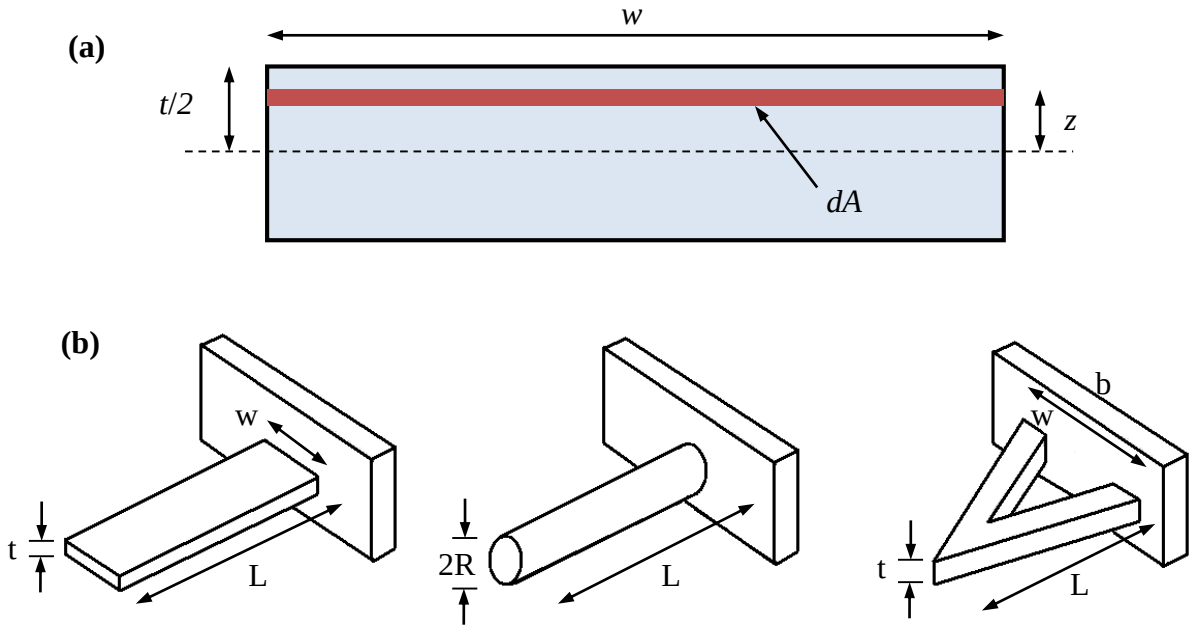


**Figure 2.2** (a) Calculation of *I* for rectangular cantilever, (b) Geometrical parameters of rectangular, cylindrical and triangular cantilever.

where, *z* is the distance from the centroid axis to the area *dA*. Therefore, *I* depends upon the cross sectional area of the cantilever [see Fig. 2.2 (a), (b)].

For rectangular beam,

$$I = \int_A z^2 dA = \int_{-t/2}^{t/2} z^2 w dz = \frac{wt^3}{12} \tag{2.03}$$

For cylindrical beam,

$$I = \frac{1}{6} R^4 \tag{2.04}$$

For triangular beam,
$$I = \frac{wt^3}{6}\left[1 + 4\left(\frac{w}{b}\right)^3\right] \tag{2.05}$$

*2.2.1.3 Spring constant:* For simple structures, the 2nd moment of inertia ($I$) and hence is the spring constant ($k$) are relatively less complicated [73]. For Young's modulus, $E$ , 2nd moment of cress-sectional area, $I$ , and length $L$, the spring constant of a rectangular cantilever is given by,

$$k = \frac{3EI}{L^3} = \frac{Ewt^3}{4L^3} \tag{2.06}$$

The preceding equations assume perfectly rigid support and are valid in the small deformation regime. Both these assumptions can be invalid in many micro scale structures, and numerical analyses using finite-element techniques should be performed to obtain $k$ value.

### 2.2.2 Beam equation

The differential equation of motion derived from Euler-Bernoulli theory is expressed as,

$$\frac{kL^3}{3}\frac{\partial^4 z(x,t)}{\partial x^4} + \frac{m}{L}\frac{\partial^4 z(x,t)}{\partial t^4} = F(x,t) \tag{2.07}$$

here, $z(x,t)$ is the time dependent vertical displacement at distance $x$. $k$ is the spring constant of the beam, $L$ is length, $m$ is the mass and $F(x,t)$ is time dependent load per unit length applied at distance $x$. To find out the undamped natural motion of oscillation of the cantilever we assume no external forces, i.e $F = 0$. We get,

$$\frac{\partial^4 z(x,t)}{\partial x^4} + \frac{3km}{L^4}\frac{\partial^4 z(x,t)}{\partial t^4} = 0 \tag{2.08}$$

Assuming time dependent harmonic solution, we get

$$z(x,t) = z(x)[\cos(\omega_n t) + \theta] \tag{2.09}$$

Here, $z(x)$ is the maximum vertical displacement of the beam at distance $x$. $\omega_n$ is the angular frequency of $n$-th mode and $\theta$ is the phase angle. Combining Eqs. (2.08) and (2.09) we get,

$$\frac{\partial^4 z(x)}{\partial x^4} - \kappa_n^4 z(x) = 0 \tag{2.10}$$

where the modal parameters, $$\kappa_n^4 = \omega_n^4 \frac{3km}{L^4} \tag{2.11}$$

and, $$\alpha_n^4 = (\kappa L)_n^4 = 3\omega_n^4 km \tag{2.12}$$

The general solution to Eq. (2.10) is:

$$z(x) = B_1 \sin(\kappa_n x) + B_2 \cos(\kappa_n x) + B_3 \sinh(\kappa_n x) + B_4 \cosh(\kappa_n x) \tag{2.13}$$

where $B_1$, $B_2$, $B_3$, and $B_4$ are arbitrary constants. While solving Eq. (2.04) for cantilever (one end free, another end clamped), the following boundary conditions should be applied [72],

For the clamped end (at $x = 0$), $$z = 0,\ \frac{\partial z}{\partial x} = 0$$

For the free end (at $x = L$), $$\frac{\partial^3 z}{\partial x^3} = 0,\ \frac{\partial^4 z}{\partial x^4} = 0$$

For the boundary conditions we get a homogeneous system of four linear equations for the unknown coefficients $B_1$, $B_2$, $B_3$, and $B_4$. This system has a nontrivial solution only if,

$$\cos(\alpha_n).\cosh(\alpha_n) + 1 = 0 \tag{2.14}$$

Through numerical solutions, the values of $\alpha_n$ for different modes can be found out as,

$\alpha_1 = 1.8751,\ \alpha_2 = 4.6941,\ \alpha_3 = 7.8548,\ \alpha_4 = 10.9956$

For $\alpha_n >> 1$, we get

$$\alpha_n = \pi\left(n - 1/2\right) \tag{2.15}$$

### 2.2.3 Natural frequency of oscillation

Equation (2.10) is a fourth order differential equation, which when solved for the appropriate boundary conditions, will allow us to find the angular frequency $\omega_n$. Putting $\omega_n = 2\pi f_n$ and rearranging we can get the expression for $n$-th mode natural frequency of bending of the cantilever as,

$$f_n = \frac{1}{4\pi}\left(\frac{\alpha_n}{L}\right)^2 \sqrt{\frac{EI}{\rho wt}} \tag{2.16}$$

where, $\rho$ is the density of the cantilever material, expressed as $\rho = m/V$, where $V$ is the volume of the cantilever express by $V = L \times w \times t$. Rearranging Eq. (2.16) and using Eqs. (2.03) and (2.06) we get the,

$$f_n = \frac{\alpha_n^2}{2\pi\sqrt{3}} \sqrt{\frac{k}{m}} \tag{2.17}$$

For 1st natural frequency, $\alpha_1 = 1.8751$, and hence we get,

$$f_1 = \frac{1}{2\pi} \sqrt{\frac{k}{m_{eff}}} \tag{2.18}$$

where, $m_{\text{eff}} = 0.2427m$. Equation (2.18) is widely used to calculate the 1st resonant frequency of rectangular cantilever. For calculating frequencies of other modes of oscillation refer to the calculations done in Ref [74].

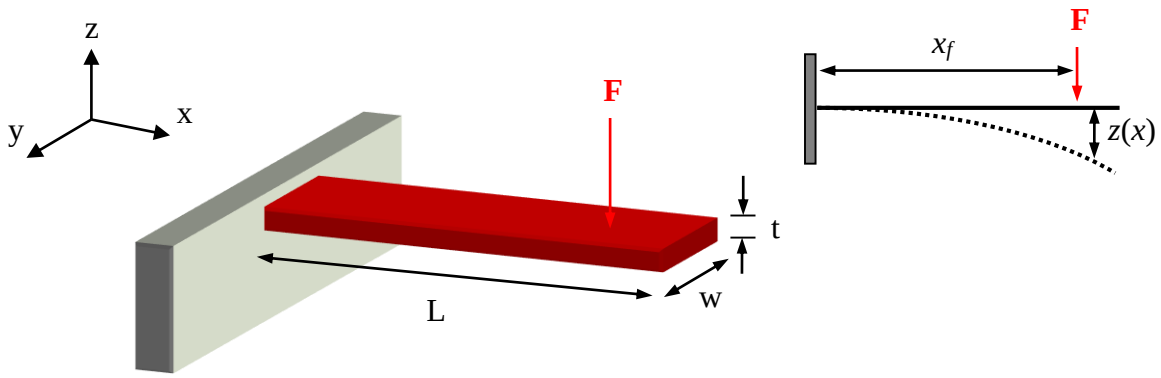


**Figure 2.3** Schematics of a cantilever showing the dimension and force exerted along *z*-axis. Inset shows the deflection due to applied force, *F* at distance *x*.

### 2.2.4 Static bending

If a force *F* is applied on the free end of the cantilever along *z*-axis (see Fig. 2.3) then the vertical displacement of the cantilever at a distance *x* from the fixed end is [75],

$$z(x) = \frac{FL}{2EI} x^2 \left(1 - \frac{x}{3L}\right) \tag{2.19}$$

where *E* is the Young's modulus, *I* is the moment of inertia, and *L* is the beam length. Equation (2.19) is valid as long as the beam deflection is negligible compared to its length (i.e., z << L). Using Eq. (2.19), the cantilever spring constant, i.e., the ratio of force to deflection on the cantilever tip, can be calculated as

$$k = \frac{F}{z(L)} \tag{2.20}$$

If a force $F$ is applied on any point $x_f$ distance away from the fixed point of the cantilever (see inset of Fig. 2.2) then the vertical displacement of the cantilever at $x$ distance from the fixed end is [76],

$$z(x) = \frac{FL}{2EI} \times \begin{cases} \frac{x_f}{L} x^2 \left(1 - \frac{x}{3x_f}\right) & x \le x_f \\ 2\frac{x_f^2}{L}\left(\frac{x_f}{3} + \frac{x - x_f}{2}\right) & x_f \le x \le L \end{cases} \tag{2.21}$$

When a point force $F$ is applied at the tip of the cantilever, the stress of the cantilever $z$ distance away from the neutral axis and $x$ distance away from the fixed end is given by,

$$\sigma_x(x) = \frac{12z(L-x)}{wt^3} F \tag{2.22}$$

The *neutral axis* is an axis in the cross section of a beam or shaft along which there are no longitudinal stresses or strains. If the section is symmetric and is not curved before a bending occurs, then the neutral axis is at the geometric centroid. Therefore the maximum stress will be at the surface (i.e. $z = t/2$). Moreover, if variation with $x$ is considered, then the maximum stress is found to be at the fixed end (i.e. $x = 0$). Longitudinal strain is directly proportional to the stress and is expressed by,

$$\varepsilon_x(x) = \frac{\sigma_x(x)}{E} = \frac{12z(L-x)}{Ewt^3} F \tag{2.23}$$

### 2.2.5 Mode of operation of a microcantilever

Depending on the measured parameter (structural deformations or resonance frequency change) the mode of sensor operation can be referred to as either static mode or

dynamic mode. In static mode, a cantilever is kept static. Static deflection can occur in microcantilever due to several phenomenon, such are: adsorbed species [77], by physically bending the cantilever, using functionalization layer to attract molecules, and by altering the ambient (changing pressure or temperature). In dynamic mode a cantilever is oscillated (by external actuation including piezo-oscillators and capacitive coupling), mostly at or very near to the resonant frequency. As seen from Eq. (2.17) the resonant frequency changes with the change in spring constant *k* and mass of the cantilever *m*. The dynamic mode can be initiated by external Piezo, acoustic wave, surface wave, periodic sinusoidal signal from electrostatic attraction.

Solution of Eq. (2.09) for cantilevers can be used to express the oscillation amplitude of a cantilever oscillating at a particular frequency. However, if deflection of only the free end is needed, then the motion of an oscillating cantilever can be analogous to lumped spring-mass system which can be described by second order differential equation [78],

$$m_{eff}\frac{d^2z}{dt^2} + D\frac{dz}{dt} + kz = F(\Omega t) \tag{2.24}$$

Here the damping constant,

$$D = \left(\frac{m_{eff}\,\omega_0}{Q}\right) \tag{2.25}$$

$m_{eff}$ is the effective mass of the cantilever, $k$ is the spring constant, and $\omega_0$ is the angular frequency.

Rewriting Eq. (2.25) we get,

$$\frac{d^2z}{dt^2} + 2\zeta\omega_0\frac{dz}{dt} + \omega_0^2 z = \frac{F(\Omega t)}{m_{eff}} \tag{2.26}$$

The resonant frequency here,

$$f_0 = \frac{\omega_0}{2\pi} = \frac{1}{2\pi}\sqrt{\frac{k}{m_{eff}}} \tag{2.27}$$

The parameter $\zeta$ is known as damping parameter and can be expressed as,

$$\zeta = \frac{D}{2\omega_0} = \left(\frac{m_{eff}}{2Q}\right) \tag{2.28}$$

Excited by external sinusoidal force of $F$ the vibration of the cantilever will be,

$$z(t) = \frac{\beta}{k}\ |F|\sin(\Omega t - \theta) \tag{2.29}$$

Where, $|F|$ is the amplitude of the applied force and $\beta$ is expressed as,

$$\beta = \frac{1}{\sqrt{\left(1-\frac{\Omega^2}{\omega_0^2}\right)^2 + \left(\frac{1}{Q}\frac{\Omega}{\omega_0}\right)^2}} \tag{2.30}$$

Now, if the applied external force (in our case capacitive force) has the same frequency as the resonant frequency (i.e. $\Omega = \omega_0$) then $\beta = Q$. In that case, the amplitude of cantilever oscillation becomes,

$$|z(t)| = \frac{Q}{k}\ |F| \tag{2.31}$$

And the phase angle $\theta$ express as,

$$\theta = \tan^{-1}\left(\frac{\frac{\Omega}{\omega_0}}{Q\left(1-\frac{\Omega^2}{\omega_0^2}\right)}\right) \tag{2.32}$$

## 2.3 Microcantilever based transduction methods

Whatever the mode of operation it may be, the mechanical movement of the microcantilever needs to be quantified and hence a suitable readout scheme is needed. Transduction is transforming a form of energy into other form; for our case it is transforming oscillation into any measurable electrical quantity. There are several transduction mechanisms.

### 2.3.1 Optical Transduction

Optical transduction is the most widely used method where a laser beam is incident on the free end of the microcantilever which reflects back to a position sensitive photo diode (PSPD)[75, 76]. This scheme is highly sensitive which offers femtoscale resolution. However this technique is not suitable array based sensing [79] as the laser spot size limitation highly affects the reliability when the cantilevers are small. Additionally, this readout makes the whole system bulky and power hungry.

### 2.3.2 Capacitive Transduction

The basic principle is that when the cantilever deflects the capacitance of a parallel plate capacitor changes [80]. Here the microcantilever is one of the two capacitor plates and other plate can either be integrated on the same chip or may be applied with a probe. This deflection technique is highly sensitive and offers higher displacement resolution. It can be easily miniaturized, utilize vacuum and consume less power. However the gap between the plates need to be very small and no change in medium is permitted [81,82].

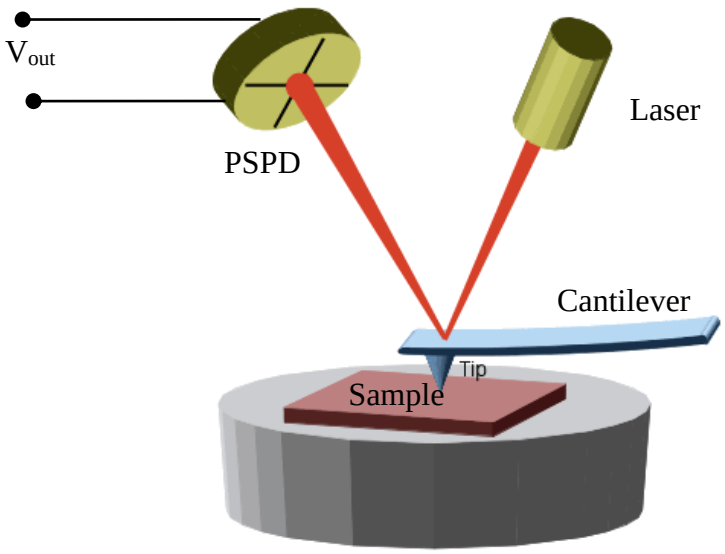


**Figure 2.4** Simplified schematic diagram of optical readout system mostly used in AFM. Inset shows the four quadrants of the PSPD with different voltage outputs.

### 2.3.3 Piezoresistive Transduction

Piezoresistance is characteristics of conductive and semiconductive materials, attributed to the change of the electrical resistance with an applied stress (strain). As the microcantilever deflects, stress maximally changes around the fixed end (or the base), which changes the resistance of the material following Poisson's formula . Generally, Wheatstone bridge configuration is used to measure the change in resistance as shown in Fig. 2.5 [63]. It compensates the effect of temperature dependent resistance change. While the miniaturization and sensitivity of this scheme are definite advantages, there are several disadvantages of such piezoresistor include non-linear relationship [81], poor sensitivity, drift and thermal, electronic and conductance fluctuation noise, and absolutely no tunability.

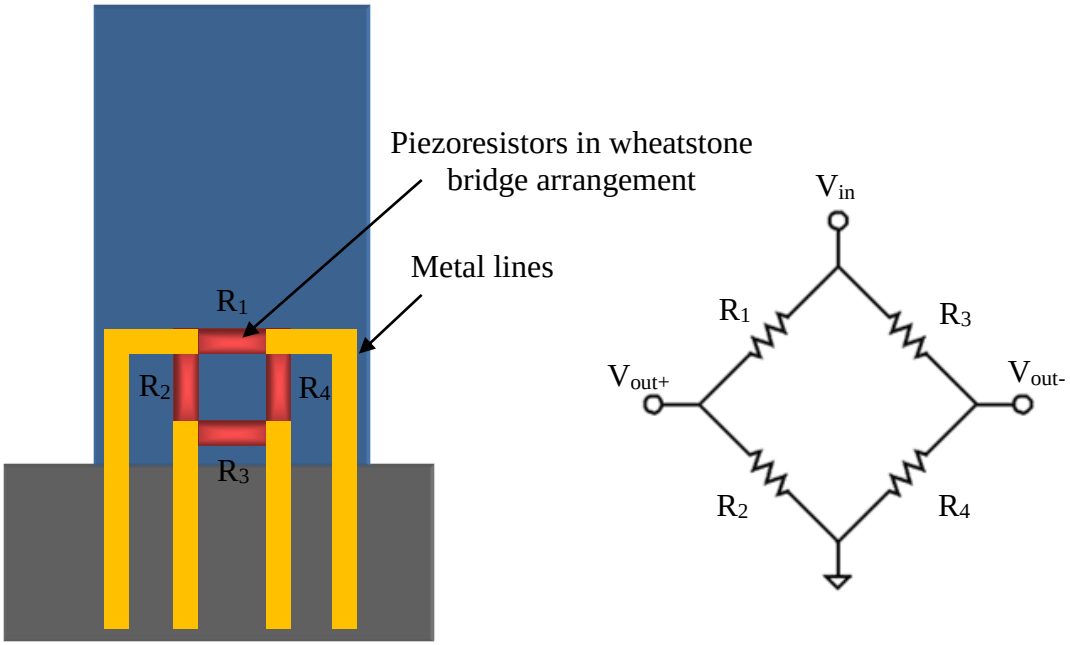


**Figure 2.5** Schematic diagram of piezoresistive transduction embedded at the base of a microcantilever. The Wheatstone bridge configuration is shown on the right.

Si is the prime material as piezoresistor but recently other materials have also attracted the research community, like GaAs [83], GaN [84], and SiC [85]. More details on piezoresistive transduction would be discussed in chapter 4. The strain sensitivity of a piezoresistive material is defined by *Gauge Factor* which is [86],

$$GF = \frac{\Delta R/R}{\varepsilon} = (1+2\nu) + \frac{\Delta\rho/\rho}{\varepsilon} \tag{2.33}$$

wherem $R$ and $\rho$ are the initial resistance and resistivity, $\Delta R$ and $\Delta\rho$ are the resistance and resistivity change resulting from the strain $\varepsilon$, $\nu$ is the Poisson's ratio.

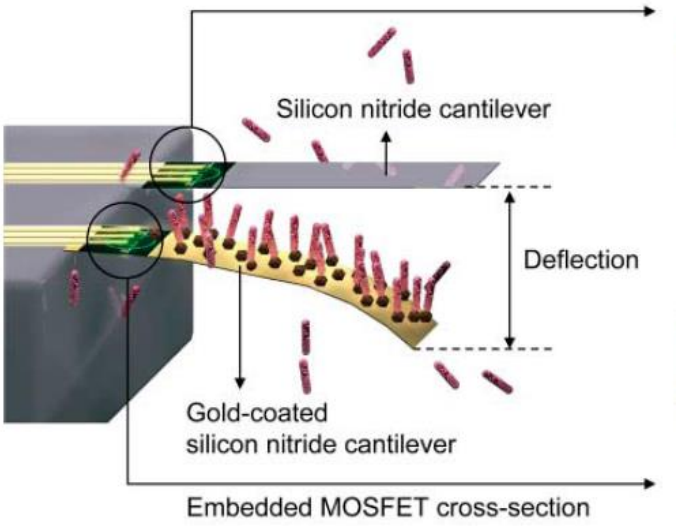


**Figure 2.6** Si MOSFET embedded SiN Microcantilever for detection of biomolecules (Figure taken from Ref. Shekhawat *et. al*.[87]).

### 2.3.4 FET based transduction

A recent research thrust on Field Effect Transistor (FET) based transduction has attained a lot of attraction. FET-based stress sensors are widely reported for micromechanical devices such as accelerometers, resonators, and parallel cantilevers for scanning probe microscopy, as well as for residual stress measurements [88,89]. Due to the strain dependent polarization and mobility, AlGaN/GaN HFET embedded microcantilevers are also fabricated and reported to be ideal for sensing applications [90]. Metal oxide semiconductor field effect transistor (MOSFET) embedded microcantilevers are also ideal candidates as it follows conventional CMOS fabrication process and several sensing had been reported earlier [87,91-94] (see Fig. 2.6).

## 2.4 Materials for microcantilever

AlGaN/GaN heterostructures offers a strain dependent 2-dimensional electron gas (2DEG) at the interface of AlGaN and GaN. Therefore a simple AlGaN/GaN resistor and AlGaN/GaN HFET embedded GaN microcantilevers are designed (described in next chapter) where the mechanical deflection of the microcantilever would translate to a change in HFET channel resistance. In this chapter, we will the physics of unique properties of AlGaN/GaN heterostructures, the formation of the 2DEG at the interface, and dependence of 2DEG on external strain.

### 2.4.1 Crystal structure

When thermodynamically stable, both AlN and GaN are wurtzite in crystal structure. In wurtzite structure, there are two interpenetrating hexagonal close-packed lattices, each displaced from the other ideally by $3/8c_0$. Each atom is tetrahedrally bonded to four atoms of the other type, and the primitive unit cell is simple hexagonal with a basis of four atoms, two of each kind. There is no inversion symmetry in this lattice along the [0001] direction, resulting in all atoms on the same plane at each side of a bond being same. Hence, a GaN crystal has two distinct faces, the Ga-face and the N-face. The arrangement of atoms for Ga-face and N-face GaN are shown in Fig. 2.7 [95]. A wurtzite crystal is characterized by three parameters, edge length of the basal hexagonal plane ($a_0$), the height of the hexagonal lattice cell ($c_0$), and the cation-anion bond length ratio ($u_0$). The substrcipt '0' indicates the parameters relate to equilibrium condition. For ideal wurtzite crystal, the ratio $c_0/a_0$ is 1.6330 ($= \sqrt{8/3}$). Table 2.1 shows the parameters for three different materials and from the c/a ratio, AlN, GaN, and InN seems to have higher asymmetry.

**Table 2.1** Crystal structural parameters for AlN, GaN, and InN

| Parameter | Ideal | AlN | GaN | InN |
|---|---|---|---|---|
| $a_0$ (Å)[a] | - | 3.112 | 3.189 | 3.54 |
| $c_0$ (Å)[a] | - | 4.982 | 5.185 | 5.705 |
| $c_0/a_0$ (exp.)[a] | - | 1.6010 | 1.6259 | 1.6116 |
| $c_0/a_0$ (cal.)[b] | 1.6330 | 1.6033 | 1.6297 | 1.6180 |
| $u_0$[c] | 0.375 | 0.380 | 0.376 | 0.377 |

[a]Ref. [96], [b]Ref. [97], [c]Ref. [98]

### 2.4.2 Spontaneous and piezoelectric polarization

The metal-nitrogen covalent bond in III-V Nitride will have stronger ionicity compared to other III-V covalent bonds, which generates macroscopic polarization in AlN, GaN or InN crystals as the $c_0/a_0$ ratio deviates from the ideal value. Since this polarization is produced without any external strain and only due to inherent property, this is called *spontaneous polarization ($P_{SP}$)*. In III- nitrides, the covalent bonds parallel to the c-axis and the other three covalent bonds in the tetrahedral structure generate the spontaneous polarization. As the $c_0/a_0$ ratio decreases from the ideal value, these three covalent bonds will be at a wider angle from the c-axis, and their resultant compensation polarization will decrease, giving rise to a stronger macroscopic spontaneous polarization (see Fig 2.7 and Table 2.2). Any external stress, the ideal $c_0$ and $a_0$ of the crystal structure will change to accommodate the new stress. Thus the polarization strength will be changed. This

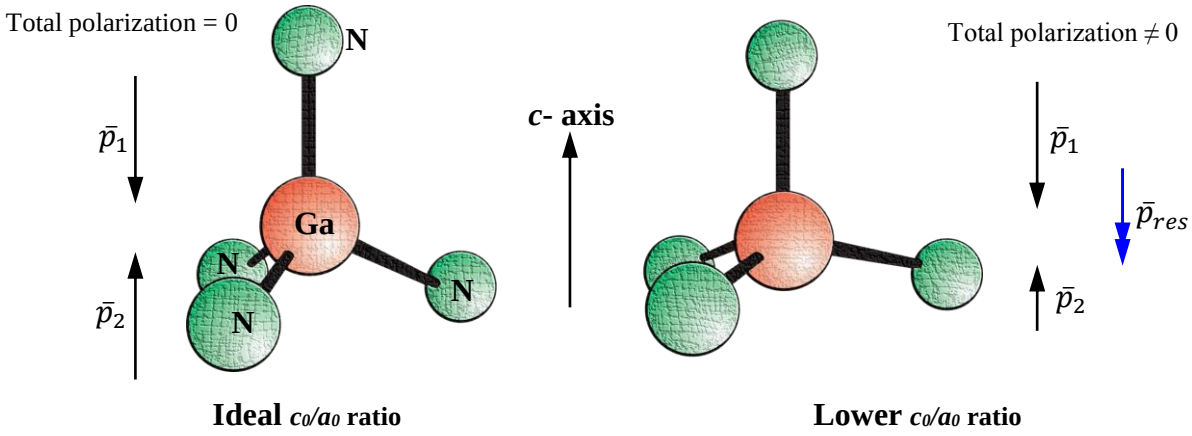


**Figure 2.7** Generation of polarization due to deviation of the $c_0/a_0$ ratio from ideal value (from reference 97).

**Table 2.2** The dependence of spontaneous polarization on the $c_0/a_0$ ratio (Ref. [97])

| Parameters | Ideal | AlN | GaN | InN |
|---|---|---|---|---|
| $c_0/a_0$ | 1.633 | 1.6033 | 1.6297 | 1.6180 |
| $P_{SP}$ ($C/m^2$) | 0 | -0.090 | -0.034 | -0.042 |

additional polarization in strained III-nitride crystals is called *piezoelectric polarization ($P_{PE}$)*. If, for example, the nitride crystal is under biaxial compressive stress, $a_0$ will decrease and $c_0$ will increase, making the $c_0/a_0$ ratio increase towards the ideal lattice, which will decrease the polarization strength of the crystal; as the $P_{PE}$ and $P_{SP}$ will act in opposite directions (see Fig. 2.8 (a)). For tensile stress, opposite things will occur and the net polarization will increase (see Fig. 2.8 (b)).

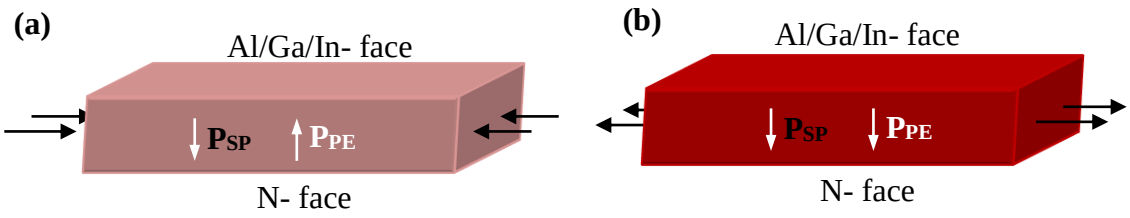


**Figure 2.8** The direction of piezoelectric polarization on Al(/Ga/In)N layer with (a) compressive, and (b) tensile stress.

When a biaxial stress is applied to the crystal along the direction perpendicular to *c*-axis, the piezoelectric polarization is expressed as [refer to Ambacher's articles[39,40]],

$$P_{PE} = e_{33}\varepsilon_z + e_{31}\left(\varepsilon_x + \varepsilon_y\right) \tag{2.34}$$

where, $e_{33}$ and $e_{31}$ piezoelectric constants of the wurtzite material (Table 2.3). If the lattice parameters are changed to *c* and *a* due to external strain, then the *z*- direction strain,

$$\varepsilon_z = (c - c_0)/c_0 \tag{2.35}$$

If the material has same strain along *x* and *y* direction (isotropic), the strain can be expressed as,

$$\varepsilon_x = \varepsilon_y = (a - a_0)/a_0 \tag{2.36}$$

The shear related strain is not considered in this work. The *z* and *x* axis strains can be related as,

$$\varepsilon_z = -2\left(\frac{C_{13}}{C_{33}}\right)\varepsilon_x \tag{2.37}$$

**Table 2.3** List of elastic and piezoelectric constants for AlN and GaN

| Parameters | AlN | GaN |
|---|---|---|
| $C_{13}$ (GPa)[a] | 108 | 106 |
| $C_{33}$ (GPa)[a] | 373 | 398 |
| $e_{31}$ (C/m$^2$) [b] | -0.53 | -0.34 |
| $e_{33}$ (C/m$^2$) [b] | 1.50 | 0.67 |

[a]Ref. [99], [b]Ref. [97]

where, $C_{13}$ and $C_{33}$ are elastic constants. Equations (2.34) and (2.37) can be combined together to obtain,

$$P_{PE} = 2\left(\frac{a-a_0}{a_0}\right)\left(e_{31} - e_{33}\frac{C_{13}}{C_{33}}\right) \tag{2.38}$$

### 2.4.3 Theory of 2DEG

The two dimensional electron gas (2DEG) is generated at the interface of AlGaN and GaN. The exact location of the 2DEG is dependent on the face on which AlGaN is grown. In general, if the polarization $P$ changes in space then there will be a charge density $\rho$ associated with such a change as, $\rho = -\nabla \cdot P$. For the wurtzitic III-nitrides, polarization is directed along the growth axis, perpendicular to the heterostructure interface. A bound sheet charge $\sigma_{\text{int}}$ formed at the interface of the two layers is related as,

$$\sigma_{\text{int}} = P_{tot,AlGaN} - P_{tot,GaN} \tag{2.39}$$

$$\sigma_{\text{int}} = (P_{SP} + P_{PE})_{AlGaN} - (P_{SP} + P_{PE})_{GaN} \tag{2.40}$$

This bound charge induced by a change in polarization of the two layers will attract compensating mobile charge at the interface.

GaN will have only spontaneous polarization component in the layer. However, AlGaN will have both spontaneous and piezoelectric polarization. So, polarization induced sheet charge density (with Al mole fraction to be x),

$$\begin{aligned}\sigma_{\text{int}} &= (P_{SP})_{GaN} - (P_{SP} + P_{PE})_{AlGaN} \\ &= P_{SP}(x) + 2\left(\frac{a(0)-a(x)}{a(x)}\right)\left(e_{31}(x) - e_{33}(x)\frac{C_{13}(x)}{C_{33}(x)}\right) - P_{SP}(0)\end{aligned} \tag{2.41}$$

Free electrons tend to compensate the high positive polarization induced sheet charge at the AlGaN/GaN interface for Ga(Al)-face or at the GaN/AlGaN interface for N-face material. Figure 2.9 shows the conduction band diagram, and charge densities at the interface and the surface. The maximum sheet carrier concentration located at these interfaces can be given as,

$$n_s(x) = \frac{\sigma_{\text{int}}(x)}{q} - \left(\frac{\varepsilon_0 \varepsilon(x)}{dq^2}\right)\left[q\phi_b(x) + E_F(x) - \Delta E_C(x)\right] \tag{2.42}$$

where $\sigma_{\text{int}}$ is the bound polarization sheet charge, $q$ is the electron charge, $\varepsilon_0$ is the permittivity of free space, $\varepsilon(x)$ is the relative dielectric constant of AlGaN, $d$ is the thickness of the AlGaN layer. $\phi_b$ is the Schottky barrier height, $E_F$ is the Fermi level at the

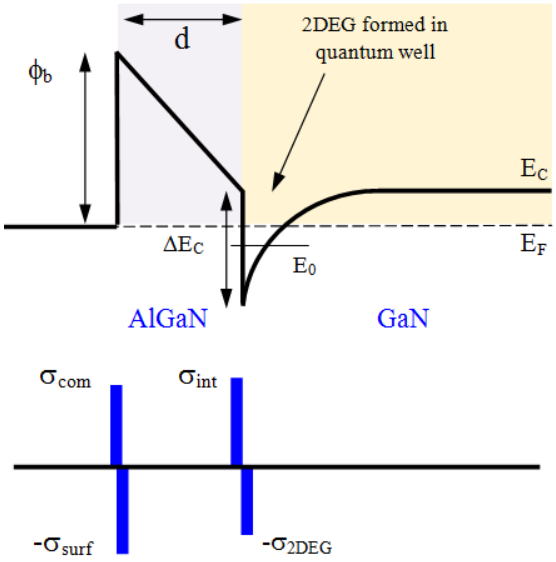


**Figure 2.9** Conduction band diagram, sheet charge densities at the surface and interface of AlGaN/GaN heterostructure.

heterointerface with respect to the GaN conduction band edge, and $\Delta E_c$ is the conduction band offset at the AlGaN/GaN interface. To determine the sheet carrier concentration from the polarization induced sheet charge density from Eq. (1.14), we use the following approximations:

Dielectric constant: $\varepsilon(x) = (-0.5x + 9.5)$ (2.43)

Schottky barrier: $\phi_b = (1.3x + 0.84)$ eV (2.44)

Where, the Fermi energy level can be expressed as,

$$E_F(x) = E_0(x) + \frac{\pi\hbar^2}{m^*(x)} n_s(x) \quad (2.44)$$

where the ground sub-band level of the 2DEG is given by,

$$E_0(x) = \left[ \frac{9\pi\hbar q^2}{8\varepsilon_0 \sqrt{8m^*(x)}} \frac{n_s(x)}{\varepsilon(x)} \right]^{2/3} \tag{2.45}$$

the, electron effective mass is $m^*(x) \approx 0.20m_0$, where $m_0$ is the rest mass of an electron. And the conduction band offset is,

$$\Delta E_C(x) = 0.7\left[E_g(x) - E_g(0)\right] \tag{2.46}$$

The bandgap of $Al_xGa_{1-x}N$ is express as,

$$E_g(x) = xE_g(AlN) + (1-x)E_g(GaN) - x(1-x)1.0 \text{ eV}$$

$$\therefore \quad E_g(x) = x6.13 + (1-x)3.42 - x(1-x)1.0 \text{ eV} \tag{2.47}$$

# CHAPTER 3

# FABRICATION OF GaN MICROCANTILEVERS EMBEDDED WITH ALGAN/GAN HFET/MOSHFET/MISHFET

Fabrications of AlGaN/GaN HFET/MOSHFET (metal-oxide-semiconductor HFET)/MISHFET (metal-insulator-semiconductor HFET) are well documented. However fabrication of heterojunction field effect transistor embedded on a microcantilever has been reported by few[90,100-103]. In this dissertation for the first time, we report the complete fabrication details, issues, and solutions of several novel AlGaN/GaN HFET/MOSHFET/MISHFET embedded GaN microcantilever. Although the principles and application of different devices vary from each other, but the fabrication processes remain the same. In this chapter we will describe the different process for a representative device and scanning electron micrograph images of various MEMS devices. All the fabrication processes were carried out in the Microelectronic Research Center (MiRC), IEN in Georgia Institute of Technology, Atlanta, GA.

## 3.1 Wafer information

A six inch AlGaN/GaN wafer grown on Silicon (111) substrate was purchased from *NTT Advanced Technology Corporation, Japan* for this work. The wafer was diced into ~ 44 (1.8 cm by 1.8 cm) square pieces. Before dicing, the wafer was spin coated with photo

resist (Shipley 1827) and then baked for 5 mins at 110°C. This is solely to protect the top surface from any damage may happen during wafer dicing. The different layers of the wafer are shown in Fig. 3.1.

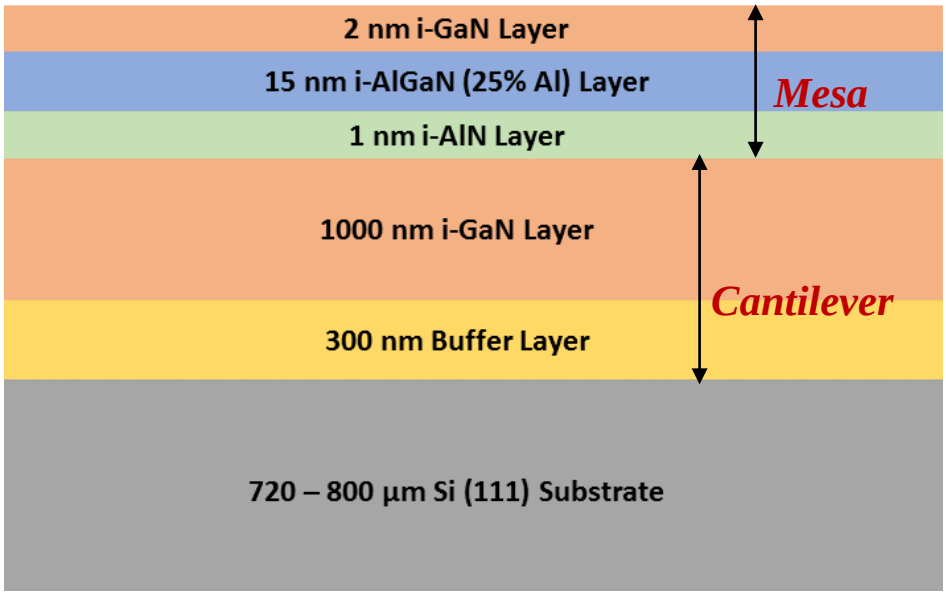


**Figure 3.1** Different layers of the AlGaN/GaN wafer grown on Si (111) substrate with mesa and cantilever layer as shown.

Silicon substrate (111) of ~ 720-800 µm thickness was used to grow the AlGaN/GaN layer [104]. A 300 nm buffer layer (not disclosed by the company) was used as a transition layer before growing 1 µm undoped GaN layer. This transition layer along with the undoped GaN form the thickness of our microcantilevers. On the top of the GaN layer, a thin layer of 1 nm AlN was used to form abrupt junction and better electron confinement in 2DEG by tuning the bandgap. Above that layer we have our active layer of AlGaN of 15 nm and 2 nm of GaN cap layer.

## 3.2 Mask design

Two 5”×5”×0.09” mask (material: chrome, substrate: quartz) was ordered from *Photo Sciences Inc., USA* after designing in *AutoCAD 2013*. There were 7 lithographic layers in the fabrication process (described in details in the next section), all the layers were designed and three copies of each layer were organized in two masks. Three layers (Mesa isolation, GaN cantilever outline, and Backside Si etch) were 1.8 cm by 1.8 cm box equal size of the sample and other three layers were 1.4 cm by 1.4 cm. These layers could be made exact size as others, that makes the alignment task easier but it will consume more space in the mask. If there is plenty space in the mask, it is better to have equal sized layers and also equal to the sample size. The mask was clear field. The back side alignment layer for through wafer Si etching should be mirrored respect to the first two top layers if the design has asymmetry. If it is a symmetric design then mirroring the back side layer would not be necessary. The wafer was diced 1.8 cm by 1.8 cm, though all the devices would fit 1.4 cm sample size. The only reason to have some empty space around the sample for handling with tweezers. Also later in this section, readers will find why it is useful to keep more space around the actual device area. The first two layers specially GaN outline layer and the back side layer should have a ‘+ sign’ for auto dicing each sample into small pieces as it will be really hard to dice the small samples further after final release of cantilevers. While designing the mask, it is easy to start from the GaN outline. After drawing the complete device, then separate each layer and organize according to the size of the mask. Photo Sciences has its own rules about drawing, and they have to be followed for faster processing. When the mask is made, the mask should be thoroughly checked for any damage, design violation, and sharpness of chrome line.

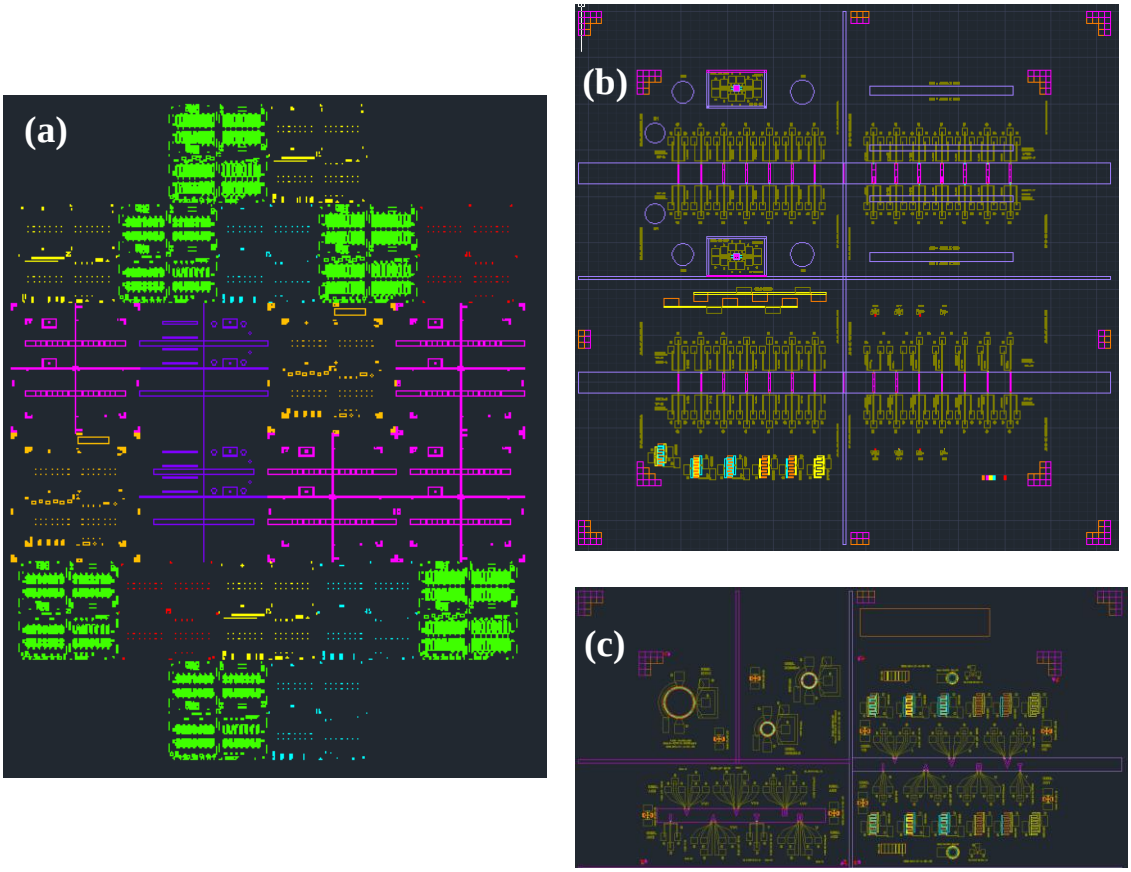


**Figure 3.2** Mask layouts: (a) The final design including all the layers separately with multiple copies. Each different color represents individual layer; (b) all litho layers are superimposed showing the schematic of the final outcome of the fabricated devices for one design (for rectangular cantilevers). The mask design has the provision for auto dicing each sample into either 4 or 8 pieces; (c) All litho layers are superimposed showing the schematic of the final outcome of the fabricated devices for another design (for differently shaped cantilevers). The mask design has the provision for auto dicing each sample into either 4 or 5 pieces. GaTech MA6 mask aligner has 4-6 inch mask holder but the opening area is of 1 inch shorter diameter. So the mask design space should be considered according to the holder size (see appendix for the pictures of different tools used in fabrication).

## 3.3 Details of the fabrication steps

In this section the fabrication related issues, problems and solutions are discussed in two subsections covering the top cantilever outline followed by through wafer Si etching from backside. The first sub-section is segmented into six sub-sections where each

lithography step and associated process steps are discussed. For further details reader are advised to refer to the appendix. Positive photo resist (PPR, SC 1827) was used for the first process step, whereas negative photo resist (NPR, NR 71) was used for the rest and NR 5 was used in Bosch process for releasing cantilevers.

### 3.3.1 Top GaN microcantilever outline embedded with AlGaN/GaN HFET/MOSHFET/MISHFET

*3.3.1.1 Step one-MESA Outline:* Mesa is the active region on which the AlGaN/GaN HFET is fabricated. This is because AlGaN/GaN layer has 2DEG throughout the wafer, therefore it is conductive all over and needs to be isolated from other patterns on the sample. Only in this layer PPR SC 1827 was used (the litho parameters are given in appendix). PECVD $SiO_2$ (300 - 400 nm) was deposited using Unaxis PECVD tool (deposition rate is 50 nm/min) at the beginning. The oxide was patterned and then etched in Plasma Therm Inductively Coupled Plasma (ICP) tool (etch rate is 180 nm/min, $CHF_3/O_2$ gas). Then used $BCl_3/Cl_2$ based dry etching recipe of GaN in ICP to etch 180-200 nm to isolate mesa. Though more than 15 nm of AlGaN etching would be sufficient but over etch is done to ensure complete isolation and also for next alignment purpose (below 100 nm thickness would be harder to see in MA6). After the etching, the PR should be completely removed from top oxide layer following resist remover, oxygen plasma

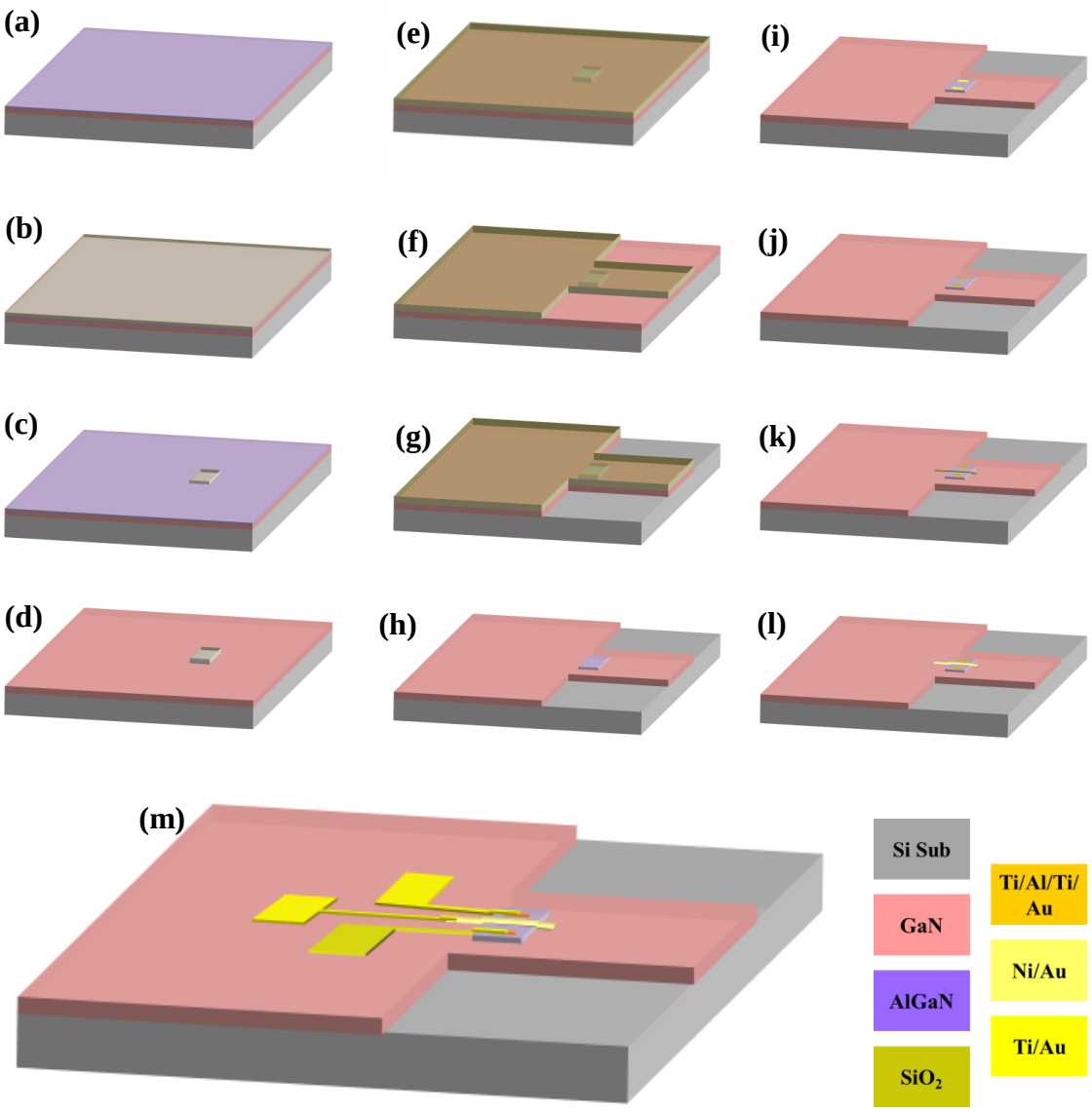


**Figure 3.3** Process flow diagram of top GaN microcantilever outline embedded with AlGaN/GaN MOSHFET. (a) A diced AlGaN/GaN on Si sample (wafer layers are shown in Fig. 3.1); (b) PECVD $SiO_2$ (300 - 400 nm) deposition; (c) Pattern the Mesa layer with PPR and ICP etching of oxide; (d) ICP etching of AlGaN; (e) PECVD $SiO_2$ (1.2 µm) deposition; (f) Pattern the Microcantilever Outline layer with NPR and ICP etching of oxide; (g) ICP etching of GaN; (h) Complete oxide etching with BOE; (i) Pattern Ohomic Contact and e-beam deposition of Ti (20 nm)/Al (100 nm)/Ti (45 nm)/Au (55 nm) metal stack; (j) Rapid thermal annealing of ohomic contacts; (k) Pattern Schottky Gate Contact and deposit PECVD $SiO_2$ (5 nm) or ALD $Al_2O_3$ (5 nm) or PLD BN (5 nm) (not all devices have gate dielectric); (l) E-beam deposition of Ni (50 nm)/Au (200 nm) metal stack; (m) Pattern Probe Contact and e-beam deposition of Ti/Au metal stack.

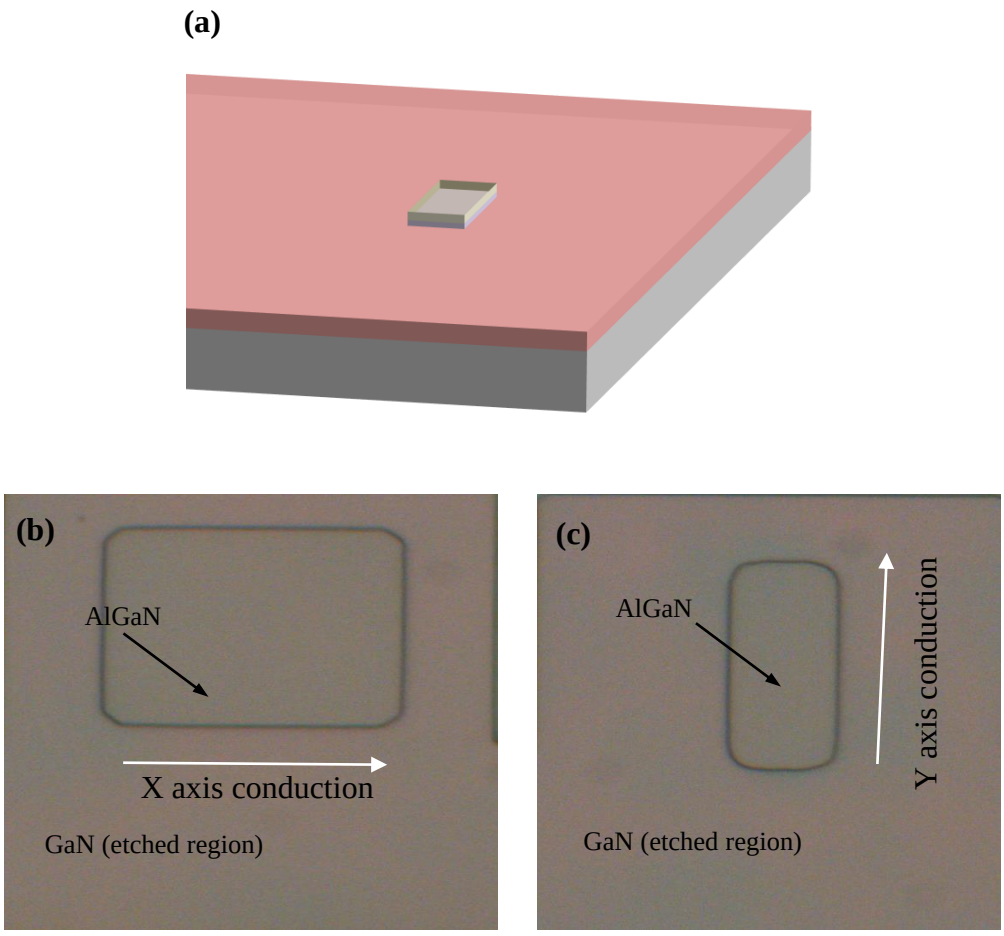


**Figure 3.4** Fabrication step 1: Mesa isolation, (a) Schematic diagram. Optical image of the mesa (b) with X axis conduction in mesa, (b) with Y axis conduction in mesa.

cleaning in Reactive Ion Etcher (RIE), and if necessary dipping in warm sulphuric acid ($H_2SO_4$) for 5-10 minutes. The resist gets crosslinked in ICP and it becomes literally impossible to remove with just resist remover or acetone. That is why it is better to have the oxide layer protecting the mesa which acts as the hard mask. Otherwise without oxide deposition, mesa etching can still be performed. It is suggested that after mesa etching, the sample should be kept in warm resist remover (Microposit 1165) for 10-30 minutes and then cleaning the sample with cleanroom swab (soaked in the same remover to make it soft

and not to scratch the sample). If this cleaning is not sufficient then oxygen plasma etching would be needed. Keep in mind that, bare AlGaN/GaN mesa should never be exposed in oxygen plasma, otherwise 2DEG would be completely damaged.

*3.3.1.2 Step 2-GaN Cantilever Outline:* In this step, GaN is etched down to make an outline for the cantilever. GaN is etched down in the pocket area up to the substrate where silicon gets exposed. This process was exactly same as step 1. Only difference is the deposited oxide is 1.2 µm thick as the remaining thickness of GaN after etching for mesa in step 1 is about 1.1 µm. Over etching (assuming 2 µm thick GaN) is performed as the etched down GaN has other layers (see Fig. 3.1). $BCL_3/Cl_2$ also etches exposed Si (verified using Tencor Profilometer) with same etch rate of 340 nm/min, but this does affect any fabrication process as ultimately the exposed Si will be etched from back completely. In this step and the next ones in this sub-section, negative photo resist (NPR) NR 71 was used (see appendix for details). After the etching of oxide similarly as step 1, resist should be removed. After resist removal, wet chemical etching of the oxide is done using Buffered Oxide Etchant (BOE).

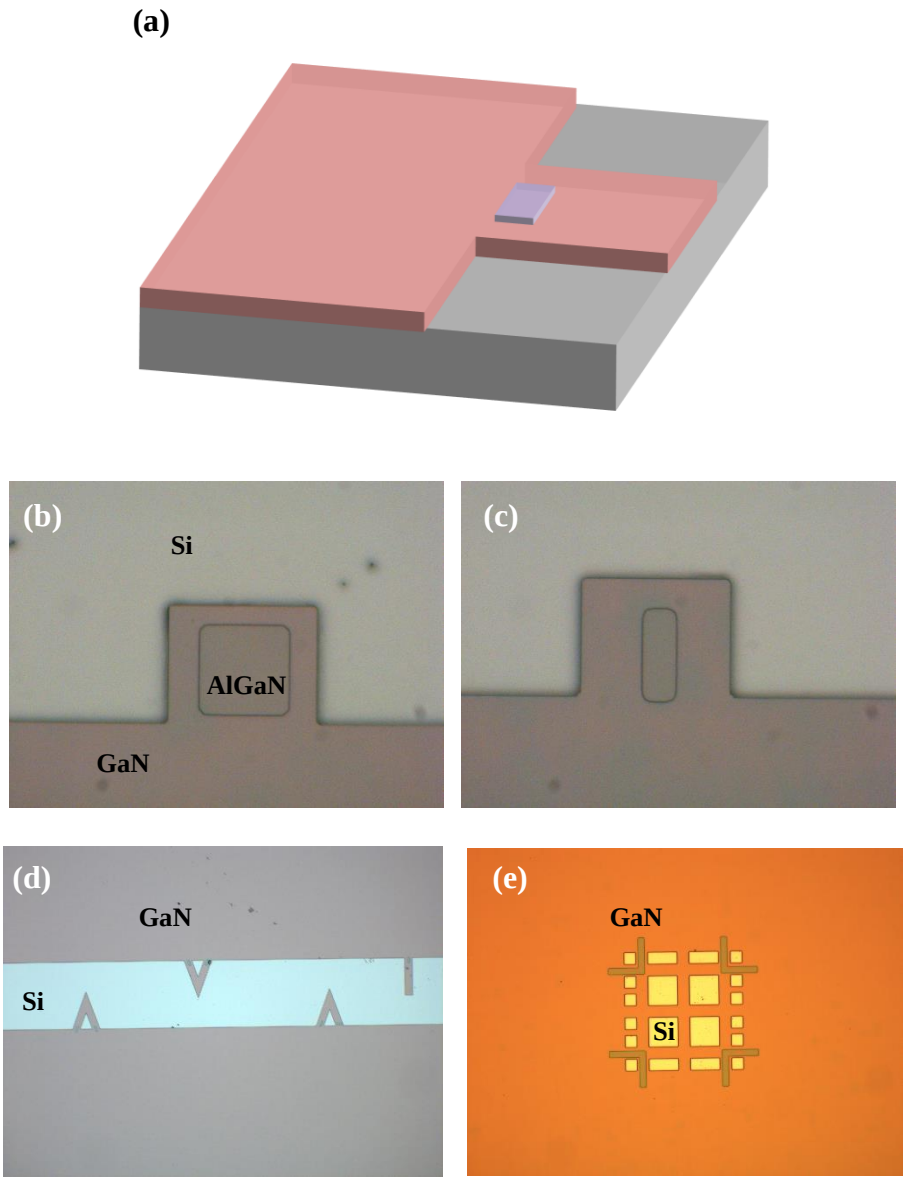


**Figure 3.5** Fabrication step 2: Top cantilever outline, (a) Schematic diagram. Optical image of devices (b) with X axis conduction in mesa, (c) with Y axis conduction in mesa, (d) different shapes of microcantilever, and (e) suspended GaN net.

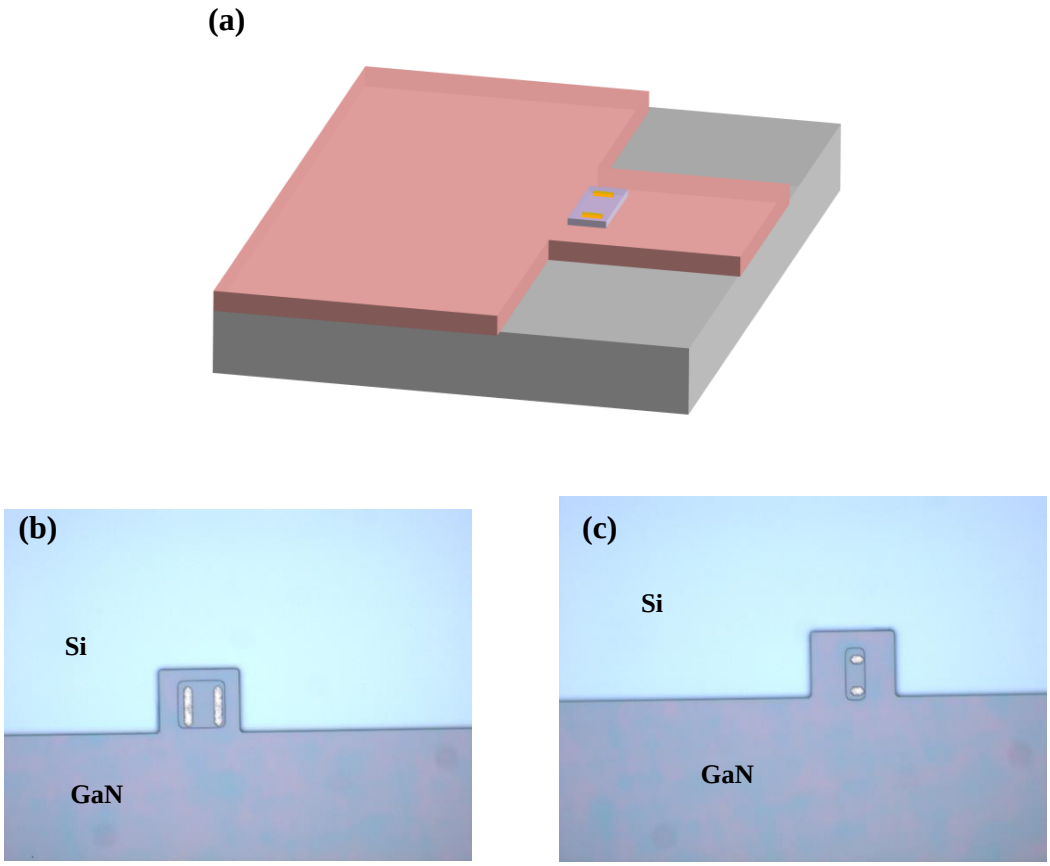


**Figure 3.6** Fabrication step 3: Ohmic contacts, (a) Schematic diagram. Optical image of devices (b) with X axis conduction in HFET, (b) with Y axis conduction in HFET.

*3.3.1.3 Step 3-Ohmic Contact:* For ohmic contact multilayer gate metal stack of Ti (20 nm)/Al (100 nm)/Ti (45 nm)/Au (55 nm) was used. Getting a good ohmic has always been a challenge [105] and multilayer metal stack gives low contact resistance [106]. The reason for choosing this metal stack is well explained[105,107]. For a good and easy metal liftoff process, overdevelopment is suggested after post bake of resist as very thin layer of resist would be always present. Also, the extra space surrounding the sample should be used to mount the sample with Kapton tape in CVC Electron Beam Evaporator's holder.

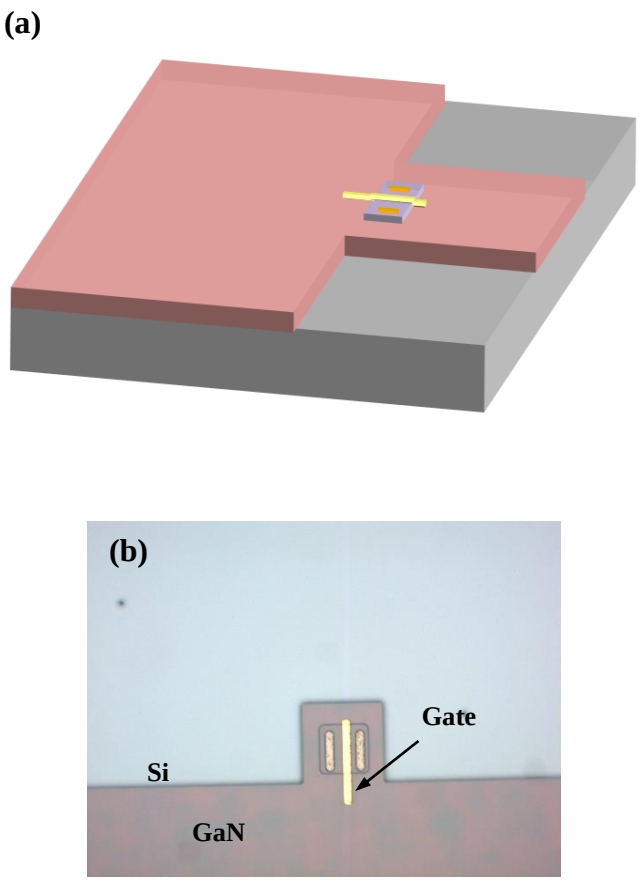


**Figure 3.7** Fabrication step 4: Schottky contacts, (a) Schematic diagram, (b) optical image of a device after deposition of Ni/Au for gate.

So that the metal does not get deposited on the edges which makes the liftoff very hard and time consuming. The metal liftoff should be done in warm resist remover (RR41), submerging the sample for as long as the unnecessary metal film comes off. After that, the sample was put in fresh warm resist remover for 10-15 minutes and the using soaked (in RR41) cleanroom swab is used to clean the sample by whirling the swab. When satisfied (checking in microscope to ensure no resist is left), the sample should be cleaned with squirting IPA after every successive whirling with swab soaked in resist remover. No oxygen plasma cleaning should be done on the sample with bare AlGaN/GaN mesa.

However as the GaN outline has already created several trenches in the sample, resist becomes highly adhesive to the surface, and so warm $H_2SO_4$ treatment can be performed. Every after 1-2 minutes, the sample should be checked to ensure no unwanted liftoff of ohmic contacts is happening. It happens because of thin layer of resist still present underneath the metal contacts. After lift-off is done, the contact is annealed in SSI RTP at 825 $^oC$.

*3.3.1.4 Step 4-Schottky Gate Formation:* Step 4 is a critical part of the processing of HFET. If the aim is to design simple piezoresistor then this step should be skipped. In this dissertation, the designed microcantilevers have many varieties in the FET part, where the samples are processed with or without gate dielectric. Liftoff process was followed to reduce the processing time and one lithography step which involves depositing dielectric materials and then patter the gate layer to etch away dielectrics from other areas on the sample. Hoewver liftoff process eliminates that need and after patterning the sample with resist, gate dielectric can be deposited followed by gate metal and finally lift off the resist as described in previous step. To create high Schottky barrier with nitride surface, higher work fucntion Schottky contacts are needed and both Pt and Ni are ideal choices for Schottky gate contact [105]. Ni is a preferred choice due to its higher adhesion property with nitrides and can be operable up to 600°C. Therefore a Ni/Au metal stack for Schottky contacts for the HFET gates.

Devices were fabricated without dielectric (HFET), with Plasma Enhanced Chemical Vapor Deposition (PECVD) of $SiO_2$ (MOSHEFT structure), Pulsed Laser Deposition (PLD) of Boron Nitride (BN), and Atomic Layer Deposition (ALD) of $Al_2O_3$ (MISHEFT structure). PECVD oxide is the mostly used gate dielectric which reduces the

leakage by several orders as HFET has high gate leakage (ref). This leakage is highly undesirable for sensor application as in later section readers will find the importance. Recently ALD $Al_2O_3$ has shown impressive performance with AlGaN/GaN HFET (ref). The PLD BN has never been studied with AlGaN/GaN structure as this newly formed dielectric has offered greater performance with Graphene based devices. However the PLD technique is very quick and can be operated at room temperature, which gives easier lift off process. The PLD was performed in Air Force Research lab and the details is not provided here. However the film thickness was 5 nm. For PECVD, 5 nm of oxide was deposited at $100^0$ C. The usual recipe and the Unaxis PECVD tool in MiRC does not allow deposition below $250^0$ C but at that temperature the resist will burn and contaminate the chamber which is not permissible. So if not possible to use the recipe with lower temperature, one has to follow the etching of oxide film with an added litho step. In case of ALD, 5 nm of $Al_2O_3$ was deposited with thermal oxide recipe at $100^0$ C. The deposition rate is 1 Å/cycle which takes more than an hour to deposit 5 nm film. This longer duration hard bakes the resist and eventually impossible to lift off especially with smaller feature size. The only option would be to have the film deposited first and the follow the etching procedure. Although devices with oxide and BN were fabricated, the $Al_2O_3$ deposited devices were not continued for further processing due to limitation of time. Moreover this dissertation will only cover the usual HFET devices, the MOSHFET and MISHFET will be described elsewhere.

*3.3.1.5 Step 5-Probe Contact:* Large metal pads (250 μm by 250 μm) are deposited for characterization which connects to the drain, source, gate and cantilever tip. Gold with

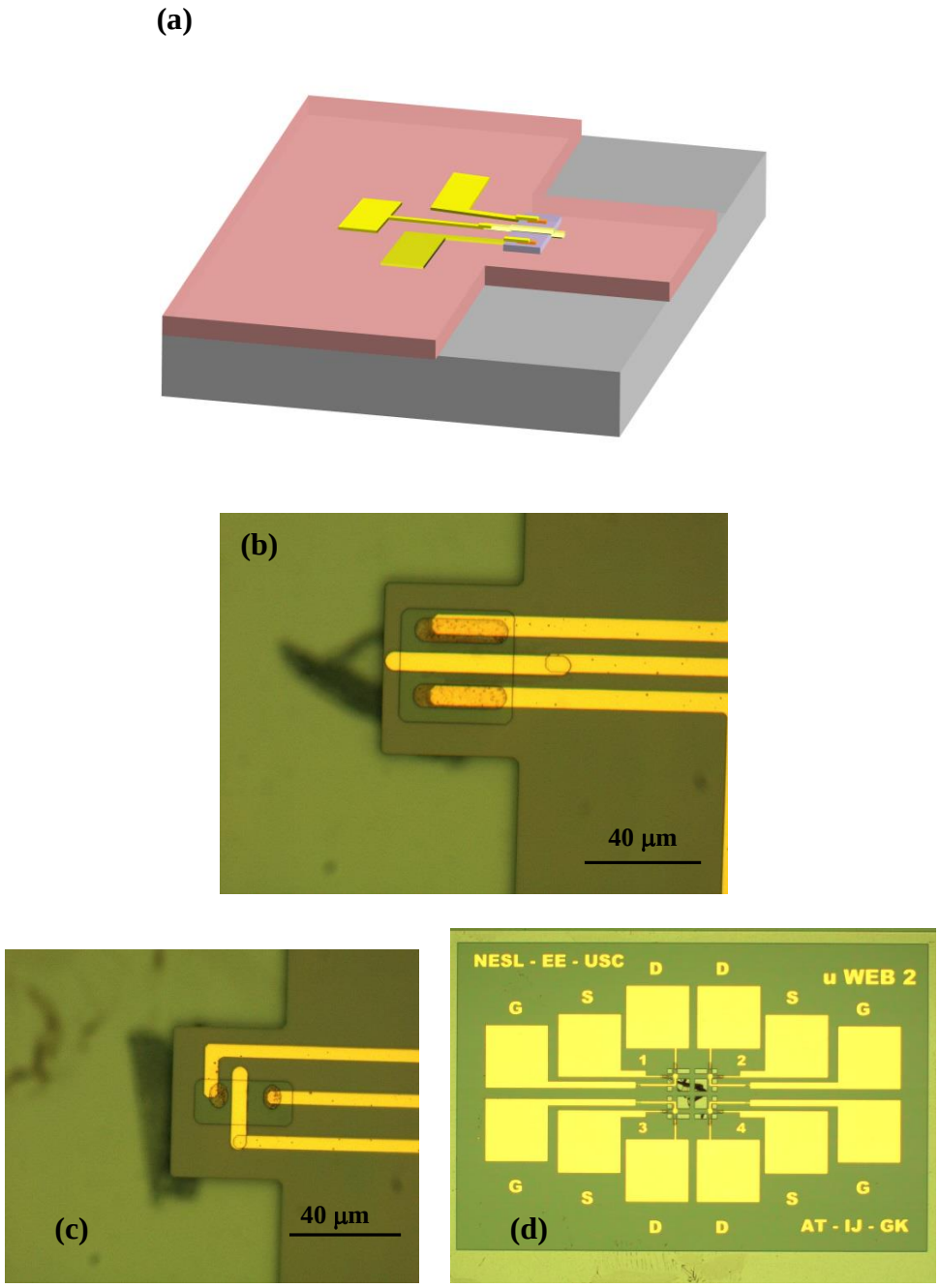


**Figure 3.8** Fabrication step 5: Probe conctacs, (a) Schematic diagram. Optical image of (a) the whole device before cantilever release with X axis conduction, (b) the whole device before cantilever release with Y axis conduction, (c) Micro Web showing all the contacts for the 4 HFETs.

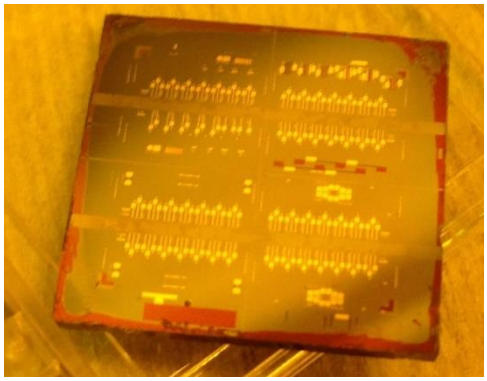

**Figure 3.9** Photograph of a processed sample after the first five steps. The sample size 1.8 cm by 1.8 cm.

adhesion layer of Ti was used for this metal deposition step. The mask layout has two probe layers with long contact and short contact. Long contacts are helpful for microfluidic channel integration, vacuum sealing of the sample, and utilizing fabricated micro-canals/discs which are patterned in step 2. The lift off process remains the same as mentioned in step 3.

### 3.3.2 Through wafer Si etch from backside using Bosch process

The cantilever is released by through wafer etching of Si using STS ICP etcher. We used 'Bosch process' where the etcher alternates between an 'etch' cycle and 'passivation' cycle. During the etch cycle, Si is isotropically etched using $SF_6$ for 10 seconds, then the etched region is passivated with a polymer ($C_4F_8$) for 7 seconds in the passivation cycle. The whole process continues alternatively as long as the cantilever is not released, resulting in a high aspect ratio Si etch with vertical side walls.

*3.3.2.1 Existing problems with previous process:* The usual practice of processing this particular layer involves depositing thick $SiO_2$ on the back side which acts as the hard mask for Si etching. Then patterning with NR 71 resist (4 µm thick), the oxide is wet chemically etched using BOE. The resist is then removed from the backside and also from the top side (which acts as a protecting layer of the devices on the top side from spinner and BOE. After that the sample is put into ICP to etch Si for releasing the cantilevers. This process is faster and easier, however there are several key factors that affect the final outcome. In ICP the selectivity is about 90:1 between Si and $SiO_2$. For a wafer of 500 µm thick (our first generation wafer from Nitronex Inc), the oxide needs to be 7-8 µm thick on the backside of the sample and also in the carrier wafer. The carrier wafer is needed for mounting small samples with cool grease before loading in the ICP chamber. Now if the pocket (where the Si will be etched) is big enough and the layer has symmetric design (see Fig. 3.10 (a)) with moderately thick Si substrate the above mentioned process works fine but will have lot of undesirable undercut of Si, resulting in over hanged cantilevers (see Fig. 3.10 (b)). As the maximum strain is supposed to be at the base and the cantilever should be the only suspended part, this process yields less sensitive devices and in some cases devices of no use. This process becomes totally inapplicable and impractical if:

(a) The thickness of Si wafer is above 600 µm, as the thickness of oxide would be more than 8 µm which would require longer tool time. Like our recent wafer which is 720-800 µm, the oxide thickness should be more than 10 µm. The PECVD tool in MiRC allows 3 µm thick film deposition at a time, but the quality becomes bad. So it is advised to deposit 2 µm thick oxide (50 nm/min deposition rate needs 40 minutes plus purging time yields about an hour), then

run clean process for 2 hours and deposit again. That means more than 14 hours of total processing time is required from that tool.

(b) If the design has asymmetry (see Fig. 3.10 (c-e)) with pocket size varying from 50 µm to 800 µm (the shorter side of the rectangular pocket or the diameter of a disc), the etch rate of Si in ICP will vary significantly as bigger pocket gets etched faster. Eventually it will take almost double the theoretical time (400 nm/cycle, each cycle is 17 seconds long) to completely release suspended structures from all the pockets. Most importantly BOE etching of that thick oxide with a large variety in pocket size is literally impossible to control, resulting in under-etched or over-etched $SiO_2$ mask and eventually a total mess after Si etching with that hard mask. The fabrication yield would be very low with this process.

(c) The tool time required for the ICP would be ~ 12 hours for releasing all the structures, assuming 1000 µm thick (taking into account for the different pocket sizes) Si and etch rate of 400 nm/cycle. That much deep Si etching would obviously result in a lot of undercut.

*3.3.2.2 New process development to release suspended structure:* To account the above mentioned problems and to ensure higher fabrication yield with zero undercut in the microcantilevers, new process was designed. The process flow is shown in details in Fig. 3.11. The details of this new process are described below:

(a) *Thinning down of bare Si substrate*: To deal with ~ 800 µm thick Si, the samples were first thinned down in STS ICP using the Bosch recipe to make the thickness about 400 µm. The other recipe can be used just with SF6 etch cycle with no passivation cycle

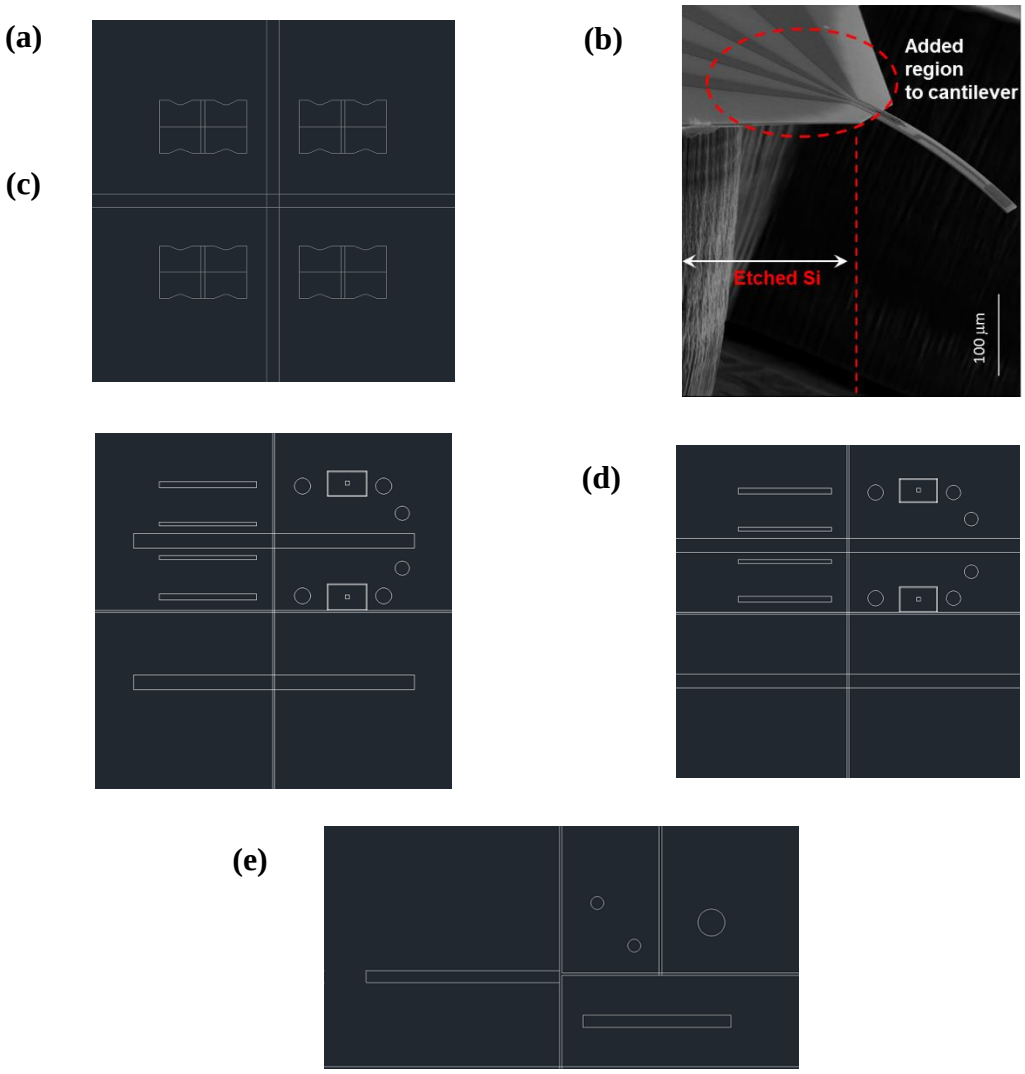


**Figure 3.10** Photograph of mask layout of backside etching layer: (a) The first generation design which have symmetric pocket and only a single variation of microcantilever. The area enclosed with white line represents the pocket from where Si will be etched. (b) SEM image of released microcantilever with previous design and processing techniques, which results in large undercut of the cantilever. (c) – (e) are mask layout of latest design with a lot of asymmetry and different pocket sizes. (c) This layout results in 4 quadrants, (d) gives 8 small pieces and (e) gives 4 pieces.

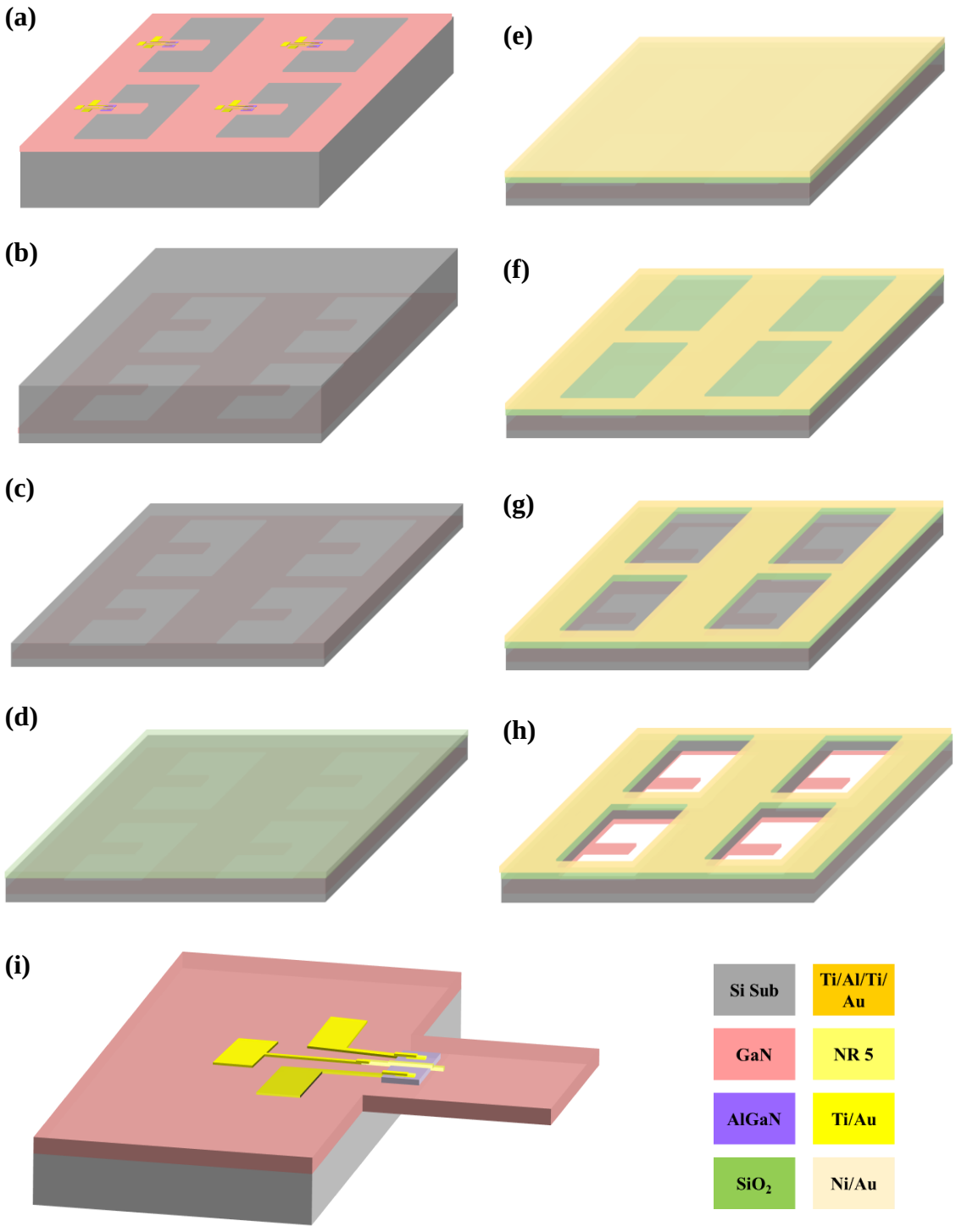


**Figure 3.11** Process flow diagram of through wafer Si etching from backside using Bosch process. (a) A complete sample after the first five processing steps (this schematics does not represent the exact device rather a simplified drawing for explaining the flow diagram); (b) Flip upside down and mount on ICP holder with cool grease precisely at the corners;

(c) Thinning down the Si substrate (~ 400 µm) in ICP ; (d) PECVD $SiO_2$ (4 µm thick) was deposited; (e) Photoresist NPR NR 5 (8 µm thick) was coated; (f) Pattern the resist layer with NR 5 and developed; (g) Etching of $SiO_2$ in RIE; (h) Through wafer Si etching in ICP using Bosch process; (i) Schematics of the released GaN microcantilever embedded with AlGaN/GaN HFET.

which would be faster. However, selectivity ratio would be lower with $SiO_2$ (measured to be 40:1 instead of 90:1). But this does not affect anything at all as long as the carrier wafer has enough oxide (in this case the thickness was 9 µm). To mount the sample cool grease was used carefully on the top side, at the corners and open area outside 1.4 cm square box. As there will be no resist removal step in this whole process, unfortunately the top surface was not protected with any resist coating. Also the resist may get cross linked for this long duration of Si etching, so if possible the resist coating on the top surface should be avoided. Another important thing is, if the cool grease is not applied enough, the samples get very hot and metal layers get peeled off from the surface (see appendix). So this step was done in intervals with 260 cycles runtime with10 minutes pause. Total 760 cycles of the Bosch recipe was run to etch ~ 350 – 400 µm Si (see Fig. 3.12 (a) and (b)) with an etch rate of ~ 500 nm/cycle (the etch rate is higher as bare Si was etched). The tool time was ~ 4 hours.

(b) *Oxide deposition*: As the thinned down sample has become ~ 400 µm thick, so a total of 4 µm thick oxide was deposited in Unaxis PECVD tool in two slots. After 2 µm deposition (50nm/min) a clean process was run for 2 hours and the final 2 µm was deposited. Though from the selectivity 5 µm thick oxide seems necessary, but the photo resist would provide the extra etching cycles. Also,

even if the oxide gets etched down but Si still remains unetched, the pattern would be already there, and the Si substrate would only get thinned down which will not harm anything. It is a good practice to prepare carrier wafer which would be the prime Si wafers or any clean Si wafer with at least 8 µm thick oxide. Each wafer should be used once in the ICP. The tool time was 2 hours and 40 minutes in Unaxis PECVD and it is same in STS PECVD 2. But the later has better quality oxide than the former with only drawback is less number of samples can be loaded. If time permits, it is better to use the later tool to deposit oxide following the same procedure.

(c) *Photolithography*: The thinned down and oxide deposited sample was patterned with NR 5 photoresist. The litho parameters are given in the appendix (similar to NR 71). The reason for using NR 5 was its thickness, minimum being 8 µm (at 3000 rpm) and maximum being 100 µm (at 500 rpm). The resist acts as a mask not only for etching oxide but also during Si etching. The selectivity was found to be 1:1 with oxide in RIE and 40:1 with Si in ICP. So there should about 4 µm resist left after etching oxide to cushion against etching the first 140 – 160 µm Si. That also helps in depositing thinner oxide film. However care should be taken to choose the thickness of the resist, as the resist gets thicker after development the profile does not remain steep and the resist loose its integrity for further processing. The optimized thickness was found to be 8 µm which gave good results. Up to 15 - 20 µm thickness would be fine with NR 5. Both NR 5 and NR 71 are good etch resist but NR 71 offers maximum thickness of 12-14 µm but is less reliable. The litho step is same as previous, but after the

development oxygen plasma cleaning can be run for 1-2 minutes to ensure no resist film is remaining in the pockets. It is not mandatory as the ultimate etching time very long which would eventually etch down the thin resist residues.

(d) *Dry etching of oxide*: The 4 µm thick oxide was etched down using NR 5 as the mask in two slots with 2 µm film being etched every time and running a complete clean process for 3 hours in between in Plasma Therm RIE. The etch rate is 50 nm/min but overetching was done (assuming 5 µm thickness) to ensure complete etching of the oxide from the pocket. A gradient of color can be seen in open eyes up to 80 – 90 µm thickness. Then microscope could be used to ensure further etching. As the backside is rough so it becomes harder to justify if few nm film of oxide is remaining. However it will again not affect due to longer etching of Si. This tool usually makes the sample contaminated which however did not affect further processing, but it is highly recommended to use Vision RIE for etching oxide. In that case, selectivity and etch rate should be measured. It is to be noted that, as the etching was done assuming 5 µm thick oxide, the remaining resist would be 3 µm, which would be good enough to support. Before optimizing the process, two samples were simultaneously processed but one was used in RIE to etch oxide and the other one was etched with BOE to compare the results. After the etching, the damages due to BOE was visible but still it was processed further. The total tool time was ~ 4 hours.

(e) *Deep Si etching with Bosch process*: The samples (~ 400 µm thick Si substrate) were mounted on carrier wafer with sufficient cool grease. While applying

grease with swab on the top surface, the nearby area surrounding the top pocket (where the GaN was etched) was avoided as the exposed cool grease (after etching Si) would deposit contaminated film and sputtered all over the sample. The Bosch recipe was used and the samples were processed for 1000 – 1200 cycles in slots of 250 cycles and 10 min pause in between, so that the samples do not get over heated. Over etching does not affect as GaN is barely etched with SF6 (about 200 – 300 nm). However in the new wafer the cantilever thickness is 1.1 µm after mesa etching. So care should be taken or this can aid in thinning down GaN slowly if different thickness of cantilever is required. Visual inspection would be enough to ensure complete etching and also the samples will be auto diced as per design. The total tool time in STS ICP was ~ 6 hours. The SEM images of the released structures are shown in details in next section. Fig. 3.16 compares the final results with previous process and the new process.

The newly developed process offers the following advantages:

1. Absolutely no undercut, no overhang, and the fabrication yield is 100% with releasing about 1000 microcantilevers and suspended structure.
2. Total process time is about 18 hours including tool time and lithography process compare to 30 hours process time with previous process.
3. The usual process is absolutely not applicable with more complex design such as this which involve dense integration of microcantilevers.
4. No BOE handling at all which not only damages metal stack but also very dangerous if exposed to human body.

There are several designs and variations of the devices being fabricated, such as : (a) length variation of the microcantilever, (b) width variation of the microcantilever, (c) HFET orientation (X axis and Y axis conduction); (d) HFET position tuning, (e) Piezoresistive and Piezotransistive design, (f) Shape variation of the cantilever (rectangle, T, U, and V shapes), (g) GaN diaphragm with AlGaN/GaN HFET, (h) size variations of the discs, (i) length variation of V shaped cantilevers, (j) HFET/MOSHFET/MISHFET embedded similar structures, and (k) Surface Acoustic Wave (SAW) devices with different schemes. This dissertation will only cover rectangular microcantilevers (with two different lengths, 250 and 300 μm) with AlGaN/GaN HFET (only the X axis current conduction based orientation). The next section will only show the SEM images. It is to be mentioned that the samples or even the full wafer should not be thinned down from the beginning with either ICP etching of Si or chemical mechanical polishing of backside Si, as the thinned down sample handling would be difficult in so many steps and eventually the samples will break at some point. The photographs of the samples in different states are shown in Fig. 3.12 – 3.15.

**(a)**

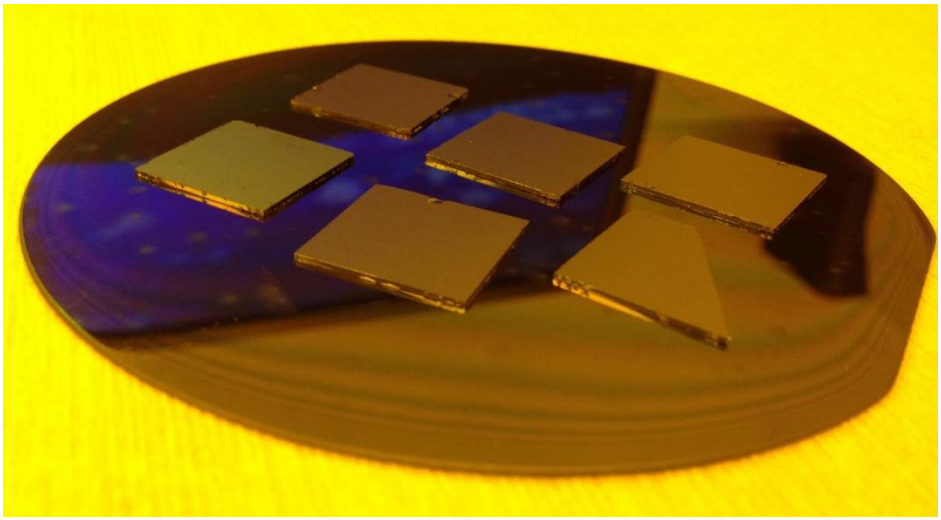

**(b)**

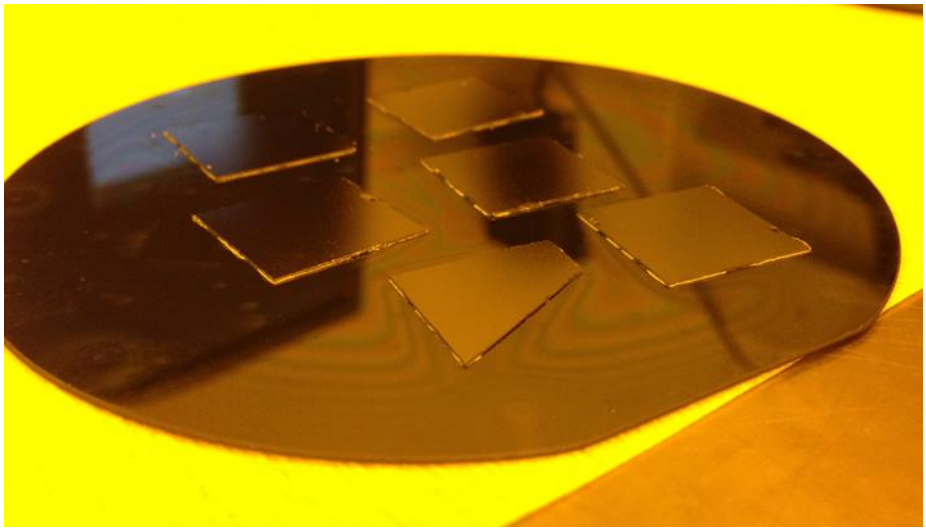

**Figure 3.12** Photograph of samples (a) before thinning down the Si substrate (b) after thinning down. The samples were dismounted carefully from the wafer with very thin syringe and sharp tweezers not to damage the devices on the top surface.

**(a)**

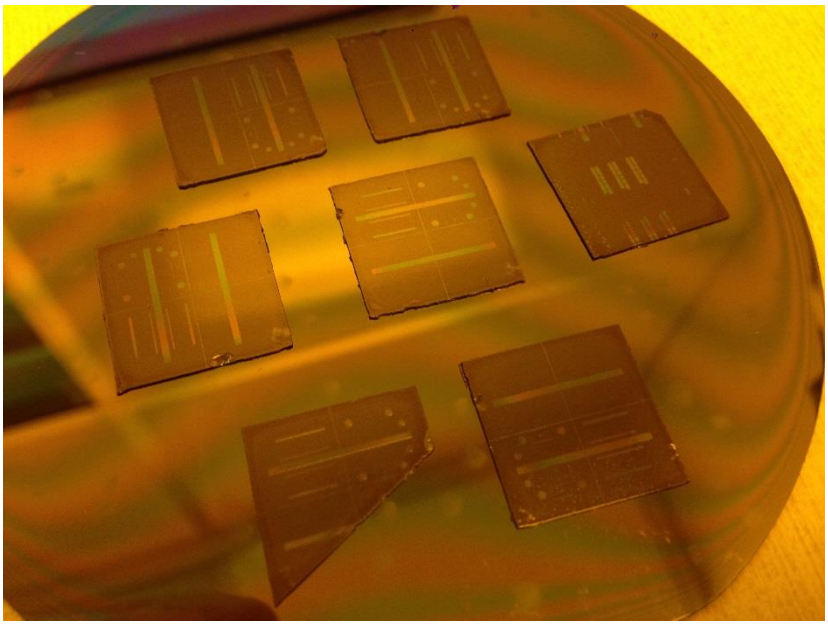

**(b)**

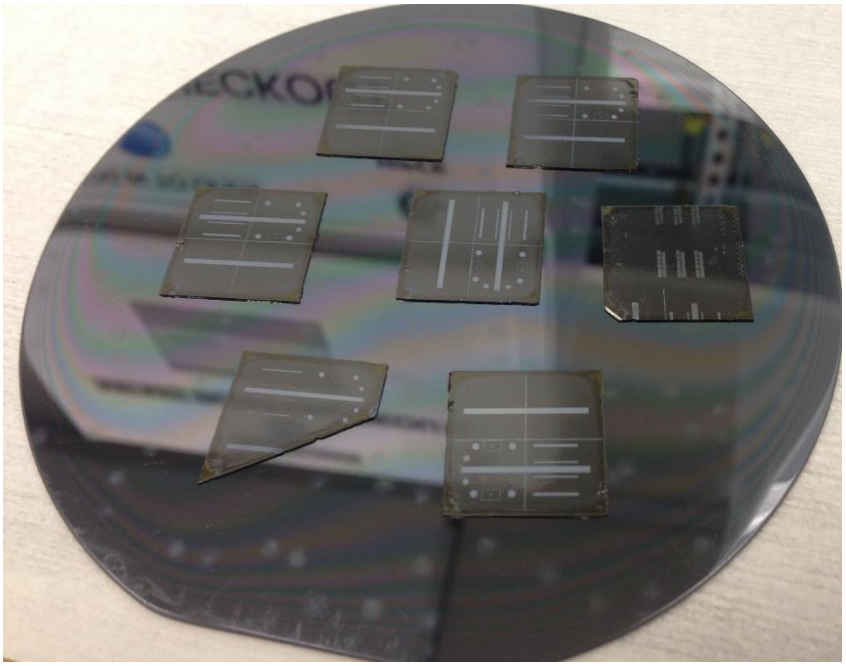

**Figure 3.13** Photograph of samples (a) after PECVD oxide deposition (b) after etching the oxide in RIE (see the color difference).

**(a)**

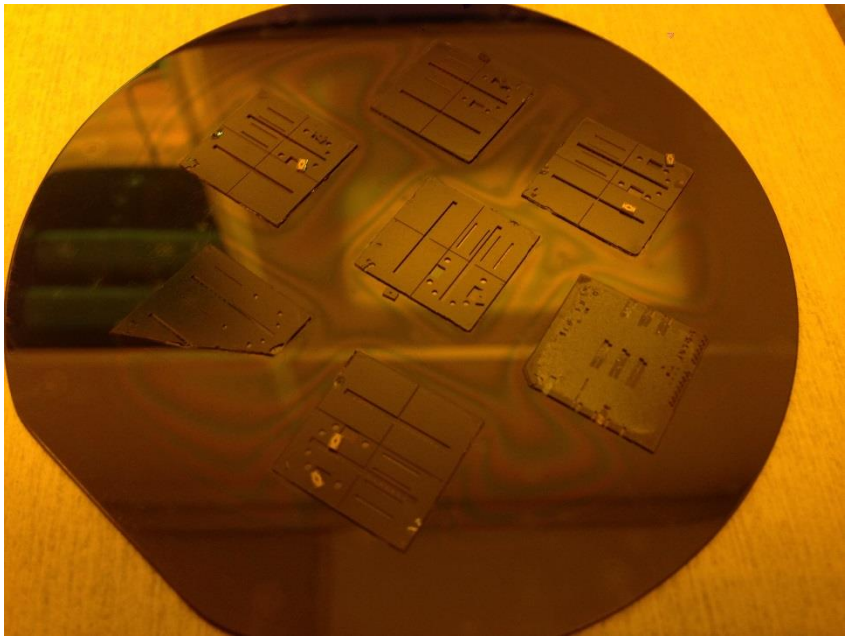

**(b)**

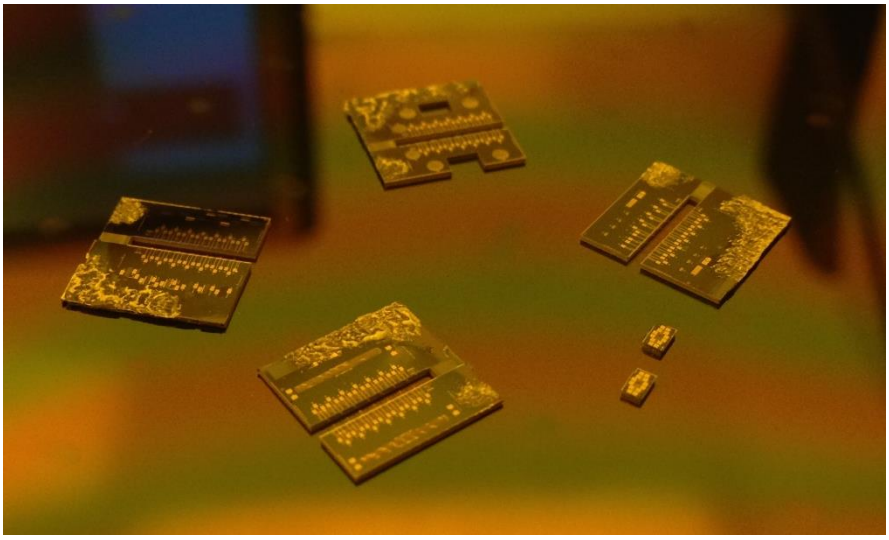

**Figure 3.14** Photograph of samples (a) after through wafer Si etching (b) auto-diced samples into 4 quadrants and two smallest pieces (called Micro Web).

**(a)**

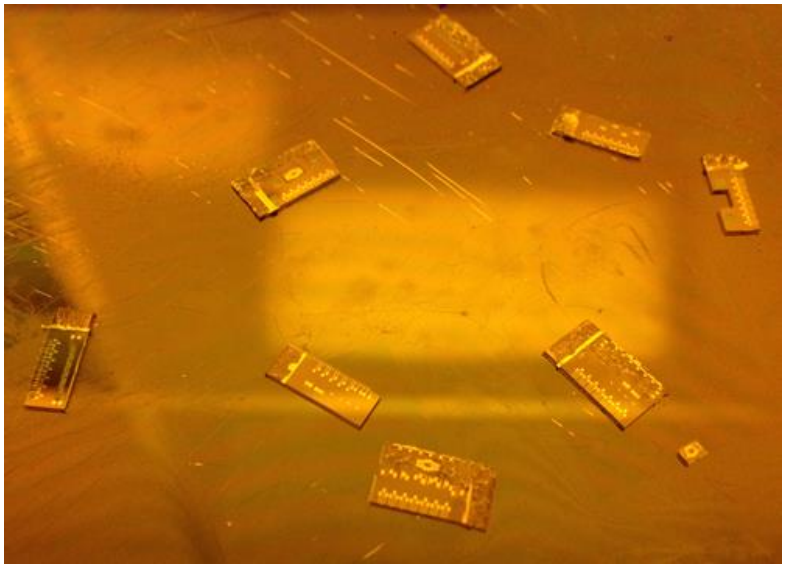

**(b)**

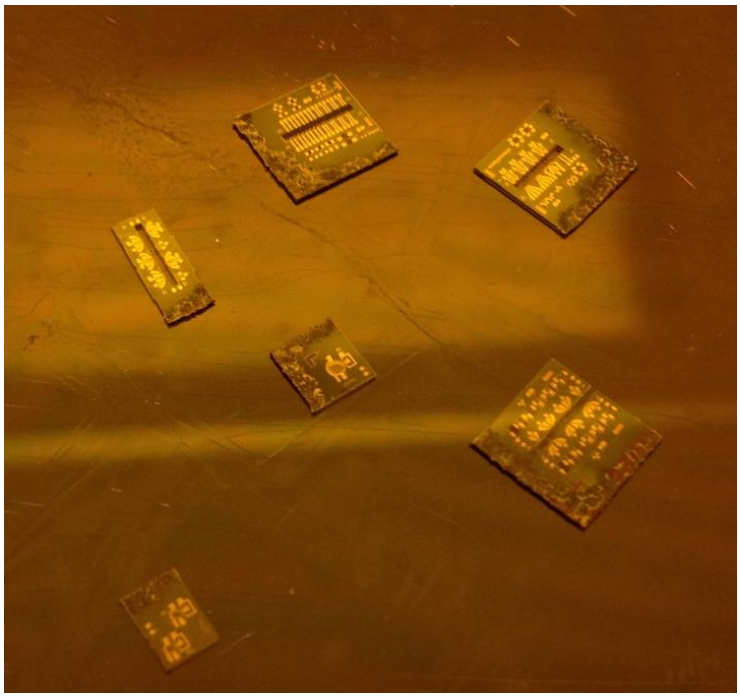

**Figure 3.15** Photograph of samples (a) auto-diced samples into 8 quadrants and two smallest pieces (called Micro Web), one of which is still attached. These samples are not from the Fig. 3.12 – 3.14.

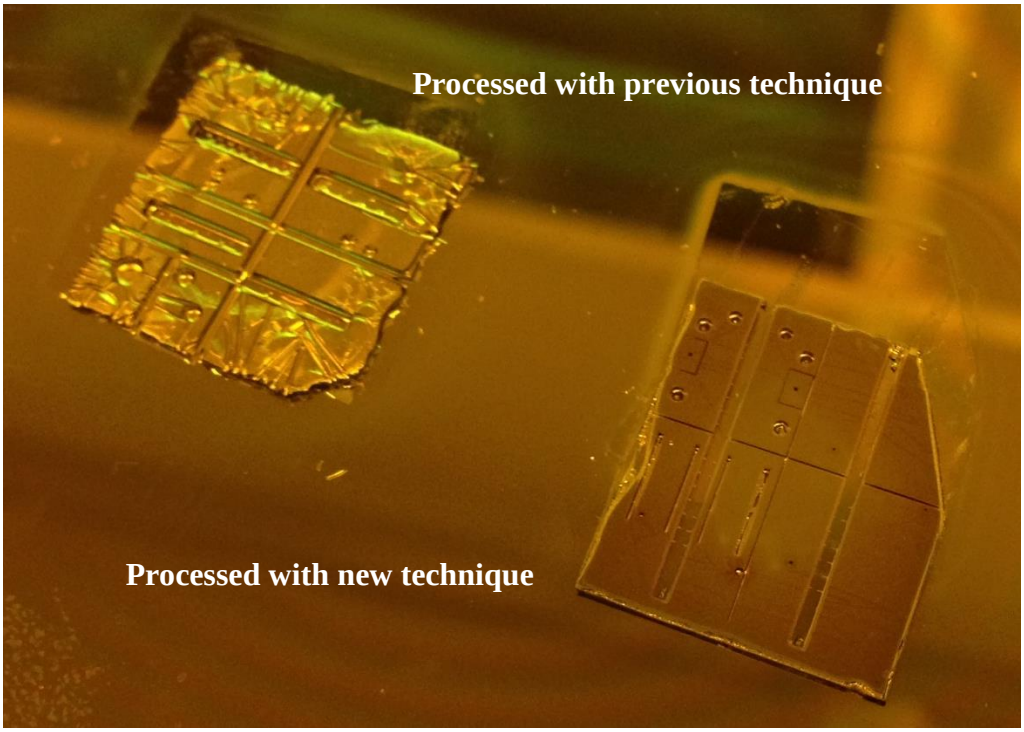


**Figure 3.16** Photograph of samples comparing the releasing of microcantilevers with two different techniques which shows the incompatibility and inapplicability of the old technique for processing sophisticated designs.

## 3.4 Scanning Electron Micrograph (SEM) gallery

**(a)**

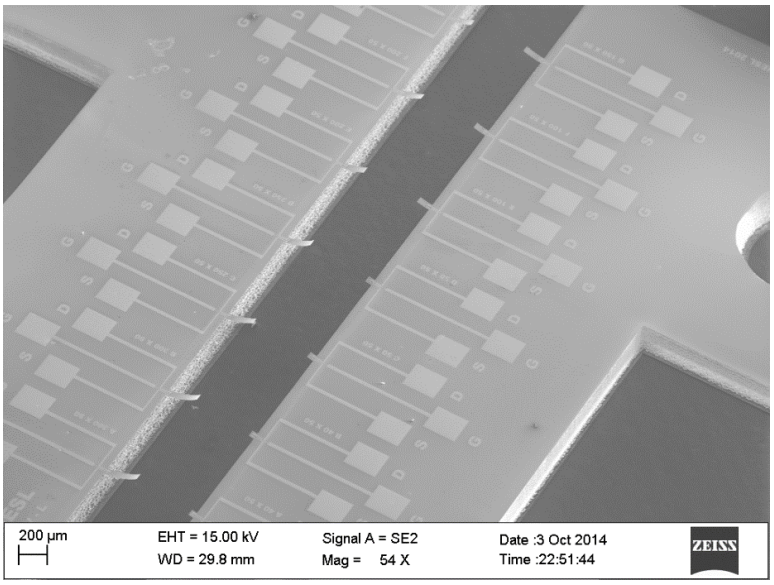


**(b)**

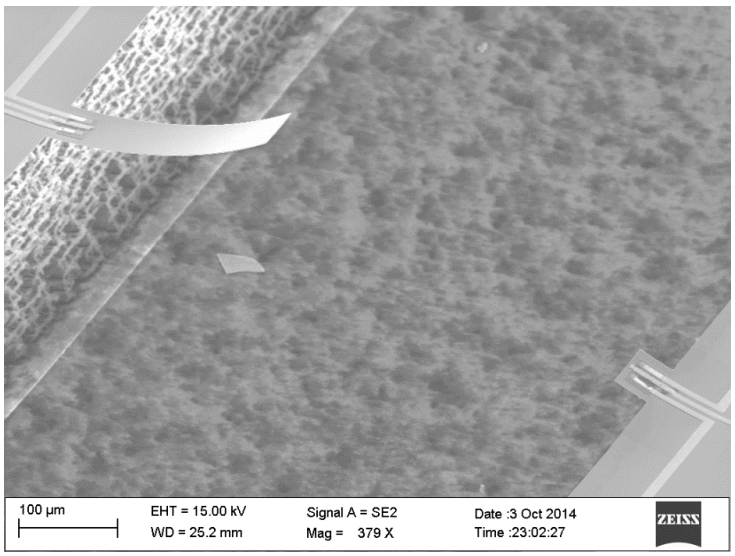


**Figure 3.17** SEM image of (a) 14 rectangular microcantilevers with length varying from 40 µm to 300 µm, width 50 µm and thickness 1 and 2 µm with different HFET orientation and position, (b) the shortest and the longest microcantilevers. The scale bar is as shown.

**(a)**

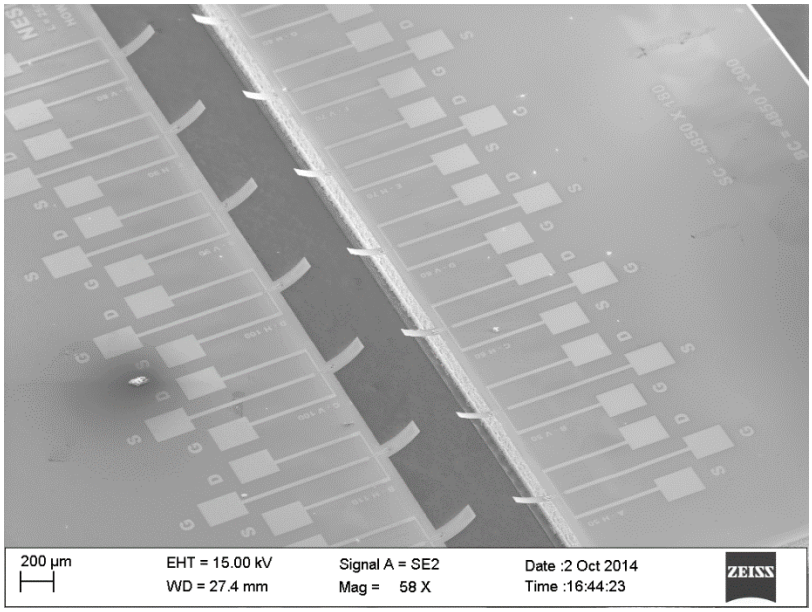


**(b)**

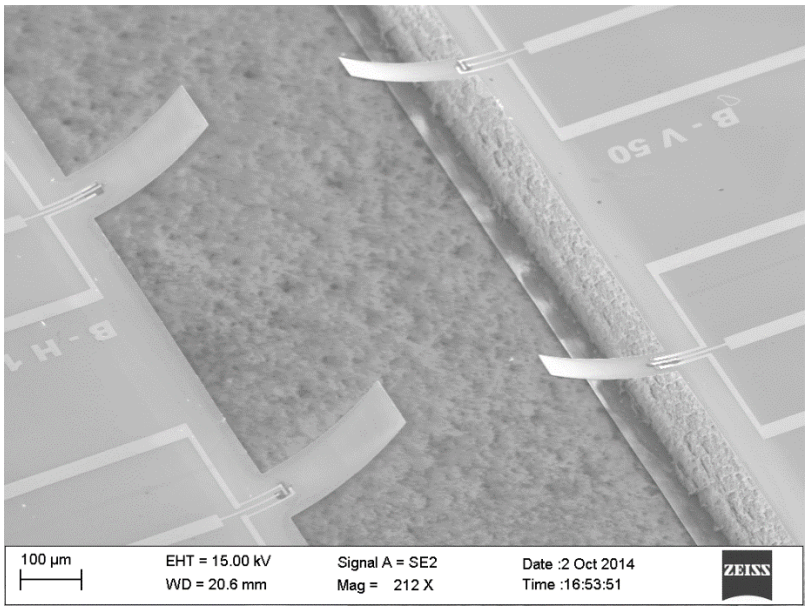


**Figure 3.18** SEM image of (a) 14 rectangular microcantilevers with width varying from 50 µm to 100 µm, length 250 µm and thickness 1 µm with different HFET orientation, (b) the thinnest and the thickest microcantilevers. The scale bar is as shown.

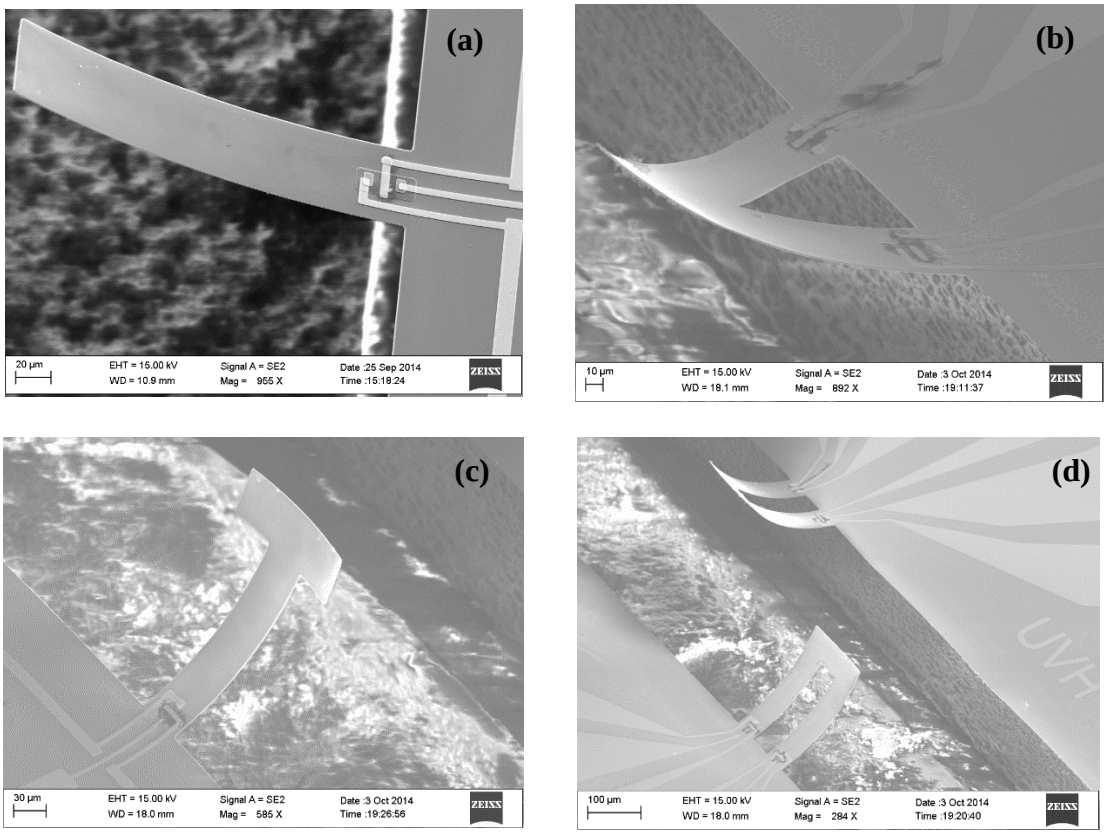


**Figure 3.19** SEM image of (a) rectangular, (b) triangular (V shaped), (c) hammer-head (T shaped), and (d) U shaped microcantilevers. Length 200 µm, width 50 µm and thickness 1 µm with different HFET orientation and position. The scale bar is as shown.

**(a)**

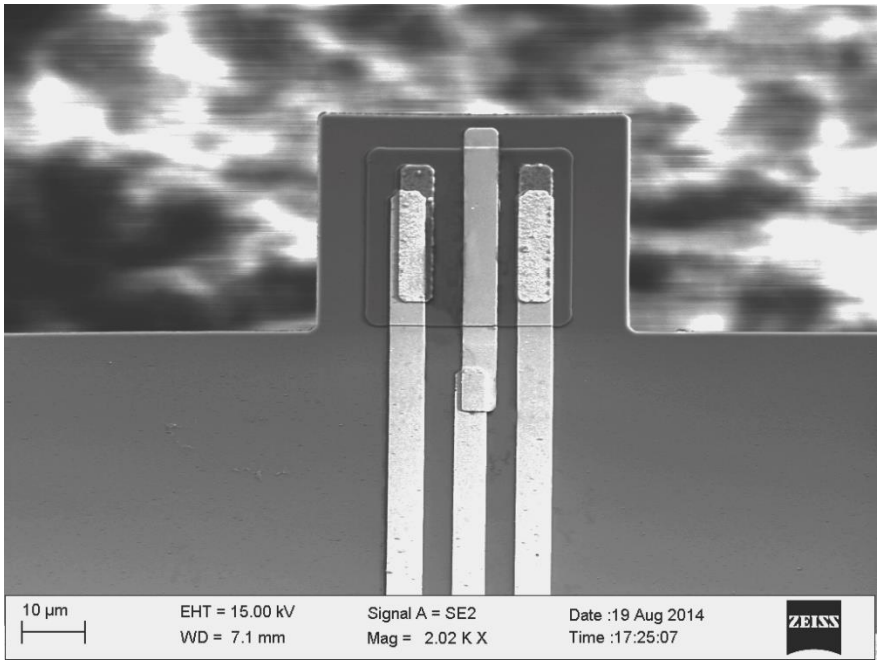


**(b)**

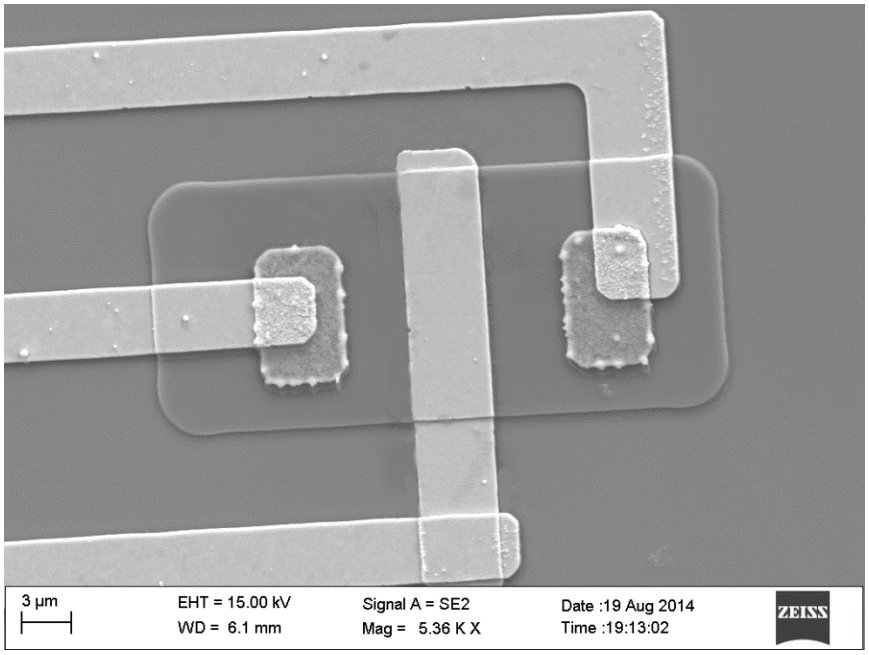


**Figure 3.20** SEM image of (a) shortest microcantilevers with embedded AlGaN/GaN HFET where current conduction in X direction (b) the current conduction is perpendicular to (a) or in Y direction. The scale bar is as shown.

**(a)**

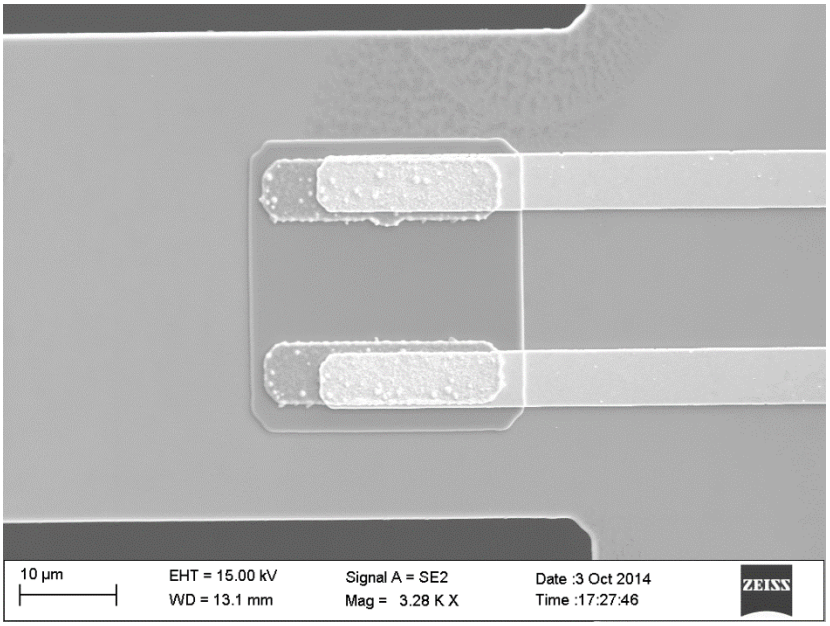


**(b)**

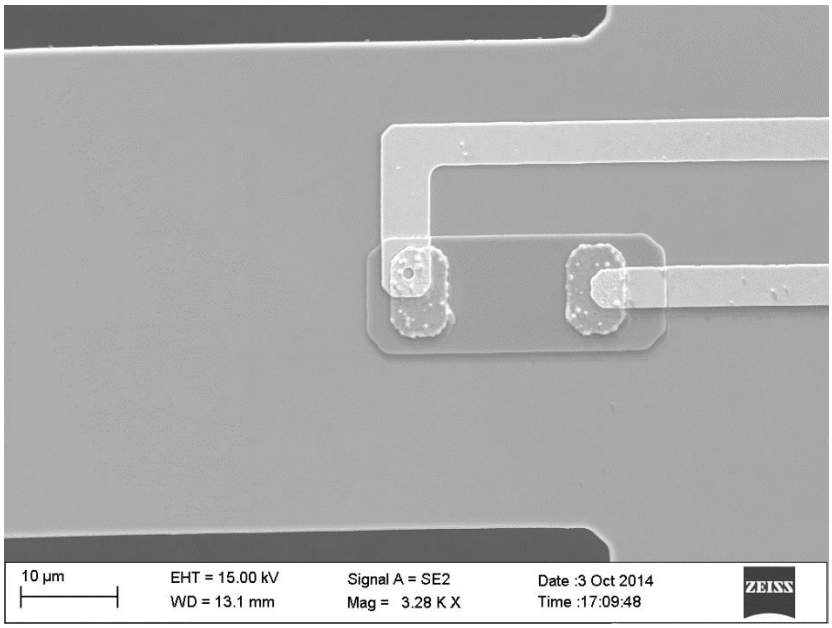


**Figure 3.21** SEM image of Piezoresistive microcantilevers (a) where current conduction in X direction in AlGaN/GaN mesa (b) the current conduction is perpendicular to (a) or in Y direction. The scale bar is as shown.

**(a)**

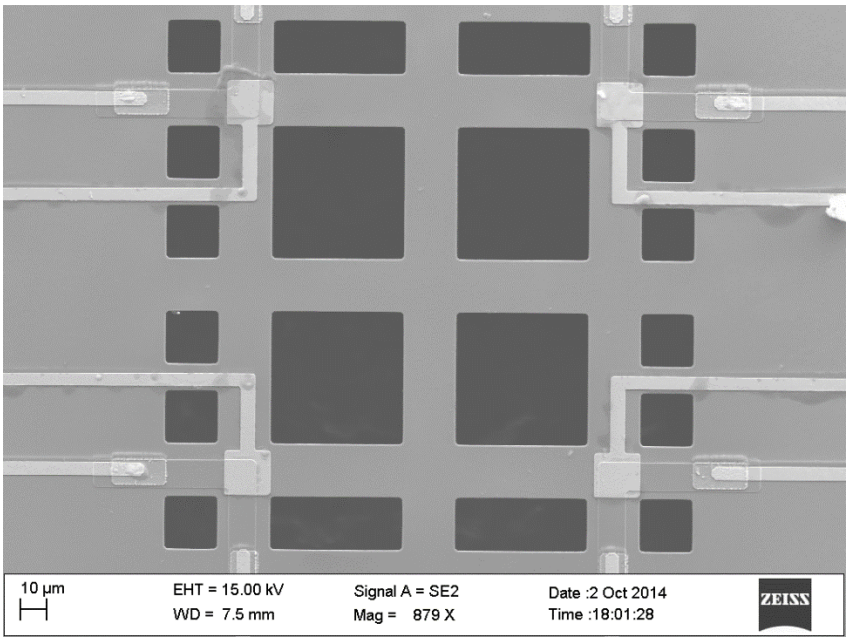


**(b)**

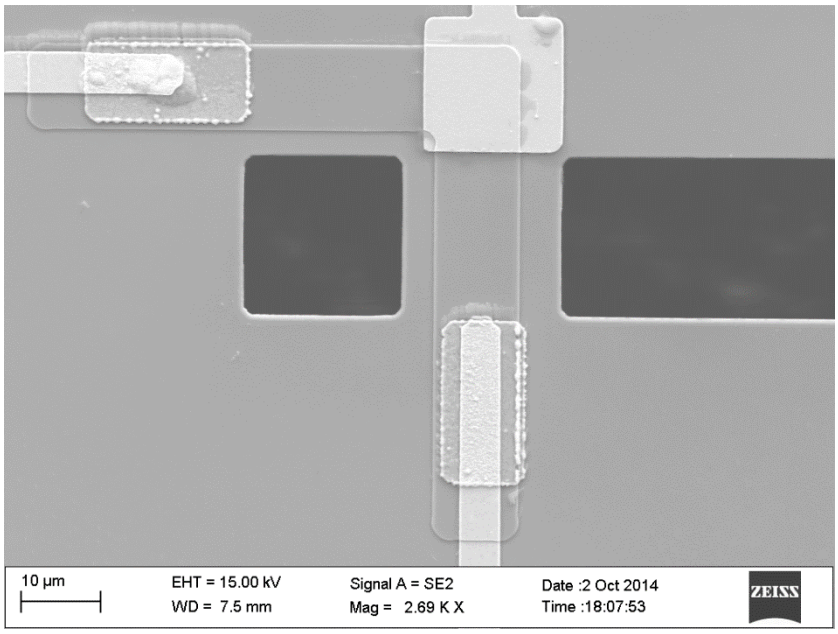


**Figure 3.22** SEM image of (a) suspended GaN film with 4 AlGaN/GaN HFET. This device is named Micro Web (b) the zoomed SEM view of one HFET. The scale bar is as shown.

**(a)**

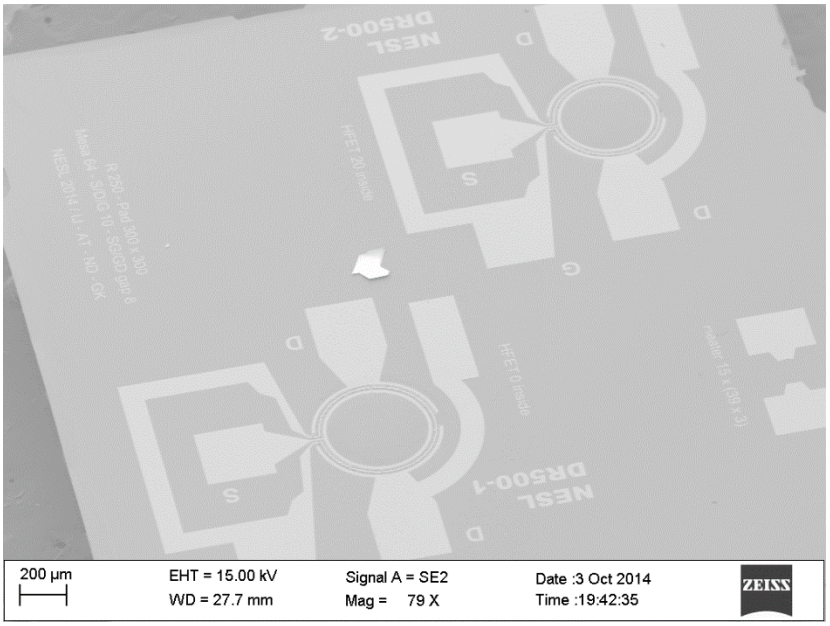


**(b)**

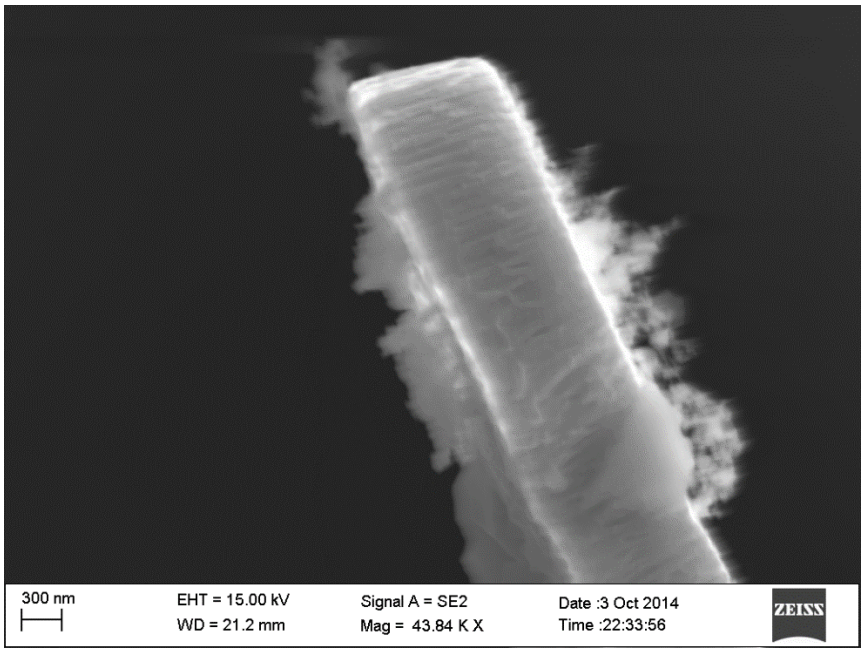


**Figure 3.23** SEM image of (a) GaN diaphragm with annular AlGaN/GaN HFET. The suspended part is not visible in SEM but is visible in optical image (b) the tip of V shaped microcantilever revealing the actual thickness of the microcantilevers is about 800 nm. The scale bar is as shown.

**(a)**

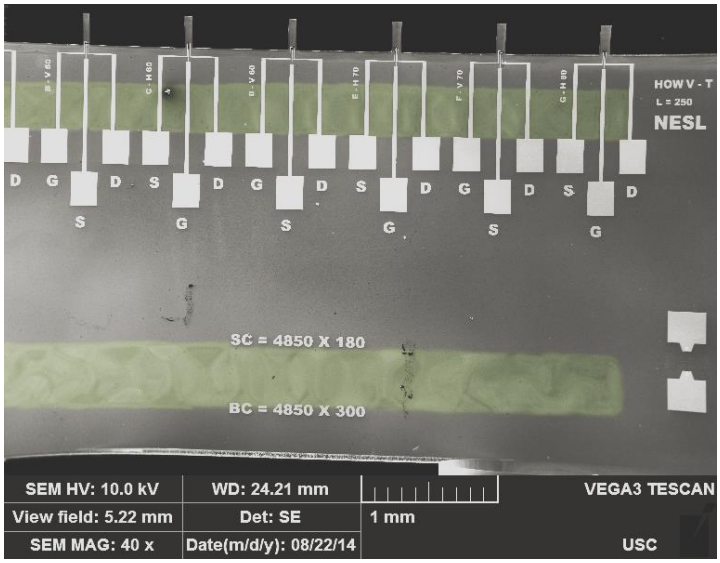


**(b)**

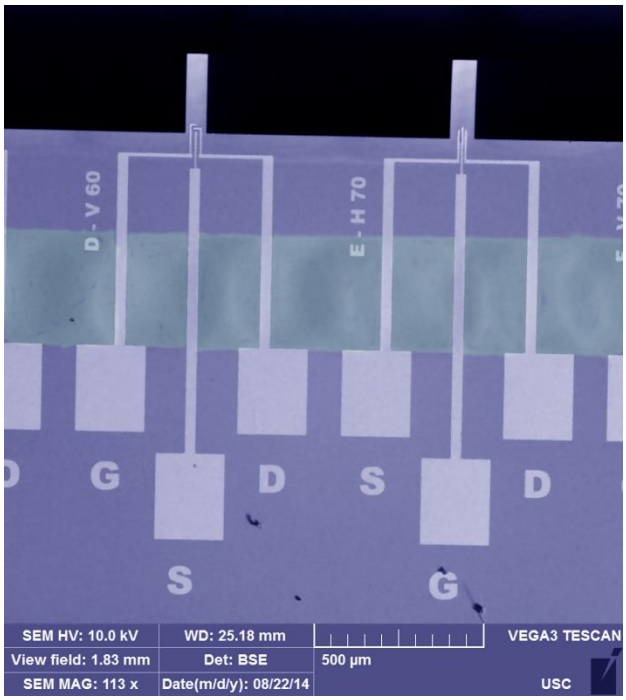


**Figure 3.24** SEM image of (a) showing two microcanals (false colored) for microfluidic integration (b) zoomed view of the canal. The scale bar is as shown.

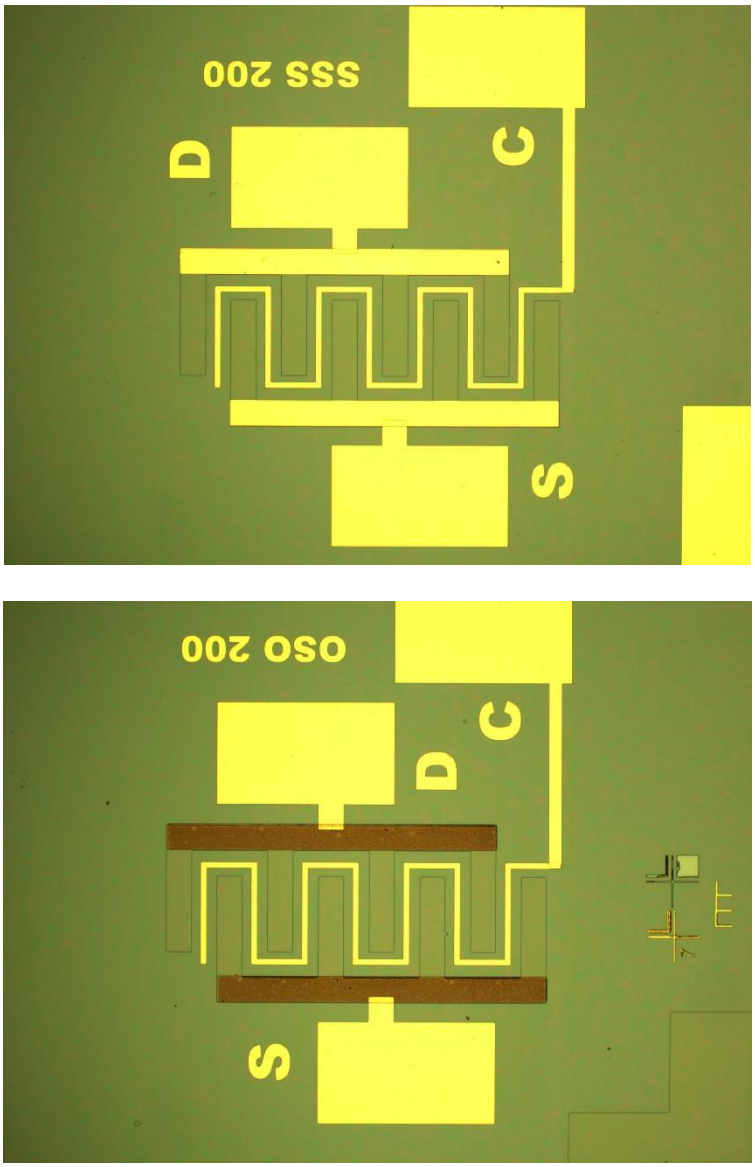


**Figure 3.25** Optical microscopy image of two SAW devices out of six different types. The SEM image would be hard to visualize different parts as the structures are bigger.

The epilayer GaN and Si(111) substrate has lattice mismatch and thermal expansion co-efficient difference [108]. Moreover during growth of GaN on Si (111) there is an internal stress distribution due to inhomogeneous outgrowth of the layer [90]. This causes a residual tensile stress component in the epilayer. The residual stress in the GaN layer is influenced

by growth conditions, layer thickness, and layer structures, as well as choice of substrate [109,110]. However, during the release of the cantilever there is a change in stress which pulls the cantilever upwards resulting in curled up structures. The longer microcantilevers have more bending compared to the shorter ones. Although different devices were fabricated with new wafer, several devices were also fabricated using a wafer bought previously from Nitronex Inc with different layers as shown in Fig. 3.26 (a). The SEM images of the fabricated devices are also shown in Fig 3.26 (b) – (d).

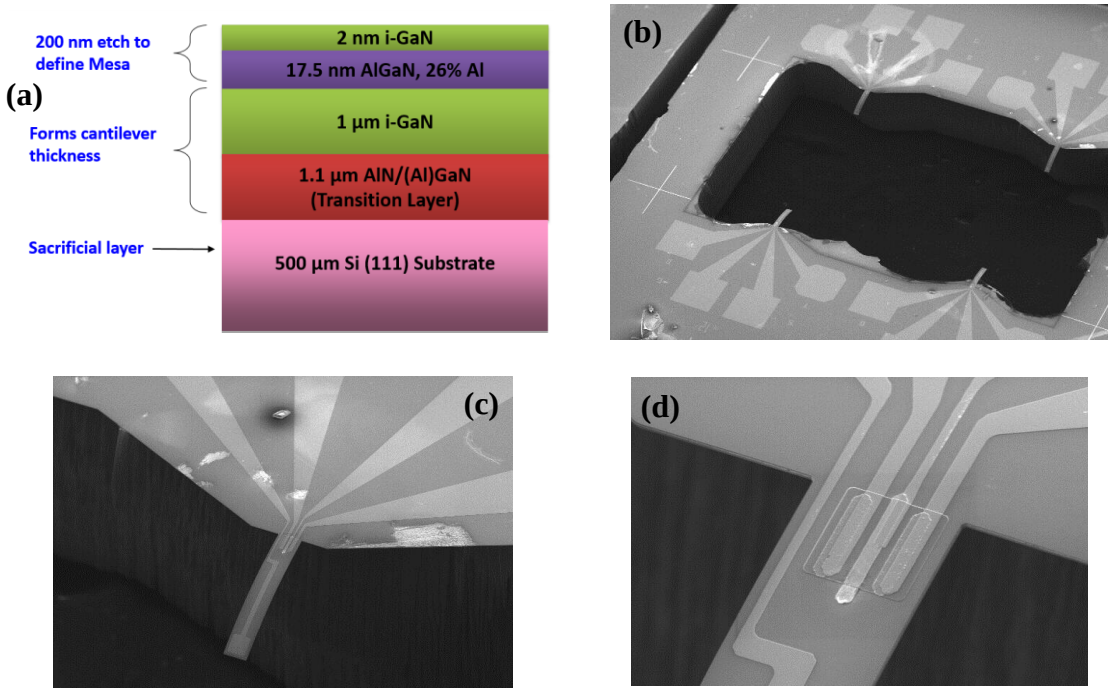


**Figure 3.26** (a) Wafer layer structure, SEM image of (b) a pocket containing four microcantilever devices (250 and 350 µm in length, width 50 µm, and thickness 2 µm, (c) One single microcantilever device with four large bonding pads for drain, gate, source and tip, (d) AlGaN/GaN HFET. Mesa can be clearly distinguished with drain, gate and source contacts on it.

# CHAPTER 4

## PIEZORESISTIVE GAN MICROCANTILEVER

GaN microcantilevers with two different dimensions of 250×50×2 $\mu m^3$ and 350×50×2 $\mu m^3$ were studied study using commercial wafers with III-V Nitride epitaxial layers on Si (111) substrate (layer structure shown in the bottom inset of Fig. 4.1). The HFET, acting as a piezoresistive deflection sensor, was integrated at the base of the cantilever (top inset of Fig. 4.1). The fabricated Si chip carrying a set of 4 GaN microcantilevers were wire bonded to a regular 28 pin chip carrier (CSB02812, Spectrum, Inc.). The source-drain resistance $R_{DS}$ for most cantilevers varied in the range of 20 - 50 kΩ, but a small percentage showed $R_{DS} \geq 500$ kΩ, which can be attributed to processing related surface and/or sub-surface damage. We studied quasi-static and dynamic responses of both of these groups in this chapter with experimental details.

### 4.1 Static Bending of microcantilevers

Figure 4.2(a) shows the quasi-static bending performances of representative low and high $R_{DS}$ devices. For the low resistance device ($R_{DS}$ = 22 kΩ), the drain current was found to increase by 1.17% [see Fig. 4.2 (a)], due to 1 μm of downward bending. The transverse

gauge factor can be calculated by the formula: $GF = (\Delta R/R)/\varepsilon_x$, where $\varepsilon_x$ is strain, $\Delta R$ is change in resistance, and $R$ is the initial resistance of the cantilever.

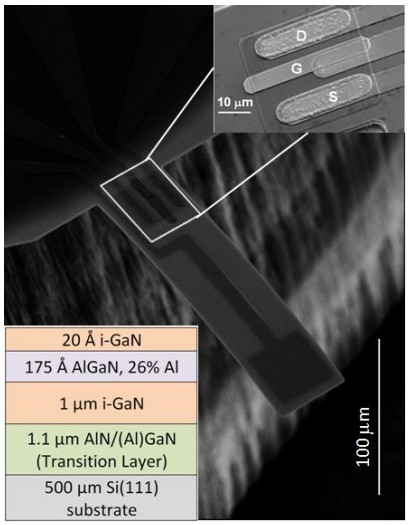


**Figure 4.1** (a) SEM image of GaN microcantilever (250×50×2 $\mu m^3$) with embedded AlGaN/GaN HFET at the base. Top inset shows the magnified image of the AlGaN/GaN HFET. The source drain length, $L_{DS}$ = 17 μm, the channel width, $W_{ch}$ = 29 μm, and the gate length, $L_G$ = 6 μm. Bottom inset shows the layer structure of the wafer.

Using $\varepsilon_x = 1.865\times10^{-5}$ for 1 μm bending of the free end of the cantilever, obtained from COMSOL simulations, we obtain GF = $-1.17\times10^{-2}/1.865\times10^{-5}$ = -627. For the high $R_{DS}$ (= 3 MΩ) device, the drain current can be seen to change by 6.3% due to 1 μm bending, which yields GF = -3532, which is the highest ever reported for these cantilevers. For other measurements in this study we used a representative high $R_{DS}$ (= 2.8 MΩ) device with GF = 1350. Higher GF observed for the high $R_{DS}$ device compared to the low $R_{DS}$ one can be attributed to lower 2DEG density, which would result in a higher channel resistance change

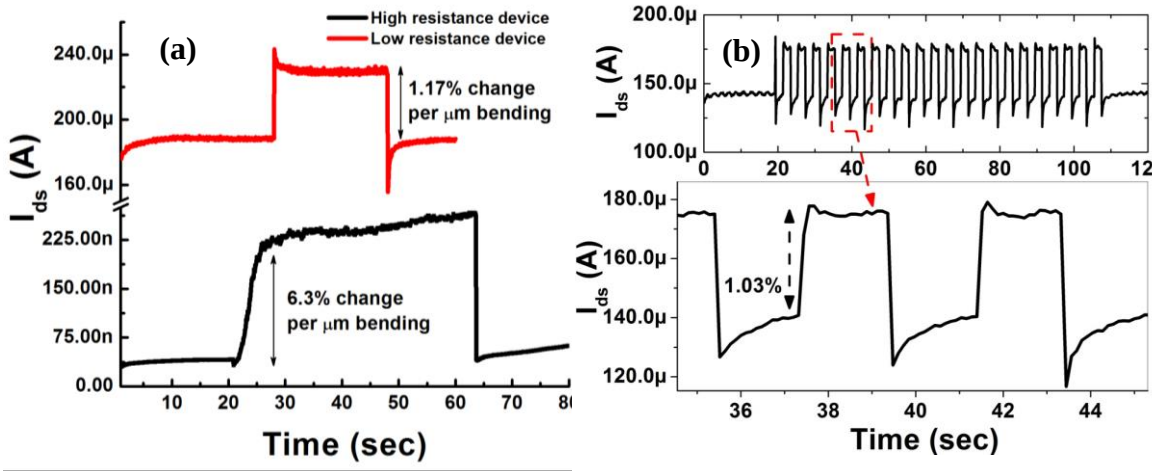


**Figure 4.2** (a) Static bending responses of two microcantilevers (250×50×2 μm$^3$) with $R_{DS}$ of 22 KΩ and 3 MΩ. (b) Low frequency dynamic bending response when the low resistance cantilever is bent by 25 μm at 0.5 Hz frequency.

due to bending, leading to a higher GF. Fig. 4.2 (b) shows the low frequency (0.5 Hz) dynamic response of the low resistance device, with alternate downward and upward bending by 25 μm. We find that the gauge factor (dc) reduces slightly to -600 in these dynamic bending conditions. We would like to point out here that the GF obtained for these devices (i.e. 600 – 3500) are much higher than those of Si cantilevers, which are typically less than 100[111,112].

## 4.2 Dynamic bending of microcantilevers

To investigate the dynamic response of the microcantilevers, we adopted three different excitation methods: (i) direct contact excitation using a piezo-chip (5×5×2 mm$^3$,

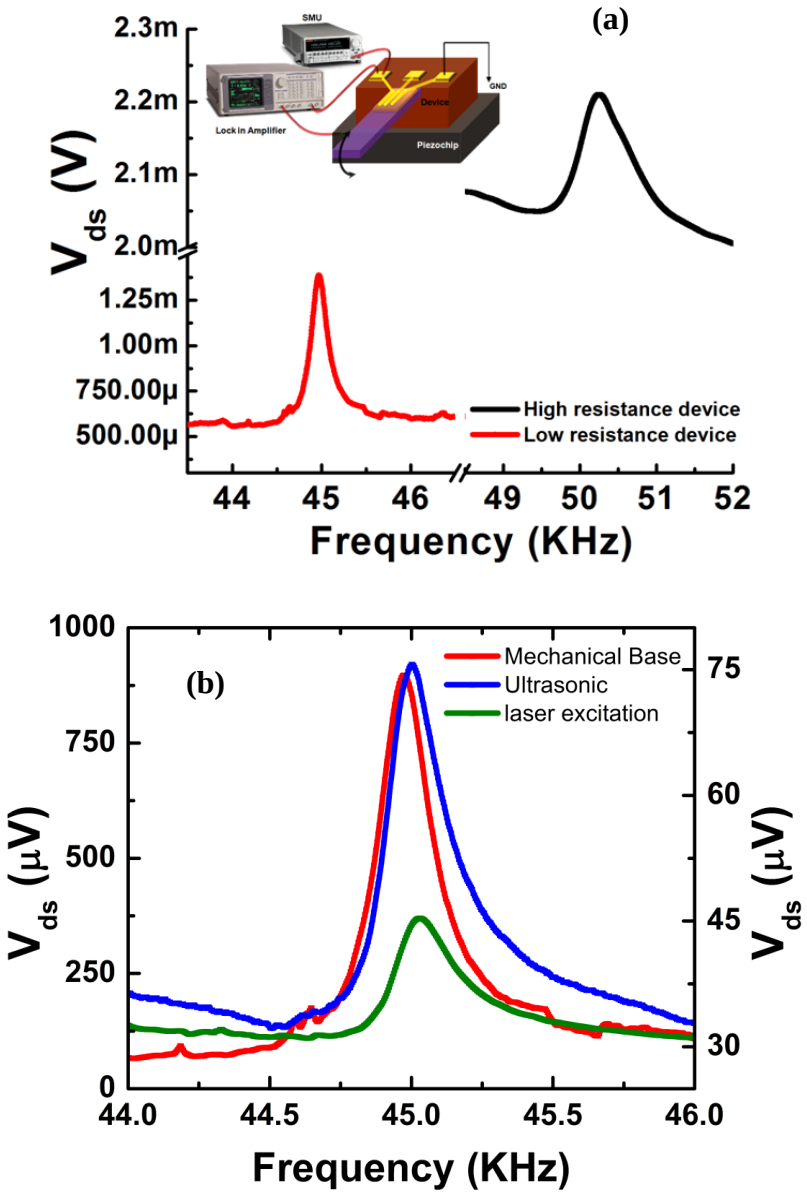


**Figure 4.3** (a) Dynamic responses of two microcantilevers with $R_{DS}$ of 22 KΩ and 2.8 MΩ. The top inset shows the measurement setup. (b) Comparison of the dynamic responses of the low $R_{DS}$ (22 KΩ) microcantilever by three different excitation approaches.

from Physic Instrumente) attached to the bottom of the chip carrier, (ii) non-contact ultrasonic excitation through air using a piezo-chip oscillation, and (iii) photoacoustic excitation using a laser (100 mW, 790 nm from World Star Technologies, Inc.) focused at

the base of the cantilever, and pulsed at resonance frequency. The measurement schematic for direct contact based excitation is shown in the inset of Fig. 4.3(a). A constant current source (Keithley Sourcemeter) provided drain currents of 10 μA and 1 μA for the low and high $R_{DS}$ microcantilevers, respectively, and a lock-in amplifier was used to measure ac voltage $V_{ds}$ generated between the source and the drain, as $R_{DS}$ changed due to cantilever oscillations. An ac voltage (1 V rms) with varying frequency was applied to the piezo chip to oscillate it. As expected, the $V_{ds}$ reached a maximum at the resonance frequencies of the cantilevers, which is measured as 0.82 mV and 0.18 mV above the off-resonance value for the low and high $R_{DS}$ devices, respectively [see Fig. 4.3(a)]. From the dynamic responses studied, we found the resonance frequencies to be in the range of 45 – 51 KHz and 29 – 35 KHz, respectively, for the shorter (250 μm) and longer (350 μm) cantilevers. The quality factor remained ~200 for the cantilevers irrespective of their length.

To determine the effectiveness of the microcantilevers for acoustic sensing at resonant frequency, $\omega_0$, we calculated their dynamic gauge factor (at $\omega_0$) $GF_{dyn}$, which can be written as:

$$GF_{dyn(peak)} = \frac{\Delta R_{DS}/R_0}{\epsilon_{peak}} = \frac{\Delta V_{DS}/V_0}{\epsilon_{peak}} \tag{4.1}$$

where the $\Delta R_{DS}$ and $\Delta V_{ds}$ are the peak changes in $R_{DS}$ and $V_{ds}$ due to oscillations, respectively, $V_0$ is the drain-source voltage off resonance, and $\varepsilon_{peak}$ is the peak stress. Assuming the amplitude of cantilever oscillations to be the same as the mechanical base (23 nm) for off resonance conditions, the maximum amplitude at resonance is 4.6 μm due to quality factor enhancement (Q = 200), which gives rise to a peak strain $\varepsilon_{peak}$ of $4.6 \times 1.865\times10^{-5} = 8.579 \times 10^{-5}$. With an initial voltage $V_0$ of 0.22 V ($I_{ds}$ = 10 μA, $R_{ds}$ = 22 KΩ),

and $V_{peak}$ of $0.82\sqrt{2}$ = 1.16 mV, the gauge factor is calculated as -61.26. Following a similar procedure the gauge factor for the high resistance device is calculated as -0.8. Clearly, the $GF_{dyn}$ values are much lower compared to their dc and low frequency dynamic values. In addition, the $GF_{dyn}$ of the high $R_{DS}$ device reduced more from its dc gauge factor ($GF_{dc}$ =-1350) compared to the low $R_{DS}$ device ($GF_{dc}$= -627). The theoretical estimates of $GF_{dc}$ for cantilevers of these dimensions are 3 – 15[100,113,114], and higher experimental GF is attributed to the interaction of trap states[90,100,115-117]. The observation of reduced GF first at low frequency (-627 to -600), and then more significantly at resonant frequency, supports the conclusion

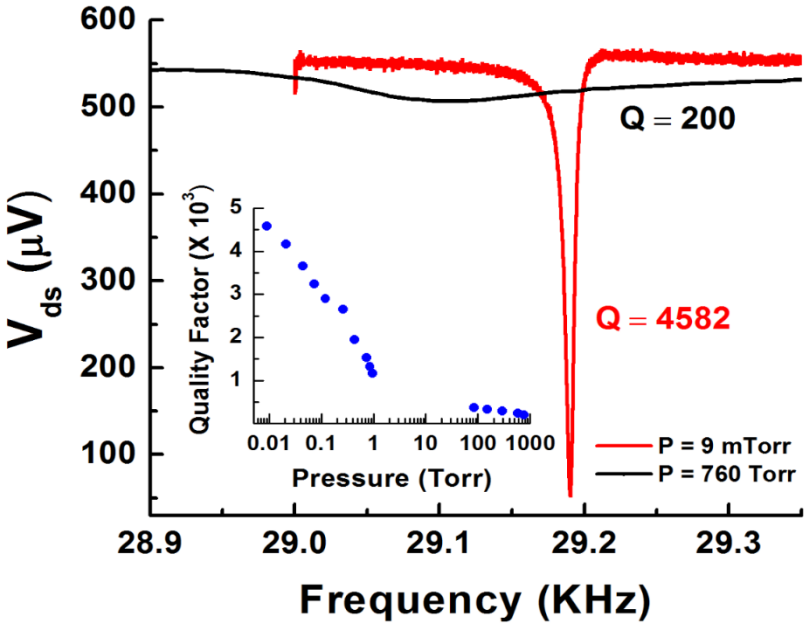


**Figure 4.4** Comparison of the quality factors of a long cantilever measured at atmospheric pressure and 9 mTorr. The inset shows the quality factor variation as a function of pressure.

that traps play a significant role in increasing the GF over theoretical estimates. At high frequencies, it is likely that the traps and/or surface donor states, responsible for pumping charge in and out of the HFET channel (as the polarization charge changes, and the Fermi level swings up and down), would not be able to respond (accept/donate charges) adequately, leading to reduction in GF, as experimentally observed.

Figure 4.3(b) compares the frequency responses of the same device (250 μm long) obtained through non-contact ultrasonic and photoacoustic methods with that of the direct excitation method. We find that all the methods yield the same resonant frequency of ~45 KHz, and Q (= $\omega_0/\Delta\omega_{half\text{-}width}$) of ~200 in air. To study the variation in Q with pressure, the cantilever was enclosed in a sealed chamber attached to a vacuum pump, and excited through photoacoustic method. Fig. 4.4 shows the resonance curves of a 350 μm cantilever in air and 9 mTorr pressure, with the inset showing the variation of quality factor as a function of pressure. We find that the cantilever Q increases sharply as the pressure is reduced, reaching a value of 4582 at 9 mTorr pressure ($\omega_0$ = 29.19 KHz, $\Delta\omega$ = 7 Hz). This enhancement in quality factor with reduction in pressure is in excellent agreement with earlier reports[118]. From these results, we also conclude that these microcantilevers can be very effectively excited by photoacoustic technique creating acoustic waves in the Si substrate.

## 4.3 Air based ultrasonic transduction

To further investigate the performance of the microcantilever as air based ultrasonic sensor, we studied the effect of varying distance and excitation amplitude of the piezochip.

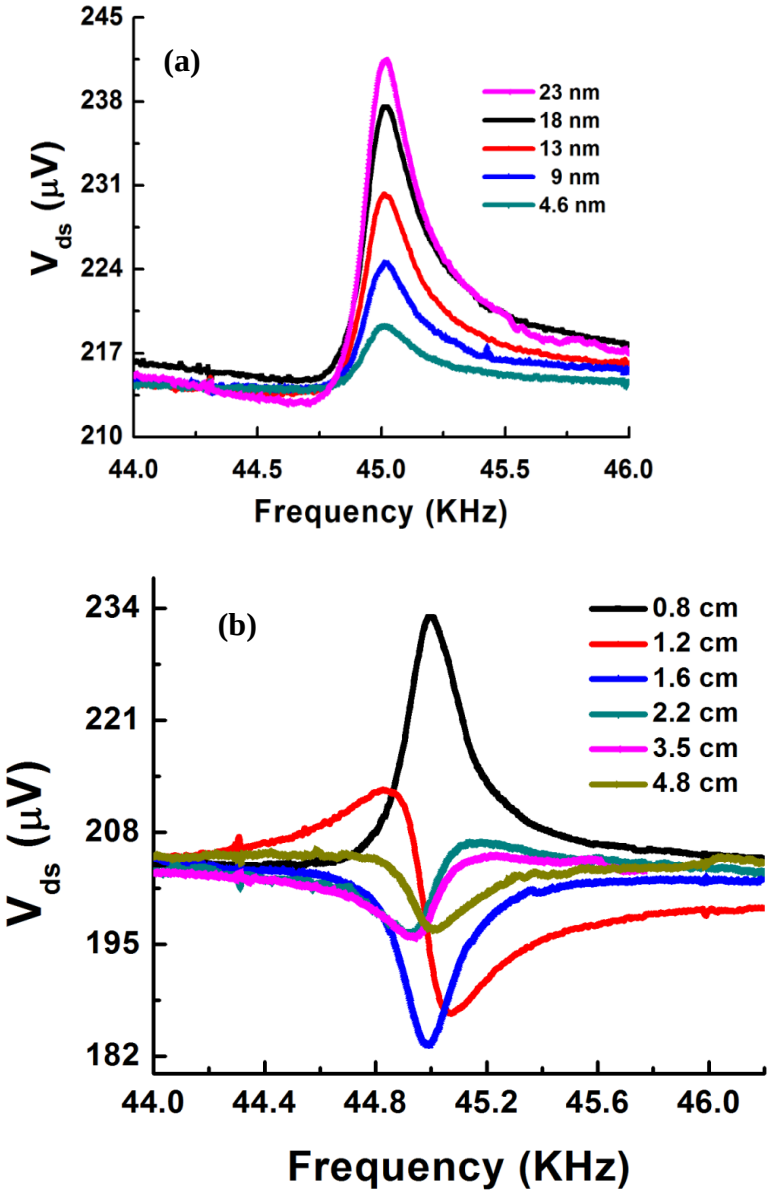


**Figure 4.5** Non-contact ultrasonic excitation of the microcantilever (a) as a function of oscillation amplitude of the piezo-chip placed 0.8 cm away, and (b) as a function of distance of the piezo-chip with a fixed oscillation amplitude of 23 nm.

First, the input ac voltage to the piezochip was varied from 0.2 V (rms) to 1 V (rms), at a fixed position 0.8 cm away from the microcantilever, which increased its vibration amplitude from 4.6 nm to 23 nm (estimated from PI datasheet). Fig. 4.5(a) shows the resonance curve of the microcantilever corresponding to different piezochip oscillation amplitude. We find that the $V_{ds}$ (corresponding to change in resonant amplitude) increases from 4.5 to 28.46 μV, increasing proportionally with the piezochip oscillation amplitude. Keeping the piezochip oscillation constant at 23 nm, and varying its position from 0.8 cm to 4.8 cm yields the cantilever response as shown in Fig. 4.5(b), where both magnitude and phase of the oscillations are seen to vary. For a plane progressive wave in air, the relationships between sound intensity ($I$), sound pressure ($p$), particle displacement ($a$), acoustic impedance of air ($Z$), and acoustic power ($P_{AC}$) are given as[119],

$$I = 4a^2\pi^2 f^2 Z = \frac{p^2}{Z} = \frac{P_{AC}}{A} \tag{4.2}$$

Assuming, the acoustic impedance of air, Z = 413.3 $Nsm^{-3}$, f = 45 KHz, a = 23 nm, and using areas of the piezochip and cantilever to be 25 $mm^2$ and 250×50 $\mu m^2$, respectively, I, p, and $P_{AC}$ at the surface of the piezochip are calculated as 17.47 $mW/m^2$, 2.69 Pa, and 0.44 μW, respectively, from equation (4.2). The peak pressure at the surface of the cantilever, positioned at r = 0.8 cm away from the piezochip, can then be calculated as 0.476 Pa [= $\sqrt{P_{AC}(Z/4\pi r^2)}$], which would exert 5.94 nN peak force on the cantilever. This would result in a resonance oscillation amplitude of 792 nm (= QF/k) assuming a quality factor Q = 200 and spring constant k = 1.5 N/m (determined from COMSOL finite element simulation). From equation (4.2) it is also clear that the peak pressure is directly proportional to amplitude of the piezochip. Thus, change in piezochip amplitude would proportionally affect the cantilever oscillation amplitude, as observed in Fig. 4.5(a). In

addition, since the peak pressure varies inversely with distance[119], the resonance amplitude of the cantilever would vary inversely with its separation from the piezochip, as observed in Fig. 4.5(b). The change in phase seen in Fig. 4.5(b) can be explained by considering the change in phase of the pressure wave reaching the microcantilever as the piezochip is moved from 0.8 cm to 4.8 cm away from the cantilever. We find that the resonant peaks occur at multiples of 0.8 cm, while the antiresonant peaks occur at multiples of 1.2 cm. Since the wavelength $\lambda_p$ of ultrasonic wave at 45 KHz frequency in air is 0.76 cm (assuming velocity of sound of 343 m/s at 20 °C), the resonant peaks are expected to occur at distances that are integral multiples of $\lambda_p$. The antiresonant ones are experimentally found to occur at distances that are multiples of $1.5\lambda_p$, but the exact mechanism of their formation is not clear to us at this point.

To determine the noise limited pressure measurement resolution by the cantilever, we calculated the overall noise from two major sources of noise for oscillating microcantilevers, Johnson and thermo-mechanical noise. Using $k_BT$ = 0.026 eV at 300 K and $R_{DS}$ = 22 KΩ, the Johnson noise is calculated as[111] $v_{noise}(\text{rms}) = i_{noise}(\text{rms}) \times R_{DS} = \sqrt{4k_BT/R} \times R_{DS} = 19.14$ nV. Since $\Delta V_{ds}$ = 1.16 mV at resonance corresponding to an oscillation amplitude of 4.6 μm (using Eq. 4.1), the equivalent noise amplitude is found to be 75.9 pm/√Hz. The thermo-mechanical noise is calculated for the same frequency, and using Q = 200, k = 1.5 N/m, and f = 45 KHz in the formula[111] as $TM_{noise}(\text{rms}) = \sqrt{4k_BTQ/(k\omega_0)} = 2.8$ pm/√Hz. The overall noise is clearly dominated by the Johnson noise, but if a larger $I_{ds}$ is used to make $V_{ds}$ comparable to commonly used value of 10 V, then the Johnson noise can go down to1.67 pm/√Hz. In off-resonance conditions, the TM noise also reduces to 2.8/200 = 0.014 pm, and the total noise becomes

basically the John son noise, i.e. 1.67 pm at 1 Hz bandwidth or 52.81 pm at 1KHz bandwidth. The noise limited resolution is comparable to that best noise performance of Si cantilevers (20 pm – 5 nm)[87,111] for a bandwidth of 1 KHz. The noise limited pressure measurement resolution of the cantilever can be calculated using Eq. (4.2) as 1.96 μPa (= 0.476 Pa×3.26 pm/792 nm) at 1 Hz bandwidth or 62 μPa for 1 KHz bandwidth.

# CHAPTER 5

## PIEZOTRANSISTIVE GAN MICROCANTILEVER

Total resistance of the HFET[120] (externally measured), $R_{DS} = R_{int} + 2R_C + 2R_{acc}$, where $R_{acc}$ is the access region resistance, $R_c$ denotes the source and drain contact resistances. $R_{int}$ is the drain-source resistance of the intrinsic transistor, where the gauge factor, GF, can be derived as (derivation is given in the last section),

$$GF = \frac{\frac{\Delta R_{DS}}{R_{DS}}}{\varepsilon} \approx -\frac{1}{\varepsilon}\left[{}^{\Delta\mu_{int}}/_{\mu_{int}} + {}^{\Delta n_{s,int}}/_{n_{s,int}}\right] \quad (5.1)$$

Here, $\mu_{int}$ and $n_{s,int}$ are the mobility and carrier concentration for the intrinsic device, and $\varepsilon$ is the average strain in the channel. It is obvious from Eqn. 5.1 that the GF depends on both changes in carrier concentration and mobility, which are strongly correlated at gate biases close to pinch-off (i.e. lower carrier concentration)[120]. Clearly, this results in a higher GF in a gated piezoresistor, where the gate voltage can be used to tune the carrier concentration to a desired (low) level where the mobility would change significantly due to change in carrier concentration, in addition to higher fractional change in the carrier concentration itself (caused by external strain). For a Si piezoresistor (i.e. p-type Si) the carrier concentration does not depend on external strain, so the additional benefit of mobility change, caused by change in carrier concentration as noted above, is absent.

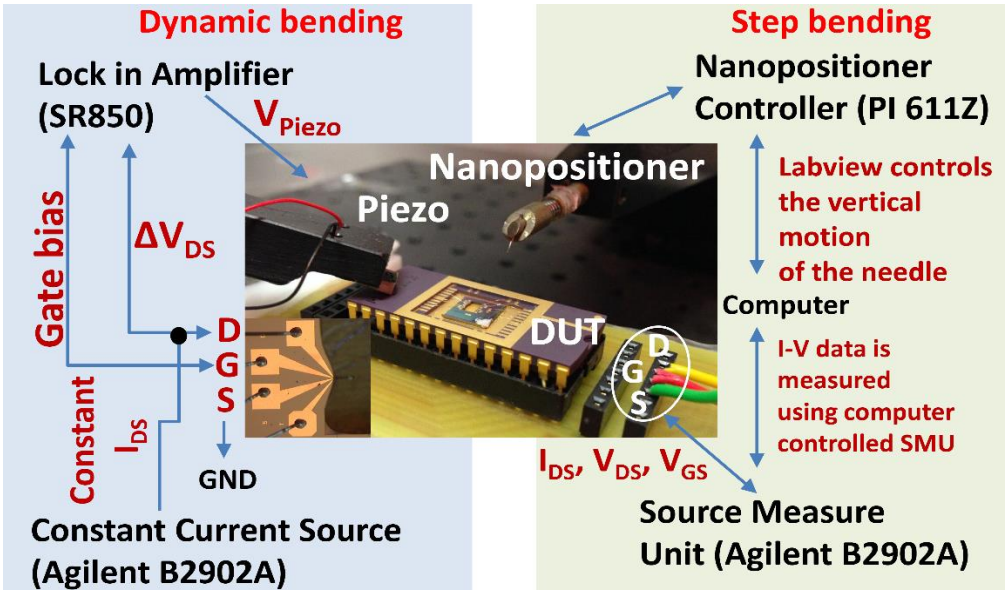


**Figure 5.1** Optical image of the experimental setup for both step (on the right) and dynamic bending (on the left) responses. The AlGaN/GaN HFET embedded GaN microcantilever (250×50×2 μm3) is shown in the magnified view.

In a simple AlGaN/GaN piezoresistor, without the possibility of gate modulation, the carrier concentration does change with strain but the additional advantage of mobility change is uncertain.

## 5.1 Step bending

To determine the step bending response (see Fig. 5.1), the microcantilever was bent down by 1 μm and released, as $V_{GS}$ was systematically varied. Downward bending causes larger tensile strain in the AlGaN layer, which in turn, generates more positive piezoelectric charge at the AlGaN/GaN interface[40], drawing excess compensating electrons ($\Delta n_s$), and thereby reducing $R_{DS}$. When the cantilever is released, excess tensile strain is reduced, and

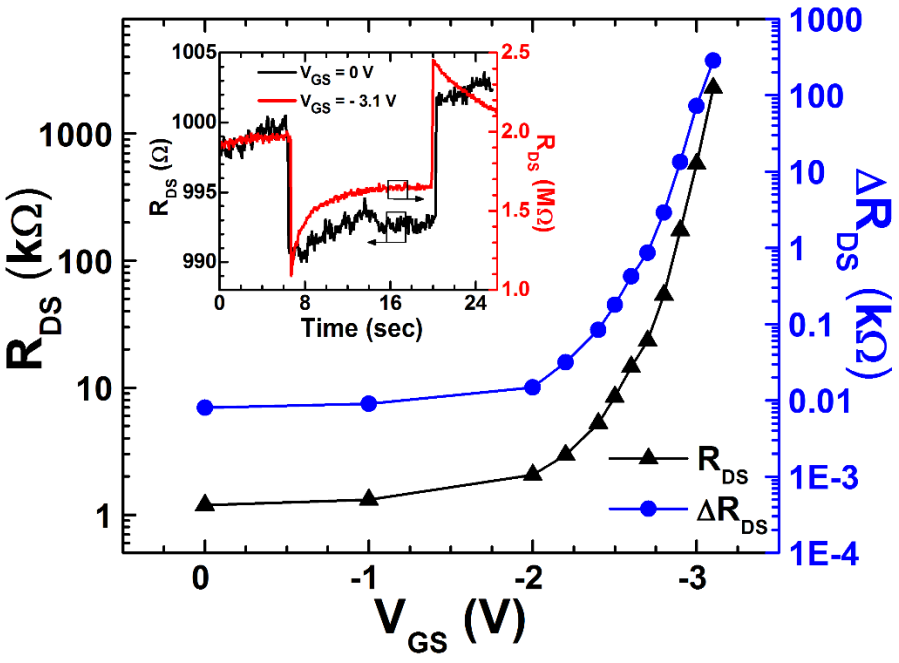


**Figure 5.2** Variation of $R_{DS}$ and $\Delta R_{DS}$ for with $V_{GS}$. Inset shows the change in $R_{DS}$ for $V_{GS}$ = 0 and – 3.1 V. $V_{DS}$ was kept at 0.5 V.

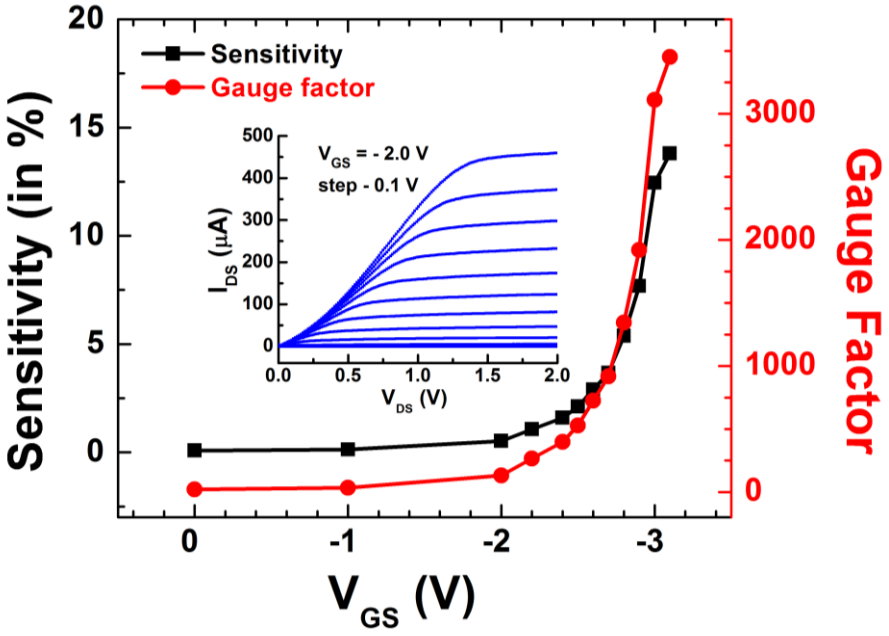


**Figure 5.3** Gate bias dependence of sensitivity and gauge factor at $V_{DS}$ = 0.5 V. The $I_{DS}$-$V_{DS}$ characteristics of the HFET is shown in the inset.

$R_{DS}$ returns to its initial value. With more negative $V_{GS}$ applied, $n_s$ reduces, which increases the ratio $\Delta n_s/n_s$ and maximizes $\Delta R_{DS}/R_{DS}$ and hence the GF. The step bending response of this device, for $V_{GS}$ = 0 and – 3.1 V, are shown in the inset of Fig. 5.2. For $V_{GS}$ = 0, we found $R_{DS}$ = 1 kΩ and $\Delta R_{DS}$ = 7 Ω, whereas $V_{GS}$ = -3.1 V yielded $R_{DS}$ = 2.16 MΩ and $\Delta R_{DS}$ = 300 kΩ. Thus, $\Delta R_{DS}/R_{DS}$ increased more by 2 orders as $V_{GS}$ approached the shutdown voltage of the HFET of - 3.2 V. The variations in $\Delta R_{DS}$ and $R_{DS}$ with $V_{GS}$ are shown in Fig. 4.2. The computed sensitivity (= $\Delta R_{DS}/R_{DS}$) increases monotonically from $V_{GS}$ = 0, and reaches a maximum value of 13.8% at $V_{GS}$ = - 3.1 V (Fig. 5.3). The average strain on the HFET was estimated as $4.3\times10^{-5}$ from the finite element COMSOL simulation. A maximum GF = 3200 is calculated at $V_{GS}$ = - 3.1 V, which decreases monotonically as the $V_{GS}$ increases to more positive values (Fig. 5.3). It is noteworthy that the maximum GF calculated here is 35 times higher than the optimized Si based piezoresistive devices (GF = 95)[112], and comparable to that of SWCNT (GF = 2900)[121]. The sensitivity of this device did not vary significantly with $V_{DS}$. However, with more negative $V_{GS}$, especially near shutdown, the HFET was operated in the saturation region (see inset of Fig. 5.3) to enable $I_{DS}$ to dominate over the gate leakage current. Although significant transients were observed for more negative $V_{GS}$ (see inset of Fig. 5.2) when the cantilever was bent down and released, we only considered the steady state values of $R_{DS}$ for calculating GF. If the maximum transient value of $R_{DS}$ is used we would get a much higher GF of ~10,000. It is possible that if the transients are minimized through proper device passivation[122] then even higher GF can be achieved.

## 5.2 Dynamic bending

For dynamic response, an oscillating piezochip was contacted to the DIP, which generated a surface wave that propagated to the cantilever to initiate oscillation (see Fig. 5.1, more details in next section). The oscillation of the microcantilever was transduced by the HFET (biased with constant $I_{DS}$ = 10 µA and $V_{GS}$ = - 2.3 V), where the $R_{DS}$ changed periodically, resulting in a periodic change in the drain-source voltage, $\Delta V_{DS}$, which was measured by the lock-in amplifier. Laser vibrometer measurements very closely matched the HFET measurements, which yielded a resonant frequency of 43.94 kHz with a quality factor of 230 as shown in Fig. 5.4. The voltage responsivity (VR) which is a more important parameter than GF for dynamic bending[123], was determined by taking the ratio of $\Delta V_{DS}$ and the oscillation amplitude considering the difference of the on-resonance peak and off-

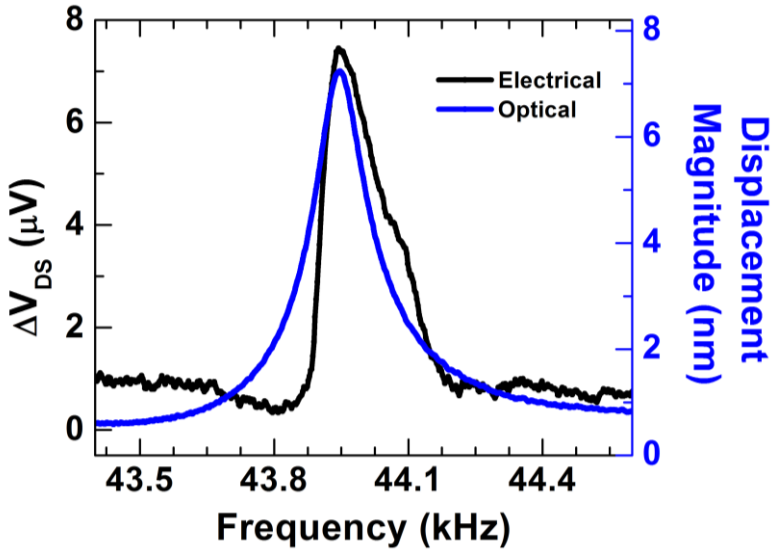


**Figure 5.4** Simultaneous optical and HFET readout of the mechanical resonance of the microcantilever $V_{GS}$ = - 2.3 V, $V_{DS}$ = 0.5 V and $I_{DS}$ = 10 µA.

resonance base. Comparing the two measurements, we find that a change in oscillation amplitude of 7.9 nm (from vibrometer) corresponded to $\Delta V_{DS}$ (rms) = 7.5 μV (from HFET). Thus the VR can be calculated as 0.95 μV/nm. Similarly as in step bending case, more negative $V_{GS}$ resulted in increased $\Delta R_{DS}$ which enhanced the responsivity, since $\Delta V_{DS} = I_{DS} \times \Delta R_{DS}$. As seen from Fig. 5.5, with decrease in $V_{GS}$, VR increases monotonically, reaching a value of 40 μV/nm with the same piezo excitation, at $V_{GS}$ = - 2.7 V and $I_{DS}$ = 10 μA. The power dissipation across the HFET was calculated using $P_{DS} = I_{DS}^2 \times R_{DS}$ for different $V_{GS}$ (Fig. 5.5) using $I_{DS}$ = 10 μA and $R_{DS}$ values from Fig. 5.2. We found $P_{DS}$ increases monotonically from 0.51 μW to 2.4 μW, as $V_{GS}$ becomes more negative, changing from – 2.3 V to – 2.7 V. The piezoresistive response of the HFET is limited mainly by the Johnson noise at high frequency which is given by, $S_J = \sqrt{4k_B T R_{DS} B}$, where $k_B T$ = 26 meV at room temperature and B is the measurement bandwidth. With B = 10 Hz, the calculated Johnson noises were 28.84 nV and 139.42 nV for $V_{GS}$ = - 2.3 V and – 2.7 V, respectively, while the corresponding signal-to-noise ratios (SNR = 20 $\log_{10}$ (VR/$S_J$)) are 30.35 dB and 49.15 dB, for 1 nm oscillation amplitude. However changing the bias current from 10 μA to 100 μA, sharply increased the SNR from 30.35 dB to 73.7 dB. Clearly there is a trade-off between three critical parameters of a HFET deflection transducer, namely, power dissipation, responsivity and SNR. For example, for $V_{GS}$ = -2.3 V, we obtained the highest responsivity of 140 μV/nm (see inset of Fig. 5.5) with an SNR of 73.7 dB, however this was achieved at the cost of higher power dissipation of 51 μW. We would like to mention here that this device and other similar devices have shown excellent repeatable and reproducible performances as mentioned above when tested several times in one year time period.

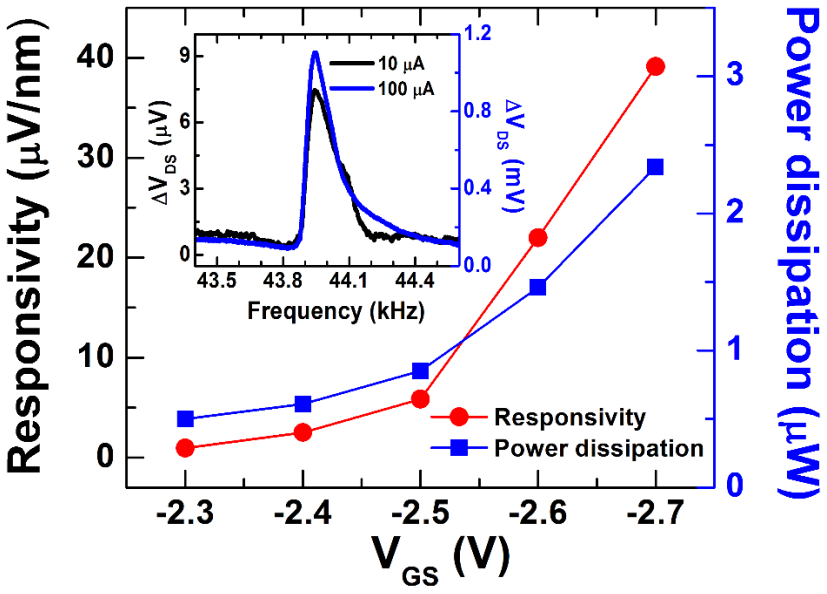


**Figure 5.5** Voltage responsivity and power dissipation of the HFET with $V_{GS}$ for $I_{DS}$ = 10 μA and tip deflection of 7.9 nm. Inset compares the amplification of $\Delta V_{DS}$ for $I_{DS}$ = 100 μA with $I_{DS}$ = 10 μA. $V_{DS}$ was kept at 0.5 V.

Our gated piezoresistor offers the advantage of utilizing the same device to cater to various application needs (i.e. requirement of low power consumption, high sensitivity, high SNR, or DC to ultrasonic frequency operations), simply by biasing the transistor. The experimental results presented here provide the necessary insights into the operation of HFET embedded micro/nano cantilever.

## 5.3 Detail schematics of experimental and measurement setup

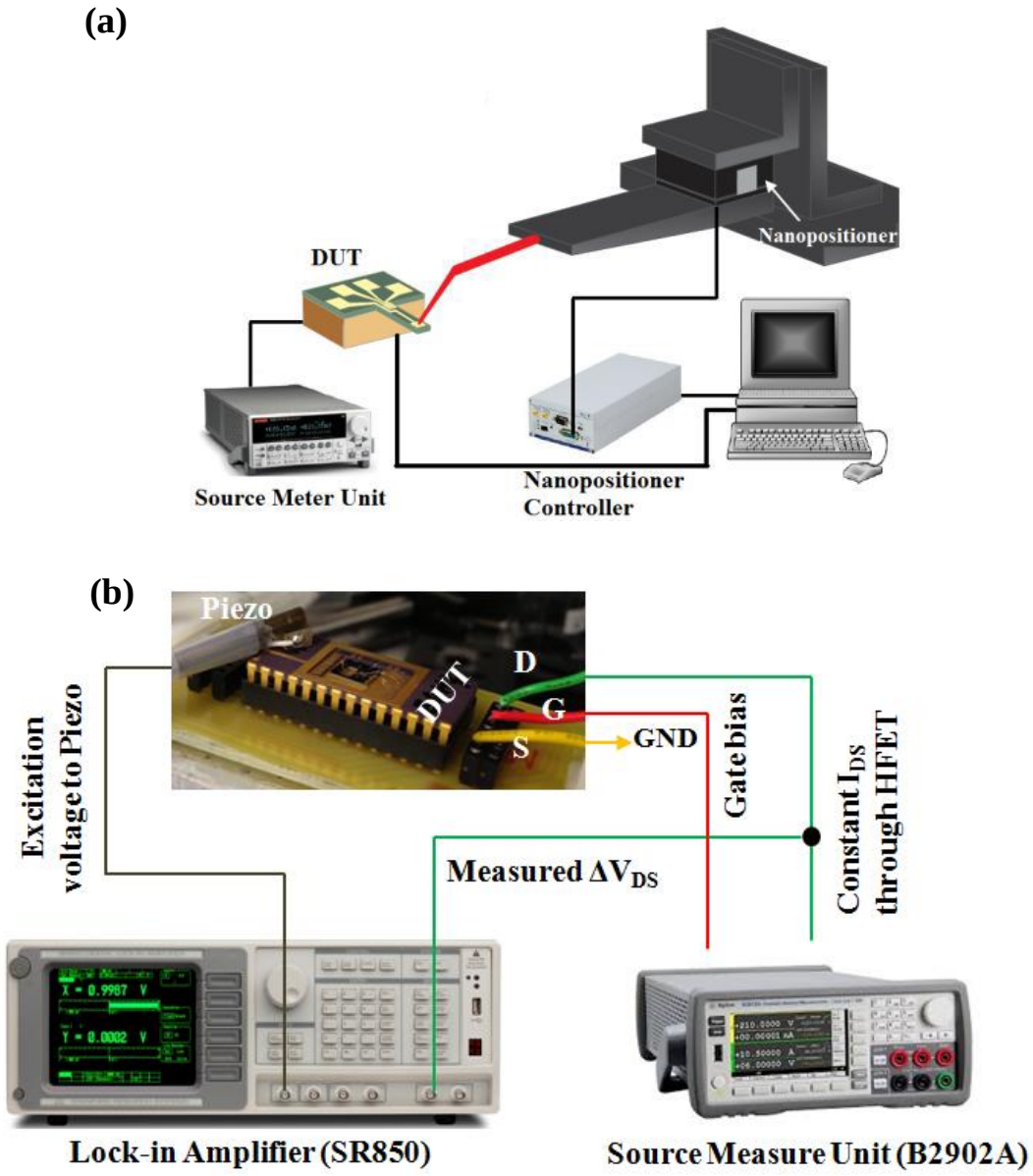


**Figure 5.6** (a) Schematics of step bending experiment where a needle attached to a nanopositioner were used to physically bend the Microcantilever. The nanopositioner's motion was controlled by controller using labview. The source measure unit measured relevant currents and voltages before and after bending the cantilever.

(b) Schematics of dynamic bending setup: The SMU supplies constant current, $I_{DS}$ through the HFET and also the gate bias. The Piezo was used to mechanically excite the Microcantilever to oscillate. A frequency swept sinusoidal voltage was supplied from the lock-in amplifier. The change in voltage across drain and source, $\Delta V_{DS}$ due to the oscillation of Microcantilever was measured by the lock-in amplifier. The drain contact of the HFET was in common ground with both the equipments. A laser vibrometer (MSA-500) (not shown in this schematics) was used to simultaneous measure the oscillation amplitude. The laser vibrometer was company calibrated and the $\Delta V_{DS}$ measurement was calibrated using the laser vibrometer measurement.

Fig. 5.6 (a) shows the setup for static bending test. The DUT is always mounted on a PCB as can be seen in Fig. 5.6 (b). This is our 2$^{nd}$ generation setup, but recently new PCB has been designed which has the provision of mounting any chip carrier up to 48 pin as shown in Fig. 5.7. One of the newly fabricated devices which was shown in chapter 3, was tested with this new setup and the relevant experimental results are described in next section. However the next chapter will describe the sensing results with the similar devices as described in chapter 4 and 5.

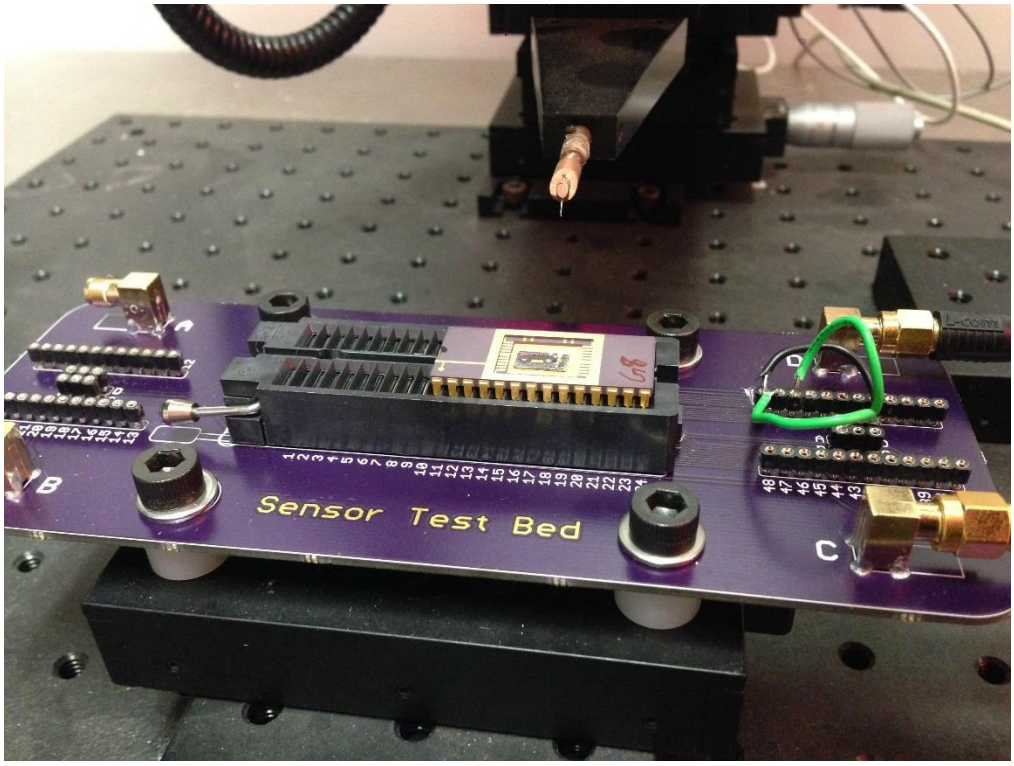


**Figure 5.7** Photograph of latest sensor test bed (made by Nick DeRoller).

## 5.4 Device performance of new microcantilevers

### 5.4.1 Rectangular Microcantilever

One of the newly fabricated microcantilevers (length is 150 μm, width 50 μm and thickness is 1 μm) was tested with the new setup as shown in Fig. 5.7. Impressive and better performances were observed. Fig. 5.8 (a) shows the transmission line measurement (TLM) results on TLM pads which yielded contact resistance of 13.39 Ω and sheet resistance of 478.1 Ω/□. Fig. 5.8 (b) and (c) show the excellent gate control of the device and very high current with low leakage as expected from usual AlGaN/GaN HFET. Similar

as described earlier, static bending test was performed and the device presented 140% change in HFET channel resistance for 10 µm bending (see Fig. 5.8 (d)).

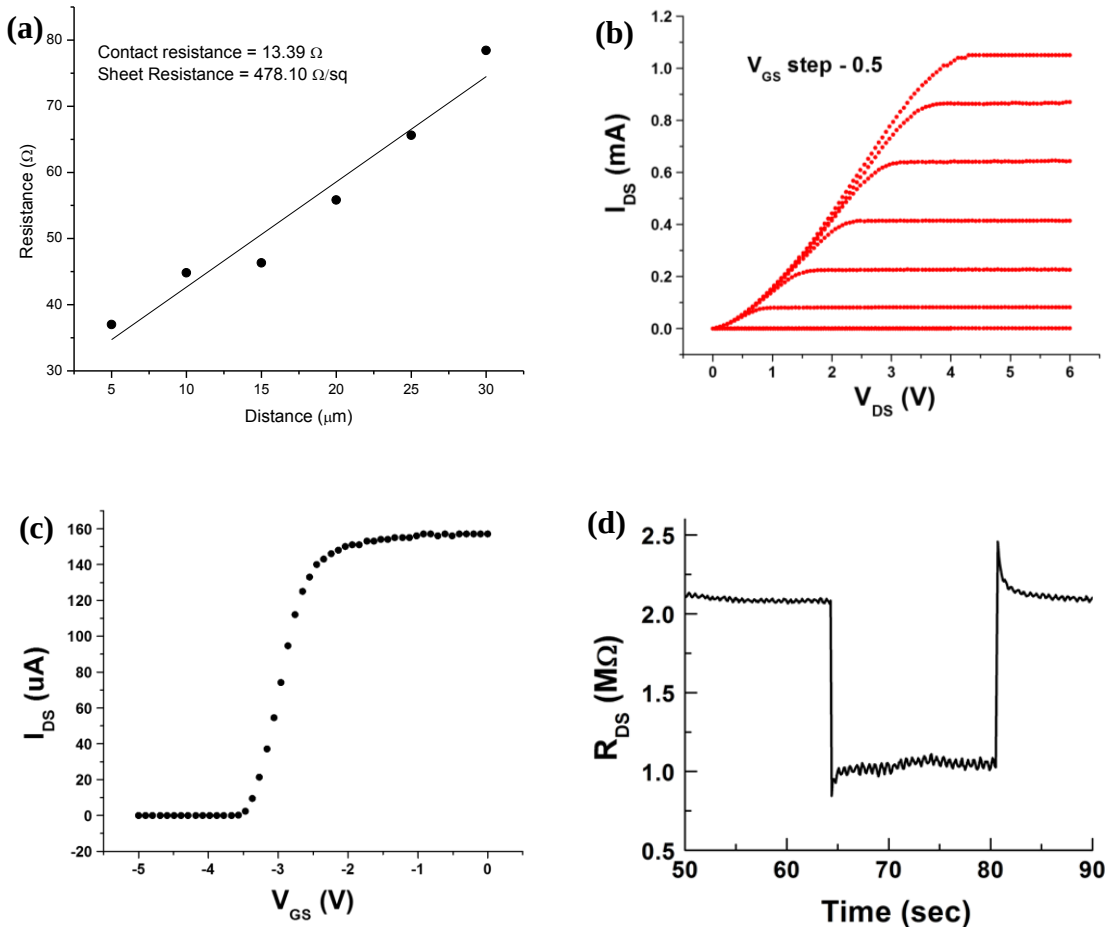


**Figure 5.8** (a) TLM data, (b) The $I_{DS}$-$V_{DS}$ characteristics of the HFET when $V_{GS}$ was swept from -2.5 V to -3.0 V with 0.5 V step, (c) The $I_{DS}$-$V_{GS}$ characteristics of the HFET when $V_{DS}$ = 0.5 V, (d) Step bending response when the new Microcantilever was bent by 10 µm magnitude which yielded $\Delta R_{DS}/R_{DS}$ to be 140%.

### 5.4.2 Triangular Microcantilever

One of the newly fabricated triangular microcantilevers (V shaped, height 250 µm, width 60 µm, and thickness 1 µm) has also been studied with both static bending and dynamic bending characterizations. The V shaped cantilevers have two arms and so two HEFT with similar or different orientations considering current conduction, were integrated. However the chosen one was with two similar HFETs identical to Fig. 3.20 (a). Two of the HFETs were either used together or separately to transduce the mechanical deflection of the V shaped Microcantilever. In that case the biasing parameters were kept same for both HFETs when acted as a single HFET. Fig. 5.9 (a) shows the SEM image of the V shaped cantilever where two HFETs are integrated.as numbered 1 and 2. Fig. 5.9 (b) shows the I-V characteristics of both the HFETs. The channel resistances ($R_{DS}$) were measured to be 850 Ω and 1.2 kΩ for devices 1 and 2 respectively. As described earlier, the higher the resistance, the higher the sensitivity (or gauge factor), so it is presumed that HFET 2 will present higher sensitivity. However as we have separate gate controls we can tune the gate bias to match the resistances to obtain equal sensitivity. The mechanical arms are symmetrical, so if the external stress is applied in the middle of the tip equal strain would be distributed at the two bases yielding equal piezoresistive changes. However in this experiment we have kept the drain-source and gate bias same and the cantilever was bent 1 µm downward and released. The bending results are shown in Fig. 5.9 (c), when HFET 1 and HFET 2 transduced separately, and when they were connected together externally (with jumper cables shorting two sources and drains). The sensitivities were measured to be 0.44% (HFET 1), 0.57% (HFET 2), and 0.48% (both) per 1 µm.

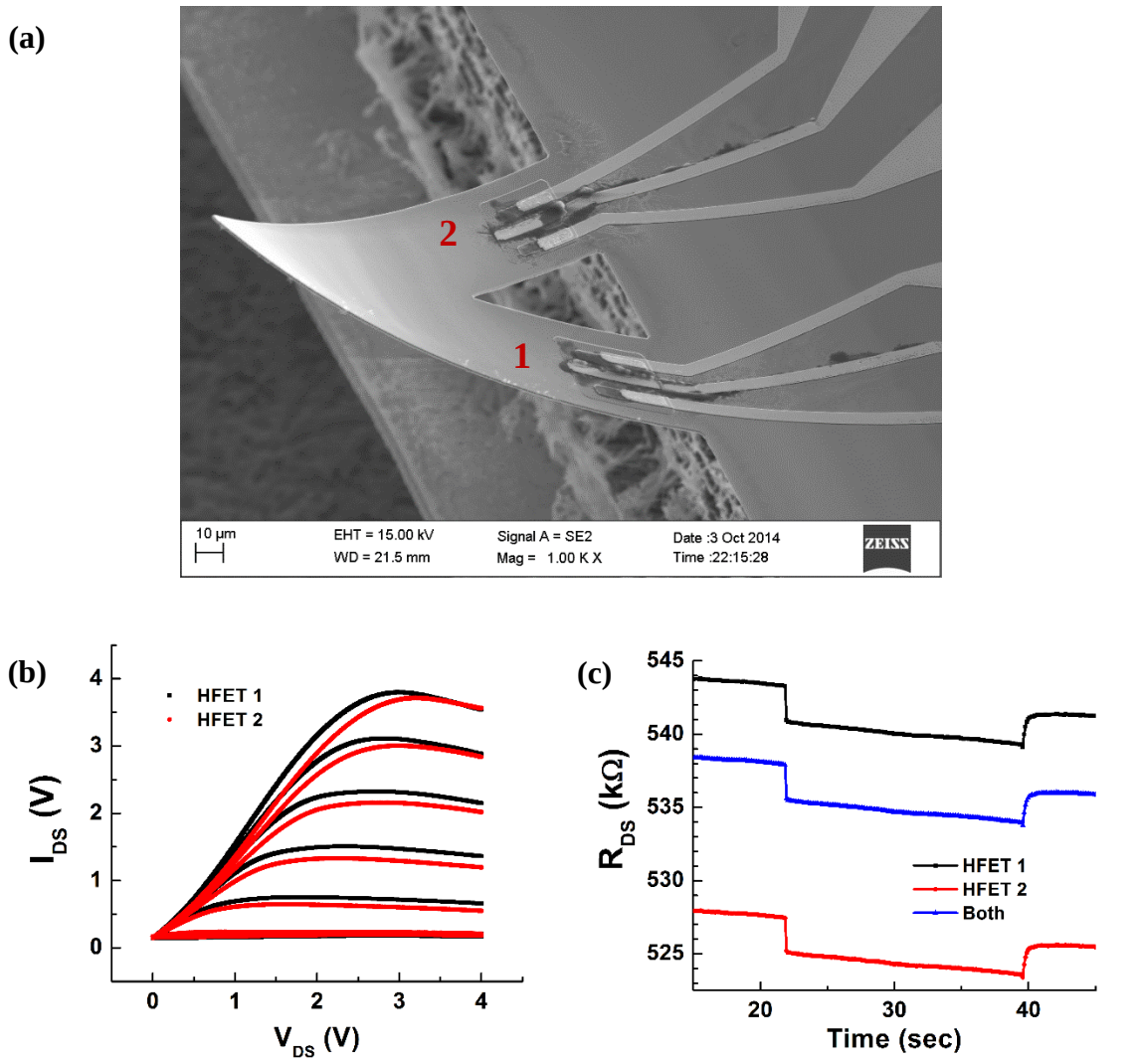


**Figure 5.9** (a) SEM image showing triangular microcantilever embedded with two HFETs (1 and 2), (b) The $I_{DS}$-$V_{DS}$ characteristics of the HFETs when $V_{GS}$ was swept from 0 V to -3.0 V with 0.75 V step, (c) Step bending response when Microcantilever was bent by 1 µm magnitude with HFET 1 and 2 are separately used (black and blue lines), and when both of them were connected together. $V_{DS}$ = 0.5 V, $V_{GS}$ = -2.7 V.

The dynamic response were also measured with this cantilever as described earlier (the measurement). The cantilever was oscillated with Piezo actuation. The resonance frequency was found 47.871 kHz and the quality factor was 371. Fortunately there was a dust particle on the cantilever which allowed us to measure the mass loading on the

microcantilever and the corresponding frequency shift. Fig. 5.10 shows the frequency downshift of the resonance frequency of the cantilever by 721 Hz when a dust was on the cantilever. The bias optimization was not performed on this particular cantilever. But the biasing parameters were: constant $I_{DS}$ = 10 µA, $V_{GS}$ = -3.0 V.

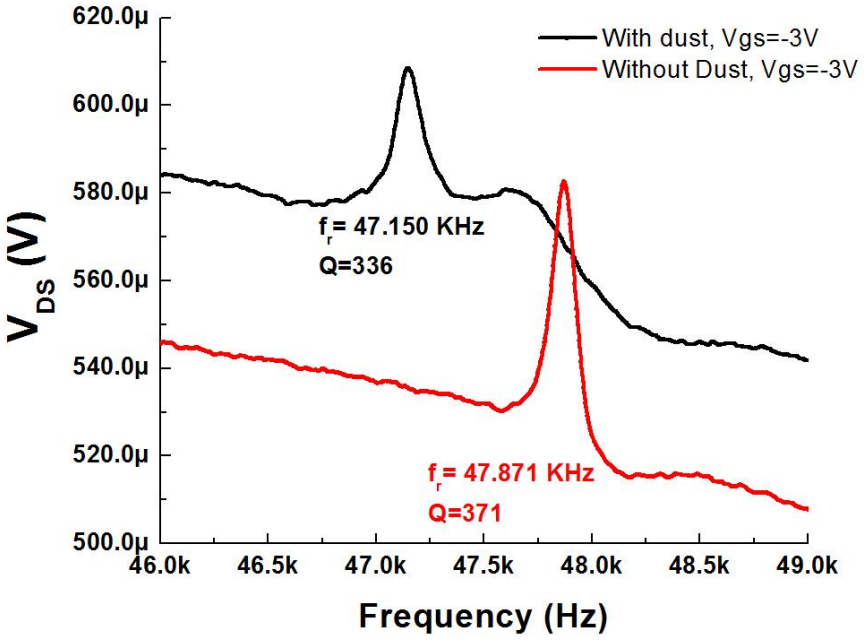


**Figure 5.10** Frequency response of a triangular microcantilever with and without mass loading.

## 5.5 Mathematical derivation of gauge factor dependence

Total resistance of the HFET (externally measured),

$$R_{DS} = R_{int} + 2R_C + 2R_{acc} \quad (5.1)$$

$R_{int}$ is the drain-source resistance of the intrinsic transistor. $R_c$ denotes the source and drain contact resistances (assumed to be equal). $R_{acc}$ is the access region resistance (resistance of the channel from the gate to the source or to the drain, which are also assumed to be equal) and is given by[120],

$$R_{acc} = \frac{L_{DG}}{q\mu_{acc}n_{s,acc}W_D} \quad (5.2)$$

Here, $L_{DG}$ is the length of the access region on the drain side, $W_D$ is the width of the channel, and $\mu_{acc}$ and $n_{acc}$ are the mobility and carrier concentrations in the access regions. $R_{int}$ is the drain-source resistance of the intrinsic device, i.e. the resistance of the channel under the gate, and given as,

$$R_{int} = \frac{L_G}{q\mu_{int}n_{s,int}W_D} \quad (5.3)$$

Here, $\mu_{int}$ and $n_{int}$ are the mobility and carrier concentrations for the intrinsic device, which can differ significantly from $\mu_{acc}$ and $n_{acc}$, especially with applied gate bias.

Taking differentials of both sides of eqn. (5.1) we get

$$\Delta R_{DS} = \Delta R_{int} + 2\Delta R_{acc} \quad (5.4)$$

Using eqns. 5.2 and 5.3 in eqn. 5.4 we get,

$$\Delta R_{DS} = -R_{int}\left[\Delta\mu_{int}/\mu_{int} + \Delta n_{s,int}/n_{s,int}\right] - 2R_{acc}\left[\Delta\mu_{acc}/\mu_{acc} + \Delta n_{s,acc}/n_{s,acc}\right] \quad (5.5)$$

Near the pinch off region (higher negative $V_{GS}$), $n_{s,int} << n_{s,acc}$, so $\Delta n_{s,int}/n_{s,int} >> \Delta n_{s,acc}/n_{s,acc}$. Also, it is well known that at high $n_s$, the μ is fairly independent of $n_s$, so $\Delta\mu_{acc}/\mu_{acc}$ will be negligible compared to $\Delta n_{s,acc}/n_{s,acc}$. Also, $n_{s,int}\mu_{int} << n_{s,acc}\,\mu_{acc,}$ so $R_{int} >> R_{acc}$. Thus from eqn. 1 we have $R_{DS} \approx R_{int}$ (neglecting $R_c$) Dividing both sides of eqn. (5.5) by $R_{DS}$ and neglecting the second term in the RHS of eqn. 5.5, we have

$$\frac{\Delta R_{DS}}{R_{DS}} \approx -\left[\Delta\mu_{int}/\mu_{int} + \Delta n_{s,int}/n_{s,int}\right] \quad (5.6)$$

Thus the gauge factor can be defined as:

$$GF = \frac{\frac{\Delta R_{DS}}{R_{DS}}}{\varepsilon} \approx -\frac{1}{\varepsilon}\left[\Delta\mu_{int}/\mu_{int} + \Delta n_{s,int}/n_{s,int}\right] \quad (5.7)$$

It is obvious from Eqn. 5.7 that the GF depends on both changes in carrier concentration and mobility, which are strongly correlated at gate biases close to pinch-off (i.e. lower carrier concentration). Clearly, this results in a higher GF in a gated piezoresistor, where the gate voltage can be used to tune the carrier concentration to a desired (low) level where the mobility would change significantly due to change in carrier concentration, in addition to higher fractional change in the carrier concentration itself (caused by external strain). For a Si piezoresistor (i.e. p-type Si) the carrier concentration does not depend on external strain, so the additional benefit of mobility change, caused by change in carrier

concentration as noted above, is absent. In a simple AlGaN/GaN piezoresistor, without the possibility of gate modulation, the carrier concentration does change with strain but the additional advantage of mobility change is uncertain.

## 5.6 Change in 2DEG concentration with bending

To support our above analytical assumption that change in 2DEG concentration ($n_s$) is the added quality of AlGaN/GaN based device, a separate experiment was conducted. The cantilever was bent as usual in two slots with 10 µm and 20 µm bending magnitude and the sensitivity was recorded using SMU. The same cantilever was later used to record the capacitance-voltage profile with a LCR meter under same magnitude of bending. The C-V curves were then integrated with respect to $V_{GS}$ to roughly calculate $n_s$ and thus the change in $n_s$ was estimated with respect to equilibrium condition for each $V_{GS}$. Fig. 5.11 (a) shows the step bending response of a microcantilever for 10 µm and 20 µm bending with $V_{GS}$ = -2.7 V and $V_{DS}$ = 0.5 V, which resulted in HFET current changes of 55% and 100% respectively. Then the same devices were again bent with same magnitudes but this time the C-V profile was recorded as shown in Fig. 5.11 (b). It is always hard to get the capacitance reading from such a small HFET contact, the frequency was 500 kHz with an ac voltage of 500 mV was applied from the LCR meter. Calibration should be done to get accurate results. From the C-V profile it was evident that, under bent state there was increment in 2DEG density. This C-V profiles were integrated with respect to $V_{GS}$ to get

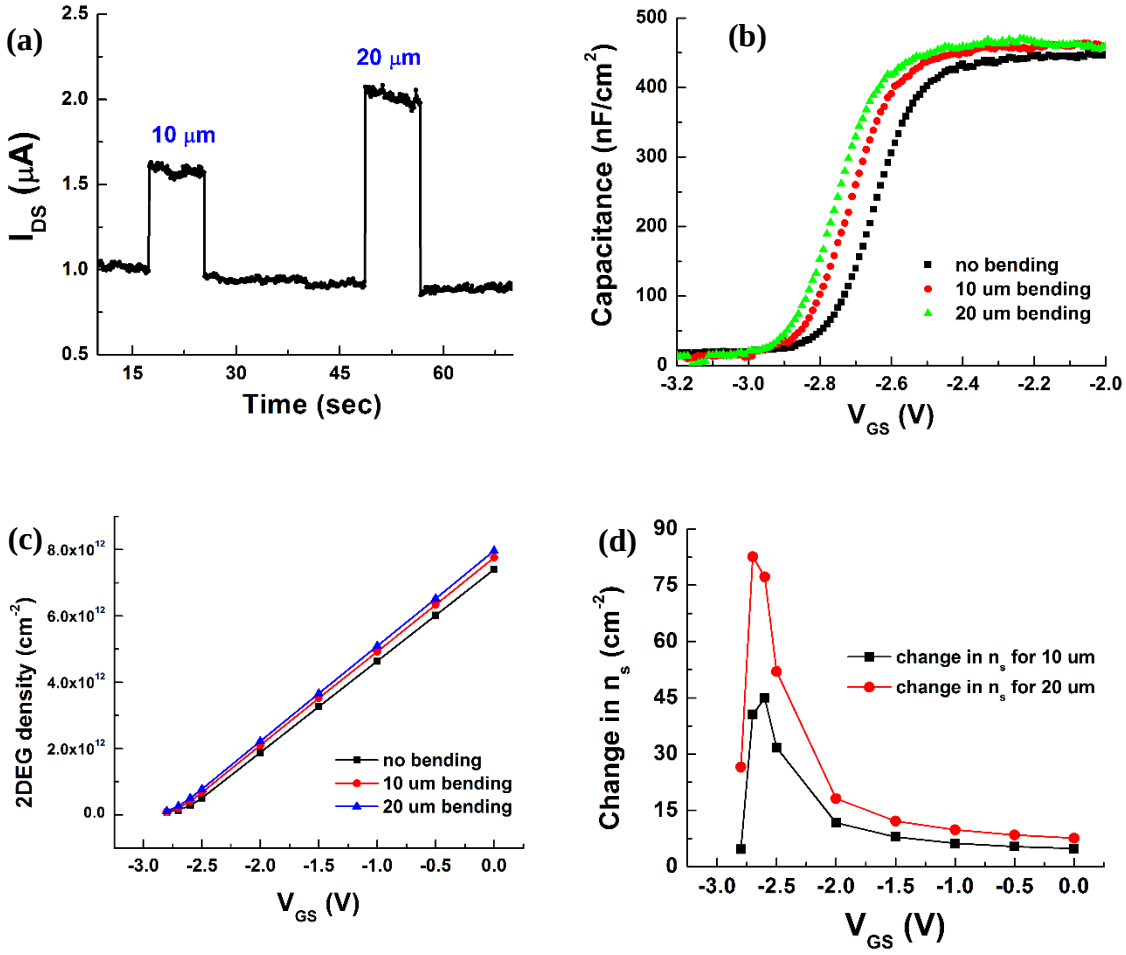


**Figure 5.11** (a) Step bending response when the new Microcantilever was bent by 10 µm and 20 µm magnitudes which yielded $\Delta I_{DS}/I_{DS}$ to be 55% and 100% respectively, (b) The $C_{GS}$-$V_{GS}$ characteristics of the HFET when $V_{GS}$ was swept from 0 V to -3.2 V with 0, 10 µm, and 20 µm bending magnitudes, (c) the 2DEG density variation with $V_{GS}$, (d) Change in 2DEG concentrations with $V_{GS}$ for 10 µm and 20 µm bending magnitudes.

the $n_s$ variation with $V_{GS}$ as shown in Fig. 5.11 (c). The profiles were subtracted from no bending condition to calculate the change in $n_s$ with $V_{GS}$ (see Fig. 5.11 (d)). For $V_{GS}$ = -2.7 V, the change in $n_s$ was found to be 43% and 87% for 10 µm and 20 µm bending respectively. This results presented a strong experimental proof that, the bending in the microcantilever will primarily change the 2DEG concentration which will change the

HFET channel resistance ultimately. This is where piezotransistive transduction offers more sensitivity than simple piezoresistors.

# CHAPTER 6

## DEMONSTRATION OF SENSING APPLICATIONS WITH PIEZOTRANSISTIVE MICROCANTILEVERS

In chapter 4 and 5, the basic performances of both piezoresistive and piezotransistive microcantilevers were discussed. From those discussions, we can understand that piezotransitive (gated piezoresistor) microcantilevers offer better performance with sensitivity, tunability, noise, and power consumption. This chapter will provide detail demonstrations of real time sensing applications of mostly piezotransistive microcantilevers as displacement sensor, acoustic transducer, and piezoresistive microcantilevers as diaphragm like pressure sensor. This chapter will end with a brief demonstration of the reliability of using these sensors after high dose of gamma radiation. The first section is divided into four sub-sections where readers will be progressed through the enhanced performance of sensing nanoscale to femtoscale displacement with a broad comparison of state-of-the-art technology including different materials and structures, revealing the superior performance of piezotransistive GaN microcantilevers. The second section would describe the application of these sensors as an effective acoustic transducer compared to commercially available microphone and would also depict pressure sensing by piezoresistive micro-disc (diaphragm like) and finally the harsh environment application of both types of sensors will be documented in the last section.

Development of ultrasensitive micro- and nano-electromechanical systems (MEMS/NEMS) has resulted in ultra-high detection sensitivity, offering sub nanometer scale displacement detection[121,124,125], zeptogram level mass sensing[126-128], single bio-molecular sensing[57,129,130], and atomic resolution imaging[131-134]. Micro and nanocantilevers, as MEMS/NEMS transducers, have been used extensively for these sensing applications. Optical transduction of cantilever motion is almost exclusively used to achieve high deflection sensitivity (in the femtometer range), but it suffers from high power requirement, challenges with miniaturization and array based operation[135]. Femto-meter scale displacement detection using nanocantilevers operating at several hundred MHz has been demonstrated[2], but is limited by its challenging fabrication and integration schemes, coupled with complicacies of impedance matching for high frequency signal transmission. Si based piezoresistive microcantilevers have been developed[112,136,137] which are easily integrate for array based operation, but have low sensitivity offering displacement resolution in the range of nanometers[138]. Instead of a simple piezoresistor, embedding a transistor at the base of the microcantilever (henceforth to be called a "piezotransistive" microcantilever) to transduce its deflection is an attractive way to dramatically improve its sensitivity by orders of magnitude[87,90], since the gate can be utilized to control the charge carrier density and the mobility of the carriers in the channel.

Recently, metal oxide semiconductor field effect transistor (MOSFET) integrated Si cantilevers have been proposed with the goal of achieving very high deflection sensitivity while avoiding the challenges associated with the aforementioned techniques[87,137]. Although these microcantilevers showed high sensitivity in the nm range for step deflections, since its high sensitivity supposedly originated from trapping effects

in the MOSFET, it is difficult to reproduce these sensors, or operate them at high frequencies. Indeed, Si based piezotransistive microcantilevers are theoretically incapable of exhibiting direct sensitivity enhancement through gate control, since the piezoresistive effects in Si originate from the variation in carrier mobility due to strain related splitting of the conduction band minima energy levels[139]. On the other hand, piezotransistive cantilevers made of piezoelectric materials can directly utilize the charge density variation caused by the deflection induced strain to exhibit high sensitivity with very high repeatability.

Due to strong piezoelectric properties of AlN and GaN, AlGaN/GaN heterojunction[22], provides a unique avenue to translate the static piezoelectric charge generated at the interface due to applied strain into a change in resistance, since the generated piezoelectric charge can proportionately modulate the density of the mobile carriers (electrons) at the interface[90,115]. In addition to changing the carrier density, the applied strain can also cause a change in carrier mobility, albeit to a lesser extent, by changing their effective mass. The utility of AlGaN/GaN heterojunction based piezoresistor (for step bending and dynamic deflection measurements) and piezotransistor (for static deflection measurements) has been demonstrated [90,100,101], however, the effect of gate on enhancing displacement sensitivity down to femtometer range in high frequency dynamic deflection mode has never been realized. In the present work, we report on the ultrahigh deflection sensitivity achieved using AlGaN/GaN heterojunction FET (HFET) embedded piezotransistive GaN microcantilever, which resulted in successful transduction of femtometer level displacement at the resonance frequency of the cantilever. The capability of measuring these extremely small displacements, verified independently

through laser vibrometry studies, has enabled detection of nanogram level explosives with high specificity using novel surface based photoacoustic technique.

Piezotransistive microcantilevers were fabricated using III-Nitride epitaxial layers grown on Si (111) substrate. The overall layer structure consists of i-GaN (2 nm)/AlGaN (17.5 nm, 26% Al)/i-GaN (1 µm)/Transition layer (1.1 µm)/Si (111) substrate (500 µm). The HFET was fabricated with initial 200 nm mesa etching followed by GaN cantilever pattern etched down using $BCl_3/Cl_2$ based inductively coupled plasma etch process.

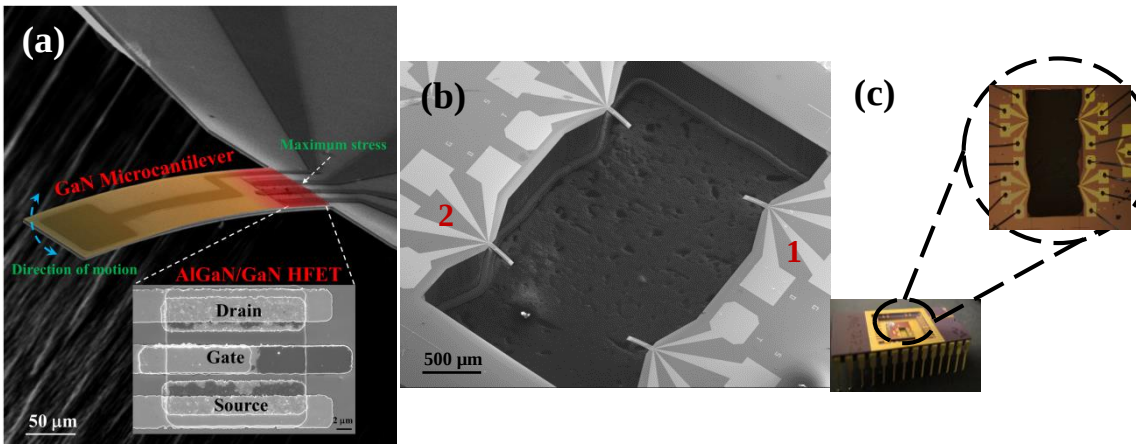


**Figure 6.1** (a) SEM image of GaN microcantilever with AlGaN/GaN HFET embedded at the base. The inset shows a magnified section containing the HFET. The microcantilever has been false color coded along the length to show the stress distribution when it is deflected due to oscillations. (b) SEM image of a representative chip with 4 microcantilevers at the edges of a rectangular trench. The microcantilevers investigated in this study are marked 1 and 2. (c) Picture of a 28 pin DIP package with the microcantilever chip wire bonded. A magnified image shows wires bonded to the bias pads.

Ohomic contacts were formed with Ti (20 nm)/Al (100 nm)/Ti (45 nm)/Au (55 nm) metal stack deposition and rapid thermal annealing. Schottky gate contact was then formed with Ni (25 nm)/Au (375 nm) deposition. Finally, through wafer Si etch was performed by "Bosch process" to release of the microcantilevers (more details in chapter 3).

## 6.1 Displacement sensor

### 6.1.1 Detection of Nanoscale static deflection

The fabricated microcantilevers had dimensions of 250 × 50 × 2 $\mu m^3$, with the embedded HFET's channel dimension being 17 × 29 × 6 $\mu m^3$. Fig. 6.1 (a) shows the Scanning Electron Micrograph (SEM) of our fabricated self-sensing piezoelectric GaN microcantilever with the AlGaN/GaN HFET (bottom inset) fabricated at its base, where the maximum stress occurs due to deflection of the microcantilever (shown with a color map in Fig. 6.1, and supported by COMSOL finite element simulations in Fig. 6.2). Each chip has 4 similar microcantilevers as shown in Fig. 6.1(b), which were wire bonded to a 28 pin dual-in-line package (DIP) (Fig. 6.1(c)) chip carrier. Apart from the conventional source, drain, and gate contacts of the HFET, there is an additional contact for electrostatic actuation of the microcantilever, which was not used in this study. The results presented in this article are from devices 1 and 2 as indicated in the SEM image of Fig. 6.1(b). Typical $I_{DS}$-$V_{DS}$ and $I_{DS}$-$V_{GS}$ characteristics of the HFET (device 1), exhibiting good gate control, are shown in Fig. 6.3 (a). Utilizing a negative gate bias the piezoresistive effect is translated into a piezotransistive effect where the 2DEG carrier concentration $(n_s)$[140] is reduced, thus increasing the $\Delta n_s/n_s$ ratio ($\Delta n_s$ is the change in 2DEG density due to strain caused by deflection of the cantilever). Fig. 6.3(b) shows the gate bias dependence of the 2DEG

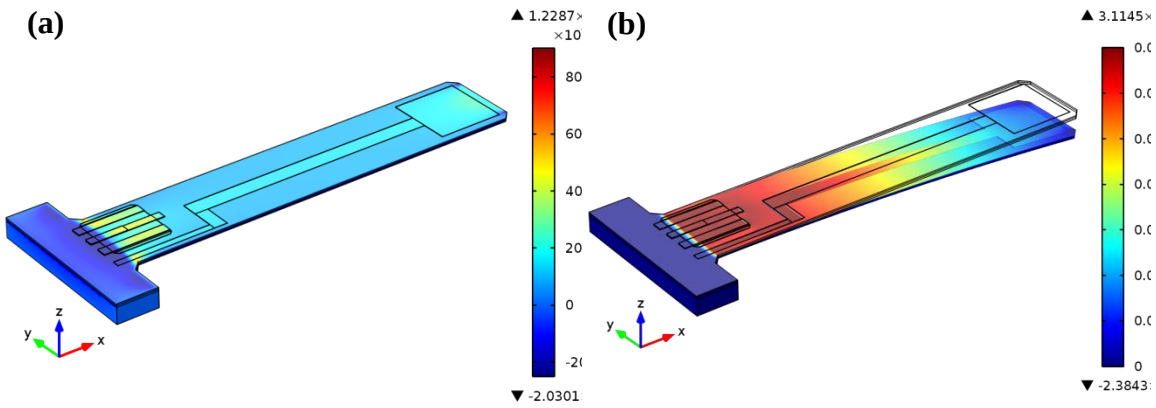


**Figure 6.2** COMSOL simulations showing stress distributions on the Microcantilever with (a) no bending, and (b) the tip bent by 30 µm. Strain values used for calculations were obtained from the simulated stress values and the Young's Modulus of GaN.

density, which was obtained for a particular gate bias by integrating the C-V characteristic. The capacitance was measured between the gate schottky contact and the source using an LCR meter (Model# HP4284A). Clearly, to maximize $\Delta n_s/n_s$, and hence $\Delta R_{DS}/R_{DS}$ ($R_{DS}$ is the channel resistance), which ultimately governs the gauge factor (GF), appropriate choice of $V_g$ is very important.

The static deflection experiments were performed by controllably bending the free end of the microcantilever using a tungsten needle with a tip diameter of 12 µm. The needle was attached to a nanopositioner bought from Physic Instrument (Model# P-611 Z, PI Inc.) and controlled using Labview (experimental setup is shown in previous chapter). A dual channel source measure unit (SMU) from Keithley (Model# 2612 A) was used to bias the HFET, and measure both the source-drain current and resistance. For device 1, under an

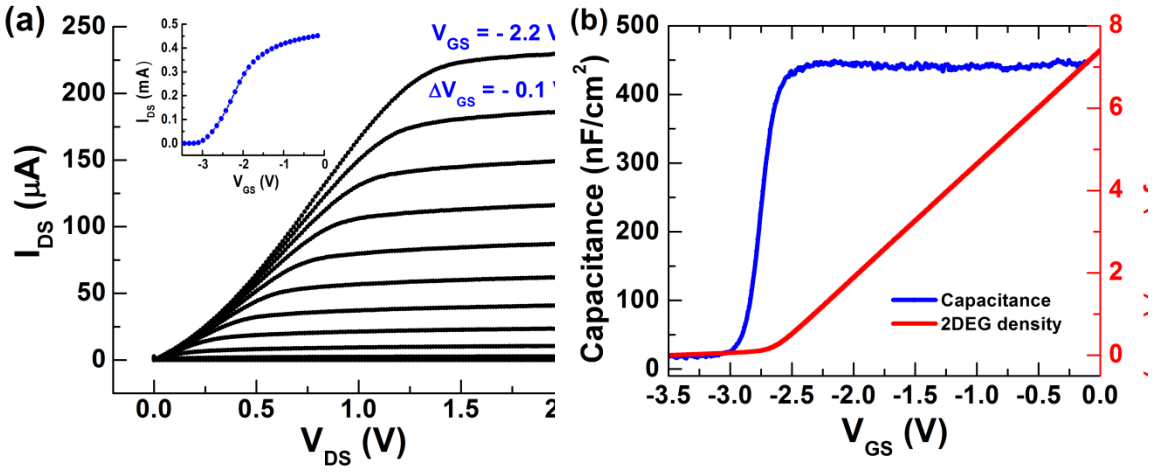


**Figure 6.3** (a) Typical I-V characteristics of the AlGaN/GaN HFET deflection transducer for microcantilever 1. Inset shows the threshold voltage of -3.1 V for the device. (b) C-V profile of HFET transducer which was processed to obtain the 2DEG density variation with gate bias.

applied gate bias of - 3.0 V (close to the threshold voltage of - 3.1 V) and a drain bias of 30 mV, the drain-source resistance ($R_{DS}$) of the HFET channel reduced by 39.3%, when the tip of microcantilever was bent 1 μm downward, and recovered back to its original magnitude when the needle was fully retracted (see Fig. 6.4 (a)). This behavior is expected since a tensile stress (downward bending) serves to attract additional electrons and increase the 2DEG density, while a compressive stress (upward bending) depletes it. For device 2, a similar 1 μm bending of the cantilever yielded 33% change in $R_{DS}$ (Fig. 6.4 (b)) when $V_{GS}$ = - 3.0 V and $V_{DS}$ = 30 mV. Both devices showed very good repeatability for step bending responses, as shown for device 2 in Fig. 6.4 (b). Gauge factor, GF, which is a very important metric for deflection sensitivity, was calculated from the bending results using

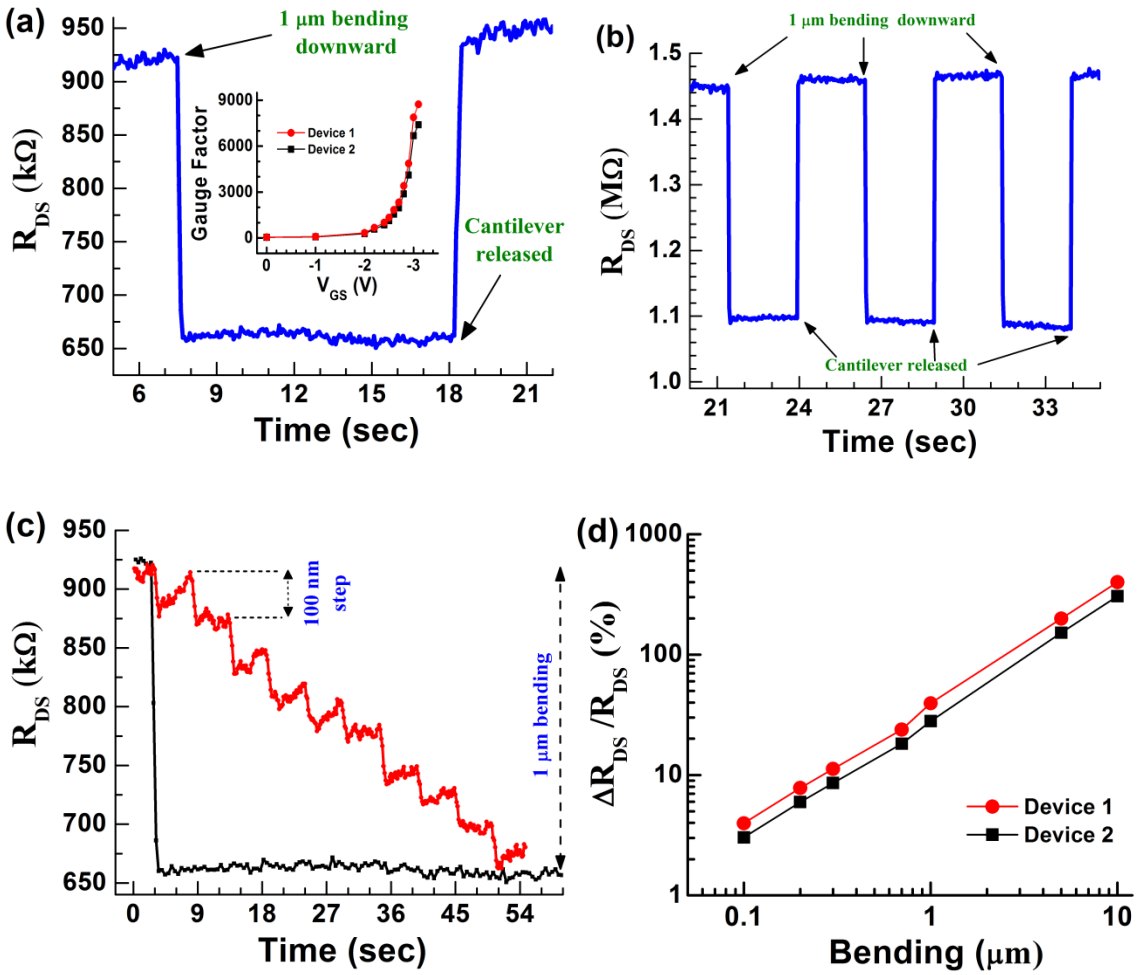


**Figure 6.4** (a) Step bending response for HFET 1 under applied biases $V_{DS}$ = 30 mV and $V_{GS}$ = -3.0 V, when the tip of the cantilever was bent 1 μm by the nanopositioner. Inset shows gate bias dependence of the gauge factor for both the HFET devices. (b) Multiple step bending responses of device 2 for 1 μm tip bending ($V_{DS}$ = 30 mV and $V_{GS}$ = -3.0 V), showing measurement repeatability. (c) Response to cantilever bending in 10 steps of 100 nm each, showing fairly repeatable and overall linear response demonstrating nanometer level deflection transduction with high sensitivity. (d) Plot of sensitivity ($\Delta R_{DS}/R_{DS}$) versus microcantilever tip bending in the range 100 nm to 10 μm shows a linear for both devices. $V_{DS}$ = 30 mV and $V_{GS}$ = -3.0 V was maintained throughout the measurements.

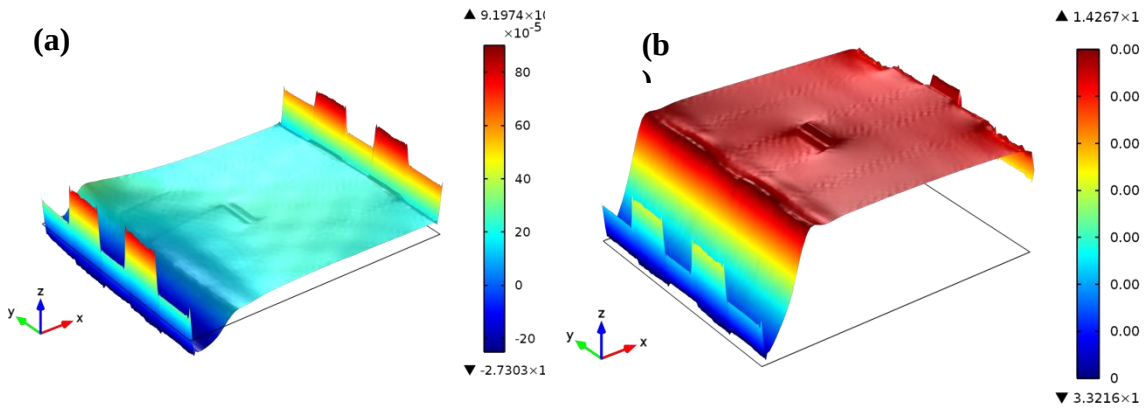


**Figure 6.5** Finite element simulations of stress distribution over the AlGaN mesa region which contains the HFET with (a) no bending and (b) the tip bent by 30 µm. Corresponding strain values were obtained from the simulations, where 30 µm bending yielded an average strain (along XY plane of the mesa) of $1.3431 \times 10^{-3}$.

the relation $GF = (\Delta R_{DS}/R_{DS})/\varepsilon_{av}$, where $\Delta R_{DS}$ is the change in $R_{DS}$ due to bending, and $\varepsilon_{av}$ is the strain in the HFET channel averaged over its width. The average strain ($\varepsilon_{av}$) was determined from finite element simulation using COMSOL software (see Fig. 6.5), which yielded $\varepsilon_{av} = 4.477\times10^{-5}$ for 1 µm bending of the free end of the microcantilever. The calculated GF for the device 1 and 2 were 8700 and 7300, respectively, for $V_{GS}$ = - 3.0 V. The former is ~43 and 3 times higher than the best GF values reported for Si piezoresistors (200) and single wall carbon nanotube based strain sensors (2900)[121]. A plot of GF against $V_{GS}$ is shown at the inset of Fig. 6.4 (a), where GF is found to decrease monotonically with the increase in $V_{GS}$, which correspondingly increases $n_s$ (see Fig. 6.3 (b)) and reduces $\Delta n_s/n_s$. Maintaining $V_{GS}$ = -3 V, the cantilevers were deflected by the same magnitude of 1 µm in 100 nm bending steps. A fairly consistent step change in $R_{DS}$ of ~3.8% per step (~500 Ω/nm) was observed for device 1 (see Fig. 6.4 (c)) and ~3.2% per step (~410 Ω/nm) for device 2. Good linearity in response over a larger dynamic bending range, from 100 nm

to 10 μm, was also observed for both devices as shown in the Fig. 6.4 (d). The dc power consumption ($P_{DC}$) calculated for both devices using the relation$P_{DC} = V_{DS}^2/R_{DS}$, were found to be 0.97 and 0.62 nW, with $V_{DS}$ = 30 mV and $R_{DS}$ = 924 kΩ and 1.45 MΩ, respectively.

### 6.1.2 Detection of Picoscale thermal vibrations of microcantilevers

To investigate if externally excited microcantilever oscillations (i.e. using a piezo chip) could be transduced efficiently by the embedded HFET with very high sensitivity, a commercially available miniature piezo actuator (5 × 5 × 2 $mm^3$) bought from PI (Model# PL 055.31) was placed in firm contact of the top surface of the DIP chip carrier (see Fig. 6.6 (a)), and vibrated by applying a variable frequency sinusoidal ac voltage to it from a lock-in amplifier (Model# SR850, Stanford Research Systems). For electronic transduction of the cantilever oscillations, a constant drain-source current (in the range of 1 – 100 μA) was maintained, and an appropriate gate bias was applied using the SMU. The amplitude of the ac voltage generated across the drain and source ($\Delta V_{DS}$) of the HFET due to cantilever oscillations was measured using the lock-in amplifier. For independent verification, simultaneous optical transduction of the cantilever oscillations was carried out using a laser Doppler vibrometer (Model# MSA 500, Polytec Inc.) as shown in Fig. 6.6 (b). The laser spot of the vibrometer was focused on the gold pad at the tip of the cantilever for better reflection, as GaN microcantilever is transparent to the wavelength (635 nm) of the laser beam. Incidentally, this underlines the utility of the piezotransistive transduction

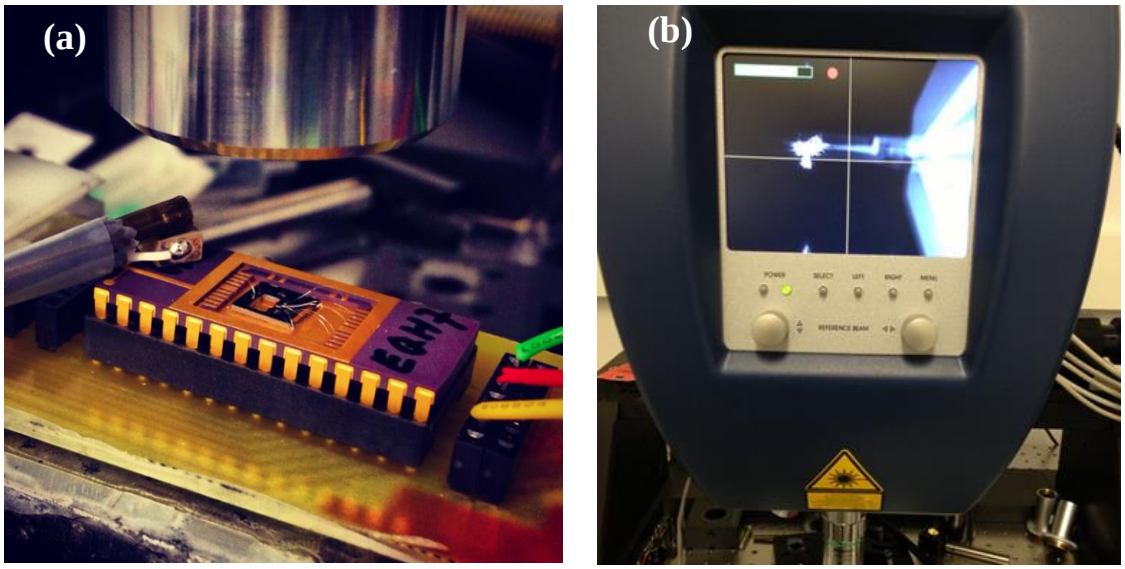


**Figure 6.6** (a) Experimental setup for simultaneous optical and electrical transduction of microcantilever deflections. A piezochip was held in contact with a DIP package, as seen in (a), to generate surface wave to oscillate the microcantilever. The electrical deflection transduction was performed by the HFET, with its signals read out by external instruments using a PCB. For optical deflection transduction, the whole package was placed under the lens of a laser vibrometer (Model# MSA500) which measured the oscillation amplitude. (b) The screen of the laser vibrometer shows the laser spot focused at the tip of the Microcantilever.

compared to the optical one, which suffers from issues like material transparency and limited or diffused reflection. Since $\Delta V_{DS} = I_{DS} \times \Delta R_{DS}$, to increase $\Delta V_{DS}$ (and correspondingly increase the sensitivity) $I_{DS}$ and/or $\Delta R_{DS}$ need to increase. While $I_{DS}$ is set by the user, $\Delta R_{DS}$ depends on the magnitude of the strain induced by the oscillation amplitude of the microcantilever and is proportional to $1/(n_s)^2$. Thus a more negative $V_{GS}$ would result in lower $n_s$ and a higher $\Delta V_{DS}$. However, following Fig. 6.3 (a), the $I_{DS}$ should be chosen carefully to operate the HFET in the linear region, since in saturation, uncontrollable voltage drop across the HFET channel may occur (since $I_{DS}$ is maintained constant, and the device characteristic shifts due to change in $n_s$ due to bending), which would make the device perform unreliably and may even damage it. On the other hand,

increasing the $V_{GS}$ allows us to choose higher $I_{DS}$ to amplify the signal proportionally. The upper limit of the $I_{DS}$ is set by the power consumption and undesirable heating of the HFET, which can also lead to increase in Johnson noise. Thus, proper optimization of $I_{DS}$ and $V_{GS}$ must be performed to maximize $\Delta V_{DS}$ and hence the deflection sensitivity. Details of the optimization process is presented in chapter 5. With $V_{GS}$ = -2.2 V and $I_{DS}$ = 100 µA, oscillation of the microcantilever 1 in open air was observed to produce a $\Delta V_{DS}$ = 12.36 µV at the resonance frequency $f_0$ = 43.934 KHz with a quality factor Q = 230 (see Fig. 6.7). Simultaneous optical measurement (using laser vibrometer) of cantilever oscillation showed its amplitude to be 8.7 pm. Different oscillation amplitudes of the cantilever 1, ranging from 8.7 pm to 2.5 nm (caused by ac excitation voltage varying from 10 to 250 mV applied to the piezo-chip), showed a linear of $\Delta V_{DS}$ as can be seen from the inset of Fig. 6.7. For device 2, an oscillation amplitude of 17 pm at its resonance frequency of 46.4 kHz (Q ~350), yielded $\Delta V_{DS}$ = 23 µV as shown in Fig. 6.8. For both the cantilevers, $f_0$ and Q determined from the electrical and the optical spectra match closely, indicating the reliability of the electrically transduced signal. The dc power consumptions ($P_{DC}$) calculated for the devices (using $P_{DC} = I_{DS}^2 \times R_{DS}$) were 51 and 56 µW, respectively, with $I_{DS}$ = 100 µA and $R_{DS}$ from the characteristics curve in Fig. 6.3 (a).

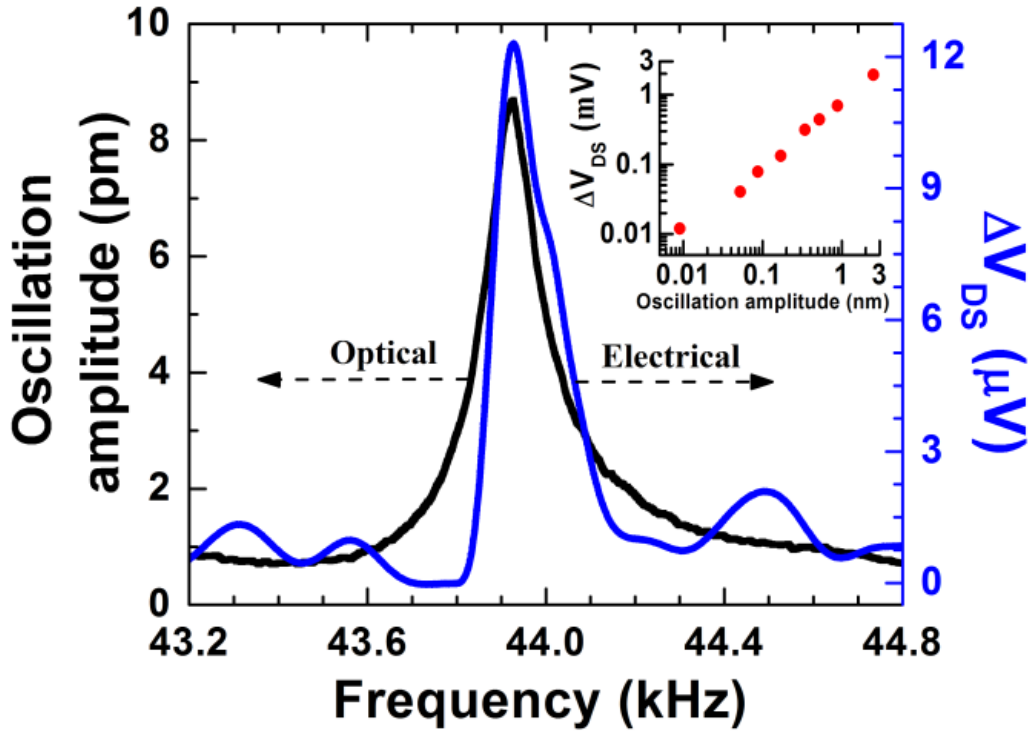


**Figure 6.7** (a) Microcantilever 1 resonance curve simultaneously measured by both electrical and optical transduction methods show a resonant frequency of 43.934 kHz. An oscillation amplitude of 8.7 pm (from laser vibrometer) for the cantilever 1 corresponds to $\Delta V_{DS}$ = 12.36 μV (from HFET 1). The ac voltage applied to Piezo oscillator was 10 mV (rms). Inset shows a linear response of the HFET for oscillation amplitudes varying over the range 8.7 pm to 3 nm by gradual increase in the excitation voltage to the Piezo from 10 to 250 mV. For the measurements, a constant bias current $I_{DS}$ = 100 μA, and gate voltage $V_{GS}$ = - 2.2 V were used.

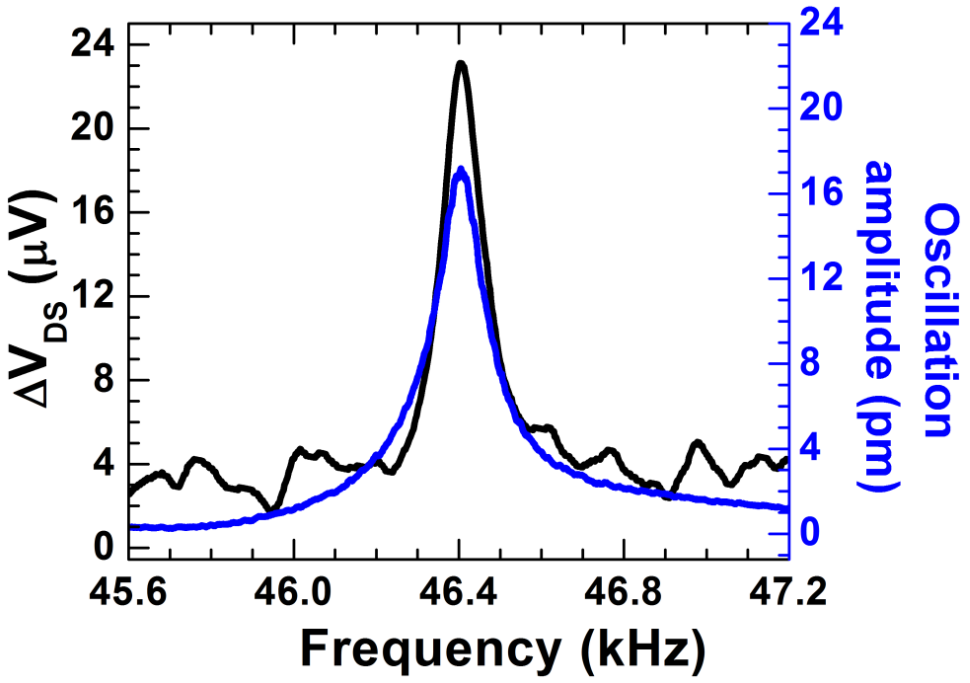


**Figure 6.8** Frequency response of the Microcantilever 2 obtained simultaneously using electrical and optical deflection transduction methods. A resonance frequency of 46.4 kHz with a Q ~350 is obtained from both measurements. An oscillation amplitude of 17 pm at the resonance frequency of the cantilever corresponds to $\Delta V_{DS}$ = 23 μV.

The ability to electrically transduce the thermal noise spectra of a microcantilever is an important benchmark for deflection sensitivity. Due to very high deflection sensitivity of the III-Nitride piezotransistive microcantilevers, they could be used to electrically transduce their own thermal oscillations for the first time, which so far has only been possible through optical transduction method. To measure the thermal noise spectra, a constant $V_{DS}$ of 0.5 V was applied to the HFET, and the change in $I_{DS}$ was amplified using a low-noise current preamplifier (Model# SR570) whose output was connected to a dynamic signal analyzer (Model# SR785, Stanford research Systems). The sensitivity of the preamplifier was set at 1 mA/V and the recorded data was averaged 3 times. The thermal oscillation spectra obtained electrically from the HFET, and optically from the

laser vibrometer (for comparison), are shown together in Fig. 6.9. The peak voltage magnitude of 4.07 μV corresponds to a peak amplitude of 3.04 pm measured using the laser vibrometer. The $f_0$ observed from the electrically transduced resonance curve differs by ~34 Hz when compared with the optically transduced one, unlike in Fig. 6.7, where they match closely. This can be explained by a change in cantilever surface conditions caused by a change in environment and time lapse, since the measurements involving electrical transduction of the thermal oscillations were performed in our laboratory at the University of South Carolina approximately one month after the optical measurements were performed at the University of Alberta in Canada. The change in surface conditions may also be partially responsible for the difference in quality factor observed between the two resonance curves. On the other hand, the electrical and optical resonance curves under mechanical excitation (shown in Fig. 6.7) were measured simultaneously at the University of Alberta, Canada, and thus match very well.

While considering thermal noise transduction by electrical means at ultrasonic frequency, two noises (Johnson and Thermomechanical noises) are important. The Johnson noise and thermo-mechanical noise for a cantilever are given by[123]

Johnson noise (V): $S_E^{1/2} = \sqrt{4\mathrm{k_B}\mathrm{TR_{DS}}\Delta f}$ (6.1)

Thermo-mechanical noise at resonance: $S_{TM,on}^{1/2} = \sqrt{4k_BTQ\Delta f/(2\pi f_0 K)}$ (6.2)

Thermo-mechanical noise off resonance (nm): $S_{TM,off}^{1/2} = \sqrt{4k_BTQ\Delta f/(2\pi f_0 QK)}$ (6.3)

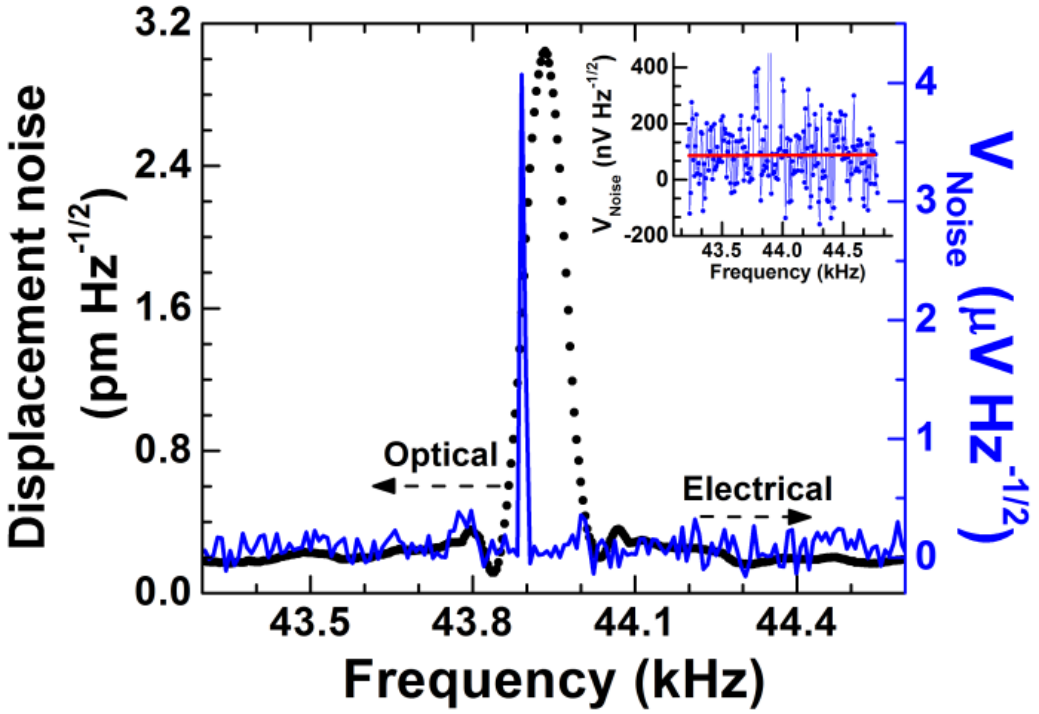


**Figure 6.9** Noise spectra of microcantilever 1 exhibits a displacement noise of 3.04 pm $Hz^{-1/2}$ (from laser vibrometer, black line) which corresponds to 4.07 μV $Hz^{-1/2}$ noise measured by HFET 1 (blue line). Inset shows a plot of the off-resonance voltage noise due to thermal oscillation of the microcantilever 1, with the averaged noise level marked by the red line. HFET 1 was biased at $V_{DS}$ = 0.5 V and $V_{GS}$ = - 2.2 V.

For $V_{GS}$ = - 2.2 V and $V_{DS}$ = 0.5 V, $R_{DS}$ was found from Fig. 6.3 (a) to be 5 kΩ and the Johnson noise using (6.1) , was calculated as 9.12 nV/√Hz for a measurement bandwidth (Δf) of 1 Hz, and using $k_BT$ = 0.026 eV at room temperature. However the voltage noise spectral density (in the inset of Fig. 6.9) was 86 nV/√Hz which actually incorporates other noise sources, such as, current preamplifier, dynamic signal analyzer, cables, etc., in addition to the Johnson noise. On the other hand, for the quality factor, Q = 230, resonant frequency, $f_0$ = 43.934 kHz (from the electrical readout as shown in Fig. 6.7), spring constant, K = 1.71 N/m (estimated from COMSOL), and measurement bandwidth, Δf = 1 Hz, the thermomechanical noise (using (6.2)) was calculated as 2.84 pm/√Hz (on

resonance) and 12.38 fm/√Hz (using (6.3) for off resonance). From Fig. 6.9, the measured voltage noise spectral density on and off resonance are 4.07 μV/√Hz and 86 nV/√Hz, respectively. The Johnson noise most likely incorporates noise from other sources, i.e. from current preamplifier, dynamic signal analyzer, cables, etc. Thus the contribution related to the cantilever's thermomechanical motion was estimated as 4.07 μV/√Hz $\left(= \sqrt{(4.07\ \mu V/\sqrt{Hz})^2 - (86\ nV/\sqrt{Hz})^2}\right)$. As a result the transduction gain or displacement responsivity was calculated as 1.43 nV/fm (4.07 μV $Hz^{-1/2}$/2.84 pm $Hz^{-1/2}$). Moreover the off-resonance noise limited displacement resolution (or minimum detectable displacement (MDD)) was estimated as 60.14 fm/√Hz (86 nV $Hz^{-1/2}$/1.43 nV $fm^{-1}$). Using the responsivity value of 1.43 nV/fm, the calculated voltage was 12.44 μV for the oscillation amplitude of 8.7 pm which excellently matches with the experimental observations as shown in Fig. 6.7. Following similar approach, for device 2, the measured noise limited displacement resolution was found to be 3.42 pm/√Hz (on resonance) and 105.2 fm/√Hz (off resonance including measurement noise) with a displacement responsivity of 1.3 nV/fm.

It is quite significant to note that the displacement responsivities of both devices (1.43 nV/fm and 1.3 nV/fm) are ~30 times higher than that previously demonstrated using a nanocantilever (0.04 nV/fm), while the noise limited resolutions at 1 Hz bandwidth (60.14 fm and 105.2 fm) are very comparable to the nanocantilever (39 fm) and almost 4 orders higher than similar sized microcantilevers (0.5 nm/√Hz)[124] with comparable $f_0$. We would like to point out here that for the first time we have demonstrated femtometer level displacement resolution with complete electrical displacement transduction for a microcantilever operating below 100 KHz. The optically measured resonance amplitude

noise of 3.04 pm/√Hz closely matches with that due to TM noise of 2.84 pm/√Hz, with a difference of only 200 fm/√Hz that is attributable to the noise level of the laser vibrometer as specified by the manufacturer (out of plane displacement resolution of <400 fm/√Hz). The off resonance displacement noise was found to be 200 fm/√Hz (Fig. 6.9) which differs by ~185 fm/√Hz from the theoretical calculation of ~15 fm/√Hz considering only the thermomechanical noise for the laser vibrometer (as Johnson noise should not affect the optical measurements).

The laser vibrometer was also used to measure the other harmonic modes of oscillation of microcantilever 1 as it can be operable at higher frequency. However due to the limitation of lock in amplifier (operable up to 100 kHz) and also the absence of high frequency power supply, the electrical readout of higher modes were not observed. Nevertheless the laser vibrometer can measure the oscillations of several points in a meshed area on the microcantilever. Although GaN is supposed to be transparent to that laser, still there would be slight reflection which would be good enough for the vibrometer to detect the oscillations and map the style of vibration of the microcantilevers. In Fig. 6.10, the different modes of the microcantilever's oscillation are shown. A special rotating XYZ positioner (from Thor labs) was used to make the tip of microcantilever parallel to the setup table so that the reflected light can be focused on the in lens detector. From the frequencies, it is evident that, this microcantilever did not follow the theoretical harmonics, which should be at multiple integers. This is usual with any microcantilever. The vibrational mode was also unusual due to large overhang which made the cantilever a coupled system with individual modes of oscillation. It is to be noted that these modes oscillation is completely experimental, no simulations were applied here.

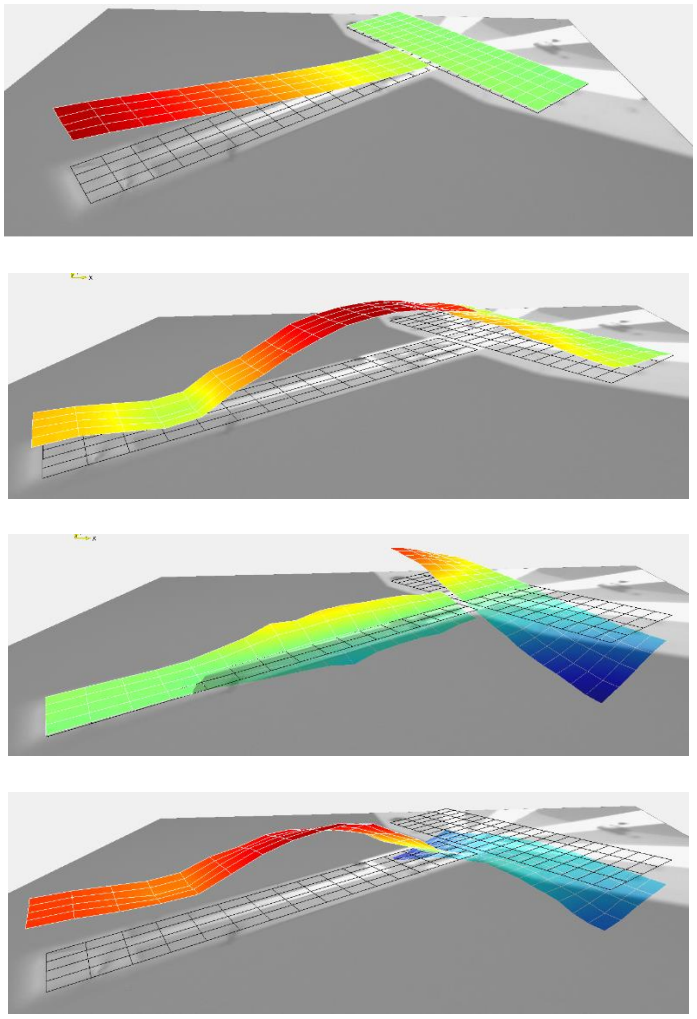

(a) First mode

$f_0$ = 43.93 kHz

(b) 2nd mode

$f_1$ = 202 kHz

(c) 3rd mode

$f_2$ = 284 kHz

(d) First mode

$f_3$ = 364 kHz

**Figure 6.10** Different modes of oscillation of the microcantilever 1.

### 6.1.3 Transduction of Femtoscale surface acoustic wave by microcantilevers

The amplitude of the mechanical vibrations (i.e. the driving amplitude of the acoustic wave $A_d$) acting on the microcantilever can be determined from the oscillation amplitude of the cantilever, $A_0$ as, $A_d = A_0/Q$. For device 1, the wave amplitude can be estimated as 37.8 fm [= 8.7 pm/230, refer to Fig. 6.7] while the thermomechanical noise

limited driving amplitude was determined as 12.35 fm/√Hz (= 2.84 pm/√Hz /230). For device 2, the wave amplitude was estimated as 48.57 fm (refer to Fig. 6.8) and the noise limited driving amplitude was found to be 9.77 fm/√Hz. In our experiment, the piezo excitation was varied to generate different driving amplitude levels over a range of 37.8 fm – 10 pm, and both the devices showed linear response over this large range as shown in Fig. 6.11. The displacement sensitivities (for detecting the driving acoustic wave) of device 1 and 2 were calculated from the slope of the linear responses in Fig. 6.11, as 170 nV/fm and 60 nV/fm, respectively. The off resonance noises (which includes Johnson noise and equipment noise) were measured as 86 nV/√Hz and 136.76 nV/√Hz for device 1 and 2, respectively, and the corresponding noise limited displacement resolutions were found as 0.51 fm/√Hz (86 nV $Hz^{-1/2}$/170 nV $fm^{-1}$) and 2.3 fm/√Hz (136.76 nV $Hz^{-1/2}$/60 nV $fm^{-1}$). The vertical dashed lines in Fig. 6.11 shows the noise limits for surface wave detection. From the above discussion, it is quite clear that the devices are capable of measuring surface wave amplitudes in the tens of fm range, which is better than the optical transduction technique[28, 29]. The measured wave amplitudes for device 1 was slightly lower (by ~22.1%) as the excitation source was located farther compared to that to device 2 [see Fig. 6.1 (b)].

To verify that the cantilever excitation amplitude is really in the femtoscale, the vibration amplitude of the top surface of the piezo-chip was measured using the laser vibrometer for various excitation voltages applied to the piezo (10 – 250 mV), and the results are shown in Fig. 6.12. For the lowest oscillation amplitude of the piezo-chip of

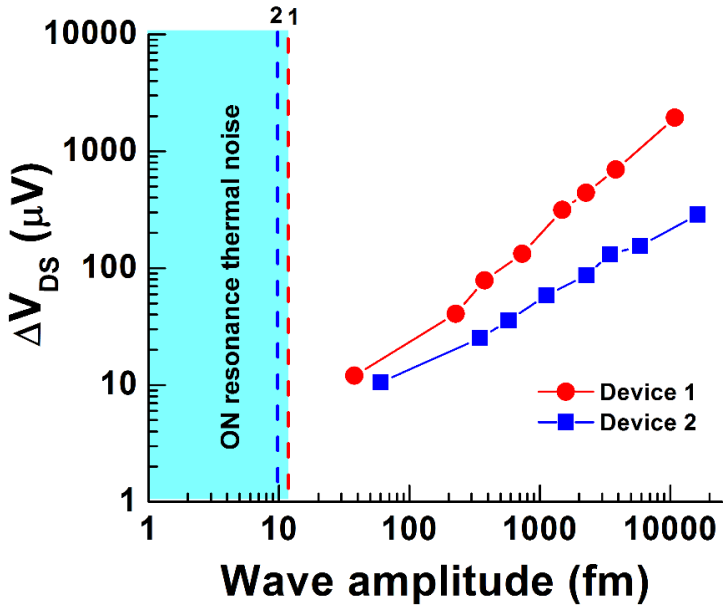


**Figure 6.11** Electrical responses of HFETs 1 and 2 corresponding to microcantilever oscillation amplitude variation caused by variation in external acoustic excitation (over a range of 37.8 fm to 10 pm) produced by the piezochip. The dashed lines parallel to the y-axis represent the on-resonance thermomechanical noise limited excitation amplitudes of 12.35 and 9.77 fm/$\sqrt{\text{Hz}}$, respectively. The responsivity (sensitivity) of the devices in transducing surface wave to electrical voltage can be estimated from the slope of linear response as 170 nV/fm and 60 nV/fm, for device 1 and 2, respectively.

400 fm, the microcantilever oscillation amplitude was found to be 8.7 pm (and $\Delta V_{DS}$ = 12.36 μV), which would result from a surface wave excitation amplitude of 37.8 fm (= 8.7 pm/230). More than tenfold reduction in the exciting wave amplitude compared to the piezo vibration can be caused by attenuation, damping introduced at the bottom surface of

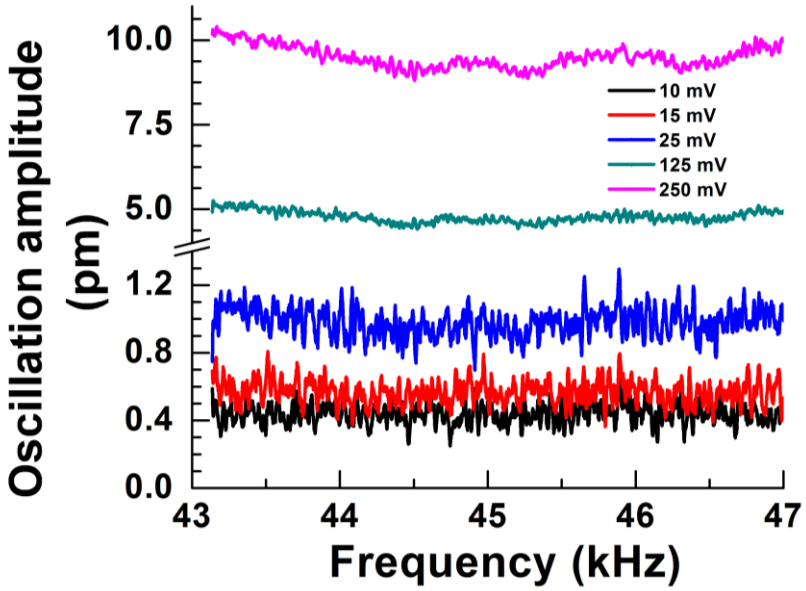


**Figure 6.12** Oscillation amplitude of the top surface (free end) of the piezochip measured using using laser vibrometer. The excitation voltage applied to the piezochip was varied from 10 to 250 mV, while the frequency was swept from 43 kHz to 47 kHz for each applied voltage. The piezochip had a flat frequency response in this frequency range, which ensures that a constant amplitude of the surface wave is generated (which excites microcantilever oscillations). Notably, the bottom plane (fixed to the surface) of the piezochip is expected to have much lower amplitude of vibration. Thus 10 mV is expected to produce an oscillation much less than 400 fm produced by the free surface. This indicates that the amplitude of exciting oscillation near the base of the microcantilever would be in the tens of fm range, as obtained from our measurements on the microcantilever.

the piezo-chip due to solid contact to the ceramic, and acoustic impedance mismatch of different media as encountered by the propagating wave.

To further investigate the femtoscale displacement transduction by the HFET, we conducted a separate set of experiments in high vacuum (10 μTorr), where we used photoacoustic excitation of the microcantilever 1 using a near infra-red (IR) pulsed laser (wavelength of 790 nm, WorldStar Technologies, Inc.). The energy of the laser pulse is absorbed by the Si substrate (since GaN is transparent to 790 nm), and the photothermal effect generates an acoustic wave which propagates through Si substrate and reaches the

cantilever to cause the oscillations. With the laser focused on a ~50 μm diameter spot (marked as position 1 in Fig. 6.13 (a)], the HFET yielded $\Delta V_{DS}$ = 61 μV, while the cantilever oscillation amplitude was found to be 60 pm [see Fig. 6.13 (b)]. The amplitude of the periodic excitation (due to the acoustic wave) can then be calculated as 260 fm assuming the same quality factor of 230. Keeping the laser focused on the same spot, the pressure was reduced to 10 μTorr, which caused the Q-factor to increase significantly to 11,000, which greatly enhanced the oscillation of the microcantilever to 3 nm as shown in Fig. 6.13 (c). Once again, a very good match is observed between the electrical and optical response curves, with the electrical signal $\Delta V_{DS}$ = 3.6 mV corresponding to 3 nm amplitude measured by the vibrometer. The amplitude of the surface wave was estimated as 272 fm (= 3 nm/11000) which is close to that estimated under ambient conditions, clearly indicating that high vacuum does not affect the acoustic wave propagation, as expected. When the laser was focused on an epoxy layer in the DIP cavity [shown as position 2 in Fig. 6.13 (a)] the microcantilever oscillation amplitude decreased significantly to 60 pm, which indicates that the exciting wave amplitude was 5.45 fm (= 60 pm/11,000). The electrical signal corresponding to the amplitude was measured as $\Delta V_{DS}$ = 71.9 μV as shown in Fig. 6.13 (d), which yields a responsivity of ~1.2 μV/pm (for transducing surface

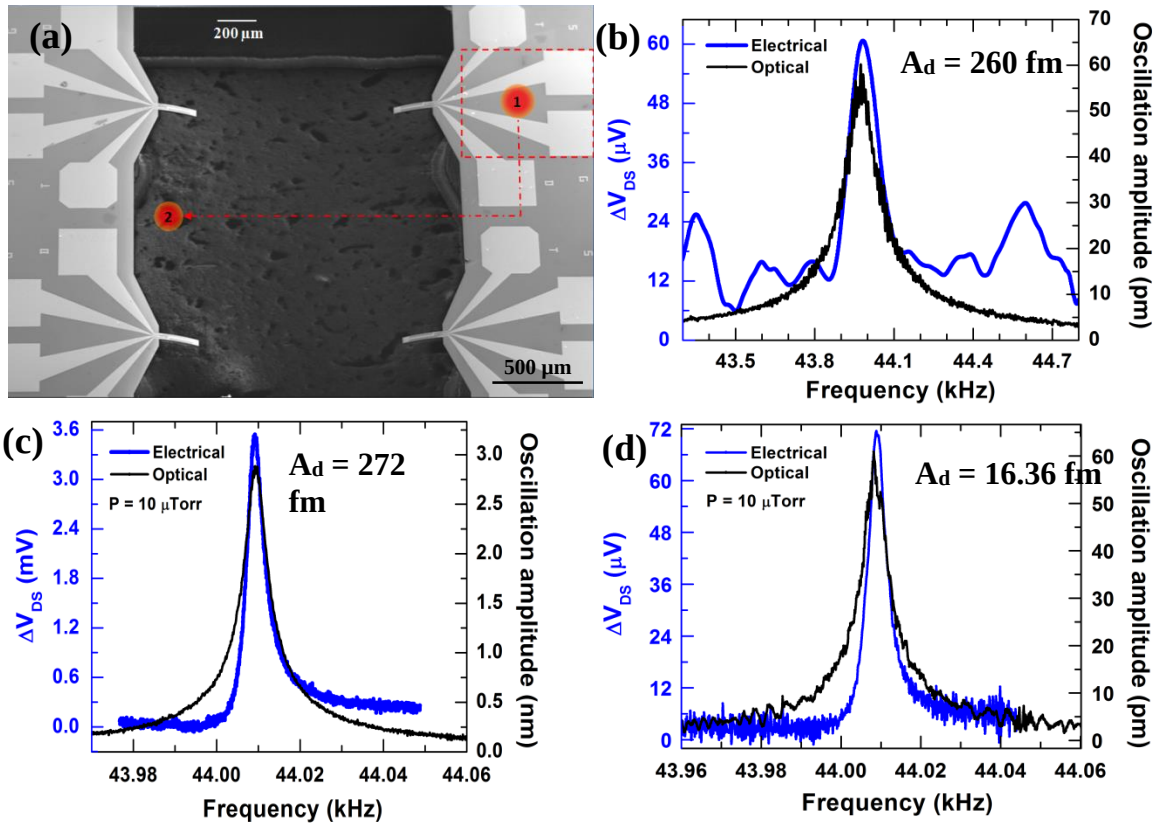


**Figure 6.13** (a) SEM image showing the positions of the laser spot (~50 µm diameter) used for photoacoustic excitation. The laser (wavelength of 790 nm) was pulsed with a variable frequency (43 kHz – 45 kHz) sinusoidal signal. (b) Frequency response of HFET 1 transduced both optically and electrically when the laser spot was focused at position 1 (measurement conducted in air). The driving amplitude ($A_d$) of the surface wave was determined to be 260 fm (oscillation amplitude, $A_0$ = 60 pm divided by the quality factor (≈ 230) of microcantilever 1). (c) Frequency response of HFET 1 when the laser spot was at position 1 in 10 µTorr pressure with $A_d$ of 272 fm. (d) Frequency response of HFET 1 when the laser spot was at position 2 at 10 µTorr, which yielded $A_d$ = 16.36 fm, and corresponding $\Delta V_{DS}$ = 71.9 µV. The HFET was biased at $V_{DS}$ = 0.5 V and $V_{GS}$ = - 2.2 V as before.

acoustic wave). At position 2, the laser power was absorbed almost completely by the epoxy used to glue the Si substrate to the bottom (Au coated) DIP. The acoustic wave generated by the epoxy is very weak but due to the high quality factor of 11,000 of the GaN microcantilever in vacuum faint acoustic wave of 5.45 fm amplitude was possible to transduce with a high voltage responsivity of 12.96 µV/fm. But no cantilever oscillation

was observed in atmospheric pressure when the laser was focused at the same spot, although similar exciting wave amplitude of 5.45 fm as in high vacuum, is expected (see above discussions). This is because, in atmospheric pressure the quality factor of the cantilever is much reduced (230), which results in the microcantilever oscillation amplitude of 1.25 pm that is smaller than the thermomechanical noise of the cantilever of 2.84 pm/$\sqrt{\text{Hz}}$ at nominal 1 Hz frequency. Therefore, only thermal oscillations of the cantilever could be observed in air with the laser focused on position 2. In vacuum, the calculated thermomechanical noise of the microcantilever increased to 19.67 pm/$\sqrt{\text{Hz}}$ (calculated using Q = 11,000, $f_0$ = 44,010 Hz, and $\Delta f$ = 1 Hz, which matches well with 19.95 pm/$\sqrt{\text{Hz}}$ observed from the optical measurement. This noise is, however, much smaller than the oscillation amplitude of the cantilever of 3 nm, which can thus be easily transduced both optically and electrically. Interestingly, the high quality factor in vacuum yields an ultralow displacement noise floor of 1.79 fm/$\sqrt{\text{Hz}}$ (= 19.95 pm/$\sqrt{\text{Hz}}$ /11,000), which puts the lower limit for detection of the exciting acoustic wave at 1.79 fm, for a bandwidth of 1 Hz. Such extremely low detection limit can open up novel opportunities for surface wave based photoacoustic analysis and detection using compact microscale sensors. The static and dynamic performances of both devices are summarized in Table 6.1.

**Table 6.1** Summary of static and dynamic bending performances of device 1 and device 2

| Device | | | 1 | 2 |
|---|---|---|---|---|
| Static Performance | Gauge Factor | | *8700* | *7300* |
| | Power consumption (nW) | | *0.97* | *0.62* |
| Dynamic Performance | Resonant Frequency (kHz) | | *43.934* | *46.4* |
| | Quality Factor | | *230* | *350* |
| | For cantilever oscillation | MDD On resonance (pm/√Hz) | *2.84* | *3.42* |
| | | MDD Off resonance (fm/√Hz) | *60.14* | *105.2* |
| | | Responsivity (nV/fm) | *1.43* | *1.3* |
| | For surface wave excitation | MDD On resonance (fm/√Hz) | *12.35* | *9.77* |
| | | MDD Off resonance (fm/√Hz) | *0.51* | *2.3* |
| | | Responsivity (nV/fm) | *170* | *60* |

### 6.1.4 Comparisons of displacement sensitivities with state-of-the-art

To put the performance of our microcantilever in perspective, we have compared the sensitivity and power consumption piezoresistive deflection sensor technologies. While the best reported GF for Si piezoresistors, the traditional workhorse for strain sensing, has been ~200, nanoscale piezoresistors of Si[141], CNT[121], ZnO[142] and $ZnSnO_3$[143] have yielded high GFs > 1000. Recently, graphene (film[144] and suspended[145]) and diamond[146] based piezoresistors have been introduced, although their reported GFs are comparatively low (< 300). Till date, one of the highest GFs has been demonstrated by $LaSrCoO_3$ of ~7000[147], although it has shown to have a strong non-linearity in response. In addition, the aforementioned piezoresistors often require controlled ambient to operate (high vacuum and/or low temperature), and can suffer from repeatability and consistency (especially those based on nanoscale materials). Our proposed piezotransistive microcantilever based sensor has demonstrated, to the best of our knowledge, the highest GF till date of 8700 (in open ambient) considering all material systems, while consuming a very low power of 0.97 nW. The GF and power consumption of various technologies are compared in Fig. 6.14 (a), which shows a general trend of increasing GF with reduction in power consumption.

Although the transducers mentioned above show very high GF, but their frequency response have not been reported using non-optical transduction methods. Piezoelectric (AlN)[148] and semiconductor/metal[123] nanocantilevers, and single electron transistor based doubly clamped nanoscale beams made of GaAs[125] and SiN[149] have shown great responses with minimum detectable displacement (MDD) below 300 fm/$\sqrt{}$Hz (in atmospheric ambient). Recently, suspended graphene[150] and CNT[151] based NEMS has demonstrated a low value of MDD (35.8 fm/$\sqrt{}$Hz and 6.25 pm/$\sqrt{}$Hz respectively), but only under high

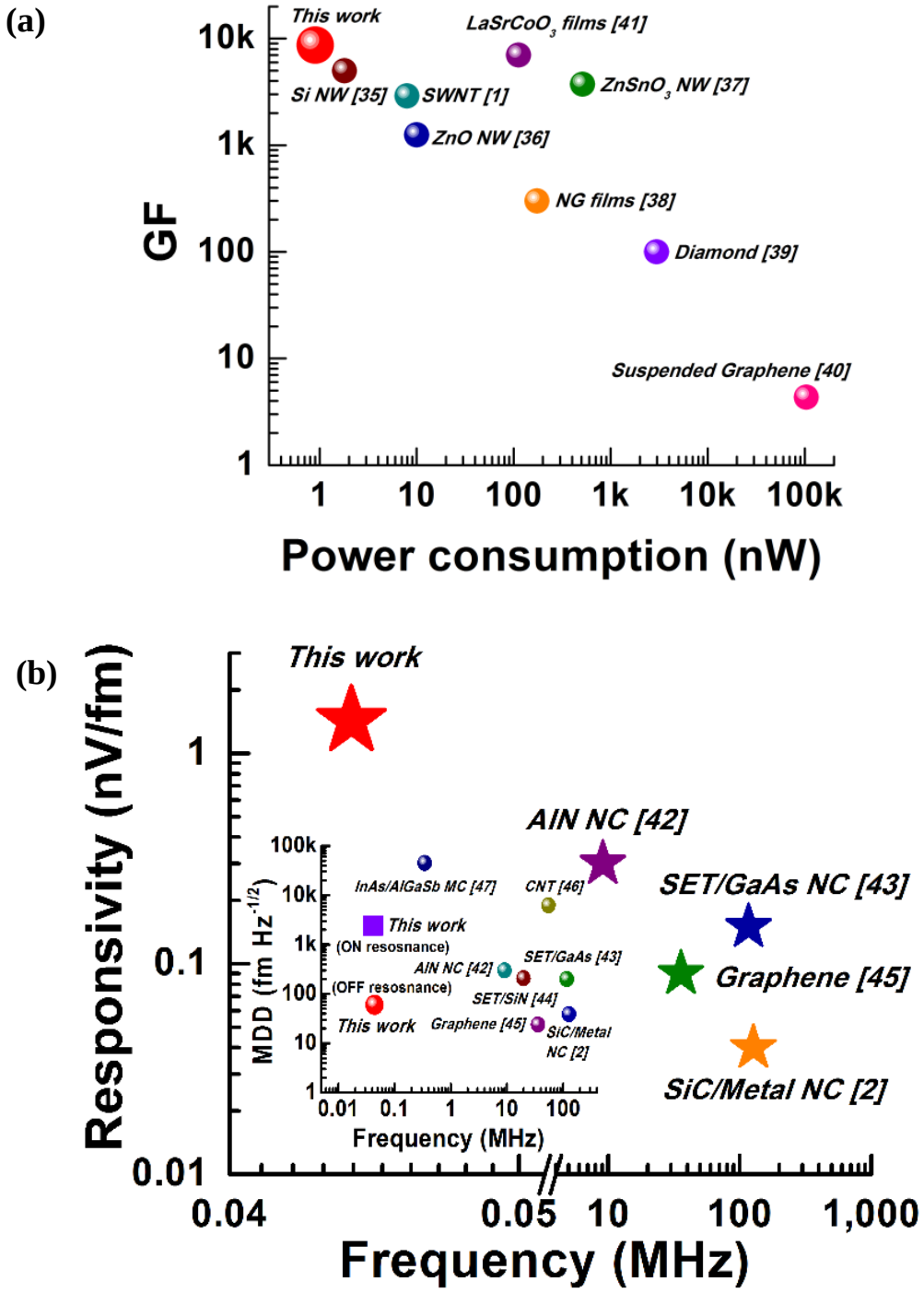


**Figure 6.14** (a) Best reported gauge factors (GF) for different device technologies plotted against device power consumption. The highest GF (8700) among all technologies reported so far is demonstrated by the piezotransistive microcantilever presented in this work, which also consumes the lowest power of 0.97 nW. (b) Plot of best reported Responsivities (in transducing mechanical oscillation of suspended structures) against frequency also demonstrates the outstanding performance (VR = 1.43 nV/fm) of our device, which clearly

fills a technology void of highly sensitive ac excitation detection in <100 kHz range. Inset shows the comparable performance with reported nano structures showing an impressive minimum detectable displacement (MDD) of 2.84 pm/√Hz at resonance, which goes down to a value of 60.14 fm/√Hz off-resonance (refer to text for accurate references).

vacuum with significant enhancement in their low quality factor. On the other hand, though our microcantilevers have picometer level thermomechanical oscillations (2.84 pm/√Hz and 3.42 pm/√Hz), but for the first time we have successfully demonstrated that femtoscale actuation amplitude can be detected in open ambient with the lowest MDD of 12.35 fm/√Hz which improves to 1.79 fm/√Hz in vacuum. Fig. 6.14 (b) and its inset compares the responsivity and MDD (inset of Fig. 6.14 (b)) of various deflection sensors as a function of frequency. Although the current piezotransistive sensor follows the general trend of responsitivity and MDD as the other technologies, it clearly fills a gap in technology delivering much superior performance at its frequency range of operation.

## 6.2 Acoustic transducer

### 6.2.1 Piezotransistive microcantilever

In this subsection, we present for the first time, transduction of ultrasonic acoustic pressure using a piezotransistive AlGaN/GaN HFET integrated on GaN microcantilever. With a periodic pressure generated in air, the microcantilever was found to oscillate, and the HFET was able to transduce the pressure variation of 150.4 μPa in ambient conditions with a tunable linear sensitivity of 33.2 mV/Pa, response time < 40 ms, and power consumption of 45 μW. The device demonstrates 3 orders higher pressure sensitivity than simple piezoresistor, and also higher than the sensitivity of commercially available Knowles microphone; thereby offering a promising alternative for cantilever enhanced

photoacoustic spectroscopy (PAS). Photoacoustic mechanism is being widely used in recent years for chemical sensing and biomedical imaging. Although the selectivity is dependent on the wavelength of the light, the ultimate sensitivity of this technique is obtained from the acoustic transducer. However the sensitivity is primarily limited by the usage of bulky condenser microphone, which suffers from low sensitivity and high power consumption. Recently Si microcantilevers have been shown as a promising alternative. However, due to low sensitivity of Si piezoresistive cantilever they are only used to transduce the pressure into displacement change, while an interferometric technique is used to measure the displacement. However, the interferometric detection hinders the possibility of miniaturization and low power consumption. Here, we propose a novel GaN microcantilever based acoustic transducer with embedded AlGaN/GaN HFET as the pressure sensor. The density of the two-dimensional electron gas (2DEG) formed at the AlGaN/GaN interface gets strongly affected by the deflection induced strain enabling high pressure sensitivity. These AlGaN/GaN HFET embedded GaN microcantilevers (Fig. as described earlier. Our latest design involves optimal biasing conditions for the HFET deflection transducer, which converts piezoelectric polarization into piezoresistance change, to tune the sensitivity and transduce ultra-low pressure.

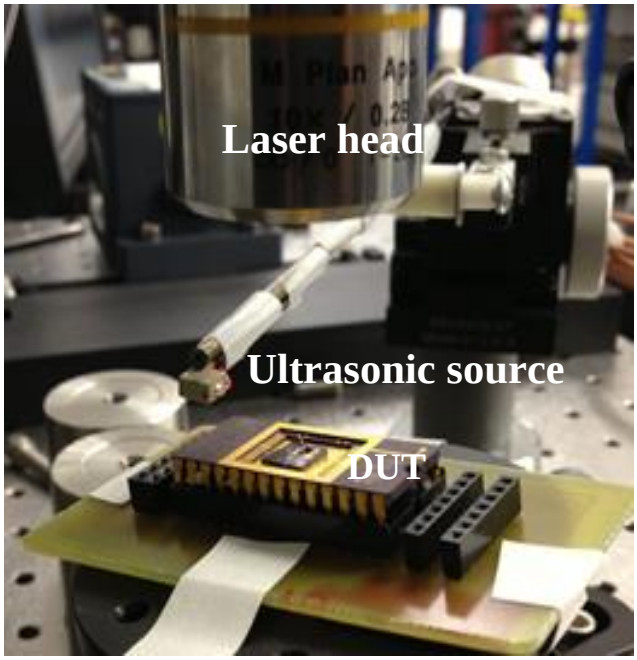


**Figure 6.15** Experimental setup showing the packaged device mounted on a printed circuit board. A piezochip, attached to a micropositioner, was used to generate ultrasound (40 KHz - 50 KHz) by exciting with sinusoidal voltage (10 mV - 100 mV). A laser vibrometer was used to measure the displacement.

Fig. 6.15 shows the experimental setup where a commercially bought piezochip was used to generate vibration in air in the ultrasonic frequency range (40-50 KHz), which can oscillate the microcantilever. The displacement of the microcantilever was recorded using a laser vibrometer (MSA-500, Polytec Inc), while the deflection induced change in the drain-source voltage ($\Delta V_{DS}$) of the HFET was simultaneously measured with a lock-in amplifier (SR850). Utilizing the transistor characteristics, applying a gate bias, $V_{GS}$ = - 2.6 V and constant current, $I_{DS}$ = 10 μA, $\Delta V_{DS}$ was found to be 44 μV (rms) when the cantilever

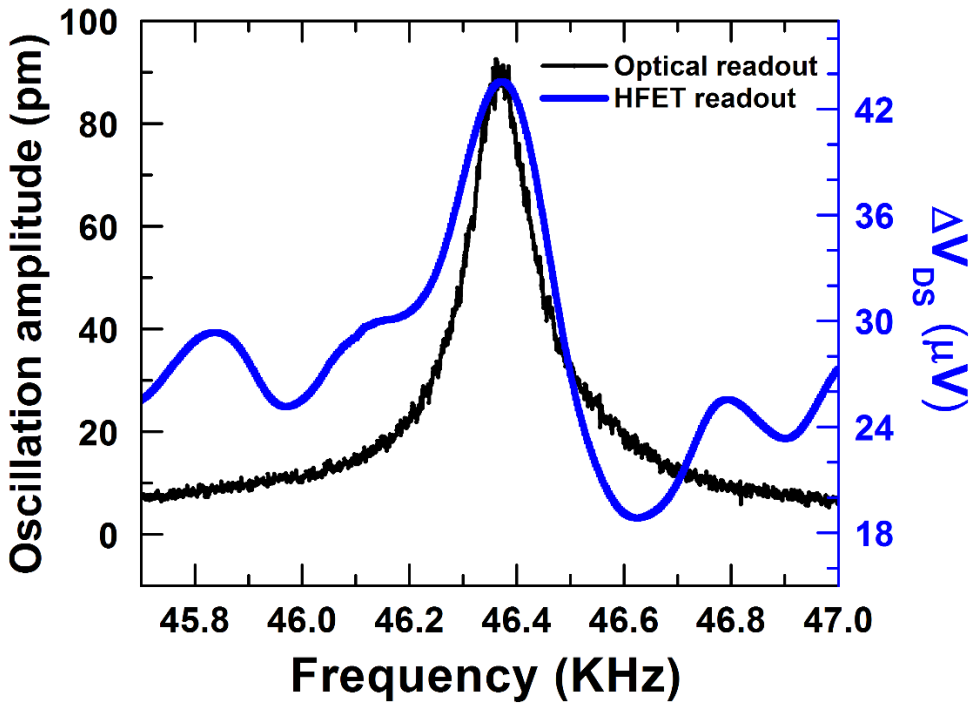


**Figure 6.16** Simultaneous optical and HFET readouts when the piezo was excited with frequency swept sinusoidal of 10 mV (rms) from 8 mm distance. HFET bias: $V_{GS}$ = - 2.6 V and constant $I_{DS}$ = 10 µA.

was oscillating with 90 pm amplitude at the resonant frequency of 46.37 KHz with a quality factor of 300 in air (see Fig. 6.16). The acoustic pressure generated by the piezochip ($P_{ex}$) was estimated (see chapter 4) as 10.8 mPa and the pressure exerted on the cantilever (placed at 8 mm distance from the piezo) was calculated to be 3.8 mPa. Figure 6.17 shows the response of the device and the corresponding pressure exerted on the cantilever for different pressure levels ($P_{ex}$) generated by the piezo-chip. The device showed excellent linear response (Fig. 6.18) with a sensitivity of 9.5 mV/Pa. Moreover, with optimized

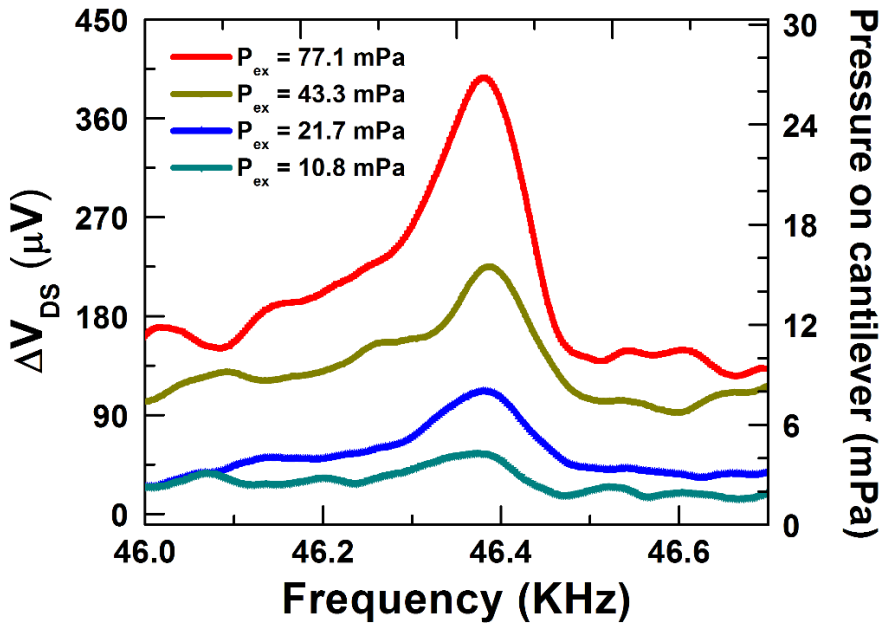


**Figure 6.17** The excitation sinusoidal voltage to the piezo was varied to generate 10.8 mPa - 77.1 mPa acoustic pressures. The displacement of the bottom surface of the piezo was measured optically and then converted into pressure. The corresponding pressures exerted on the cantilever and the respective readouts from the HFET are shown. HFET bias: $V_{GS}$ = - 2.6 V and constant $I_{DS}$ = 10 μA.

biasing conditions, i.e. $V_{GS}$ = - 2.3 V and $I_{DS}$ = 100 μA, much higher sensitivity of 33.2 mV/Pa (3 orders higher than simple piezoresistor[7, 8]) was obtained with a very low power consumption of 45 μW. A separate experiment conducting the noise performance of the device yielded thermomechanical noise limited resolution of 150.4 μPa/√Hz (at resonance) with a Johnson noise of 2 μPa/√Hz. To measure the static pressure variation, the

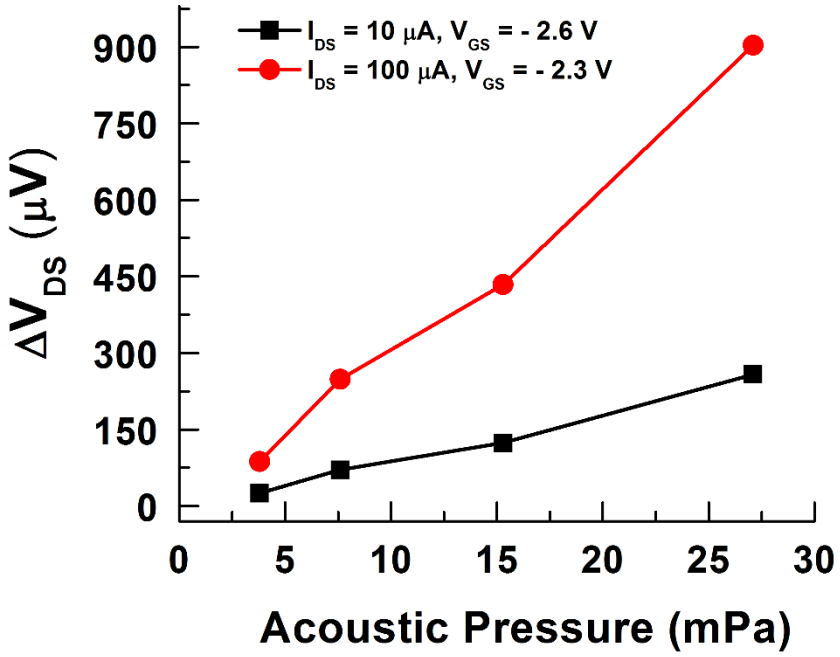


**Figure 6.18** Pressure sensitivity of the HFET with different biasing conditions. The optimized bias of the HFET, with $V_{GS}$ = - 2.3 V and $I_{DS}$ = 100 μA, resulted in the maximum sensitivity of 33.2 mV/Pa consuming only 45 μW.

microcantilever was placed in vacuum (750 μPa) and excited using photoacoustic technique with pulsed laser, while the vacuum pressure was varied. The HFET yielded $\Delta V_{DS}$ = 1.1 mV, corresponding to a pressure change of 50 μPa. The device was later compared with a commercially available microphone (Knowles, FG-23629) with the distance between the piezo-chip and the sensor varied systematically. The simultaneous responses from both devices exhibit superior sensitivity and repeatability of the AlGaN/GaN HFET (Fig. 6.19) as an acoustic transducer, with a response time less than 40

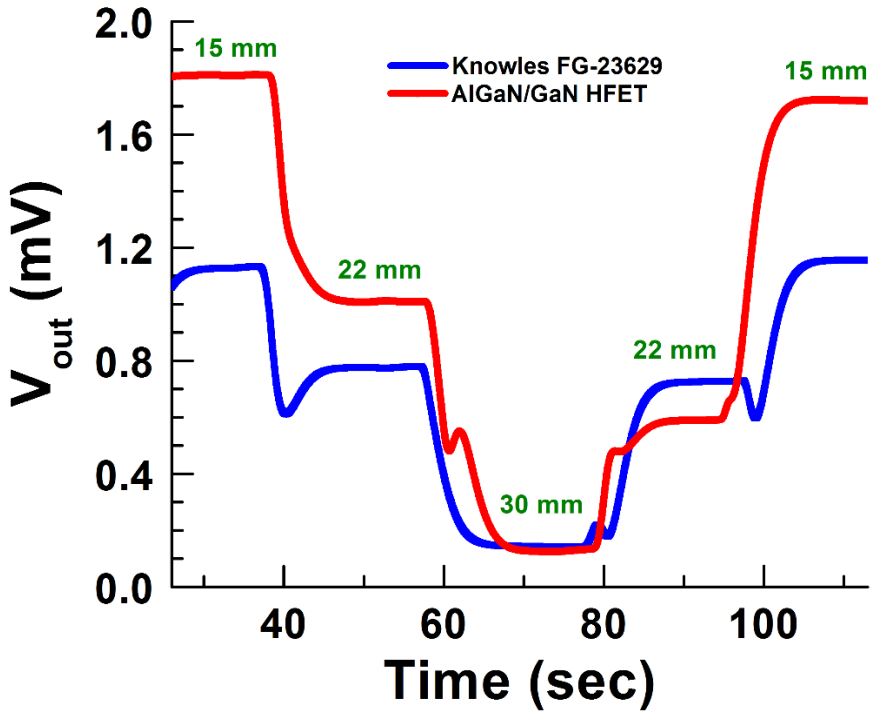


**Figure 6.19** Performance comparison between the HFET and a commercial microphone (Knowles FG-23629) with varying the distance between the piezo-chip and the detectors. The piezo was excited with sinusoidal voltage of 0.5 V (rms) at a fixed frequency of 46.37 KHz, which was exerting a periodic pressure of 308.4 mPa. The distance based sensitivity of the AlGaN/GaN HFET (114.3 µV/mm) is found to be twice than that of the microphone (57.14 µV/mm). HFET bias: $V_{GS}$ = - 2.3 V and constant $I_{DS}$ = 100 µA.

ms, and a sensitivity of 114.3 µV/mm, which is twice than that of the Knowles microphone (57.1 µV/mm). Moreover, our devices are almost 150 times smaller than the microphone.

The results presented here demonstrate the unprecedented performance of AlGaN/GaN HFET embedded GaN microcantilever as an acoustic transducer, which can be a superior alternative in cantilever enhanced photoacoustic spectroscopy offering higher sensitivity, low power consumption, and miniaturization.

### 6.2.2 Piezoresistive diaphragm like microresonator

Diaphragm (or disc) like pressure sensors are widely used everywhere (e.g. microphones). As this discs are closely packed around its edge, there is no way for acoustic pressures to escape as oppose to microcantilevers where the surroundings are open. To utilize this feature, GaN diaphragms (or disc resonators) were fabricated as described in chapter 3. Like microcantilevers, these discs have both piezoresistive and piezotransistive versions. However only the piezoresistive ones were tested and in this subsection, only those results are presented.

The tested microdiscs are shown in Fig. 6.20 (a) where two different sizes of discs can be seen. Fig. 6.20 (b) shows the zoomed image where it can be found that, the mesa was not annular. If the mesa was made annular around the edge then the strain on the 2DEG would be more prominent. In the latest devices, this design criteria was maintained. To test the larger disc, a wire bonded device was placed in a vacuum chamber and the pressure was varied. The typical linear I-V characteristics are shown in Fig. 6.21 (a). The bottom surface (Si) on the sample was glued and sealed on the IC chip to ensure the pocket is in atmospheric pressure. If there is even a small leak, the pressure sensitivity would become very negligible. By keeping the package in such, the vacuum valve in the chamber can have a full control to change the pressure difference. When the chamber started to vacuum, 1 atm in the pocket pulled the disc downward and resistance decreased (similarly as mentioned in chapter 4 and 5) as a result the change in resistance was positive as shown in

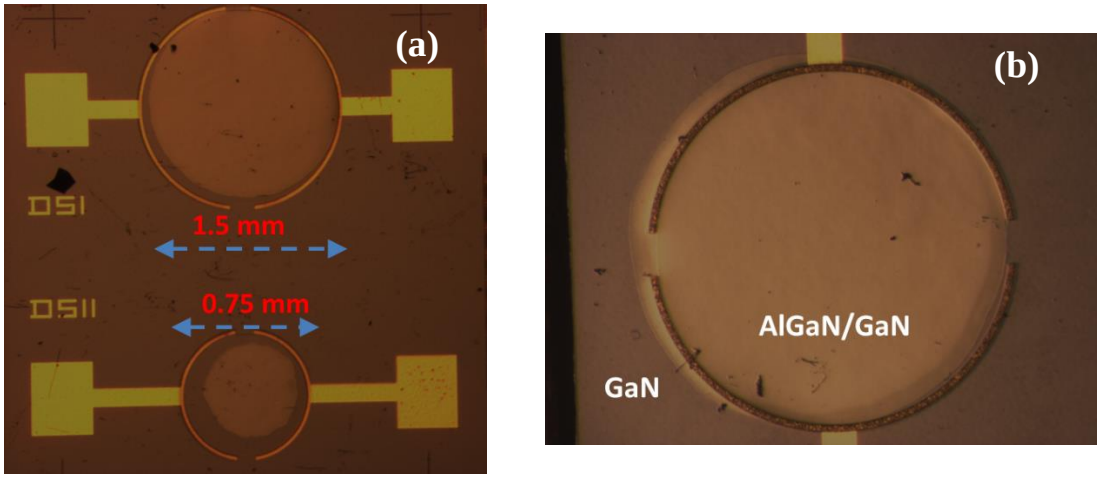


**Figure 6.20** Optical microscope image of (a) AlGaN/GaN micro-disc resonators with 0.75 mm and 1.5 mm diameters, (b) zoomed view of the larger disc showing the materials.

Fig. 6.21 (b). If the pressure change was increased, the change in the channel resistance of the mesa also increased (see Fig. 6.21 (c)). This disc resonator also showed good repeatability in successive cycles of pressure change (see Fig. 6.21 (d)). The response time is very fast in several micro-seconds when the pressure in the chamber dropped below atmospheric pressure (760 Torr). However when the pressure was brought back to atmosphere, the response seemed slow, this was solely due to slower pressure transfer into the chamber from ambient as oppose to abrupt pressure release. The sensitivity was calculated as 0.32% per 280 Torr with a noise limited resolution of 7 Torr pressure change.

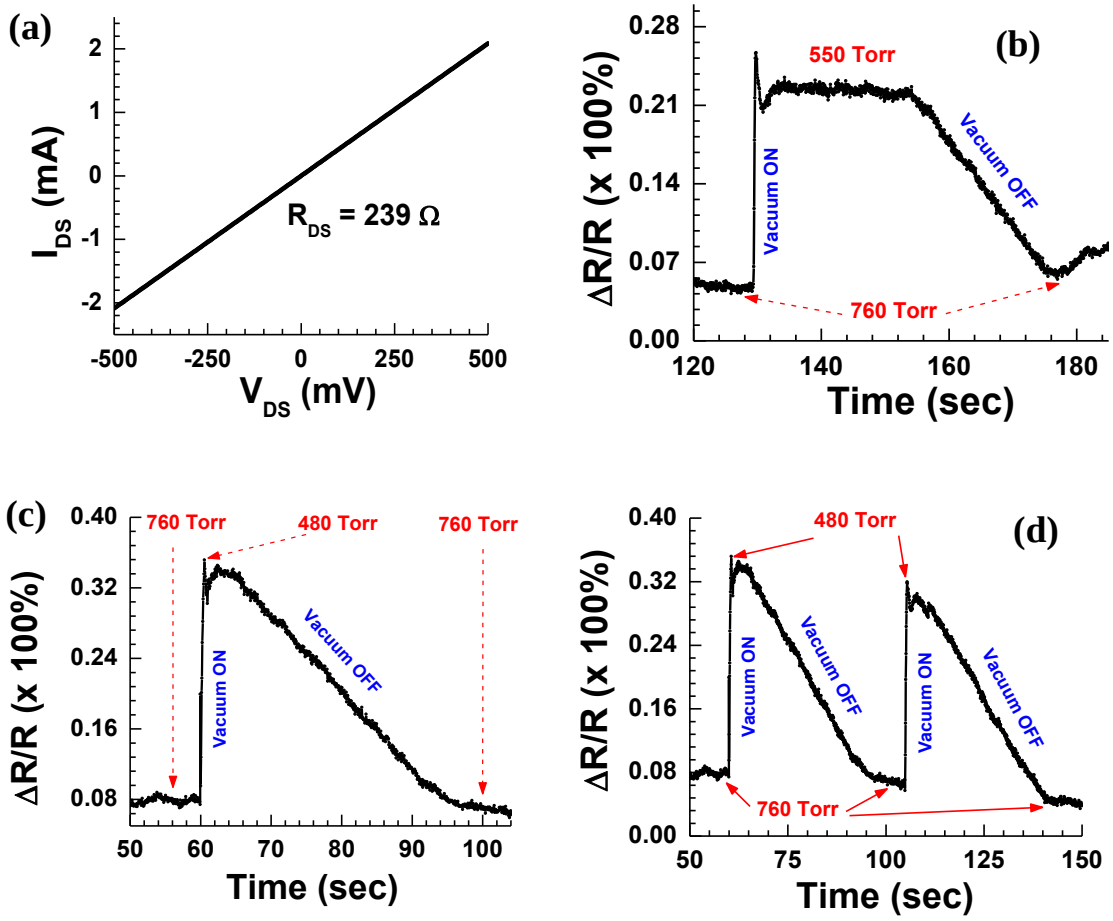


**Figure 6.21** (a) I-V profile of AlGaN/GaN mesa, change in piezoresistance for a pressure change of (b) 210 Torr, (c) 280 Torr, (d) Repeatability in piezoresistive change over several cycles of pressure change of 280 Torr (two cycles are shown).

## 6.3 Performance of microcantilever in harsh environment

The prime reason for using III-V nitrides is that they can operate in harsh environment mostly high temperature, high pressure and radiation. Lot of works had been published on the high temperature performance of AlGaN/GaN HFET. The HFET operates reliably, however the reliability of HFET sensing specially with microcantilevers have not been studied. We tried several times to do such experiment, however the PCB was not possible to design to withstand temperature higher than $120^{O}$ C. But the PCB can be

designed and such experiments can be conducted with cautions. However the radiation effects were studied with the sensors with a collaboration to Savannah River National Lab.

Due to their wide bandgap, III-V Nitride materials are expected to be radiation hard and operate in harsh environment without degradation. To investigate the capability of the microcantilevers for operating in a high radiation environment (i.e. in the event of a nuclear accident), we collaborated with Dr. Ricardo Torres of the Savannah river National Laboratory (SRNL) located in Aiken, SC. We used the Variable Dose Irradiation facility (VDIF) at SRNL to perform systematic testing of our piezotransistive microcantilevers as a function of hours of exposure to Gamma radiation over a 3 month time period. The gamma irradiator (Model 484, J.L. Shepard) has two Co-60 sources (6000 Ci, each) and was calibrated in 2002 using dose-rate vs. distance data. The sensor remained stationary at 8.25 cm from the sources while purged in high purity Ar. The sources are lowered to the test chamber only for the duration of the test, and the sensor was removed shortly after. Fig. 6.22 shows the image of the chamber. The doses were applied in month's interval. Table 6.2 summarizes the dose summary.

To verify the radiation hardness of our rectangular microcantilever sensors, we compared their deflection before and after exposure to a high dose of gamma radiation. No change in HFET resistance was observed before and after 10 MRad dose (see Fig. 6.23 (a)). Fig. 6.23 (b) shows deflection response of the sensor to 5 and 10 μm deflection steps before and after exposure to 10 MRad of radiation (at $7.5 \times 10^4$ Rad/hr for 133 hours) from

**Figure 6.22** Picture of the irradiation testing equipment J. L. Sheperd Model 484 at SRNL facility equipped with $^{60}$Co radiation sources for Gamma Irradiation.

Co-60 sources. Although it is quite a high dose of radiation (for comparison, Si devices tolerate only a few hundred KRads of radiation dose before degrading), we find the resistance as well as the sensitivity of the sensor to be essentially unchanged, which clearly underlines the capability of these device to operate in high radiation environment with high reliability. We would like to note here that gamma radiation was chosen due to its prevalence in an accident situation, unlike neutron flux, which will pretty much go down to zero as the reactor is automatically shut down. In a severe accident, the gamma radiation can rise up to $10^4$ rad/hr. Thus, this test indicates that the device can not only survive at such a high gamma fluence, but survive long enough (several days at least) to provide valuable information after the accident.

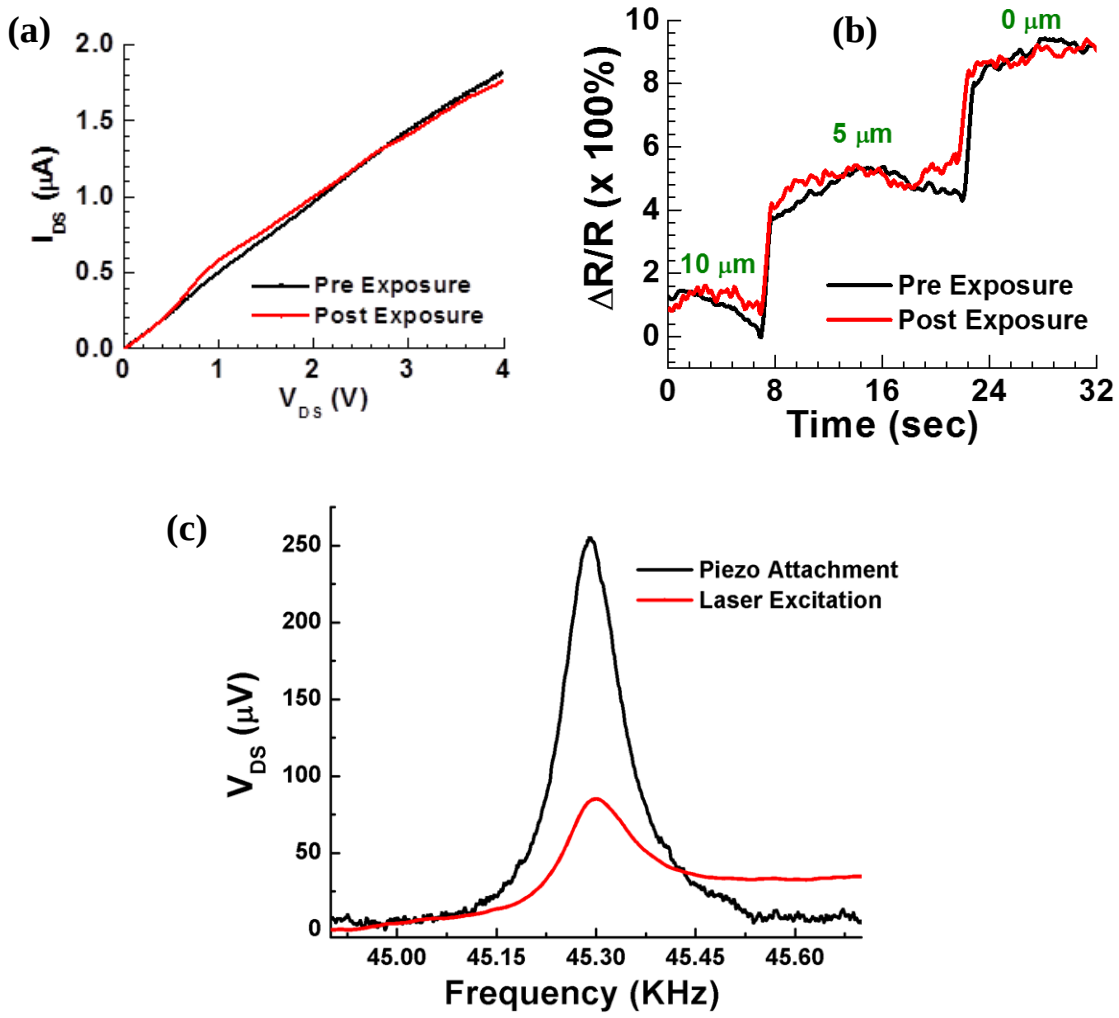


**Figure 6.23** (a) No resistance change was observed after pre and post exposure (10 MRad), (b) Linear response of the AlGaN/GaN HFET deflection transducer, before and after exposure to 10 MRad Gamma radiation dose, (c) Dynamic response of the microcantilever.

The dynamic response of the cantilever was also recorded pre and post exposure with both Piezo and laser excitation method. The resonance curves as shown in Fig. 6.23 (c) proved that the no material degradation occurred as the frequency did not shift from 45.30 kHz, even though the cantilever was very thin (2 μm). The laser based surface wave excitation method strongly depends on the material quality to transduce the wave from bulk Si to GaN

surface. As the HFET presented the frequency response efficiently with high responsivity, the quality of GaN surface remained unchanged. These experiments demonstrated the superior performance of piezotransistive GaN microcantilevers over Si based technology.

**Table 6.2** Details of Co-60 irradiation

| **Model 484 with piezotransistive GaN Microcantilever** | | | | | | |
|---|---|---|---|---|---|---|
| Start Date | Test # | Sensor | Rad/hr | Irradiation Time (min) | Test Dose (Rad) | Cummulative Dose (Rad) |
| 3/18/2013 | 1 | Sensor 1 | 7.69E+04 | 390 | 5.00E+05 | 5.00E+05 |
| 4/16/2013 | 2 | Sensor 1 | 7.61E+04 | 1181 | 1.50E+06 | 2.00E+06 |
| 5/22/2013 | 3 | Sensor 2 | 7.47E+04 | 401 | 4.99E+05 | 4.99E+05 |
| 6/7/2013 | 4 | Sensor 2 | 7.43E+04 | 1206 | 1.49E+06 | 1.99E+06 |
| 8/21/2013 | 5 | Sensor 2 | 7.20E+04 | 1665 | 2.00E+06 | 3.99E+06 |
| 9/12/2013 | 6 | Sensor 2 | 7.17E+04 | 2092 | 2.50E+06 | 6.49E+06 |
| 10/3/2013 | 7 | Sensor 2 | 7.12E+04 | 2940 | 3.49E+06 | 9.98E+06 |

# CHAPTER 7

# PHOTOACOUSTIC SPECTROSCOPY OF CHEMICALS WITH PIEZOTRANSISTIVE MICROCANTILEVERS

Photoacoustic Spectroscopy (PAS) is usually a technique for material characterization. However recent advancement in PAS has broaden the research and development of PAS based sensing and imaging fields. This chapter is dedicated for PAS based chemical sensing. This chapter is divided into three sections, firstly, a brief introduction to the basic principal along with its history, main components of PAS, and review of several applications. Secondly an experimentation of using our sensor in PAS like system. Finally, a novel scheme of PAS system will be proposed with experimental demonstration for detecting nanogram level chemicals.

## 7.1 Photoacoustic Spectroscopy: principal, history and applications

### 7.1.1 Basic principal

The photoacoustic system is based on the excitation of molecules in a sample materials by infrared light. The excitation of molecules depends on the intensity and wavelength of the incoming light along with the absorption spectrum and the absorption area of the molecules.

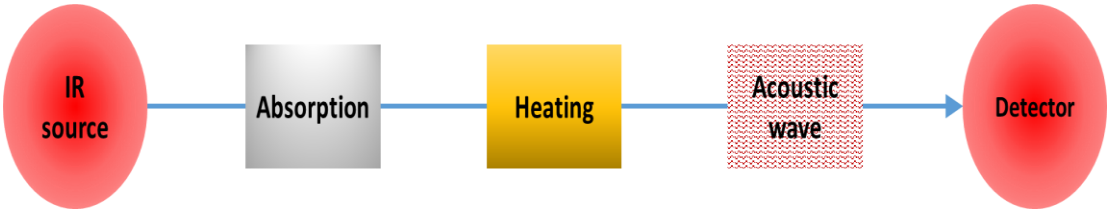


**Figure 7.1** The basic physics behind PAS.

The non-radiative decay of excited molecules as they thermally expand and contract due to generated thermal fluctuations develops pressure variations (see Fig. 7.1[152]). A typical photoacoustic spectroscopy system is shown in Fig. 7.2. An optical source usually a laser source emitting IR radiation, is chopped/pulsed with an electrical or a mechanical modulator and directed to a closed cell containing sample. Absorption of pulsed IR by the sample molecules, expands or contracts the sample as a whole. The modulation frequency of the IR beam defines the frequency of the generated acoustic wave. Sound waves thus created are converted into an electric signal tranduced by an acoustic detector, for example a condenser microphone. The signal can be seen in the spectrum as a peak at a particular signature modulation frequency[152-154].

PAS system offers high sensitivity and selectivity. The selectivity of a PAS system depends mostly on a laser which can be tuned to different wavelengths. Each molecule has unique absorption spectrum, i.e. they absorb radiation only at certain wavelengths. To put it simply, the absorption peaks of different components do not overlap. Thus the selectivity can be achieved simply by tuning the source wavelength and comparing the database of absorption peaks (e.g. Fourier Transform Infrared Spectroscopy, FTIR). However the peaks sometimes overlap and some statistical/mathematical algorithm must be used for

ensured selective detection. The alternative would be to use a differential system, which will benefit to separate different molecules. On the other hand, the sensitivity of the PAS system can be increased by increasing the signal or by decreasing the noise, which is increasing signal to noise ratio. High power IR source, efficient design of PA cell, and

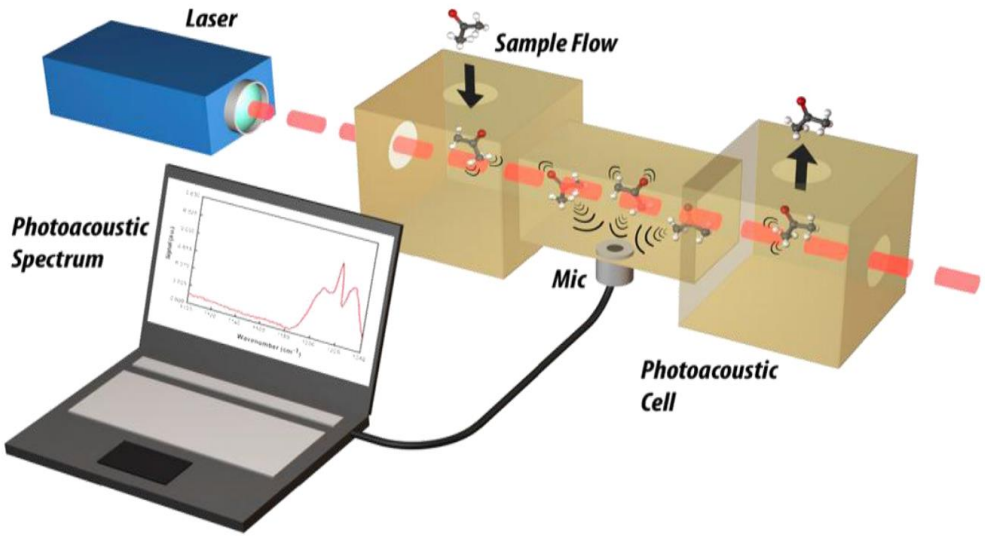


**Figure 7.2** Schematics of simplified PAS system.

using highly sensitive detectors, the sensitivity can be increased. The noise can be decreased by designing PA cell properly[155-159].

### 7.1.2 History of PAS

The photoacoustic effect was discovered by A.G. Bell in 1880. He found that thin discs emitting sound when exposed to a rapidly chopped beam of sunlight (see Fig. 7.3[160]).

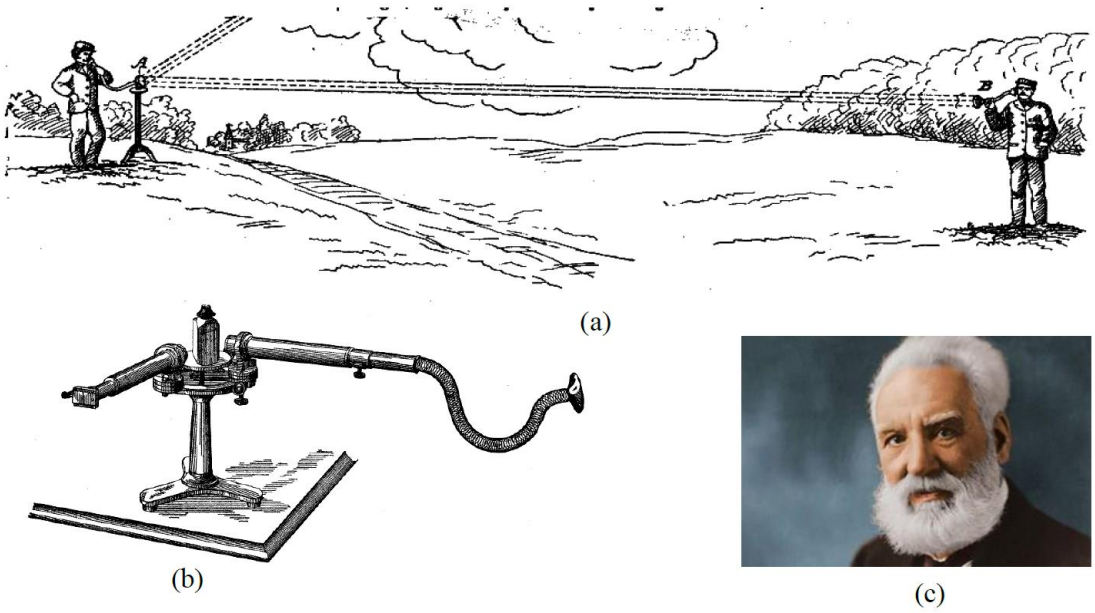


**Figure 7.3** (a) PAS experiment by A. G. Bell (c); (b) Spectrophone proposed by Bell.

By placing different substances in contact with the ear using a hearing tube, he was able to detect the substances and their respective absorptions with both the visible and the invisible regions of the solar spectrum. This work was continued by Tyndall and Rontgen, who performed experiments with solid, liquid and gaseous samples. These works made other researchers delved into the photoacoustic spectroscopy but the experimental method was limited by the absence of high powered light sources and the insensitivity of conventional detectors. However, the first significant improvement in the photoacoustic spectroscopy was in 1938 when Viengerov used a blackbody radiator and an electrostatic microphone to measure gas concentrations. Later Luft continued the development, by discovering differential design using two photoacoustic cells and broadband infrared source offering enhancement in selectivity and sensitivity. The invention of the laser made the long waited

light source available. In 1968, Kerr and Atwood demonstrated a laser illuminated absorption spectrophone. Using then available lock-in amplifiers, they managed to record low photoacoustic signal which enabled them to measure low concentrations of air pollutants. Kreuzer after three years experimented with intensity modulated infrared HeNe-laser to measure ppm level methane in nitrogen using PAS. Even with immense trials by Rontgen and Tyndall with photoacoustic effect in solid materials, gas spectroscopy saw bright light in advancement. Parker in 1970's revived the interests on solid phase PAS. Rosencwaig and Gersho continued his path to explain the theory of photoacoustic in solids. End of the 1970's, the mechanisms behind the photoacoustic effect in solids were well understood[160-162]. It was at this time that the number of applications and publications on PAS increased from a few per year to nearly 600 in 2010.

### 7.1.3 Components of PAS

Photoacoustic spectroscopy is constituted with three main components: chopped light, photoacoustic cell, and acoustic detector. Tunable laser and ceramic blackbody radiator are mostly used as the light source. A modulator is needed, either electrical or mechanical choppers. However mechanical choppers have more noise and cannot operate at high frequency compared to electrical ones. The modulated or pulsed light is then pass through a special cell where the sample gets exposed to light. The design of the photoacoustic cell takes into account sample volume and absorption length. The dimension of the PA cell is limited by the beam size since the absorption of the walls. There can be non-resonant (single pass) or resonant (multipass) cell. Fig. 7.4[162] shows different types of typical PA cells. For the acoustic detector part, mostly condenser microphone is used. The

other options would be piezoelectric sensor. The membrane microphones have limited dynamic range due to their structure and therefore they limit the sensitivity of the photoacoustic system. Ried and White in 1996 fabricated cantilever type microphone. As the technology in micro MEMS (specially cantilever) has advanced, cantilever replaced the traditional microphone in a PAS system. Wilcken and Kauppinen demonstrated impressive sensitivity with cantilever as the microphone with optical readout system.

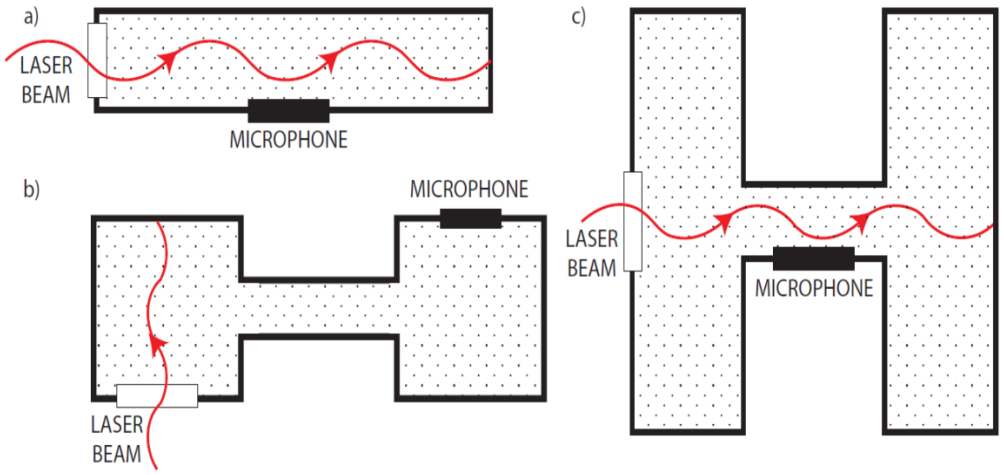


**Figure 7.4** PA cells: (a) A pipe resonator (b) Helmholtz resonator (c) A buffered resonator

### 7.1.4 Applications of PAS

Photoacoustic Spectroscopy has evolved after initial research to product development offering many applications. One of the prime applications is, trace gas detection. PAS can selectively detect a particular gas in a mixture which are released from the power plants and the car exhausts. It also offers nitrogen detection in microbiology and noninvasive breath analysis. Photoacoustic spectroscopy is also used in military and

**Table 7.1** Trace gas detection with PAS

| Chemicals | NIR Laser-PAS | QCL-PAS | QE-PAS |
|---|---|---|---|
| $NH_3$ | 6 ppb (500 mW) | 30 ppb (2 mW) | 6 ppb (20 mW) |
| $C_2H_2$ | 10 ppm (3.5 mW) | | 30 ppb (57 mW) |
| $CO_2$ | 30 ppm (4.5 mW) | | 18 ppm (4.4 mW) |
| $CH_4$ | 27 ppb (18 mW) | | 240 ppb (16 mW) |
| $N_2O$ | | 80 ppb (10 mW) | 7 ppb ( 19 mW) |

homeland security to detect explosive ordnances and chemical warfare agents. PAS has high selectivity, sensitivity, high signal-to-noise ratio (SNR), long-term stability, parts per million (ppm) level of detection, very low false detection, large dynamic range, , identifying mixture of components, and fast response. Additional properties desired include usually portability and a low price. Other than PAS, nonspectroscopic techniques like chemiluminescence and gas chromatography are also used for trace gas detection. However they require extra preparations of samples, and in some cases not feasible to apply in real time. Other optical spectroscopic techniques such as Raman spectroscopy,

**Table 7.2** Glucose detection methods using PAS

| Schemes | Glucose concentration (mg/dl) | Solution | Limitation |
|---|---|---|---|
| QCL/FTIR | 13.8 | Whole blood | Hardly convertible to *in vivo sensing* |
| QCL/FTIR | 9.4 | Aqueous solution | |
| QCL/FTIR | 4 | Aqueous solution | |
| Photothermal radiometry with two QCLs | 0-440 | homogeneous aqueous phantom | sense glucose concentrations at the sample surface and not in deep epidermal layers |
| Pulsed $CO_2$ laser PA detection | 18-450 | Blood and solution | |

fluorescence spectroscopy require an optical detector, and the problems with optical readout has been explained earlier. Table 7.1 gives a comparison of different techinques for detecting trace gas (green labeled shows the lowest concentration). Apart from trace gas detection, PAS has been intensively used to detect glucose in blood non-invasively. No reliable non-invasive glucose monitoring devices are currently available. Researchers in Institute for Quantum Electronics (ETH, Zurich) implemented PAS to track glucose *in vitro*

in deep epidermal layers. Different PAS schemes were utilized to detect glucose concentration as low as 4 mg/dl. Table 7.2 summarizes the different PAS schemes used to detect glucose. Another important application of PAS, which recently attracted researchers in medical imaging is the Photoacoustic Microscopy (PAM). Dr. Wang in Texas A&M reported functional photoacoustic microscopy (fPAM) (Fig. 12), which provides multi-wavelength imaging of optical absorption and permits high resolution imaging. Dr. Wang also used PAS principal for imaging rat's brain using PAM[163-171].

## 7.2 Photoacoustic detection of Acetone in air

Our devices were also used in cantilever enhanced photo acoustic spectroscopy in a very simple setup (shown in Fig. 7.5) to sense different molecules. The simple mechanism of photo-acoustic spectroscopy is demonstrated by continuous expansion and contraction of molecules because of absorption and release of energy of a pulsating light source. Thus the molecules generate acoustic waves of a particular frequency depending on the pulse frequency. This acoustic wave is thus an ultrasonic sound wave if the frequency is above 20 KHz. For this experiment we used a PDMS block (1 cm×1 cm×20 mm) with an Au (100 nm)/Ti (20 nm) coated thin PDMS membrane (200 μm) and a cavity in the middle (see Fig. 7.5 and Fig. 7.6). We found that acetone generates acoustic wave by absorbing light from laser of 790 nm wavelength and Fig. 7.7 shows resonance characteristics generated by acetone. The pulsing frequency is swept from 44.4 KHz to 45.4 KHz and the resonance frequency is found to be 45.03 KHz. The 180° phase shift is due to the distance between the sensing cantilever and the PDMS block. It also shows the resonant and antiresonant behavior of microcantilever which strongly depends on the position of the ultrasonic

source, the wavelength of laser, and the velocity of the wave. For our case the wavelength is estimates as 0.76 cm and the position of the source was at 1.6 cm which is at 1.5 times of the wavelength. The background signal which is due to the PDMS block and the membrane is also plotted in the same figure to show the selective signature of our sensor. In Fig. 7.6 (b) the cross sectional schematic is shown on the inset. Acetone is a self evaporating material, so the voltage across the drain and source of the HFET is supposed to change when the cavity becomes empty of acetone and there will no more acetone to generate the acoustic wave. We found the voltage across the drain and source decreases by 7.13% (in Fig. 7.8) when acetone completely evaporates from the tub of the PDMS block.

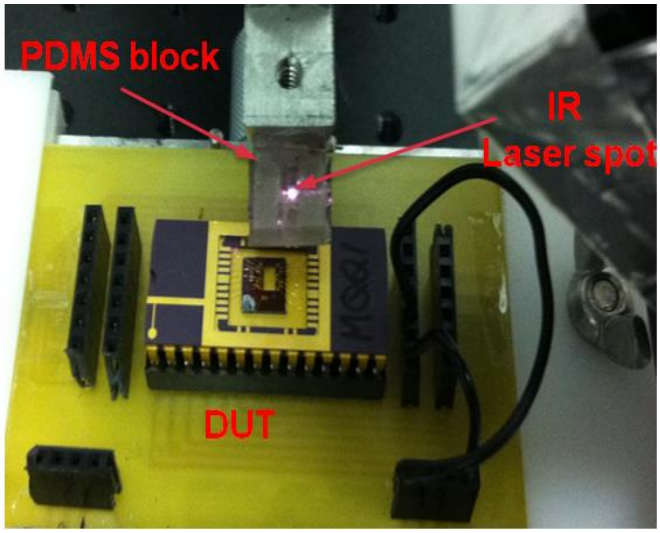


**Figure 7.5** Simple photo Acoustic Spectroscopy setup for sensing Acetone.

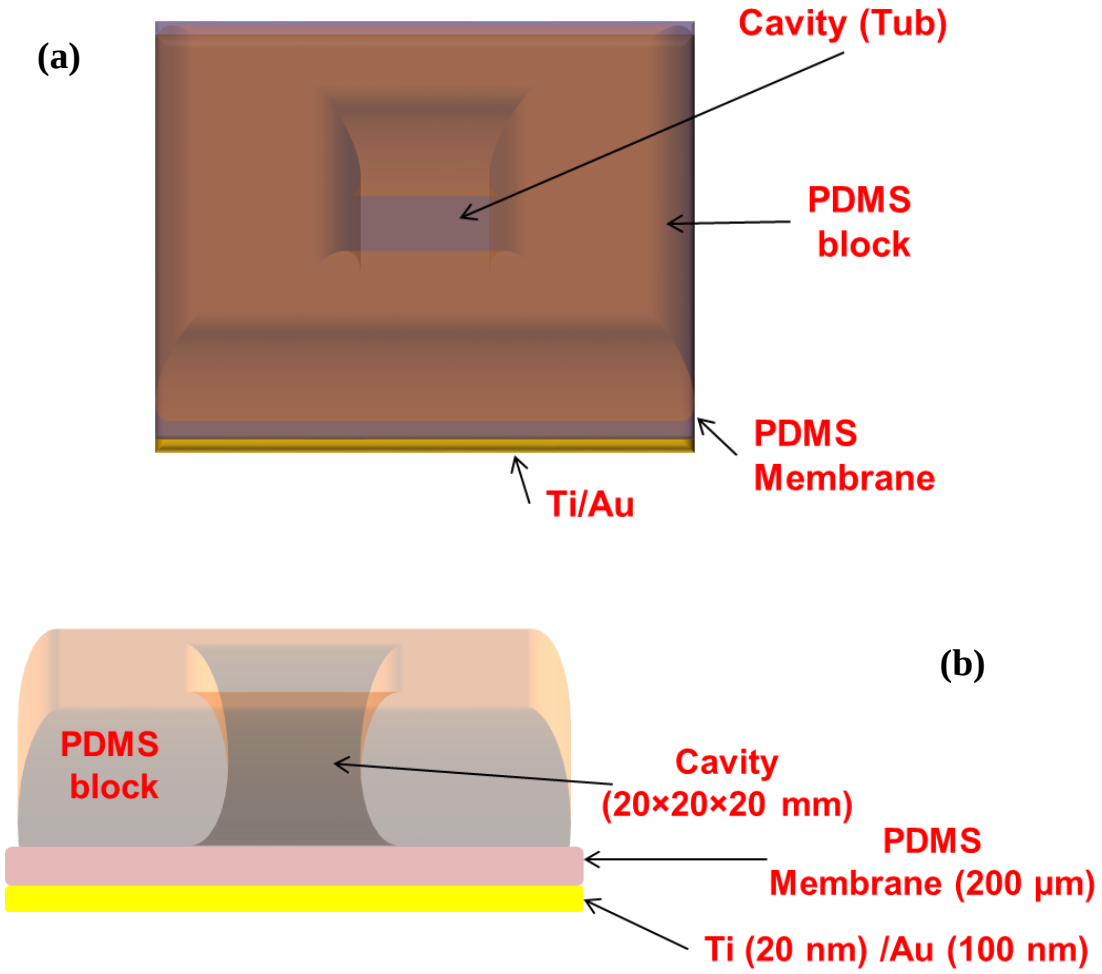


**Figure 7.6** (a) Schematics of PDMA holder, (b) cross sectional view of the schematics.

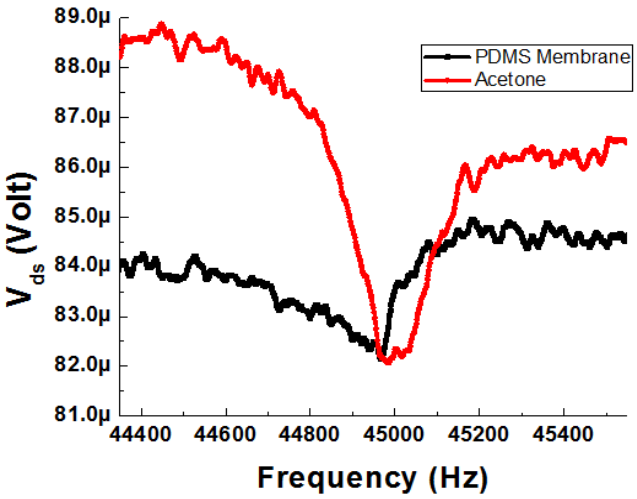


**Figure 7.7** Dynamic response of the cantilever when acetone generated acoustic wave.

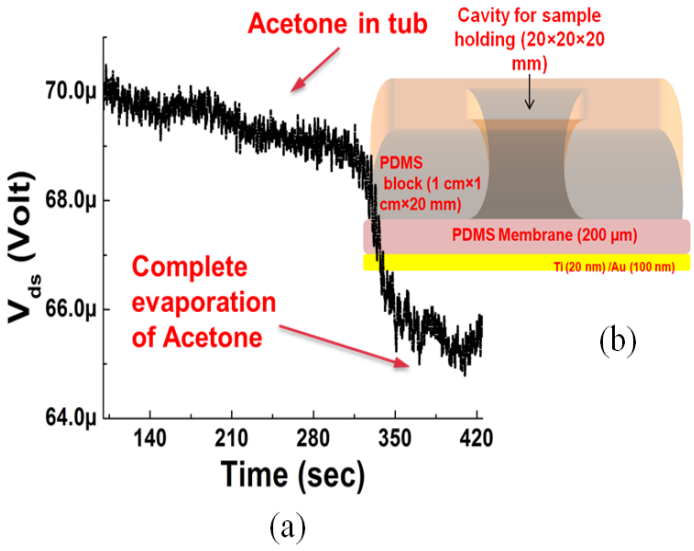


**Figure 7.8** Acetone sensing: (a) 7.13% change in voltage magnitude when acetone completely evaporates from the cavity of the PDMS block (b) The cross sectional view of the PDMS block.

## 7.3 Piezotransistive transduction of surface based PAS of chemicals

The ultrahigh sensitivity of the electrical transduction method to surface waves enabled us to perform unique detection of surface deposited analytes through photoacoustic spectroscopy. Two different analytes, polystyrene (PS) and RDX, were chosen to demonstrate photoaocustic detection using these piezotransistive microcantilevers. These analytes were deposited near the base of a microcantilever [shown in the insets of Fig. 7.9 (a) and (b)], and a tunable wavelength ($\lambda$ = 7.1 μm to 8.0 μm with 20 nm resolution, 5 mW) mid-IR quantum cascade laser (QCL, Daylight Solutions, UT-8) was focused on them and pulsed at the resonance frequency of the microcantilever (43.93 kHz). The experimental setup is shown in Fig. 7.10. In our experiments we initially deposited PS, which was later removed using a tweezer to deposit RDX at the same location. More details are provided at the end. Approximately 300 nl of both the analytes were deposited using their standard solutions (1 mg/ml) using a capillary glass tube and allowed to dry. The background signal was initially recorded from the HFET prior to analyte coating, using a lock-in amplifier, with the HFET biased at $V_{DS}$ = 0.5 V, $V_{GS}$ = -2.2 V, and $I_{DS}$ = 100 μA. The HEFT output signal recorded after analyte coating was subtracted from the background signal recorded prior to coating, to obtain the final photoacoustic spectrum of the analytes. The microcantilever oscillation amplitude varied depending on the extent of IR absorption by the deposited analyte over the mid-IR wavelength range. The IR absorption peaks of polystyrene are shown in Fig. 7.9 (a), which closely matches the representative absorption peaks reported earlier[172,173]. The IR absorption signature peaks of RDX (~300 ng) are shown in Fig. 7.9 (b), which are also in excellent agreement with previous reports[174]. From

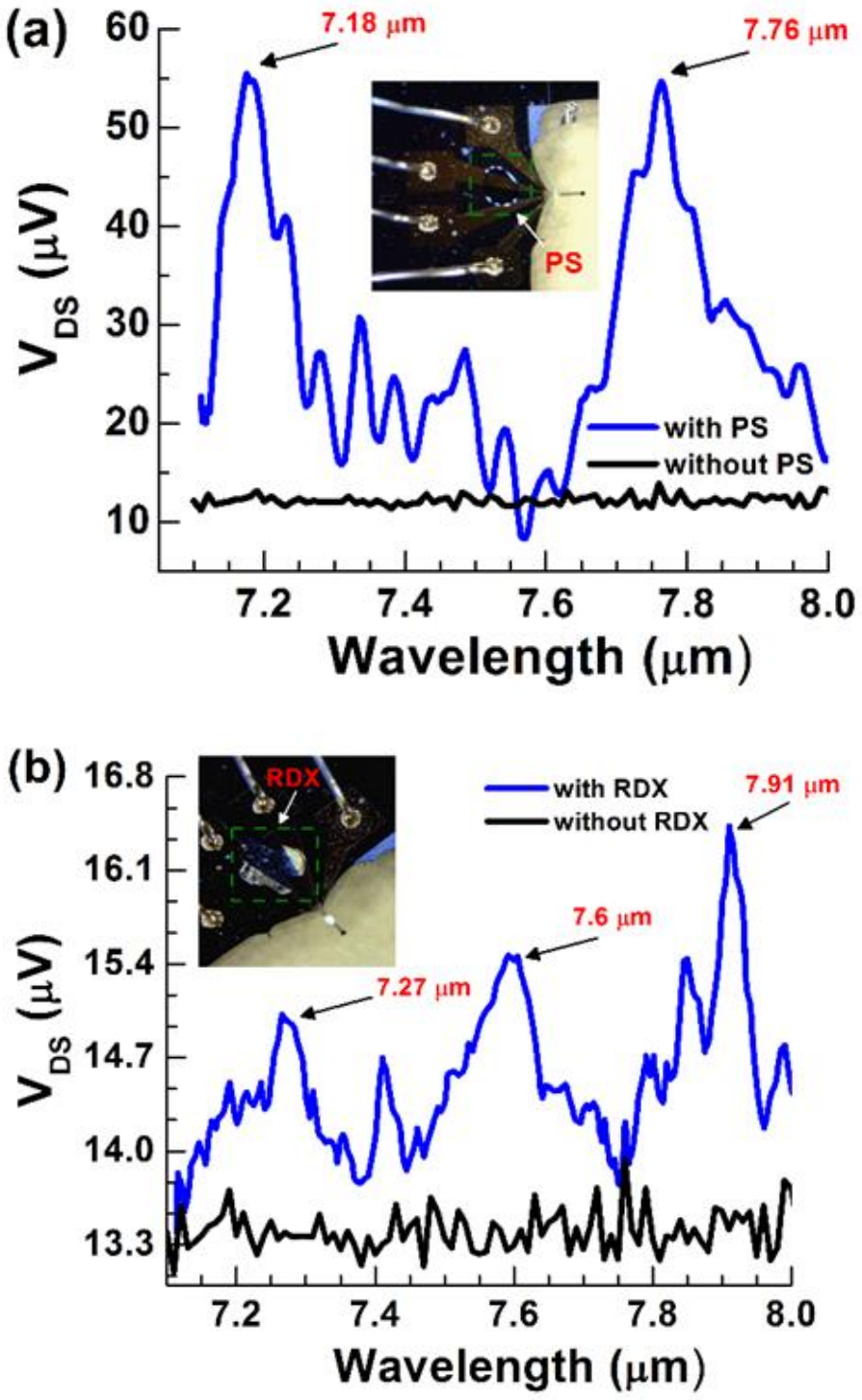


**Figure 7.9** (a) Photoacoustic spectroscopy of Polystyrene (PS) with piezotransistive transduction exhiiting two characteristic peaks at 7.18 and 7.76 μm. Inset shows the optical image of deposited PS near the base of microcantilever 1. (b) Photoacoustic spectroscopy of RDX with piezotransistive transduction revealing three characteristic peaks at 7.27, 7.6

and 7.91 μm. Inset shows the optical image of deposited RDX near the base of microcantilever 1.

Fig. 7.9 of the magnitudes of $\Delta V_{DS}$ corresponding to the signature peaks of PS and RDX the amplitude the exciting wave can be determined to be in the femtoscale range (~100 – 300 fm) using the amplitude-$\Delta V_{DS}$ correlation in chapter 6.

Mass loading on Microcantilever and thus detecting the attached mass with frequency shift is a usual trend. However it lacks in selectivity if no functionalization layer is used and if used then the reusability of the cantilever is not possible always. However we conducted a separate experiment with RDX sensing. For the detection of RDX we first followed the conventional method of frequency shifting of the microcantilever due to attached mass. Another similar cantilever with a resonant frequency of 46.36 kHz and quality factor of 210 was used. Before attaching RDX, the resonant frequency was first recorded from the HFET following the same procedure as described earlier for mechanical excitation. Then a heating cell with injection line with $N_2$ under the cell was used to vaporize RDX solution (1 mg/ml) which was put on quartz wool and the sensor was connected with the cell at 5 cm gap. Then the cell was heated up with $N_2$ blowing for about 1 minute and the frequency response was again recorded from the HFET. A frequency shift of 10 Hz was observed (see Fig. 7.11) and the corresponding attached mass was estimated as 34 pg from finite element comsol simulation. The resolvable frequency shift of 1 Hz would result in noise limited mass resolution of 3.4 pg. This method of detecting RDX lacks in selectivity considering the chance of undesirable attachment of unwanted mass

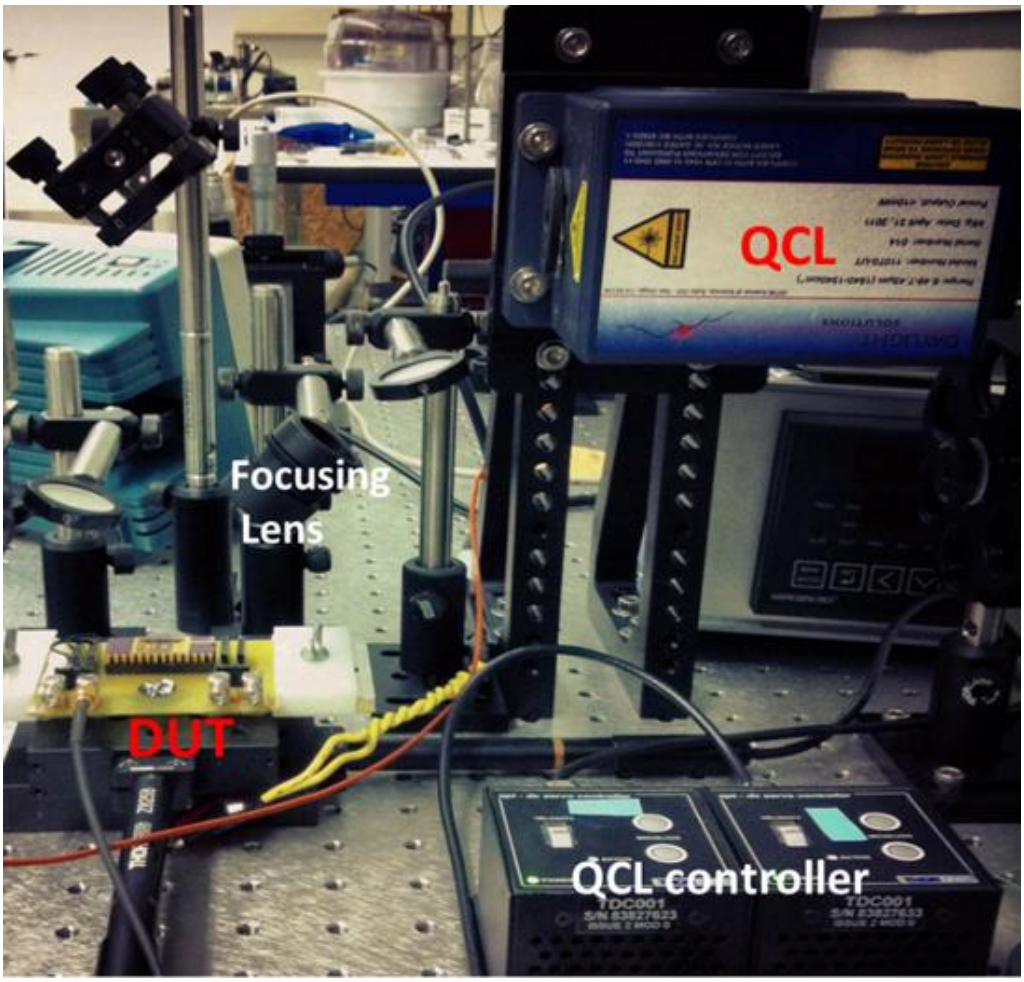


**Figure 7.10** Experimental setup for the piezotransistive microcantilever based photoacoustic spectroscopy of analytes. The analytes were deposited near the cantilever base (as shown in the insets of Fig. 7.9 (a) and (b)). The IR spot was focused on the analytes using the focusing lens arrangement. The quantum cascade laser (QCL) was pulsed at the resonance frequency of the microcantilever (43.93 kHz), and the electrical deflection signal from the HFET was measured. The QCL controller controlled the movement of both the stage and the QCL. The HFET was biased at $V_{DS}$ = 0.5 V, $V_{GS}$ = -2.2 V, and a constant $I_{DS}$ = 100 µA. The lock-in amplifier, SMU and QCL power supplies are not shown in the image.

unless a dedicated functionalization layer is not used which on the other hand limits the reusability of the cantilever. For this reason we used photoacoustic approach to detect RDX with the same cantilever which was used for the static and dynamic bending experiments

described previously. A mid IR wavelength tunable ($\lambda$ = 7.1 μm to 8.1 μm) quantum cascade laser (Daylight Solutions, UT-8) was pulsed at 43.93 kHz and focused near the base of the cantilever where 300 nl of standard RDX solution (1mg/ml) was coated using capillary glass tube. The background signal was first recorded from the HFET before the coating of RDX. After the coating of RDX, the generated acoustic wave from RDX propagated through the GaN surface initiated oscillation of the microcantilever which varied the oscillation magnitude due to the dependence of IR absorption of RDX. The HEFT output was again recorded and subtracted from the background signal. We successfully observed three IR absorption signature peaks of RDX weighted about 300 ng which exactly matches with previous study.

We would like to point out several novel aspects of the sensing methodology. First, here that for the first time we have demonstrated unique detection of small amount of surface deposited analyte using photoacoustic spectroscopy. Second, and perhaps more significantly, the detection has been possible with complete electrical deflection transduction due to the development of novel and highly sensitive piezotransistive microcantilevers operating in the tens of KHz range. Third, the microcantilever does not need to be modified in any way, and thus can remain pristine and be used repetitively. Fourth, the microcantilever can be enclosed in vacuum, which would further enhance the detection sensitivity enabling detection pictograms of analytes. Finally, an array of piezotransistive microcantilevers can be easily fabricated, which would enable rapid and simultaneous detection of a large variety of analytes with a microscale footprint.

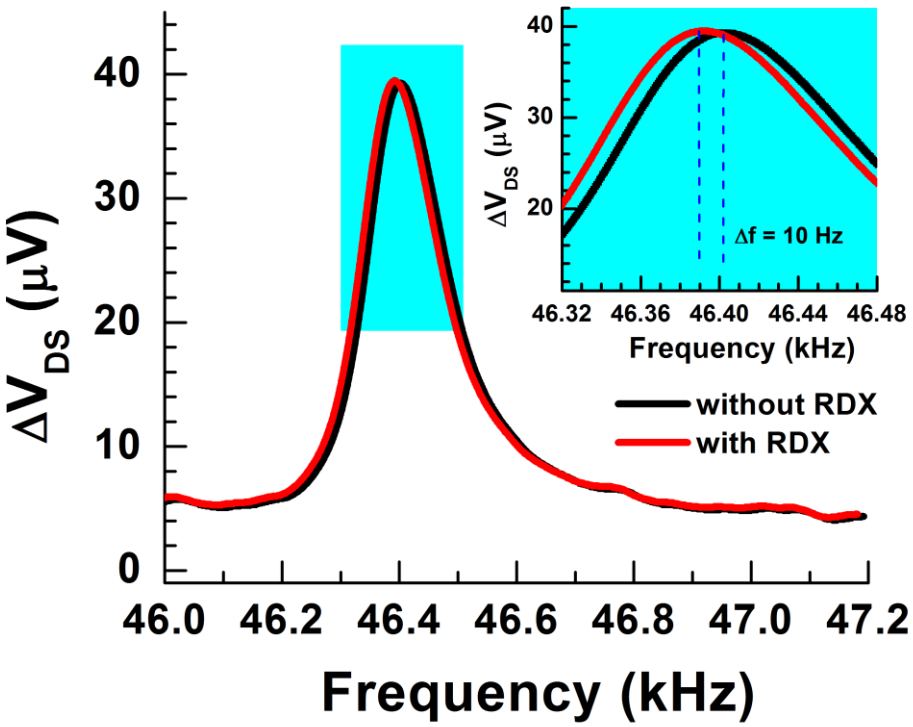


**Figure 7.11** Shift in resonant frequency of a microcantilever due to RDX mass (34 picogram) attachment on the cantilever.

# CHAPTER 8

## CONCLUSION AND FUTURE PROSPECTS

Micro/Nano cantilever based electromechanical systems (MEMS/NEMS) have fueled the development of a large variety of sensors based on changes in physical parameters such as mass, displacement, force and stress. Though optical transduction of displacement in microcantilevers offers high sensitivity, difficulty in miniaturization and high power requirements limit their usage in many of the aforementioned applications. Therefore, self-sensing microcantilevers that are capable of detecting their own deflections are highly desirable. These cantilevers have been realized using Si, and more recently, with single walled carbon nanotubes (SWCNTs) and metal-semiconductor piezoresistors, but they suffer from either low sensitivity or a complex fabrication process. Recently, a promising approach based on transistor embedded self-sensing cantilevers has been proposed, which takes advantage of the gate to enhance the deflection transduction sensitivity of a piezoresistor. AlGaN/GaN heterojunctions, which have been widely used in microwave devices, taking advantage of the high density of two dimensional electron gas (2DEG) formed at their interface, offer unique opportunity for realizing highly sensitive piezoresistors (as deflection transducers), since both the density and mobility of the 2DEG can be modulated by strain.

In this dissertation, several AlGaN/GaN piezoresistive and piezotransistive GaN microcatilevers were fabricated, which exhibited extremely high gauge factor of 8700 and an ultra-high responsivity of 1.43 nV/fm in transducing the cantilever oscillations, which is at least an order higher than state-of-the-art. The outstanding sensitivity of the microcantilevers, verified by analytical calculations and laser vibrometry measurements, enabled them to detect femtoscale acoustic wave excitation amplitudes, and demonstrate a novel surface based photoacoustic spectroscopy to detect nanogram level surface deposited analytes. These microcantilevers, which are operable over a broad range of frequencies spanning from dc to several tens of kHz fill a long standing technological void, and can have a transformative impact on a large variety of fields requiring ultrasensitive measurements, including scanning probe based imaging and MEMS/NEMS sensing applications.

## 8.1 Major contributions of this dissertation

III-V Nitride HFETs have been prevailing in microwave and power electronics, but recently their applications in sensing arena are getting broader. However, in reported works one will find the application of HFET separate to the application of III-V MEMS. Only in a handful of demonstrations, FET based MEMS/NEMS are documented.

Thus chapter 2 describes the basic but highly important background of microcantilever based MEMS and the uniqueness of AlGaN/GaN HFET. Chapter 3 presents a detail description of fabrication and associated issues of AlGaN/GaN HFET embedded GaN microcantilevers. A new process was developed to release these suspended structure with high yield. Several novel devices were fabricated which showcased more

dense integration of microcantilevers with the provision of integrating microfluidic channels. MEMS device processing with III-V Nitride was always a challenge, specially with dense profile (56 variety of microcantilevers with HFET embedded, 12 suspended devices, 8 SAW devices) compare to previous design (only 16 microcantilevers) in a same sample. Also the new wafer with half the thickness of previous GaN, proposed complexity. But this chapter would help future readers to fabricate such devices with a detail guideline.

The devices presented high sensitivity both in static and dynamic state. Chapter 4 and 5 documented the performance of those devices as highly sensitive piezoresistor and piezotransistor. High guage factor of 3500 was reported. A novel transduction method namely Piezotransistive Microcantilever was proposed to tranduce ultrasound vibrations in solid and in air medium along with surface propagated acoustic wave excitation. The devices presented high quality factor in vacuum, and the gate tunability of the HFET offered high sensitivity, low power consumption, and high signal-to-noise ratio.

Chapter 6 described several real time applications of these devices as displacement sensor, and acoustic transducer. Femtoscale displacement was sensed with high precision, linearity, and simpler transduction scheme. These devices were shown to sense static deflection of 100 nm, picometer thermal vibration and femtoscale displacement of excitation source, presenting gauge factor of 8700, voltage responsivity of 1.43 nv/fm, and a minimum detectable displacement of 9.77 fm/$\sqrt{\text{Hz}}$ . These microcantilevers were able to survive 10 MRad dose of Co-60 radiation with absolutely no degradation in HFET sensitivity and material integrity.

Finally we introduce in chapter 7, a novel scheme of photoacoustic spectroscopy was discussed, where the piezotransistive microcantilevers were shown to detect nanogram

level chemical analytes replacing conventional microphone or optical readout system. Piezotransistive Microcantilever enhanced PAS were shown to offer miniaturization, low power consumption, fast response, high sensitivity and selectivity in detecting chemicals.

## 8.2 Future prospects of this dissertation

Though a lot of work has been demonstrated including design, fabrication, and sensing applications of AlGaN/GaN HFET embedded GaN microcantilevers, this field is very new and a lot more is expected from such work. The eminent possibilities would be:

(a) To optimize the design from the fabricated devices which would offer even higher sensitivity consuming less power.

(b) Theoretical modeling of HFET response with mechanical deformation correlated with 2DEG, would be necessary to predict the performance before processing.

(c) Integration of microfluidic channel with the current devices, to facilitate surface based PAS scheme, which would be necessary to maintain continuous flow of sample and real time application.

(d) The fabricated Micro Webb could be used in PAS which would develop the system for multimodal sensing at the same time.

(e) Vacuum packaging of the devices may be done to utilize the high quality factor with higher signal-to-noise ratio.

# REFERENCES


1 Arshak, A. *et al.* Review of the potential of a wireless MEMS and TFT microsystems for the measurement of pressure in the GI tract. *Medical engineering & physics* **27**, 347-356, doi:10.1016/j.medengphy.2004.11.002 (2005).

2 Cao, B. Y., Sun, J., Chen, M. & Guo, Z. Y. Molecular momentum transport at fluid-solid interfaces in MEMS/NEMS: a review. *International journal of molecular sciences* **10**, 4638-4706, doi:10.3390/ijms10114638 (2009).

3 Chuang, W. C., Lee, H. L., Chang, P. Z. & Hu, Y. C. Review on the modeling of electrostatic MEMS. *Sensors* **10**, 6149-6171, doi:10.3390/s100606149 (2010).

4 Ni, M. *et al.* Cell culture on MEMS platforms: a review. *International journal of molecular sciences* **10**, 5411-5441, doi:10.3390/ijms10125411 (2009).

5 Cockerham, K. *et al.* Application of MEMS technology and engineering in medicine: a new paradigm for facial muscle reanimation. *Expert review of medical devices* **5**, 371-381, doi:10.1586/17434440.5.3.371 (2008).

6 Grabiec, P., Domanski, K., Janus, P., Zaborowski, M. & Jaroszewicz, B. Microsystem technology as a road from macro to nanoworld. *Bioelectrochemistry* **66**, 23-28 (2005).

7 Ingham, C. J. & van Hylckama Vlieg, J. E. MEMS and the microbe. *Lab on a chip* **8**, 1604-1616, doi:10.1039/b804790a (2008).

8 Mittermuller, M. & Volmer, D. A. Micro- and nanostructures and their application in gas chromatography. *The Analyst* **137**, 3195-3201, doi:10.1039/c2an35184f (2012).

9 Polla, D. L. *et al.* Microdevices in medicine. *Annual review of biomedical engineering* **2**, 551-576, doi:10.1146/annurev.bioeng.2.1.551 (2000).

10 Staples, M., Daniel, K., Cima, M. J. & Langer, R. Application of micro- and nano-electromechanical devices to drug delivery. *Pharmaceutical research* **23**, 847-863, doi:10.1007/s11095-006-9906-4 (2006).

11 Zhang, H., Hutmacher, D. W., Chollet, F., Poo, A. N. & Burdet, E. Microrobotics and MEMS-based fabrication techniques for scaffold-based tissue engineering. *Macromolecular bioscience* **5**, 477-489, doi:10.1002/mabi.200400202 (2005).

12 Zhou, Q., Lau, S., Wu, D. & Shung, K. K. Piezoelectric films for high frequency ultrasonic transducers in biomedical applications. *Progress in materials science* **56**, 139-174, doi:10.1016/j.pmatsci.2010.09.001 (2011).

13 Engel, A., Lyubchenko, Y. & Muller, D. Atomic force microscopy: a powerful tool to observe biomolecules at work. *Trends in cell biology* **9**, 77-80 (1999).

14 Falvo, M. R. *et al.* Nanometre-scale rolling and sliding of carbon nanotubes. *Nature* **397**, 236-238, doi:10.1038/16662 (1999).

15 Roberts, C. J., Williams, P. M., Davies, M. C., Jackson, D. E. & Tendler, S. J. Atomic force microscopy and scanning tunnelling microscopy: refining techniques for studying biomolecules. *Trends in biotechnology* **12**, 127-132, doi:10.1016/0167-7799(94)90090-6 (1994).

16 Shao, Z. & Yang, J. Progress in high resolution atomic force microscopy in biology. *Quarterly reviews of biophysics* **28**, 195-251 (1995).

17 Alvarez, M. *et al.* Nanomechanics of the formation of DNA self-assembled monolayers and hybridization on microcantilevers. *Langmuir : the ACS journal of surfaces and colloids* **20**, 9663-9668, doi:10.1021/la0489559 (2004).

18 Franosch, T. *et al.* Resonances arising from hydrodynamic memory in Brownian motion. *Nature* **478**, 85-88, doi:10.1038/nature10498 (2011).

19 Glos, D. L., Sauser, F. E., Papautsky, I. & Bylski-Austrow, D. I. Implantable MEMS compressive stress sensors: Design, fabrication and calibration with application to the disc annulus. *Journal of biomechanics* **43**, 2244-2248, doi:10.1016/j.jbiomech.2010.04.006 (2010).

20 Khemthongcharoen, N. *et al.* Piezoresistive microcantilever-based DNA sensor for sensitive detection of pathogenic Vibrio cholerae O1 in food sample. *Biosensors & bioelectronics* **63**, 347-353, doi:10.1016/j.bios.2014.07.068 (2015).

21 Kurra, N., Reifenberger, R. G. & Kulkarni, G. U. Nanocarbon-scanning probe microscopy synergy: fundamental aspects to nanoscale devices. *ACS applied materials & interfaces* **6**, 6147-6163, doi:10.1021/am500122g (2014).

22 Lee, D., Kim, S., Jeon, S. & Thundat, T. Direct detection and speciation of trace explosives using a nanoporous multifunctional microcantilever. *Analytical chemistry* **86**, 5077-5082, doi:10.1021/ac500745g (2014).

23 LeMieux, M. C. *et al.* Polymeric nanolayers as actuators for ultrasensitive thermal bimorphs. *Nano letters* **6**, 730-734, doi:10.1021/nl0525305 (2006).

24 Mashaghi, A. *et al.* Label-free characterization of biomembranes: from structure to dynamics. *Chemical Society reviews* **43**, 887-900, doi:10.1039/c3cs60243e (2014).

25 Pandya, H. J., Kim, H. T., Roy, R. & Desai, J. P. MEMS based Low Cost Piezoresistive Microcantilever Force Sensor and Sensor Module. *Materials science in semiconductor processing* **19**, 163-173, doi:10.1016/j.mssp.2013.12.016 (2014).

26 Redhu, S. K., Castronovo, M. & Nicholson, A. W. Digital imprinting of RNA recognition and processing on a self-assembled nucleic acid matrix. *Scientific reports* **3**, 2550, doi:10.1038/srep02550 (2013).

27 Saif, M. T., Sager, C. R. & Coyer, S. Functionalized biomicroelectromechanical systems sensors for force response study at local adhesion sites of single living cells on substrates. *Annals of biomedical engineering* **31**, 950-961 (2003).

28 Sepaniak, M., Datskos, P., Lavrik, N. & Tipple, C. Microcantilever transducers: a new approach in sensor technology. *Analytical chemistry* **74**, 568A-575A (2002).

29 Steffens, C. *et al.* Microcantilever sensors coated with doped polyaniline for the detection of water vapor. *Scanning* **36**, 311-316, doi:10.1002/sca.21109 (2014).

30 Teva, J. *et al.* A femtogram resolution mass sensor platform, based on SOI electrostatically driven resonant cantilever. Part I: electromechanical model and

parameter extraction. *Ultramicroscopy* **106**, 800-807, doi:10.1016/j.ultramic.2005.12.016 (2006).

31 Wang, B., Huang, F., Nguyen, T., Xu, Y. & Lin, Q. Microcantilever-Based Label-Free Characterization of Temperature-Dependent Biomolecular Affinity Binding. *Sensors and actuators. B, Chemical* **176**, 653-659, doi:10.1016/j.snb.2012.02.045 (2013).

32 Neudeck, P. G., Okojie, R. S. & Chen, L. Y. High-temperature electronics - A role for wide bandgap semiconductors? *P Ieee* **90**, 1065-1076, doi:Pii S0018-9219(02)05578-0 Doi 10.1109/Jproc.2002.1021571 (2002).

33 Wilson, S. A. *et al.* New materials for micro-scale sensors and actuators An engineering review. *Mat Sci Eng R* **56**, 1-129, doi:DOI 10.1016/j.mser.2007.03.001 (2007).

34 Mishra, U. K., Parikh, P. & Wu, Y. F. AlGaN/GaN HEMTs - An overview of device operation and applications. *P Ieee* **90**, 1022-1031, doi:Pii S0018-9219(02)05582-2 Doi 10.1109/Jproc.2002.1021567 (2002).

35 Pearton, S. J. *et al.* GaN-based diodes and transistors for chemical, gas, biological and pressure sensing. *J Phys-Condens Mat* **16**, R961-R994, doi:Pii S0953-8984(04)78067-4Doi 10.1088/0953-8984/16/29/R02 (2004).

36 Ambacher, O. Polarization induced effects in AlGaN/GaN heterostructures. *Acta Phys Pol A* **98**, 195-201 (2000).

37 Ambacher, O. *et al.* High performance polarization induced AlGaN/GaN HEMTs. *Inst Phys Conf Ser*, 483-487 (2000).

38 Ambacher, O. *et al.* Two-dimensional electron gases induced by spontaneous and piezoelectric polarization in undoped AlGaN/GaN HETS. *Inst Phys Conf Ser*, 493-497 (2000).

39 Ambacher, O. *et al.* Two dimensional electron gases induced by spontaneous and piezoelectric polarization in undoped and doped AlGaN/GaN heterostructures. *J Appl Phys* **87**, 334-344, doi:Doi 10.1063/1.371866 (2000).

40 Ambacher, O. *et al.* Two-dimensional electron gases induced by spontaneous and piezoelectric polarization charges in N- and Ga-face AlGaN/GaN heterostructures. *J Appl Phys* **85**, 3222-3233, doi:Doi 10.1063/1.369664 (1999).

41 Dimitrov, R. *et al.* Two-dimensional electron gases in Ga-face and N-face AlGaN/GaN heterostructures grown by plasma-induced molecular beam epitaxy and metalorganic chemical vapor deposition on sapphire. *J Appl Phys* **87**, 3375-3380, doi:Doi 10.1063/1.372353 (2000).

42 Murphy, M. J. *et al.* Normal and inverted AlGaN/GaN based piezoelectric field effect transistors grown by plasma induced molecular beam epitaxy. *Mrs Internet J N S R* **4**, art. no.-G8.4 (1999).

43 Wilfinge.Rj, Bardell, P. H. & Chhabra, D. S. Resonistor - a Frequency Selective Device Utilizing Mechanical Resonance of a Silicon Substrate. *Ibm J Res Dev* **12**, 113-& (1968).

44 Heng, T. M. S. Trimming of Microstrip Circuits Utilizing Microcantilever Air Gaps *IEEE Trans. Microw. Theory Tech.* **MT19**, 652-& (1971).

45 Petersen, K. E. Micromechanical Membrane Switches on Silicon. *IBM J. Res. Dev.* **23**, 376-385 (1979).

46 Binnig, G., Quate, C. F. & Gerber, C. Atomic Force Microscope. *Phys. Rev. Lett.* **56**, 930-933 (1986).

47 Itoh, T. & Suga, T. Force sensing microcantilever using sputtered zinc oxide thin film. *Appl. Phys. Lett.* **64**, 37-39 (1994).

48 Cleveland, J. P., Manne, S., Bocek, D. & Hansma, P. K. A nondestructive method for determining the spring constant of cantilevers for scanning force microscopy. *Rev. Sci. Instrum.* **64**, 403-405 (1993).

49 Lang, H. P. & Gerber, C. in *Stm and Afm Studies On* Vol. 285 *Topics in Current Chemistry* 1-27 (Springer-Verlag Berlin, 2008).

50 Thundat, T., Warmack, R. J., Chen, G. Y. & Allison, D. P. Thermal and ambient-induced deflections of scanning force microscope cantilevers. *Appl. Phys. Lett.* **64**, 2894-2896 (1994).

51 Thundat, T., Wachter, E. A., Sharp, S. L. & Warmack, R. J. Detection of mercury vapor using resonating microcantilevers. *Appl. Phys. Lett.* **66**, 1695-1697 (1995).

52 Chen, G. Y., Thundat, T., Wachter, E. A. & Warmack, R. J. Adsorption-induced surface stress and its effects on resonance frequency of microcantilevers. *Journal of Applied Physics* **77**, 3618-3622 (1995).

53 Oden, P. I., Datskos, P. G., Thundat, T. & Warmack, R. J. Uncooled thermal imaging using a piezoresistive microcantilever. *Appl. Phys. Lett.* **69**, 3277-3279 (1996).

54 Datskos, P. G. *et al.* Remote infrared radiation detection using piezoresistive microcantilevers. *Appl. Phys. Lett.* **69**, 2986-2988 (1996).

55 Wachter, E. A. *et al.* Remote optical detection using microcantilevers. *Rev. Sci. Instrum.* **67**, 3434-3439 (1996).

56 Pinnaduwage, L. A., Boiadjiev, V., Hawk, J. E. & Thundat, T. Sensitive detection of plastic explosives with self-assembled monolayer-coated microcantilevers. *Appl. Phys. Lett.* **83**, 1471-1473, doi:10.1063/1.1602156 (2003).

57 Pinnaduwage, L. A. *et al.* A microsensor for trinitrotoluene vapour. *Nature* **425**, 474-474, doi:10.1038/425474a (2003).

58 Pinnaduwage, L. A. *et al.* Detection of 2,4-dinitrotoluene using microcantilever sensors. *Sensors and Actuators B-Chemical* **99**, 223-229, doi:10.1016/j.snb.2003.11.011 (2004).

59 Hansen, K. M. *et al.* Cantilever-based optical deflection assay for discrimination of DNA single-nucleotide mismatches. *Analytical Chemistry* **73**, 1567-1571 (2001).

60 Wu, G. H. *et al.* Bioassay of prostate-specific antigen (PSA) using microcantilevers. *Nature Biotechnology* **19**, 856-860 (2001).

61 Wu, G. H. *et al.* Origin of nanomechanical cantilever motion generated from biomolecular interactions. *Proceedings of the National Academy of Sciences of the United States of America* **98**, 1560-1564 (2001).

62 Lange, D., Hagleitner, C., Hierlemann, A., Brand, O. & Baltes, H. Complementary metal oxide semiconductor cantilever arrays on a single chip: Mass-sensitive detection of volatile organic compounds. *Analytical Chemistry* **74**, 3084-3095, doi:10.1021/ac011269j (2002).

63 Thaysen, J., Boisen, A., Hansen, O. & Bouwstra, S. Atomic force microscopy probe with piezoresistive read-out and a highly symmetrical Wheatstone bridge arrangement. *Sens. Actuator A-Phys.* **83**, 47-53 (2000).

64 Yang, Y. M., Ji, H. F. & Thundat, T. Nerve agents detection using a Cu2+/L-cysteine bilayer-coated microcantilever. *J. Am. Chem. Soc.* **125**, 1124-1125 (2003).

65 Gunter, R. L., Delinger, W. G., Manygoats, K., Kooser, A. & Porter, T. L. Viral detection using an embedded piezoresistive microcantilever sensor. *Sens. Actuator A-Phys.* **107**, 219-224, doi:10.1016/s0924-4247(03)00379-0 (2003).

66 Gfeller, K. Y., Nugaeva, N. & Hegner, M. Micromechanical oscillators as rapid biosensor for the detection of active growth of Escherichia coli. *Biosens. Bioelectron.* **21**, 528-533, doi:10.1016/j.bios.2004.11.018 (2005).

67 Shih, W. Y., Li, X. P., Gu, H. M., Shih, W. H. & Aksay, I. A. Simultaneous liquid viscosity and density determination with piezoelectric unimorph cantilevers. *Journal of Applied Physics* **89**, 1497-1505 (2001).

68 Lee, J. H., Kim, T. S. & Yoon, K. H. Effect of mass and stress on resonant frequency shift of functionalized $Pb(Zr_{0.52}Ti_{0.48})O_3$ thin film microcantilever for the detection of C-reactive protein. *Appl. Phys. Lett.* **84**, 3187-3189, doi:10.1063/1.1712028 (2004).

69 Lavrik, N. V. & Datskos, P. G. Femtogram mass detection using photothermally actuated nanomechanical resonators. *Appl. Phys. Lett.* **82**, 2697-2699, doi:10.1063/1.1569050 (2003).

70 Ilic, B. *et al.* Attogram detection using nanoelectromechanical oscillators. *Journal of Applied Physics* **95**, 3694-3703, doi:10.1063/1.1650542 (2004).

71 Burg, T. P. *et al.* Weighing of biomolecules, single cells and single nanoparticles in fluid. *Nature* **446**, 1066-1069, doi:10.1038/nature05741 (2007).

72 Han, S. M., Benaroya, H. & Wei, T. Dynamics of transversely vibrating beams using four engineering theories. *J. Sound Vibr.* **225**, 935-988 (1999).

73 Burnham, N. A. *et al.* Comparison of calibration methods for atomic-force microscopy cantilevers. *Nanotechnology* **14**, 1-6 (2003).

74 McFarland, A. W. *PhD Thesis* PhD thesis, Georgia Institute of Technology, (2005).

75 Senturia, S. D. *Microsystem Design*. (Kluwer Academic Publishers, 2001).

76 Archer, R. R. *et al. An Introduction to the Mechanics of Solids*. 2nd edn, (McGraw-Hill, 1972).

77 Hu, Z. Y., Thundat, T. & Warmack, R. J. Investigation of adsorption and absorption-induced stresses using microcantilever sensors. *Journal of Applied Physics* **90**, 427-431 (2001).

78 Sasaki, N. & Tsukada, M. The relation between resonance curves and tip-surface interaction potential in noncontact atomic-force microscopy. *Jpn. J. Appl. Phys. Part 2 - Lett.* **37**, L533-L535 (1998).

79 Lavrik, N. V., Sepaniak, M. J. & Datskos, P. G. Cantilever transducers as a platform for chemical and biological sensors. *Rev. Sci. Instrum.* **75**, 2229-2253, doi:10.1063/1.1763252 (2004).

80 Blanc, N., Brugger, J., deRooij, N. F. & Durig, U. Scanning force microscopy in the dynamic mode using microfabricated capacitive sensors. *J. Vac. Sci. Technol. B* **14**, 901-905 (1996).

81 Goeders, K. M., Colton, J. S. & Bottomley, L. A. Microcantilevers: Sensing chemical interactions via mechanical motion. *Chem. Rev.* **108**, 522-542, doi:10.1021/cr0681041 (2008).

82 Amirola, J. *et al.* Micromachined silicon microcantilevers for gas sensing applications with capacitive read-out. *Sensors and Actuators B-Chemical* **111**, 247-253, doi:10.1016/j.snb.2005.07.053 (2005).

83 Dehe, A., Fricke, K., Mutamba, K. & Hartnagel, H. L. A piezoresistive GaAs pressure sensor with GaAs/AlGaAs membrane technology. *J. Micromech. Microeng.* **5**, 139-142 (1995).

84 Bykhovski, A. D., Kaminski, V. V., Shur, M. S., Chen, Q. C. & Khan, M. A. Piezoresistive effect in wurtzite n-type GaN. *Appl. Phys. Lett.* **68**, 818-819 (1996).

85 Shor, J. S., Goldstein, D. & Kurtz, A. D. Characterization of n-type beta SiC as a piezoresistor *IEEE Trans. Electron Devices* **40**, 1093-1099 (1993).

86 Witt, G. R. The electromechanical properties of thin films and the thin film strain gauge. *Thin Solid Films* **22**, 133-156 (1974).

87 Shekhawat, G., Tark, S. H. & Dravid, V. P. MOSFET-embedded microcantilevers for measuring deflection in biomolecular sensors. *Science* **311**, 1592-1595, doi:DOI 10.1126/science.1122588 (2006).

88 Akiyama, T., Staufer, U. & de Rooij, N. F. Fast driving technique for integrated thermal bimorph actuator toward high-throughput atomic-force microscopy. *Rev. Sci. Instrum.* **73**, 2643-2646, doi:10.1063/1.1488148 (2002).

89 Lange, D., Hagleitner, C., Herzog, C., Brand, O. & Baltes, H. Electromagnetic actuation and MOS-transistor sensing for CMOS-integrated micromechanical resonators. *Sens. Actuator A-Phys.* **103**, 150-155 (2003).

90 Zimmermann, T. *et al.* Piezoelectric GaN sensor structures. *Ieee Electr Device L* **27**, 309-312, doi:Doi 10.1109/Led.2006.872918 (2006).

91 Tark, S. H., Srivastava, A., Chou, S., Shekhawat, G. & Dravid, V. P. Nanomechanoelectronic signal transduction scheme with metal-oxide-semiconductor field-effect transistor-embedded microcantilevers. *Appl. Phys. Lett.* **94**, 104101 doi:10410110.1063/1.3093874 (2009).

92 Wang, J., Wu, W. G., Huang, Y. & Hao, Y. L. < 100 > n-type metal-oxide-semiconductor field-effect transistor-embedded microcantilever sensor for observing the kinetics of chemical molecules interaction. *Appl. Phys. Lett.* **95**, 124101 doi:12410110.1063/1.3231074 (2009).

93 Tosolini, G., Villanueva, G., Perez-Murano, F. & Bausells, J. Silicon microcantilevers with MOSFET detection. *Microelectronic Engineering* **87**, 1245-1247, doi:10.1016/j.mee.2009.11.125 (2010).

94 Mostafa, S. *et al.* Integrated MOSFET-Embedded-Cantilever-Based Biosensor Characteristic for Detection of Anthrax Simulant. *Ieee Electron Device Letters* **32**, 408-410, doi:10.1109/led.2010.2098015 (2011).

95 Koley, G. *PhD Dissertation* PhD thesis, Cornell University, (2003).

96 Edgar, J. H. *Properties of Group III Nitrides*. (INSPEC, 1994).

97 Bernardini, F., Fiorentini, V. & Vanderbilt, D. Accurate calculation of polarization-related quantities in semiconductors. *Phys. Rev. B* **63**, 193201, doi:193201 (2001).

98 Bernardini, F., Fiorentini, V. & Vanderbilt, D. Spontaneous polarization and piezoelectric constants of III-V nitrides. *Phys. Rev. B* **56**, 10024-10027 (1997).

99 Vurgaftman, I., Meyer, J. R. & Ram-Mohan, L. R. Band parameters for III-V compound semiconductors and their alloys. *Journal of Applied Physics* **89**, 5815-5875 (2001).

100 Qazi, M., DeRoller, N., Talukdar, A. & Koley, G. III-V Nitride based piezoresistive microcantilever for sensing applications. *Appl Phys Lett* **99**, doi:Artn 193508, Doi 10.1063/1.3657467 (2011).

101 Talukdar, A., Qazi, M. & Koley, G. High frequency dynamic bending response of piezoresistive GaN microcantilevers. *Appl Phys Lett* **101**, doi:Artn 252102Doi 10.1063/1.4772489 (2012).

102 Chu, S. N. G. *et al.* Piezoelectric polarization-induced two dimensional electron gases in AlGaN/GaN heteroepitaxial structures: Application for micro-pressure sensors. *Mat Sci Eng a-Struct* **409**, 340-347, doi:DOI 10.1016/j.msea.2005.05.119 (2005).

103 Kang, B. S. *et al.* Effect of external strain on the conductivity of AlGaN/GaN high-electron-mobility transistors. *Appl Phys Lett* **83**, 4845-4847, doi:Doi 10.1063/1.1631054 (2003).

104 Brown, J. D. *et al.* AlGaN/GaN HFETs fabricated on 100-mm GaN on silicon (111) substrates. *Solid-State Electronics* **46**, 1535-1539 (2002).

105 Liu, Q. Z. & Lau, S. S. A review of the metal-GaN contact technology. *Solid State Electron* **42**, 677-691, doi:Doi 10.1016/S0038-1101(98)00099-9 (1998).

106 Fan, Z. F. *et al.* Very low resistance multilayer ohmic contact to n-GaN. *Appl. Phys. Lett.* **68**, 1672-1674 (1996).

107 Wang, D. F. *et al.* Low-resistance Ti/Al/Ti/Au multilayer ohmic contact to n-GaN. *J Appl Phys* **89**, 6214-6217, doi:Doi 10.1063/1.1350617 (2001).

108 Cimalla, V., Pezoldt, J. & Ambacher, O. Group III nitride and SiC based MEMS and NEMS: materials properties, technology and applications. *J. Phys. D-Appl. Phys.* **40**, 6386-6434, doi:10.1088/0022-3727/40/20/s19 (2007).

109 Fu, Y. K., Gulino, D. A. & Higgins, R. Residual stress in GaN epilayers grown on silicon substrates. *Journal of Vacuum Science & Technology a-Vacuum Surfaces and Films* **18**, 965-967 (2000).

110 Tripathy, S., Lin, V. K. X., Vicknesh, S. & Chua, S. J. Micro-Raman probing of residual stress in freestanding GaN-based micromechanical structures fabricated by a dry release technique. *Journal of Applied Physics* **101**, 063525 doi:06352510.1063/1.2713089 (2007).

111 Doll, J. C., Park, S. J. & Pruitt, B. L. Design optimization of piezoresistive cantilevers for force sensing in air and water. *J Appl Phys* **106**, doi:Artn 064310Doi 10.1063/1.3224965 (2009).

112 Yu, X. M., Thaysen, J., Hansen, O. & Boisen, A. Optimization of sensitivity and noise in piezoresistive cantilevers. *J Appl Phys* **92**, 6296-6301 (2002).

113 Chu, M., Koehler, A. D., Gupta, A., Nishida, T. & Thompson, S. E. Simulation of AlGaN/GaN high-electron-mobility transistor gauge factor based on two-dimensional electron gas density and electron mobility. *J Appl Phys* **108**, doi:Artn 104502Doi 10.1063/1.3500465 (2010).

114 Koehler, A. D. *et al.* Extraction of AlGaN/GaN HEMT Gauge Factor in the Presence of Traps. *Ieee Electr Device L* **31**, 665-667, doi:Doi 10.1109/Led.2010.2048195 (2010).

115 Eickhoff, M., Ambacher, O., Krotz, G. & Stutzmann, M. Piezoresistivity of AlxGa1-xN layers and AlxGa1-xN/GaN heterostructures. *J Appl Phys* **90**, 3383-3386, doi:Doi 10.1063/1.1398602 (2001).

116 Liu, Y. *et al.* Effect of hydrostatic pressure on the current-voltage characteristics of GaN/AlGaN/GaN heterostructure devices. *J Appl Phys* **99**, doi:Artn 113706Doi 10.1063/1.2200742 (2006).

117 Yilmazoglu, O., Mutamba, K., Pavlidis, D. & Mbarga, M. R. Strain sensitivity of AlGaN/GaN HEMT structures for sensing applications. *Ieice T Electron* **E89c**, 1037-1041, doi:DOI 10.1093/ietele/e89-c.7.1037 (2006).

118 Keskar, G., Elliott, B., Gaillard, J., Skove, M. J. & Rao, A. M. Using electric actuation and detection of oscillations in microcantilevers for pressure measurements (vol 147, pg 203, 2008). *Sensor Actuat a-Phys* **148**, 472-472, doi:DOI 10.1016/j.sna.2008.08.015 (2008).

119 Ver, I. L. Practical Examples of Noise and Vibration Control - Case-History of Consulting Projects. *Noise Control Eng* **35**, 115-125, doi:Doi 10.3397/1.2827775 (1990).

120 Dang, X. Z. *et al.* Measurement of drift mobility in AlGaN GaN heterostructure field-effect transistor. *Appl Phys Lett* **74**, 3890-3892, doi:Doi 10.1063/1.124214 (1999).

121 Stampfer, C. *et al.* Nano-electromechanical displacement sensing based on single-walled carbon nanotubes. *Nano letters* **6**, 1449-1453 (2006).

122 Koley, G., Tilak, V., Eastman, L. F. & Spencer, M. G. Slow transients observed in AlGaN/GaN HFETs: Effects of SiNx passivation and UV illumination. *Ieee T Electron Dev* **50**, 886-893 (2003).

123 Li, M., Tang, H. X. & Roukes, M. L. Ultra-sensitive NEMS-based cantilevers for sensing, scanned probe and very high-frequency applications. *Nat Nanotechnol* **2**, 114-120 (2007).

124 Li, M., Tang, H. X. & Roukes, M. L. Ultra-sensitive NEMS-based cantilevers for sensing, scanned probe and very high-frequency applications. *Nature nanotechnology* **2**, 114-120, doi:10.1038/nnano.2006.208 (2007).

125 Knobel, R. G. & Cleland, A. N. Nanometre-scale displacement sensing using a single electron transistor. *Nature* **424**, 291-293, doi:Doi 10.1038/Nature01773 (2003).

126 Gil-Santos, E. *et al.* Nanomechanical mass sensing and stiffness spectrometry based on two-dimensional vibrations of resonant nanowires. *Nature nanotechnology* **5**, 641-645, doi:Doi 10.1038/Nnano.2010.151 (2010).

127 Yang, Y. T., Callegari, C., Feng, X. L., Ekinci, K. L. & Roukes, M. L. Zeptogram-scale nanomechanical mass sensing. *Nano letters* **6**, 583-586, doi:10.1021/nl052134m (2006).

128 Jensen, K., Kim, K. & Zettl, A. An atomic-resolution nanomechanical mass sensor. *Nature nanotechnology* **3**, 533-537, doi:10.1038/nnano.2008.200 (2008).

129 Fritz, J. Cantilever biosensors. *Analyst* **133**, 855-863, doi:Doi 10.1039/B718174d (2008).

130 Johnson, B. N. & Mutharasan, R. Sample Preparation-Free, Real-Time Detection of microRNA in Human Serum Using Piezoelectric Cantilever Biosensors at Attomole Level. *Anal Chem* **84**, 10426-10436, doi:Doi 10.1021/Ac303055c (2012).

131 Dai, H. J., Hafner, J. H., Rinzler, A. G., Colbert, D. T. & Smalley, R. E. Nanotubes as nanoprobes in scanning probe microscopy. *Nature* **384**, 147-150, doi:Doi 10.1038/384147a0 (1996).

132 Minne, S. C., Manalis, S. R. & Quate, C. F. Parallel atomic force microscopy using cantilevers with integrated piezoresistive sensors and integrated piezoelectric actuators. *Applied Physics Letters* **67**, 3918, doi:10.1063/1.115317 (1995).

133 Tortonese, M., Barrett, R. C. & Quate, C. F. Atomic resolution with an atomic force microscope using piezoresistive detection. *Applied Physics Letters* **62**, 834, doi:10.1063/1.108593 (1993).

134 King, G. M., Carter, A. R., Churnside, A. B., Eberle, L. S. & Perkins, T. T. Ultrastable Atomic Force Microscopy: Atomic-Scale Stability and Registration in Ambient Conditions. *Nano letters* **9**, 1451-1456, doi:Doi 10.1021/Nl803298q (2009).

135 Boisen, A., Dohn, S., Keller, S. S., Schmid, S. & Tenje, M. Cantilever-like micromechanical sensors. *Rep Prog Phys* **74**, doi:Artn 036101Doi 10.1088/0034-4885/74/3/036101 (2011).

136 Saya, D. *et al.* Si-piezoresistive microcantilevers for highly integrated parallel force detection applications. *Sensor Actuat a-Phys* **123-24**, 23-29, doi:DOI 10.1016/j.sna.2005.04.031 (2005).

137 Singh, P. *et al.* Microcantilever sensors with embedded piezoresistive transistor read-out: Design and characterization. *Sensors and Actuators A: Physical* **171**, 178-185, doi:10.1016/j.sna.2011.08.012 (2011).

138 King, W. P., Kenny, T. W. & Goodson, K. E. Comparison of thermal and piezoresistive sensing approaches for atomic force microscopy topography measurements. *Applied Physics Letters* **85**, 2086-2088, doi:Doi 10.1063/1.1787160 (2004).

139 Sun, Y., Thompson, S. E. & Nishida, T. Physics of strain effects in semiconductors and metal-oxide-semiconductor field-effect transistors. *J Appl Phys* **101**, doi:Artn 104503Doi 10.1063/1.2730561 (2007).

140 Marso, M., Bernat, J., Javorka, P. & Kordos, P. Influence of a carrier supply layer on carrier density and drift mobility of AlGaN/GaN/SiC high-electron-mobility transistors. *Applied Physics Letters* **84**, 2928-2930, doi:Doi 10.1063/1.1704854 (2004).

141 Neuzil, P., Wong, C. C. & Reboud, J. Electrically Controlled Giant Piezoresistance in Silicon Nanowires. *Nano letters* **10**, 1248-1252, doi:Doi 10.1021/Nl9037856 (2010).

142 Zhou, J. *et al.* Flexible piezotronic strain sensor. *Nano letters* **8**, 3035-3040, doi:Doi 10.1021/Nl802367t (2008).

143 Wu, J. M. *et al.* Ultrahigh Sensitive Piezotronic Strain Sensors Based on a ZnSnO3 Nanowire/Microwire. *Acs Nano* **6**, 4369-4374, doi:Doi 10.1021/Nn3010558 (2012).

144 Zhao, J. *et al.* Ultra-sensitive strain sensors based on piezoresistive nanographene films. *Appl Phys Lett* **101**, doi:Artn 063112Doi 10.1063/1.4742331 (2012).

145 Imboden, M., Williams, O. A. & Mohanty, P. Observation of Nonlinear Dissipation in Piezoresistive Diamond Nanomechanical Resonators by Heterodyne Down-Mixing. *Nano letters* **13**, 4014-4019, doi:Doi 10.1021/Nl401978p (2013).

146 Smith, A. D. *et al.* Electromechanical Piezoresistive Sensing in Suspended Graphene Membranes. *Nano letters* **13**, 3237-3242, doi:Doi 10.1021/Nl401352k (2013).

147 Rata, A. D., Herklotz, A., Nenkov, K., Schultz, L. & Dorr, K. Strain-induced insulator state and giant gauge factor of La(0.7)Sr(0.3)CoO(3) films. *Physical review letters* **100**, doi:Artn 076401Doi 10.1103/Physrevlett.100.076401 (2008).

148 Karabalin, R. B. *et al.* Piezoelectric nanoelectromechanical resonators based on aluminum nitride thin films. *Appl Phys Lett* **95**, doi:Artn 103111Doi 10.1063/1.3216586 (2009).

149 LaHaye, M. D., Buu, O., Camarota, B. & Schwab, K. C. Approaching the quantum limit of a nanomechanical resonator. *Science* **304**, 74-77, doi:DOI 10.1126/science.1094419 (2004).

150 Bunch, J. S. *et al.* Electromechanical resonators from graphene sheets. *Science* **315**, 490-493, doi:DOI 10.1126/science.1136836 (2007).

151 Sazonova, V. *et al.* A tunable carbon nanotube electromechanical oscillator. *Nature* **431**, 284-287, doi:Doi 10.1038/Nature02905 (2004).

152 Rai, A. K. & Singh, J. P. Perspective of photoacoustic spectroscopy in disease diagnosis of plants: A review. *Instrum Sci Technol* **31**, 323-342, doi:Doi 10.1081/Ci-120025569 (2003).

153 Bruszis, H. D. Physical Foundations and Application of Photoacoustic-Spectroscopy (Review). *Ind Lab+* **52**, 225-230 (1986).

154 Kirkbright, G. F. Some Applications of Photoacoustic-Spectroscopy to the Study of Chemical-Systems in the Condensed Phase - a Tutorial Review. *J Phys-Paris* **44**, 99-108, doi:DOI 10.1051/jphyscol:1983615 (1983).

155 Chrobak, L. & Malinski, M. Design and optimisation of the photoacoustic cell for nondestructive photoacoustic spectroscopy. *Nondestruct Test Eva* **28**, 17-27, doi:Doi 10.1080/10589759.2012.667408 (2013).

156 Tavakoli, M., Tavakoli, A., Taheri, M. & Saghafifar, H. Design, simulation and structural optimization of a longitudinal acoustic resonator for trace gas detection using laser photoacoustic spectroscopy (LPAS). *Opt Laser Technol* **42**, 828-838, doi:DOI 10.1016/j.optlastec.2009.12.012 (2010).

157 Ducharme, D., Tessier, A. & Leblanc, R. M. Design and Characteristics of a Cell for Photoacoustic-Spectroscopy of Condensed Matter. *Review of Scientific Instruments* **50**, 1461-1462, doi:Doi 10.1063/1.1135740 (1979).

158 Aamodt, L. C. & Murphy, J. C. Size Considerations in Design of Cells for Photoacoustic Spectroscopy .2. Pulsed Excitation Response. *J Appl Phys* **49**, 3036-3045, doi:Doi 10.1063/1.325318 (1978).

159 Aamodt, L. C., Murphy, J. C. & Parker, J. G. Size Considerations in Design of Cells for Photoacoustic Spectroscopy. *J Appl Phys* **48**, 927-933, doi:Doi 10.1063/1.323710 (1977).

160 Wu, R. H. & Su, Q. D. Progress in theories and applications on the chemistry of photoacoustic phase. *Prog Chem* **13**, 87-93 (2001).

161 Koskinen, V., Fonsen, J., Roth, K. & Kauppinen, J. Progress in cantilever enhanced photoacoustic spectroscopy. *Vib Spectrosc* **48**, 16-21, doi:DOI 10.1016/j.vibspec.2008.01.013 (2008).

162 Li, J. S., Chen, W. D. & Yu, B. L. Recent Progress on Infrared Photoacoustic Spectroscopy Techniques. *Appl Spectrosc Rev* **46**, 440-471, doi:Doi 10.1080/05704928.2011.570835 (2011).

163 Cheng, K. & Cheng, Z. Near Infrared Receptor-Targeted Nanoprobes for Early Diagnosis of Cancers. *Curr Med Chem* **19**, 4767-4785 (2012).

164 Galanzha, E. I. & Zharov, V. P. Photoacoustic flow cytometry. *Methods* **57**, 280-296, doi:DOI 10.1016/j.ymeth.2012.06.009 (2012).

165 Cristescu, S. M., Persijn, S. T., Hekkert, S. T. L. & Harren, F. J. M. Laser-based systems for trace gas detection in life sciences. *Appl Phys B-Lasers O* **92**, 343-349, doi:DOI 10.1007/s00340-008-3127-y (2008).

166 Sathiyamoorthy, K. & Vijayan, C. Photoacoustic investigations on self-organization effects in metalloporphyrins on glass substrates. *Mater Lett* **61**, 4156-4159, doi:DOI 10.1016/j.matlet.2007.01.070 (2007).

167 Elia, A., Di Franco, C., Lugara, P. M. & Scamarcio, G. Photoacoustic spectroscopy with quantum cascade lasers for trace gas detection. *Sensors* **6**, 1411-1419, doi:Doi 10.3390/S6101411 (2006).

168 Ryczkowski, J. & Pasieczna, S. Recent applications of FT-IR/PAS in surface science. *J Phys Iv* **109**, 79-88, doi:Doi 10.1051/Jp4:20030655 (2003).

169 Herbert, S. K., Han, T. & Vogelmann, T. C. New applications of photoacoustics to the study of photosynthesis. *Photosynth Res* **66**, 13-31, doi:Doi 10.1023/A:1010788504886 (2000).

170 Palmer, R. A. & Jiang, Y. Photoacoustic Molecular-Spectroscopy and Chemical Characterization. *J Phys Iv* **4**, 337-344, doi:Doi 10.1051/Jp4:1994780 (1994).

171 Amato, G., Benedetto, G., Boarino, L., Maringelli, M. & Spagnolo, R. Photoacoustic and Photothermal Deflection Spectroscopy of Semiconductors. *Iee Proc-A* **139**, 161-168 (1992).

172 Tetard, L. *et al.* Optical and plasmonic spectroscopy with cantilever shaped materials. *J Phys D Appl Phys* **44**, doi:Artn 445102Doi 10.1088/0022-3727/44/44/445102 (2011).

173 Lee, D. *et al.* Photoacoustic spectroscopy of surface adsorbed molecules using a nanostructured coupled resonator array. *Nanotechnology* **25**, doi:Artn 035501Doi 10.1088/0957-4484/25/3/035501 (2014).

174 Kim, S. *et al.* Molecular recognition using receptor-free nanomechanical infrared spectroscopy based on a quantum cascade laser. *Scientific reports* **3**, doi:Artn 1111Doi 10.1038/Srep01111 (2013).

# APPENDIX A

# PROCESS FLOW FOR CANTILEVER FABRICATION

Details of device fabrication has been described in chapter 3. This appendix gives more detail about process flow, steps required and associated parameters. First part will detail about process flow and the second part will give the description.

**Step 1: MESA Isolation**

| *Step* | *Description* | *Process Details* |
|---|---|---|
| 1.1 | $SiO_2$ mask deposition | Equipment: Uniaxis Plasma Enhanced Chemical Vapor Deposition (PECVD)<br>200 nm $SiO_2$ deposition (300 °C, $SiH_4$ = 400 sccm, $N_2O$ = 900 sccm, 900 mtorr, RF = 25 W. Deposition rate is ~ 50 nm/min). |
| 1.2 | Lithography | Photoresist: Microposit SC1827<br>Spin: 3000 rpm at 750 rpm/sec for 30 secs (thickness: ~3 µm)<br>Soft Bake: 115˚C for 5 mins on hotplate<br>(7-8 mins if put on a carrier wafer or glass slide)<br>Exposure: λ = 405 nm, UV density = 450 mJ/cm$^2$<br>Developer: MF 319 for 1:15-2:00 min<br>Hard Bake: 80˚C for 5 mins on hotplate (before ICP etc) |
| 1.3 | $SiO_2$ etch in ICP | Equipment: Plasma Therm ICP with $C_4F_8$ Plasma<br>Sample mount on 4" $SiO_2$/Si wafer with cool grease.<br>$SiO_2$ etch for 1:30 mins ($C_4F_8$ = 15 sccm, $CO_2$ = 28 sccm, Ar = 5 sccm, 5 mtorr, RF1 = 40 W, RF2 = 800W, DC=158 V. Etch rate is ~ 180-200 nm/min).<br>▪ Etch time depends upon etch rate, 1:30 min should be sufficient to etch down 200 nm $SiO_2$.<br>▪ Clean process is run between $SiO_2$ etch and GaN etch |
| 1.4 | AlGaN/GaN etch in ICP | Equipment: Plasma Therm ICP with $Cl_2/BCl_3$ Plasma<br>Sample mount on 4" $SiO_2$/Si wafer with cool grease.<br>GaN etch for 25 secs ($Cl_2$ = 32 sccm, $BCl_3$ = 8 sccm, Ar = 5 sccm, 5 mtorr, RF1 = 70 W, RF2 = 500W, DC=225 V. Etch rate is ~ 350 nm/min).<br>▪ Etch time depends upon etch rate, etching down AlGaN is enough, however further GaN etching needed to ensure total mesa isolation and visibility of the etched pattern for subsequent processing, in this case 25 sec etching was performed which confirms 150 nm etching |
| 1.5 | PR removal | Clean with Microposit 1165 resist remover, acetone, methanol, and isopropanol. Then put in 120 ˚C $H_2SO_4$ (96%) for 3 min and/or 2 min $O_2$ plasma descum<br>Equipment: Plasma Therm RIE with $O_2$ Plasma (50 sccm $O_2$, RF power 300 W) |

| | | |
|---|---|---|
| **Step 2: Top Cantilever outline** | | |
| 2.1 | $SiO_2$ mask deposition | Equipment: Uniaxis Plasma Enhanced Chemical Vapor Deposition (PECVD)<br>1 µm $SiO_2$ deposition (300 °C, $SiH_4$ = 400 sccm, $N_2O$ = 900 sccm, 900 mtorr, RF = 25 W. Deposition rate is ~ 50 nm/min). |
| 2.2 | Lithography | Photoresist: Futurrex NR71-3000P<br>Spin: 3000 rpm at 750 rpm/sec for 40 secs (thickness: ~4 µm)<br>Soft Bake: 150°C for 5 min in oven (on glass slide or Si wafer)<br>Exposure: λ = 365 nm, UV density = 280 mJ/cm$^2$,<br>Post Exposure Bake: 100°C for 5 min in oven (on glass slide or Si wafer)<br>Developer: RD6 for 35~45 secs |
| 2.3 | $O_2$ plasma descum | Equipment: Plasma Therm RIE with $O_2$ Plasma for 30 secs<br>50 sccm $O_2$, RF power 300 W |
| 2.4 | $SiO_2$ etch in ICP | Equipment: Plasma Therm ICP with $C_4F_8$ Plasma<br>Sample mount on 4" $SiO_2$/Si wafer with cool grease.<br>$SiO_2$ etch for 10 mins ($C_4F_8$ = 15 sccm, $CO_2$ = 28 sccm, Ar = 5 sccm, 5 mtorr, RF1 = 40 W, RF2 = 800W, DC=158 V. Etch rate is ~ 200 nm/min).<br>▪ Etch time depends upon etch rate, 10 min should be sufficient to etch down 1 µm $SiO_2$. |
| 2.5 | GaN etch in ICP PR removal | Equipment: Plasma Therm ICP with $Cl_2/BCl_3$ Plasma<br>Sample mount on 4" $SiO_2$/Si wafer with cool grease.<br>GaN etch for 7 mins ($Cl_2$ = 32 sccm, $BCl_3$ = 8 sccm, Ar = 5 sccm, 5 mtorr, RF1 = 70 W, RF2 = 500W, DC=225 V. Etch rate is ~ 350 nm/min).<br>▪ Etch time depends upon etch rate, with GaN etch rate of 350 nm/min, it should take 7 min to etch the remaining GaN |
| 2.6 | PR removal | Clean with Futurrex RR41 resist remover, acetone, methanol, and isopropanol. Then put in 120 °C $H_2SO_4$ (96%) for 3 min and/or 2 min $O_2$ plasma descum<br>Equipment: Plasma Therm RIE with $O_2$ Plasma (50 sccm $O_2$, RF power 300 W) |
| 2.6 | Removal of $SiO_2$ | Removal of remaining $SiO_2$ with Buffered Oxide Etch (BOE) for 20 mins |
| **Step 3: Ohmic contacts** | | |
| 3.1 | Lithography | *Same as step 2.2* |
| 3.2 | Metal depostion | Equipment: CVC E-beam metal evaporator<br>Deposition of following metal stack at pressure below $2\times10^{-6}$ torr<br>Titanium (Ti) : 20 nm, Aluminum (Al): 100 nm,<br>Titanium (Ti): 45 nm, Gold (Au): 55nm |

| | | |
|---|---|---|
| 3.3 | Metal liftoff | Metal liftoff in warm (80 ºC) RR41 resist remover and rubbing by RR41 soaked foam swab; rinse in warm acetone; squirted at by acetone, methanol, isopropanol; blow dried by $N_2$ |
| 3.4 | RTP | Equipment: SSI Rapid Thermal Annealer (RTP)<br>Purge: 8 SLPM $N_2$<br>Anneal (no $N_2$): ramp to 525 ºC at 55 ºC/sec, hold 20 sec, ramp to 825 ºC at 60 ºuntil<br>Ramp down: 8 SLPM $N_2$ until 250 ºC<br>Overshoot: 25 ºC, Limit: 900 ºC |
| **Step 4: Schottky contacts** | | |
| 4.1 | Lithography | *Same as step 2.3* |
| 4.2 | Metal deposition | Equipment: CVC E-beam metal evaporator<br>Deposition of following metal stack at pressure below $2\times10^{-6}$ torr<br>Nickel (Ni) : 50 nm<br>Gold (Au): 200 nm |
| 4.3 | Metal liftoff | *Same as step 3.3* |
| **Step 5: Probe contact pads** | | |
| 5.1 | Lithography | *Same as step 2.3* |
| 5.2 | $O_2$ plasma descum | Equipment: Plasma Therm RIE with $O_2$ Plasma for 30 secs<br>50 sccm $O_2$, RF power 300 W |
| 5.3 | Metal deposition | Equipment: CVC E-beam metal evaporator<br>Deposition of following metal stack at pressure below $2\times10^{-6}$ torr<br>Titanium (Ti): 20 nm<br>Gold (Au): 250 nm |
| 5.3 | Metal liftoff | *Same as step 3.3* |
| **Step 6: Through wafer Si etch from backside** | | |
| 6.1 | Thick $SiO_2$ mask deposition (backside) | Equipment: Uniaxis Plasma Enhanced Chemical Vapor Deposition (PECVD)<br>4 µm $SiO_2$ deposition (300 °C, $SiH_4$ = 400 sccm, $N_2O$ = 900 sccm, 900 mtorr, RF = 25 W. Deposition rate is ~ 50 nm/min). |
| 6.2 | Lithography (backside) | Photoresist: Futurrex NR5-8000P<br>Spin: 3000 rpm at 1000 rpm/sec for 40 secs (thickness: ~8 µm)<br>Soft Bake: 150˚C for 1 min on hotplate<br>**Backside alignment**<br>*Same as step 2.1* |
| 6.3 | $SiO_2$ dry etch (backside) | $SiO_2$ etch with RIE (see chapter 3 for details) |

| | | |
|---|---|---|
| 6.4 | Through wafer Si etch (backside) | Equipment: STS ICP (Bosch Process)<br>Sample mount on 4" $SiO_2$/Si wafer with cool grease.<br>Carrier wafer should have at least 9 μm PECVD oxide. Thermally grown oxide can be of lesser thickness.<br>Si etch for as many cycles as needed, typically 1000 cycles for 400 μm Si substrate.<br>Etch cycle: 10 sec ($SF_6$ = 130 sccm, $O_2$ = 13 sccm, 94 mtorr, RF1 = 10 W, RF2 = 600W,<br>Passivation cycle: 7 sec ($C_4F_8$ = 100 sccm, 94 mtorr, RF1 = 0 W, RF2 = 600W. |

**Dicing and Cleaning of Wafer:**

The top surface of the 6'' diameter AlGaN/GaN on Si wafer is spin coated with a photoresist and diced into 1.8 cm x 1.8 cm square pieces. The bottom side of the wafer is glued to a blue tape with cool grease before dicing, which is later dissolved in acetone. Then individual pieces are carefully removed from the blue tape using metal and plastic tweezers; plastic tweezers are used as they are less likely to scratch the surface. Each piece is put in hot acetone for about a minute, followed by ultrasonication in acetone for about 30 s and then it is rinsed in methanol and isopropanol. Finally the pieces are blow-dried with $N_2$ flow. Before using the pieces for fabrication, they are cleaned again individually. During the first two steps of fabrication (mesa isolation by AlGaN etch and cantilever outlining by GaN etch), the sample should be cleaned thoroughly (with sonication) in between any two steps, as plasma processes leave insoluble residues and dirt from the chamber on the sample. However, once the first metallization is done, the sample should not be sonicated ever, as it can damage the metal on the surface. But organic cleaning should be performed to reduce the chances of having organic residues before going for each lithography step.

**Photolithography:**

Karl Suss MA6/BA6 mask aligner with backside aligner is used for all alignment/exposure steps. Resist coating is done using SCS G3P8 spinner. A 1'' diameter vacuum chuck is used and the sample is placed at the center of the chuck. The chuck should be cleaned thoroughly before loading the sample as debris sitting on the surface can make the vacuum ineffective throwing away the sample. Also, the spindle of the spinner, the O-ring and the inside of the chuck should also be cleaned to ensure a good vacuum. Sometimes the groove inside the chuck may get flattened; causing serious loss of vacuum, so chucks should be checked for good grip with the spinner spindle. Before photoresist is dispensed with a pipette, first the spinner should be let run to see whether the sample is sitting firmly or not. Then photoresist should be dispensed in a way that there is no or minimum air bubbles in the dispensed resist. The whole sample should be covered up to the edge with resist, but should not be overflown. Once spinning is done, little amount of Acetone is put on a cleanroom wipe and the backside of the sample is rubbed against it to remove any photoresist that might get to the bottom of the sample. This is important because that resist could get hard during the baking process and glue the sample to the glass slide being used as a carrier plate for baking.

Next step is the hard baking. Both positive and negative resists require soft or pre-exposure bake to remove excess solvent from the photoresist which is crucial for the photolithography process. Negative resists are more sensitive to baking; important parameters are the baking temperature, time, uniformity in spatial distribution of temperature throughout the baking time.

The sample is then allowed to cool down to room temperature and is ready for exposure. The proper UV channel (wavelength) has to be selected and lamp has to be turned on for a minute before the beginning of the process to stabilize the power. Then an UV photometer is used to measure the intensity of the UV source through a transparent region of the mask. Since the exposure dose is known for a given thickness of a given photoresist, exposure time is obtained by dividing dose by measured intensity. All the parameters such as exposure time, alignment gap and contact mode (hard) are set in the mask aligner control system. A double sided scotch tape is used to load the sample of the vacuum chuck. The other method of loading a sample on the chuck is to cover the whole chuck with a blue tape, make a small hole on it and put the sample there. The blue tape holds vacuum everywhere else and provides vacuum grip to the sample; but the sample could be tilted or even moved because of the flow of air under the tape. That is why using the double sided tape is the best way to deal with it. However, care must be taken to release the sample after exposure as the sample can be tightly glued to the tape. Isopropanol can be used to soften the glue if it is too hard on the sample.

The next step is hard bake which is similar to the soft bake; parameters are given in the appendix. Then the sample is developed in a developer solution (RD6 for negative resist NR71 and MF-319 for positive resist SC1827). For both photoresists, it is good to have the samples overdeveloped for about 10-15 seconds (could be up to 40 s for NR71), but the patterns must be checked after every 5-10 s to make sure that there is no distortion. The sample is then rinsed in running de-ionized water for some time to completely remove the developer from the surface and dried with $N_2$ blow gun.

**Plasma Etching and Oxide Deposition:**

For plasma etching in ICP, the samples have to be loaded on a Si carrier wafer. The wafer should not have any cracks or signs of breakage as this plasma system (Plasma Therm ICP) has a loadlock to load wafers automatically using an arm. Also helium is flown from the bottom of the wafer to cool down, so the wafer should be able to withstand this mechanical stress. Cool grease is used to make a thin layer on the wafer and the sample is placed on and firmly pressed against it. Care must be taken to make sure that cool grease does not spread outside the sample area (i.e. do not get exposed to open air), otherwise ICP will sputter it back to the sample top surface and cause micro-masking, making the sample unusable.

Since ICP is observed to burn the photoresist, making it nearly impossible to remove any more. Also, $O_2$ plasma (descum process) cannot be used on bare AlGaN region as it will destroy the 2DEG completely. Any plasma process with $O_2$ in it MUST be avoided if AlGaN mesa is exposed to the plasma. However, hot $H_2SO_4$ (not with H2O2 or not Piranha solution) can remove some residual resist over time, but still the safest practice is to use a hard oxide mask for etching.

In order to achieve this, we deposit PECVD $SiO_2$ on top AlGaN/GaN, the thickness of the oxide is same or comparable to the thickness of AlGaN/GaN being etched. Then the oxide is coated with photoresist and patterned with photolithography. After that, the oxide is etched using $CHF_3/O_3$ plasma, turning it into a mask for the AlGaN/GaN right below it. The resist is washed away using resist remover (RR41 for negative photoresist NR71 and Mircroposit 1165 for positive photoresist SC1827). Hot $H_2SO_4$ and $O_2$ plasma in RIE can safely be used on top the oxide mask to remove any residual resist; any polymeric residue

MUST be removed before going to the next step. Finally the AlGaN/GaN layer is etched using $BCl_3/Cl_2$ plasma in ICP. It is found out that the selectivity is almost 1:1 for GaN and Si for the etch recipe, causing Si to be etched a little bit as well once GaN is etched fully. This is in general not a problem; but is important to know because without knowing this, a wrong conclusion can be made with a profilometer which would show a depth of the trench higher than the GaN thickness. That additional depth will come from etching of Si. Anyways, once all these are done, the oxide is finally washed away using buffered HF (BHF) solution.

**Metal Deposition and Lift-off:**

For metal deposition, negative resist NR71 is used. Since the GaN etching is done already, there will be deep trenches in the samples, causing edge beads to form near the trenches. But during the baking steps, they normally flat out a lot, making the patterns more uniform. After developing and drying the patterned sample, the samples are mounted on a metal chuck using Kapton tape. All four edges of each sample should be covered with the tape so that metal does not deposit at the edge; this makes the lif-off process easier and faster. The samples mounted on the chuck are then introduced into the metal evaporator (CVC E-beam evaporator). The chamber is evacuated using a cryo pumping system until pressure goes below 5 μT (< 3 μT recommended) and then different metal layers are deposited one by one. Standard procedure is to wait for 5-10 minutes in between two metal layers and to wait for 10 minutes before the chamber can be vented after the last metal layer is deposited. The samples are then removed from the chuck by peeling off the tapes completely; care should be taken not to scratch the top surface of the sample. The samples are vertically mounted on a plastic holder and put in hot RR41 resist remover. Once the metal layers peel

off, the samples are taken out and rubbed with a foam swab soaked in hot RR41. This is very important as it helps to remove the resist residues from the surface and from the trenches. Finally the samples are rinsed in hot Acetone, followed by methanol and isopropanol.

**Process flow:**

**AlGaN Mesa Isolation:**

The AlGaN mesa was isolated with $BCl_3/Cl_2$ plasma etch in Plasma-Therm ICP. 200 nm PECVD $SiO_2$ is deposited using Unaxis PECVD and positive photoresist Microposit SC1827 was used for lithography. Oxide is then etched using $CHF_3/O_2$ ICP and resist residues are removed thoroughly, followed by ~180 nm etching of AlGaN/GaN. Although AlGaN thickness is only ~15 nm, 180 nm etching is done to increase visibility of the etched layer. Too thin na film cannot be seen in the subsequent lithography step. The oxide is not removed at this stage as it is not needed to go away at this point.

**GaN Outlining:**

About ~1 μm $SiO_2$ is deposited using PECVD, Futurrex NR71 negative resist is used to pattern the GaN outline on it. The oxide etching and resist removal are done, followed by GaN over-etching (Si is also etched once GaN is etched). This over-etching is done to ensure complete removal of GaN from the trench. The oxide is then removed using BHF solution.

**Ohmic Contact:**

Ohmic contact involves a metal stack of Ti/Al/Ti/Au of thicknesses 20/100/45/55 nm. After lift-off is done, the contact is annealed in SIS RTP at 825 $^{o}$C (in two ramp steps). This also removes any residual negative resist that might be on the surface. Deposition

and annealing parameters are given in the appendix. After this step is done, the sample should never be introduced to ultra-sonication again.

**Schottky Contact:**

Schottky contact involves a metal stack of Ni/Au of thicknesses 50/200 nm. After this is done, the sample should not be heated up to high temperature (much lower than 400 $^{o}$C) as that will make Ni diffuse into the semiconductor, making it slightly ohmic.

**Probe Contact:**

Probe contact involves a metal stack of Ti/Au of thicknesses 20/250 nm. Before metallization is done, right after developing and drying the sample, a 20-30 s $O_2$ plasma should be employed to remove any resist residue sitting on the ohmic and schottky metals. The mask should be designed in a way that even with a slight misalignment, the access region (effective channel region) does not get exposed after the development.

**Bosch Process:**

See chapter 3.

# BIOGRAPHY

**Abdul Hafiz Ibne Talukdar** received the B.Sc. in Electrical and Electronic Engineering (EEE) from Bangladesh University of Engineering and Technology (BUET), Dhaka, Bangladesh, in 2008 and Masters in Science degree from the King Abdullah University of Science and Technology (KAUST), Saudi Arab, with a prestigious 'KAUST Graduate Fellow Award' in May 2011. He later joined University of South Carolina, Columbia, SC in June 2011 and worked as a research assistant towards his PhD degree in Dr. Goutam Koley's Nanoscale Electronics and Sensors Lab (NESL). At University of South Carolina, he investigated the novel Piezotransistive III-V Nitride Microcantilevers. He designed, fabricated and studied AlGaN/GaN HFET embedded Microcantilever transduction to propose a novel chemical sensing with piezotransistive microcantilever enhanced photoacoustic spectroscopy. He has published 8 journal articles in peer reviewed journals, 7 of them he is the first author and also authored 10 conference proceedings; five of them he presented in renowned conferences. One of his journals was featured as the Top 25 hottest articles in 2013 by Elsevier. He was awarded with two Travel Grants in 2012 and 2013 to present his scholarly works in the highly reputed conferences. He has a total citations of 94 with an excellent h-index of 5 and i10-index of 4. He also participated in scholarly research competition, the '3 minute Dissertation Presentation' and in 'Oral Presentation' in the 'Graduate Student Day 2014 and 2013' where he achieved Winner award in both. He is going to New Orleans, LA to represent USC in '3 minute Dissertation Presentation' at national level. He is also a member of The Institute of Electrical and Electronics Engineers (IEEE) since 2007. He has already received a full time offer almost a year and a half before his graduation, as a PTD Mod and Integration Yield Engineer in INTEL Corporation.